

# Three-Dimensional Inkjet-Printed Metal Nanoparticles: Ink and Application Development

*Jake Sadie*



Electrical Engineering and Computer Sciences  
University of California at Berkeley

Technical Report No. UCB/EECS-2017-168

<http://www2.eecs.berkeley.edu/Pubs/TechRpts/2017/EECS-2017-168.html>

December 1, 2017

Copyright © 2017, by the author(s).  
All rights reserved.

Permission to make digital or hard copies of all or part of this work for personal or classroom use is granted without fee provided that copies are not made or distributed for profit or commercial advantage and that copies bear this notice and the full citation on the first page. To copy otherwise, to republish, to post on servers or to redistribute to lists, requires prior specific permission.

THREE-DIMENSIONAL INKJET-PRINTED METAL NANOPARTICLES:  
INK AND APPLICATION DEVELOPMENT

by

Jacob Alexander Sadie

A dissertation submitted in partial satisfaction of the  
requirements for the degree of

Doctor of Philosophy

in

Engineering - Electrical Engineering and Computer Sciences

in the

Graduate Division

of the

University of California, Berkeley

Committee in charge:

Professor Vivek Subramanian, Chair  
Professor Michel M. Maharbiz  
Professor John W. Morris Jr.

Fall 2015



Abstract

THREE-DIMENSIONAL INKJET-PRINTED METAL NANOPARTICLES:  
INK AND APPLICATION DEVELOPMENT

by

Jacob Alexander Sadie

Doctor of Philosophy in Engineering - Electrical Engineering and Computer Sciences

University of California, Berkeley

Professor Vivek Subramanian, Chair

The field of printed electronics is a rapidly-emerging area of research and development primarily concerned with low-cost fabrication materials and processes for electronic devices. As conventional, silicon-based electronics continue to push the physical boundaries of scaling in order to eke out increased performance for electronic devices, the field of printed electronics instead focused on niche applications where form, function, and cost are more important than absolute performance. To date, the application of printed materials and processes has yet to make a large impact in industry. However, while the application space currently being explored is vast, certain applications within the realm of printed electronics are particularly poised for adoption to industrial processes. Namely, the application of printed conductors.

This work emphasizes this point by exploring a particular application of conductive materials of interest to the electronics industry at-large: packaging interconnects. Without high-performing, robust interconnects, packaged electronic devices and circuits may both suffer from degraded performance due to sub-par electrical performance and fail well before their expected lifetime. Therefore, the development of improved materials and processes for the purpose of fabricating electrical interconnects is of interest to all corners of the electronics community. Unfortunately, in order to fabricate these structures with printed materials and processes, the printed electronics community must first overcome a number of barriers, most of which are discussed in this work.

First, the development of stable jetting conditions for inks containing metal nanoparticles is discussed. A general yet powerful approach to the formulation of rudimentary inks is developed. In tandem with developing strategies for creating reliable inks with respect to jetting, both the solubility enhancement and bound ligand minimization of metal nanoparticles are explored in order to ultimately boost the performance of printed conductors. Using a heuristic-driven experimental approach, metal nanoparticles with very high solubility (nearly 40% by mass) and relatively low ligand content are achieved.

Next, two applications of three-dimensional printing of metal nanoparticle inks are explored. The first is the fabrication of freestanding pillars with the intention of replacing existing solder bump materials and processes. The process parameters most important to this technique, jetting frequency and substrate temperature, are thoroughly explored using both commercially-available as well as custom-made metal nanoparticle inks. In addition, characterization methods including electrical, mechanical, and chemical techniques are applied in order to investigate the sintering process for these three-dimensional features. Ultimately, the electrical and mechanical performance of freestanding pillars are shown to outcompete existing solder bump structures at process conditions that do not exceed 200 °C.

The second application explored is the development of a single-step filling and bumping process for through-silicon vias (TSVs). Using the process developed for freestanding pillars as a foundation, fully-filled TSV processes are developed and studied in detail. The effects of process parameters such as jetting frequency and substrate temperature are investigated. Finally, arrays of successfully filled and bumped TSVs are finally bonded using thermocompression flip-chip bonding and electrically and mechanically characterized. The results indicate that, indeed, printed TSVs provide robust electrical and mechanical interfaces for electronic applications.

## Acknowledgements

During my tenure as a Ph.D. student I have read many (parts of) dissertations in order to conduct my research. While there is much to learn from a dissertation (and I am certain all readers of this dissertation will find themselves enthralled in a page-turner they simply cannot put down), the section of a dissertation that I read without fail is the acknowledgements page. Earning this degree is a test of fortitude that should not be overlooked, and it is something that cannot be accomplished alone. This page is typically the only glimpse into the human side of the dissertation writer, and it is always a joy to discover who helped this writer achieve their goal.

For me, I wish to first acknowledge my adviser, Vivek Subramanian. Through his support and encouragement over the years, I have undoubtedly learned the value of taking a level-headed, thoughtful, and systematic approach to all sorts of problems, research-related or otherwise. Vivek's ability to help guide his students with just the right mixture of oversight, enthusiasm, and tough love has helped me immensely. I will always appreciate his approach to fostering his students. On top of this, he also has a great collection of scotch that you can enjoy if you ask just right.

Next, my family members, though spread far and wide across the country, have been unconditional cheerleaders for my success. My parents, sister, grandparents, and aunt and uncle have all blessed me with love and understanding as I have pursued this degree. Though I am sure there is a disconnect between their and my understanding of the specific impact of this work, the true value of my family's support lies in their belief and trust in both me and my goals. They have and always will help keep me grounded.

My research group and colleagues at Berkeley were instrumental to my success. They helped keep me on my toes and think critically about the problems I wanted to solve. Though I was surrounded by so many great people, life would have been much tougher without having the following people around. Steve Volkman, your insightfulness and willingness to continually probe deeper in order to understand the world are characteristics that I cherish and value greatly. Sarah Swisher, having you as a colleague that also valued my quirky nature and awful sense of humor helped keep me sane in the office and the lab. You cannot know how important that was for me. Himmi Nallan, without your drive and curiosity, much of this work would have been impossible. Thank you for never giving up. Dr. Niels Quack and Dr. Emory Chan, you each exemplify the ideal research collaborator through your passion, breadth of knowledge, and ability to foster the ideas of those around you. I was lucky to work with each of you.

Finally, my closest friends helped make my time as a graduate student somehow pass by at warp speed. Luke Segars, you're a friend for life and the brother I never had. Having you as my roommate has been one of the best parts of graduate school. Ryan Schoen and Tom Buckley, your ability to move in and almost immediately support me has been an incredible gift that I will not forget. And last, but most definitely not least, Rachel Traylor, meeting you three years ago certainly changed my life. Beyond your ability to push me in my academic endeavors, your friendship and love has been the most valuable addition to my personal life. You and me, together.

## Table of Contents

Chapter 1. Inkjet Printing and Semiconductor Packaging .....	1
1.1. Introduction .....	2
1.2. Semiconductor Packaging .....	6
1.2.1. Processing, Classification, and Evolution of Semiconductor Packaging.....	7
1.2.2. Advanced Packaging Structures.....	14
1.3. Inkjet Printing .....	17
1.3.1. Components of Inkjet Printer Systems.....	17
1.3.2. Inkjet Printer Classification .....	18
1.3.3. Electronic Inks for Packaging Applications .....	23
1.3.4. Ink-Nozzle and Ink-Substrate Interactions .....	27
1.4. Dissertation Outline.....	32
Chapter 2. Controlled Jetting Performance of Nanoparticle-based Ink Formulations ....	33
2.1. Introduction .....	34
2.1.1. Fundamental Operation of Piezoelectric Inkjet Nozzles.....	34
2.1.2. Droplet Formation in Piezoelectric Inkjet Nozzles.....	38
2.2. Custom Ink Formulation for Jettability Experiments .....	42
2.2.1. Materials .....	42
2.2.2. Ink Fluid Characterization Procedures.....	42
2.2.3. Jettability Definition and Characterization Framework.....	43
2.3. Jettability Window and Ink Design Rules.....	47
2.3.1. Ca-We Jettability Window.....	47
2.3.2. Modulating Jettability via Co-Solvent Addition .....	48
2.3.3. Modulating Jettability via Nanoparticle Loading.....	51
2.3.4. General Ink Formulation Design Rules.....	52
2.4. Summary.....	54
Chapter 3. Metal Nanoparticle Solubility Enhancement via Heuristic Optimization .....	55
3.1. Introduction .....	56
3.1.1. Metal Nanoparticle Solubility .....	56
3.1.2. Heuristic Optimization.....	58
3.2. Metal Nanoparticle Synthesis.....	61
3.2.1. Standard Synthesis .....	61
3.2.2. High-Throughput Robotic Synthesis .....	62
3.2.3. Characterization .....	65

3.3.	Heuristic Optimization Study .....	68
3.3.1.	Parameter Space.....	68
3.3.2.	Baseline Tests .....	68
3.3.3.	Multi-generation Optimization .....	71
3.4.	Summary.....	75
Chapter 4.	Inkjet-printed Pillars for Solder Bump Replacement .....	76
4.1.	Introduction .....	77
4.1.1.	Pillar Critical Dimension and Pitch Requirements.....	77
4.1.2.	Pillar Process and Performance Metrics.....	78
4.2.	Three-dimensional Inkjet Printing Processes .....	80
4.2.1.	Printing .....	80
4.2.2.	Sintering .....	83
4.3.	Three-dimensional Inkjet Printing Freestanding Pillars .....	84
4.3.1.	Materials.....	84
4.3.2.	Characterization .....	84
4.3.3.	Process Development with Commercial Gold Nanoparticle Ink.....	86
4.3.4.	Process Advancement with Custom Silver Nanoparticle Ink.....	98
4.4.	Summary.....	105
Chapter 5.	Inkjet-printed Through-silicon Vias for Chip Stacking .....	106
5.1.	Introduction .....	107
5.1.1.	TSV Critical Dimension and Pitch Requirements.....	107
5.1.2.	TSV Process and Performance Metrics.....	108
5.2.	Three-dimensional Inkjet Printing Through-silicon Vias (TSVs) .....	111
5.2.1.	Materials.....	111
5.2.2.	Characterization .....	112
5.2.3.	Process Development with Commercial Gold Nanoparticle Ink.....	113
5.3.	Summary.....	121
Chapter 6.	Conclusions and Outlook.....	122
6.1.	Nanoparticle-based Ink Formulation .....	123
6.1.1.	Review.....	123
6.1.2.	Future Work.....	123
6.2.	Heuristic Optimization of Nanoparticle Solubility and Chemistry .....	125
6.2.1.	Review.....	125
6.2.2.	Future Work.....	125
6.3.	Three-dimensional Inkjet Printing for Semiconductor Packages .....	127

6.3.1. Review.....	127
6.3.2. Future Work.....	127
6.4. Conclusion .....	129
References.....	130
Appendix A.....	139
Appendix B.....	140
Appendix C.....	142
Appendix D.....	144
Appendix E.....	153

# Chapter 1. Inkjet Printing and Semiconductor Packaging

---

Over the past half-century, the semiconductor industry has revolutionized the world by relentlessly advancing the capabilities of electronics. What makes electronics so attractive is their ability to perform very complicated computational tasks with extreme speed, performance, and reliability. Indeed, from simple discrete transistors to monolithic integrated circuits to multi-component systems, the progress of the semiconductor industry has ushered in incredible technologies that have changed the operation of individuals, businesses, economies, and society as a whole. Further, the demand for electronics to become even more pervasive and ubiquitous has only continued to grow with time. These demands will require the careful re-examination of the current materials and processes used for electronic fabrication. In some cases, simple process tuning may suffice to meet the new performance demands. However, in many cases, it is likely that new processes and materials may be necessary to meeting the demands. This dissertation will explore the latter scenario.

## 1.1. Introduction

Modern integrated circuits are very complicated. Figure 1.1 shows a schematic view of the many layers that exist in a modern integrated circuit. First, there is typically a logic layer that may easily include over a billion nanoscale silicon transistors. Next, numerous metal layers that provide local metal interconnections between these transistors exist above the logic layer. Finally, a single layer that provides interconnections between the networked transistors and external components lies at the top of the stack. This complicated structure grew out of many years of advancements to become what it is today. The interdisciplinary nature of the semiconductor industry is a large reason for the incredible advancements that have occurred over the past five decades. Advances in physics, chemistry, materials science, manufacturing, and many other disciplines were critical to realizing the modern, silicon-based electronic devices in existence today. These disciplines will also be critical to realizing new materials, processes, and devices that will drive future applications of integrated circuits.

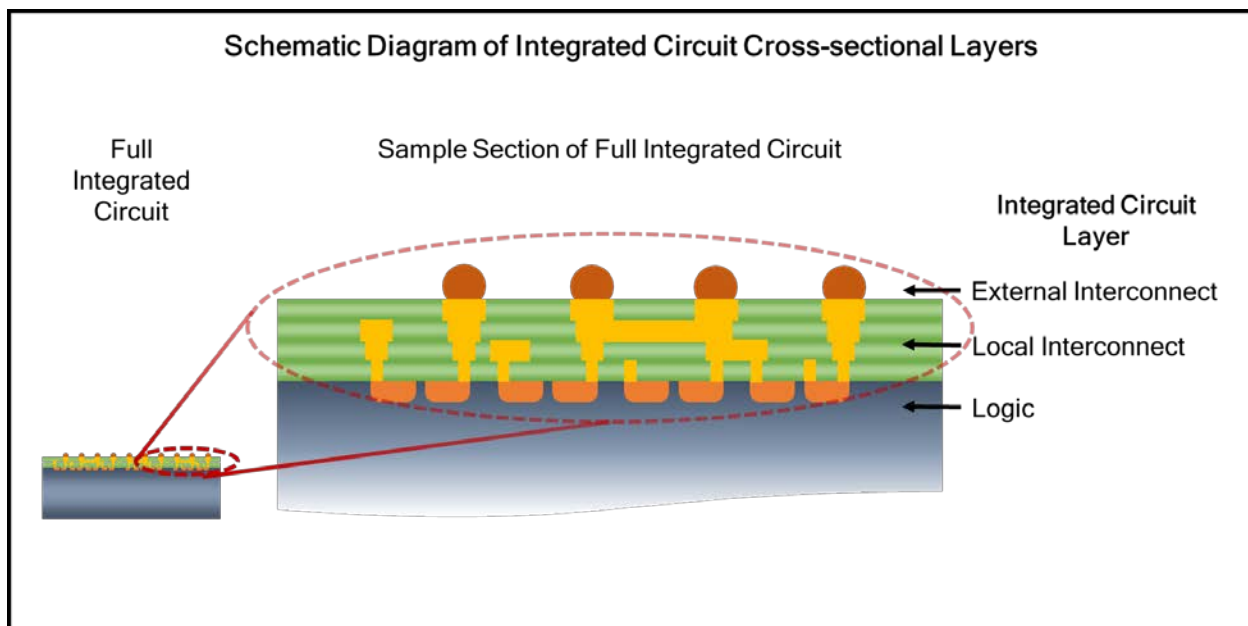


Figure 1.1. Schematic diagram of a modern integrated circuit showing the logic, local interconnection, and external interconnection layers.

The seemingly unabated performance enhancement of integrated circuits over time has mainly been achieved by the continuous shrinking of the individual transistors that comprise the one billion or more transistors in microprocessors. However, there are two key reasons why simply continuing to shrink transistors will not suffice for the realization of future electronics. First, as transistors have continued to scale down well below the single micron scale, the expected boost in transistor performance has begun to diminish with each generation. Therefore, the performance of other components of the integrated circuit must be considered when determining the performance of the integrated circuit as a whole. As such, the electrical interconnections between the transistors as well as between the integrated circuit and external components have rapidly assumed larger roles in determining the system performance. Second, many demands for new electronic-based applications no longer require supreme performance as much as they

require novel platforms and capabilities that are not easily deliverable by monolithic silicon processing. An example might be the integration of a microprocessor with a flexible substrate or the direct integration of optoelectronic devices with conventional silicon logic devices. These new, non-traditional integration schemes will still demand low cost and high reliability. To date, incremental modifications to conventional semiconductor manufacturing materials and processes have been capable of meeting the cost, performance, and reliability demands of electronic applications. However, the time is now ripe for the introduction of new materials and processes in order to realize these future demands for both traditional as well as novel electronic form factors.

The integrated circuit layer common to all of these applications is the top-most external interconnection layer that serves to interconnect the functional logic with external components. This layer is considered the beginning of what is referred to as the electronic package. The package's role is to electrically and mechanically connect the logic chip with a secondary mount board that allows for the very small interconnects to fan out into larger connections more amenable for direct connection with circuit boards. The package is also often hermetically sealed in order to prevent degradation over time, however the heart of the package is the interconnect layer that bridges the gap between the logic chip and the secondary mount board. The scale, density, material, and shape of these interconnects has varied often throughout the years. Today, the most common interconnections are gold wire bonds and lead-tin eutectic solder bumps. While these materials have been sufficient for decades, performance limitations, health concerns (primarily for the lead-containing eutectic), and form factor limitations have all led to interest in new processes and materials for electronic package interconnects.

Despite their lower conductivity relative to gold used in wire bonds, eutectic solders are widely used in the semiconductor packages. The reason for this is that they allow for a bonding process called flip-chip bonding, which requires a peak process temperature of roughly 200 °C. The primary benefit of the flip-chip process is the potential to achieve a smaller package footprint when compared to wire bonding processes. However, eutectic materials suffer from lower conductivity and worse electromigration performance. Therefore, materials and processes that aim to replace these interconnects must meet and exceed these limitations while maintaining process temperatures that do not exceed current thermal budgets.

An interesting material that might satisfy all of these conditions is a metal nanoparticle or, more specifically, a colloidal suspension of metal nanoparticles. These particles are often encapsulated with carbon-based materials that bind to the nanoparticle core. When subjected to moderate heat treatments, these bonds break and allow the nanoparticle cores to diffuse and sinter together. This process is facilitated by a property unique to metal nanoparticles called melting point depression, whereby the very high surface area-to-volume ratio of the metal nanoparticle results in a dramatic decrease in the material's melting point. Using these materials, therefore, it may be possible to fabricate three-dimensional structures that act as replacement features for eutectic solder bumps that ultimately provide higher conductivity, improved electromigration resistance, and decreased process temperatures.

The next issue, however, is determining how these metal nanoparticle suspensions are processed and whether or not these processes are reasonable alternatives to conventional blanket film deposition/lithography processes associated with eutectic solder bump fabrication. Because the suspensions are liquid in nature, solution processing techniques have been the primary route to distributing and patterning these materials. Solution processing includes blanket films deposited with spin processes or aerosol jet processes and patterned films deposited using gravure printing, inkjet printing, and stencil printing, to name a few.

Because the desired feature is a three-dimensional structure, non-contact techniques will be required in order to deposit large features. Furthermore, because an effort should be made to eliminate the patterning and etching steps associated with blanket film process flows, only processes that allow for direct patterning should be considered. This leaves inkjet printing as the obvious method for the fabrication of these features. While inkjet printing does not boast the lowest minimum feature size of the patterned solution processing techniques listed, the feature sizes capable with inkjet printing directly overlap with both the current and future demands for the interconnect features. Therefore, assuming processes can be successfully developed, inkjet printing stands out as a well-suited process alternative for interconnect fabrication.

Inkjet printing, however, is a process technique that requires a substantial amount of development in order to realize the desired features, even for planar patterns. Much of the process development revolves around the interactions between the ink and the nozzle and between the ink and the substrate. With respect to metal nanoparticle inks, many exist in commercial capacities, indicating the demand and interest for such materials and processes. However, these commercially-available inks may or may not be well-matched with the target application of fabricating three-dimensional structures. Therefore, both process and material development may be necessary to realize this goal.

Indeed, this material and process development is the central focus of this dissertation. This will include investigations into a number of the challenges associated with realizing these three-dimensional features with inkjet-printed metal nanoparticle inks. For example, developing custom ink formulations is of specific interest because it should directly lead to higher electrical and mechanical performance. Ink formulation for nanoparticle-based inks involves both the appropriate solvent selection as well as the optimization of the nanoparticle material itself, and each of these will also be discussed in detail. Further, the process development for three-dimensional fabrication is critical to the realization of packaging structures. Both the process development as well as characterization of fabricated structures are important aspects of this problem, and will be discussed at length in the later chapters of this dissertation.

Before visiting these specific problems, however, the remainder of this chapter will introduce key concepts related to both semiconductor packaging as well as inkjet printing. The topics discussed here will include common materials, processes, and the state-of-the-art for each individual subject. In addition, the future demands for semiconductor packaging discussed will help establish the high potential for inkjet-

printed metal nanoparticles to be a viable alternative to conventional materials and processes.

## 1.2. Semiconductor Packaging

Semiconductor packaging is the term often used to describe both the structures and processes that serve to establish robust mechanical and electrical connections between an integrated circuit(s) and a discrete component(s) to form a larger system [1]. Figure 1.2 helps demonstrate the relationship between the integrated circuit, interconnects, the package, and a multi-component system. Without a package, communication between the circuit and components of the larger system would be impossible. In addition to providing electrical and mechanical connections, packaging often also serves to isolate the environment in which the integrated circuit resides from the environment in which the system exists. Therefore, vapor permeation resistance and thermal management are additional functions of semiconductor packages.

For many decades, the overall performance of an integrated circuit was primarily determined by the performance of the semiconductor devices within the circuit. However, as integrated circuits have grown in complexity due to the relentless scaling of the past half-century, the packages housing these circuits have likewise become increasingly complex and the performance of modern packages has assumed an increasingly large factor in overall system performance [2]. Not only must modern packages facilitate communications with integrated circuits containing billions of transistors, but they must also dissipate an incredible amount of heat, provide mechanical durability, and be thin enough to fit into extremely small spaces such as mobile phones. Thus far packages have successfully evolved by both incorporating new materials and adopting new form factors. The following sections will first describe the fundamental components of traditional semiconductor packages and then describe the advanced packaging structures under current development in order to meet the growing demands of highly-scaled integrated circuits.

Since the beginning of semiconductor industry in the 1960s, packaging processes have been vital to incorporating integrated circuits into complex systems. While the packages have advanced and kept pace with the rapidly evolving integrated circuits to date, the continuing demand for computational performance will very soon require new materials and new processes to meet the demands of next-generation packages. Though alternative materials and processes are already being actively explored using conventional fabrication techniques, the potential for novel materials such as metal nanoparticles and new manufacturing processes such as inkjet printing to meet next-generation packaging requirements have not been considered. Before considering these materials and applications, let us first consider the conventional materials and processes commonly found in semiconductor packaging.

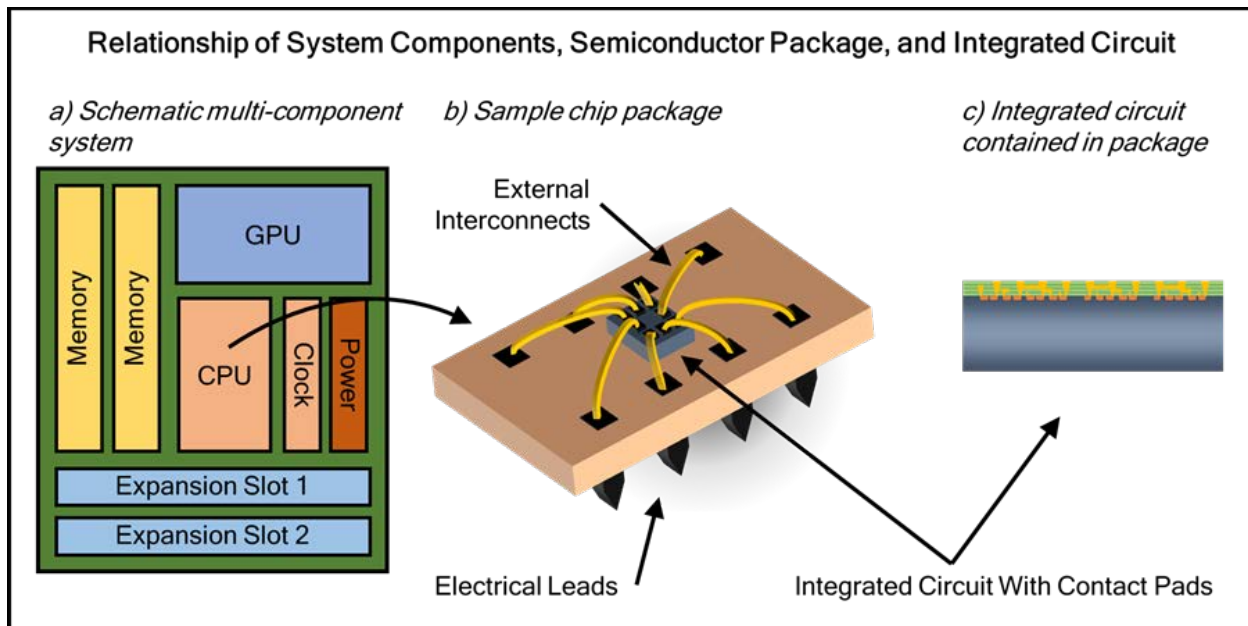


Figure 1.2. Relationship between a) a multi-component electronic system, b) a single package, and c) the integrated circuit housed within a package.

### 1.2.1. Processing, Classification, and Evolution of Semiconductor Packaging

A semiconductor package can be thought of as a system with the following three electrical components: 1) an integrated circuit with small electrical contact pads at the upper-most layer, 2) large electrical leads/pins that interface with the external system, and 3) interconnects that attach the small pads to the large leads/pins. Figure 1.2b highlights these three specific components. (Though it also serves a vital role with respect to package reliability, because it is not an electrical component of the package, not pictured in this schematic is a plastic molding used to encapsulate each package after interconnects are created.) Over time, the increased scaling of the integrated circuit component has resulted in two major constraints on packages. First, the number of electrical leads required to realize the complete functionality of the integrated circuit has increased as a direct consequence of the increase in number of transistors included in integrated circuits. Second, due to ever-changing constraints on the application intended for these scaled integrated circuits, more often than not the package footprint and height are also often scaled down with each generation. Therefore, with time, different processes, materials, and form factors of packages have been developed in order to meet these demands.

#### A. *Semiconductor Packaging Processes: Die Attach and Bonding*

As Figure 1.2b indicates, each package includes a single integrated circuit chip. These chips typically have a footprint of a few  $\text{mm}^2$ . However, because integrated circuits are typically fabricated on very large wafers, the first step in packaging an integrated circuit is dicing the wafer into individual die and then placing these die directly onto the package substrate. The placement and bonding of these die is typically accomplished by high-speed pick-and-place tools called die bonders. The most common materials used to bond the die to the package substrate are epoxies, solders, or eutectics formed directly between the die back side and the substrate metallization [3].

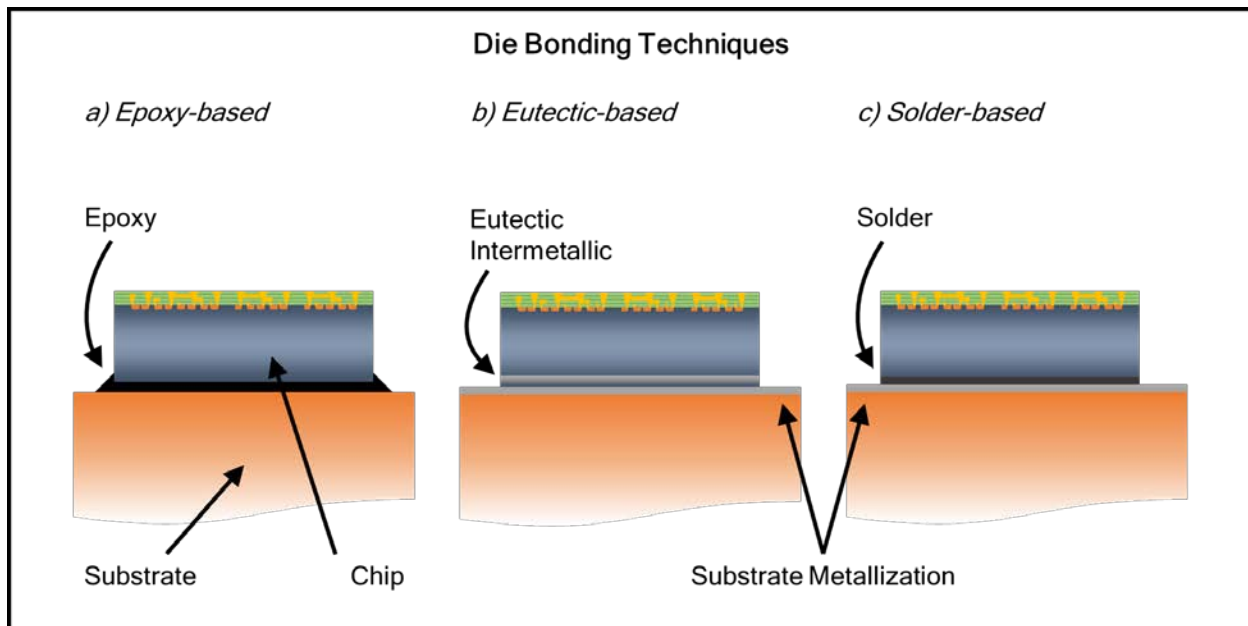


Figure 1.3. a) Epoxy-based, b) Eutectic-based, and c) Solder-based die bonding techniques common to electronic packaging.

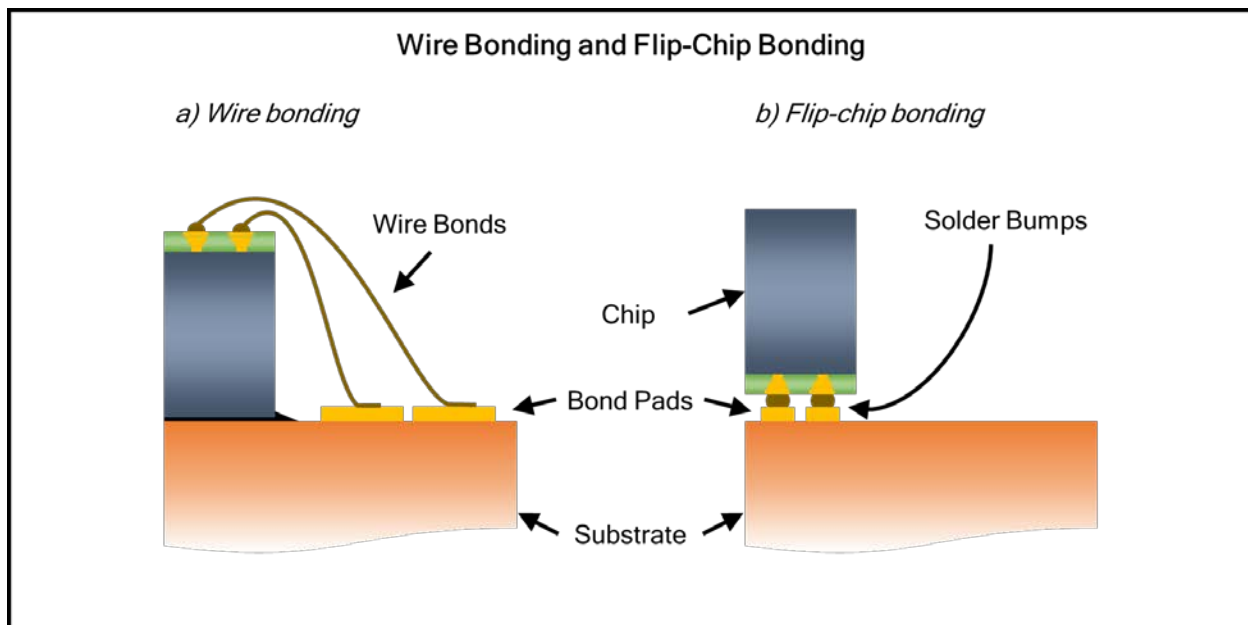


Figure 1.4. Comparison of the two most common package interconnect methods: a) wire bonding and b) flip-chip bonding.

Figure 1.3 shows a schematic comparison of each of these bonding schemes. Note that in each situation, the fabricated die is oriented such that contact pads are facing upward. In the epoxy-based technique, an epoxy is sandwiched between the die and the substrate, which later hardens to provide a robust mechanical fixture. In eutectic bonding schemes, the silicon chip is either left bare or metallized on the back side. After the chip is placed onto a metallized substrate pad, the interface is heated and a eutectic intermetallic layer is formed. Finally, solder-based bonding schemes involve placing the

die onto a solder layer deposited onto a metallized substrate. After heating, the solder reflows to form a mechanical connection. The benefit of each of the final two bonding techniques is that a metal connection is created between the die and package, which allows for improved heat dissipation during operation.

While die bonding is an important aspect of packaging, as mentioned earlier, the heart of the package is the electrical interconnect. Without this component, communication between the logic and the outside world would be impossible. As packages have evolved over the years, the primary driver for advances in packaging performance and size have been enabled by advances in metal interconnection techniques [4]. The two techniques that are the main drivers in this field are wire bonding and, more recently, flip-chip bonding. Figure 1.4 provides a schematic comparison of each of these types of bonds.

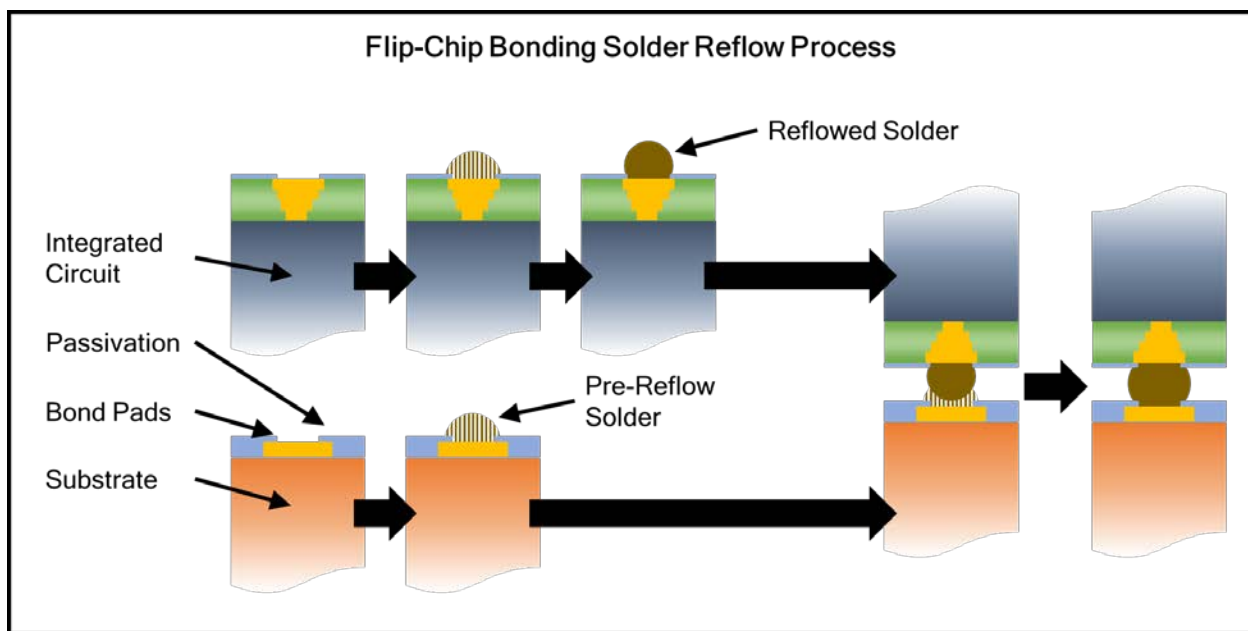


Figure 1.5. Solder reflow process in flip-chip bonding. Both the integrated circuit and substrate are passivated such that only the bond pads are exposed. After solder deposition onto each of the bond pads, the integrated circuit solder bumps are reflowed to create solid solder balls. The integrated circuit is flipped onto the non-reflowed solder bumps on the substrate and a final reflow process creates the chip to substrate bond.

Wire bonding is by far the most common method for creating electrical contacts between the integrated circuit and the electrical leads of the package. The wire bonding process involves making connections between the integrated circuit bond pads and the package bond pads by feeding a wire through a custom tool that automatically bonds and breaks the wire. These interconnections extend upward and outward from the integrated circuit bond pad and land on a pre-existing lead within the package as shown in Figure 1.4a. The materials used in wire bonding tend to be highly conductive metals such as gold and copper and the minimum feature sizes of these interconnects can approach 10  $\mu\text{m}$ . While small, highly conductive features are clearly attractive when it comes to packaging highly-scaled integrated circuits, the main drawback of wire bonding is that connections

are restricted to the periphery of the package. Two factors are responsible this limitation. First, making many bonds near the center of the chip may be difficult because they would start to intersect the potentially short the bonds along the edge of the chip. Second, the centrally-located bonds would require the wire to extend higher above the chip, imposing additional limitations on the package design. Another drawback of wire bonding is the serial nature of the process. Because only one bond can be formed at a time, it is very difficult to parallelize the process and improve throughput.

Alternatively, flip-chip bonding using eutectic solders is able to overcome many of the limitations of wire bonding. The flip-chip structure is highlighted in Figure 1.4b. The biggest difference of note in flip-chip bonding is that chips are oriented such that the integrated circuit bond pads are facing downward. Figure 1.5 outlines the bonding process for eutectic solder bumps used in flip-chip bonding. In order to successfully bond the integrated circuit bond pads to the package bond pads, solder paste is first placed onto each bond pad on the chip as well as the package. This is usually accomplished with a stencil printing process. Then, the chip is heated using a carefully controlled heat treatment to the solder's eutectic temperature. For lead-tin solder, the most commonly used solder, this is 183 °C. At this temperature, the eutectic material changes from a solid to a liquid phase. Due to differential wetting between the bond pad and the passivation layer on the chip, the liquid forms a ball. This process is called reflow. After cooling, the solder solidifies. Then, using special tool, the chip is picked up and placed upside-down onto the bond pads of the package substrate. A final reflow process occurs, resulting in a robust electrical and mechanical connection between the two bond pads. This process would not be possible without the use of eutectic materials. However, when compared to wire bonding, solder materials tend to be less conductive. Despite this, solder bumping remains a very interesting alternative to wire bonding, primarily because it a) allows for interconnections to be created across the entire surface area of the chip and b) is a process that is much more parallel wire bonding. That is, all of the solder bumps can be deposited, reflowed, and bonded in a three distinct process steps. For these reasons, and more to be discussed in subsequent sections, flip-chip bonding is a very attractive process for creating chip-to-package interconnects.

### *B. The Evolution of Packaging Form Factors*

As mentioned previously, packages have thus far successfully evolved to meet continuously-evolving performance and size demands. The clearest way to observe this evolution is to compare both the form and the count of the electrical leads in packages as a function of integrated circuit transistor count. Figure 1.6 shows the exponential growth of integrated circuit transistor count as a function of time (often referred to as Moore's Law [5]) for a number of Intel processors and the exponential growth of the electrical leads for the corresponding packages. In addition to the increasing number of connections, the form of these leads have evolved from simple dual in-line packages (DIPs) to pin grid arrays (PGAs) to ball grid arrays (BGAs) to land grid arrays (LGAs) over time. Figure 1.7 shows a sample image of each of these package types. As these images indicate, the size, shape, density, and absolute count of connections evolved with each generation. DIPs are capable of creating up to 64 connections between the integrated circuit and the external system, whereas LGAs are capable of achieving over

2000 connections in a similar footprint. Table 1.1 presents a comparison of the capabilities of these different package form factors.

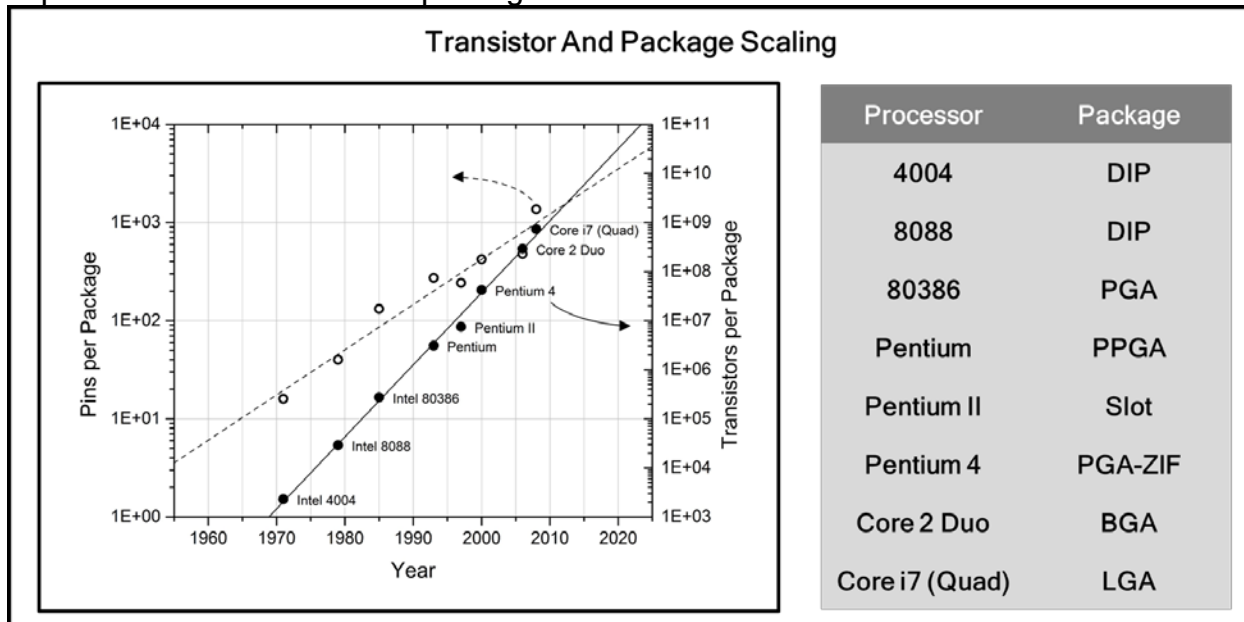


Figure 1.6. IC scaling trends as a function of transistor count and pins per package. Inset table identifies package form factor for respective packages.

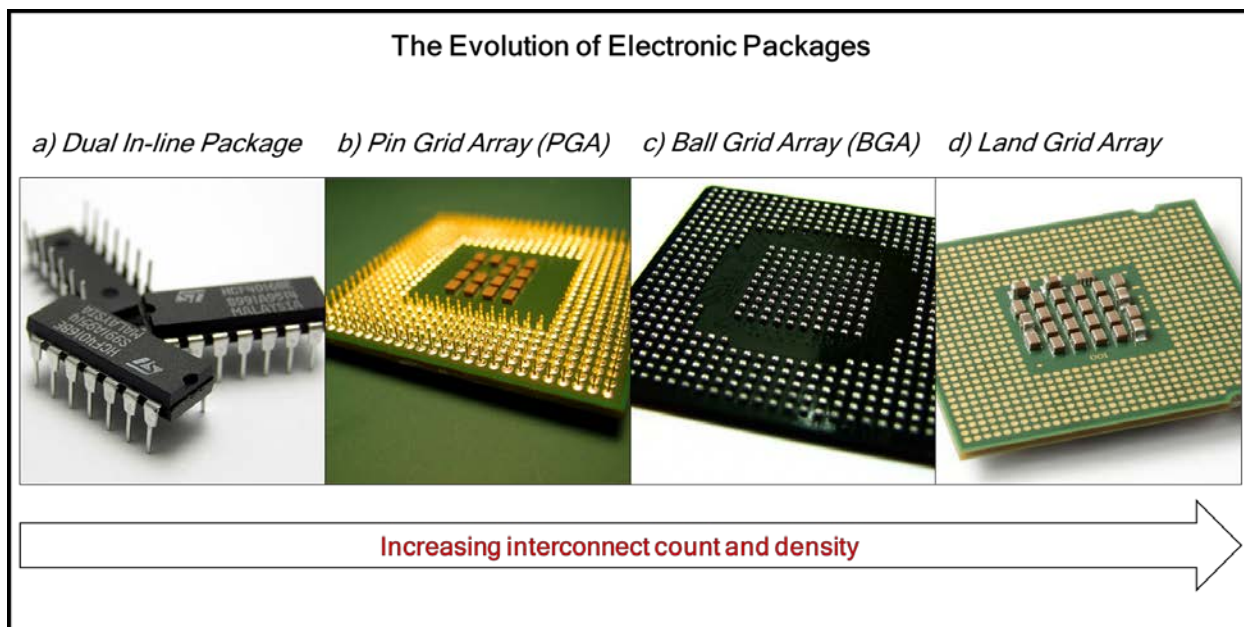


Figure 1.7. The evolution of electronic packages from a) dual inline packages (DIPs) to b) pin grid arrays (PGAs) to c) ball grid arrays (BGAs) to d) land grid arrays (LGAs).

As Table 1.1 indicates, three major characteristics of packages are the lead type, mount type, and interconnect type. The lead type generally describes the geometry of the leads used in the package. For example, the primary difference between the PGA and BGA package types is that PGAs use tall, narrow pins to interconnect the package with the system while BGAs use short, wide balls. In addition, the arrangement of the leads may

either be in a row formation or array formation. Based on the count, width, and pitch limitations described in the table, it is clear that arrays offer superior lead density than row-based packages.

Table 1.1. Lead, mount, and interconnect details for commonly used electronic packages.

		DIP	QFP	PGA	BGA	LGA
Leads	Type	Leadframe	Gull Wing	Pin	Solder Ball	Pad
	Arrangement	Row	Row	Array	Array	Array
	Count	4 – 64	32 – 304	169 – 940	196 – 615	771 – 2011
	Width [μm]	380 – 500	220 – 450	200 – 500	400 – 600	250 – 630
	Pitch [mm]	1.78 – 2.54	0.40 – 1.00	1.27 – 2.54	1.00 – 1.27	0.50 – 1.27
Mount	Through-Hole	Y	--	Y	--	--
	Surface Mount	--	Y	--	Y	Y
	Socket	Y	--	Y	--	Y
Interconnects	Wire Bond	Y	Y	Y	Y	Y
	Materials	Copper, Gold, Silver Alloys				
	Width [μm]	12.5 – 75				
	Pitch [μm]	35 – 60				
	Flip Chip	--	--	Y	Y	Y
	Materials	--	--	Solder Alloys, Copper Pillars, Gold Stud Bumps		
Width [μm]	--	--	20 – 50			
Pitch [μm]	--	--	40 – 250			

Furthermore, the mount type of a package is an important consideration for a given application. Through-hole mounts require the package leads to fit through pre-patterned holes in a system board. Then, the packages are typically bonded both electrically and mechanically to the board by applying solder to each pin from the back side of the board. Surface mounts, on the other hand, do not require the leads to extend through the mount board. Rather, the leads typically land onto pre-patterned metal pads on the board and are subsequently bonded using solder. Finally, socket mounts create electrical and mechanical connections between the package and board via additional platforms already integrated onto the board. These platforms contain narrow holes arranged in a pattern that matches the layout of the package and do not require solder in order to establish electrical or mechanical connections. As Table 1.1 indicates, different package types may be able to take advantage of one or more mount type, and there is no general trend for mount type as a function of desired lead density. Therefore, the mount type should be selected strictly based on the design constraints of each individual application.

The final package characteristic to be considered is the interconnect type. As mentioned previously, the two most popular interconnect types are wire bonds and solder bumps. As Table 1.1 indicates, each of the package types identified are compatible with wire bond interconnects. Conversely, only newer package types such as PGAs, BGAs, and LGAs are compatible with flip chip bonds using eutectic solder bumps. Because newer package types tend to require many more connections, wire bonds are not a feasible solution. Flip-chip eutectic solder bonds, however, are able to span the entire area of the integrated circuit, enabling high I/O densities and absolute I/O counts. This is the

primary reason flip-chip interconnects are only seen in high density packages. In addition to the increased density, flip-chip bonding schemes are also the foundation of small-footprint packages due to the ability to position interconnects across the entire integrated circuit area.

### C. *Chip-Scale Packaging (CSP) and Wafer-Scale Packaging (WSP)*

These packages, with total footprints that barely exceed the footprint of the integrated circuit itself, are referred to as chip-scale packages (CSPs). In a CSP, the leads of the package are located directly on top of the integrated circuit bond pads, essentially making the leads and interconnects a single feature. Figure 1.8 shows the difference between a non-CSP and a CSP. The primary benefits of CSPs are reduced footprint, increased interconnect density, and reduced electrical losses between the integrated circuit and the mount point.

The creation of a CSP may be accomplished in a few ways. First, a secondary board may still exist in the package, as shown in Figure 1.8b. In this scenario, the package board acts as an interposer and the integrated circuit is typically bonded directly to the interposer using flip-chip bonding. Alternatively, since the lead and interconnect dimensions are on a similar scale, it is also possible to simply directly attach the chip onto a board without the need of the package substrate acting as an interposer. While this sounds easier and cheaper, the drawback of directly attaching the chip without placing it in a package is the omission of the molding that would help seal and protect the chip. With respect to interconnect type, flip-chip bonding has been the biggest enabler of CSPs. Because wire bonding results in interconnect fan-out, it is impossible to make a CSP using wire bonds. Therefore, CSP interconnects are often eutectic solder bumps that are flip-chip bonded to the package substrate.

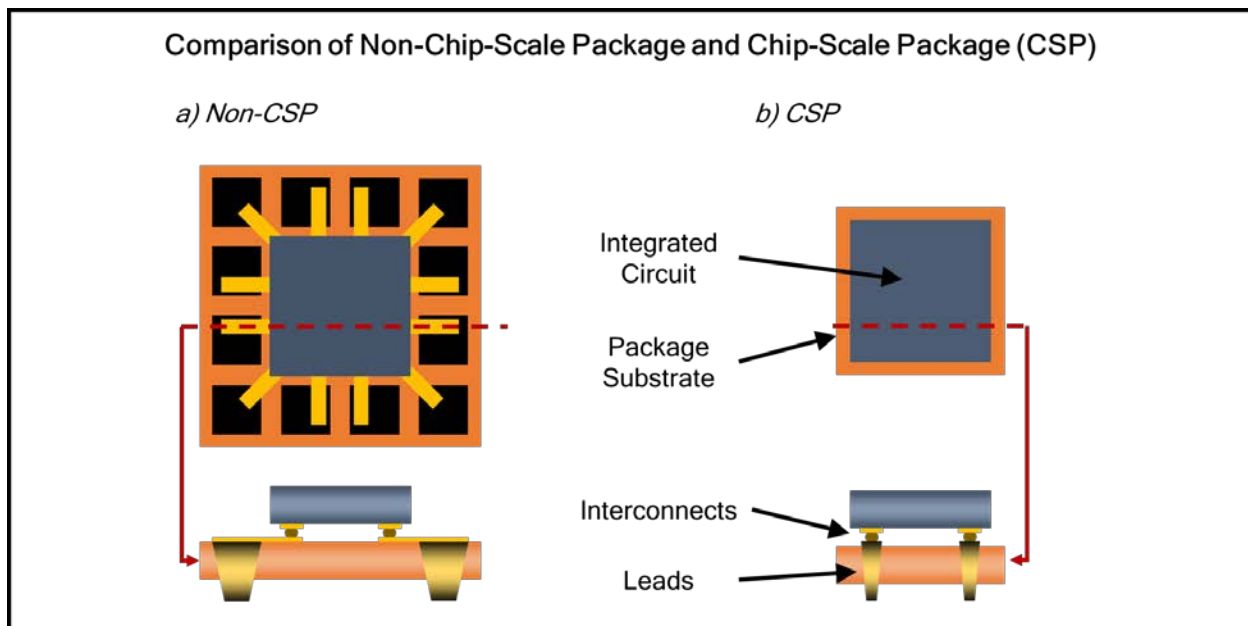


Figure 1.8. Comparison of non-chip-scale package and chip-scale package.

While a CSP with a footprint equal to the chip footprint may simply include a smaller package substrate, the most popular way of achieving a true CSP is by performing what is referred to as wafer-scale packaging (WSP). WSP takes advantage of the advances in wafer-scale processes commonly used for logic device fabrication. In WSP, solder bump interconnects and passivation layers are deposited onto bond pads for all of the die fabricated on a single wafer. Then, dicing the wafer results in creating hundreds of die immediately ready for flip-chip bonding. In this way, the introduction of WSP has boosted the throughput of packaging processes as well as reduced the package footprint to a true CSP. Therefore, future packaging processes and materials that are compatible with WSP will be the most attractive replacements for current packaging process flows.

#### *D. Packaging Performance Metrics*

Finally, in order to compare current and future process flows, establishing performance metrics is critical. The fundamental performance metrics for semiconductor packages can be divided into two categories: interconnect material properties and overall system capabilities. Because package interconnects must provide both electrical and mechanical connections between the integrated circuit and the external system, material properties such as conductivity, elasticity, and shear strength are three critical performance metrics. Increased conductivity reduces power loss, making the overall system more efficient. Furthermore, because packages may be subjected to both normal and transverse forces during use, both the elastic modulus and shear strength of interconnects must be sufficient to prevent mechanical failures. Generally, wire bonding results in better electrical performance than flip-chip bonding due to the higher conductivity of materials used. In contrast, flip-chip bonding results in higher mechanical durability due to the robustness of reflowed solder ball joints as compared to fragile wire bonds. However, both processes encapsulate their bonds with a filler material in order to improve the mechanical performance of the package.

The other important package performance metrics deal primarily with the electrical leads/pins. As mentioned earlier, as integrated circuits become more complex, the number of input/output connections required to realize the full potential of the circuit increases. Therefore, number of interconnects in the package will also increase, meaning the total quantity of interconnects as well as the interconnect density become important performance metrics. The major factors affecting both count and density are the bond/bump dimension and pitch, which are roughly equivalent for leading edge bonding and bumping process. Therefore, because the wire bonding process limits interconnects to the perimeter of chips only whereas flip-chip processes permit bonds across the entire chip area, both the total number and the density of interconnects possible is generally lower than flip-chip interconnects of the same dimension and pitch.

#### **1.2.2. Advanced Packaging Structures**

Despite conventional wire bonds and flip-chip solder bumps being capable of meeting the performance demands of semiconductor packages to date, packages in the future may require more advanced technologies in order to ensure the package itself does not limit the overall system performance. Three new packaging structures are gaining a lot

of traction in order to meet this demands: copper pillars, gold stud bumps, and through-silicon vias (TSVs).

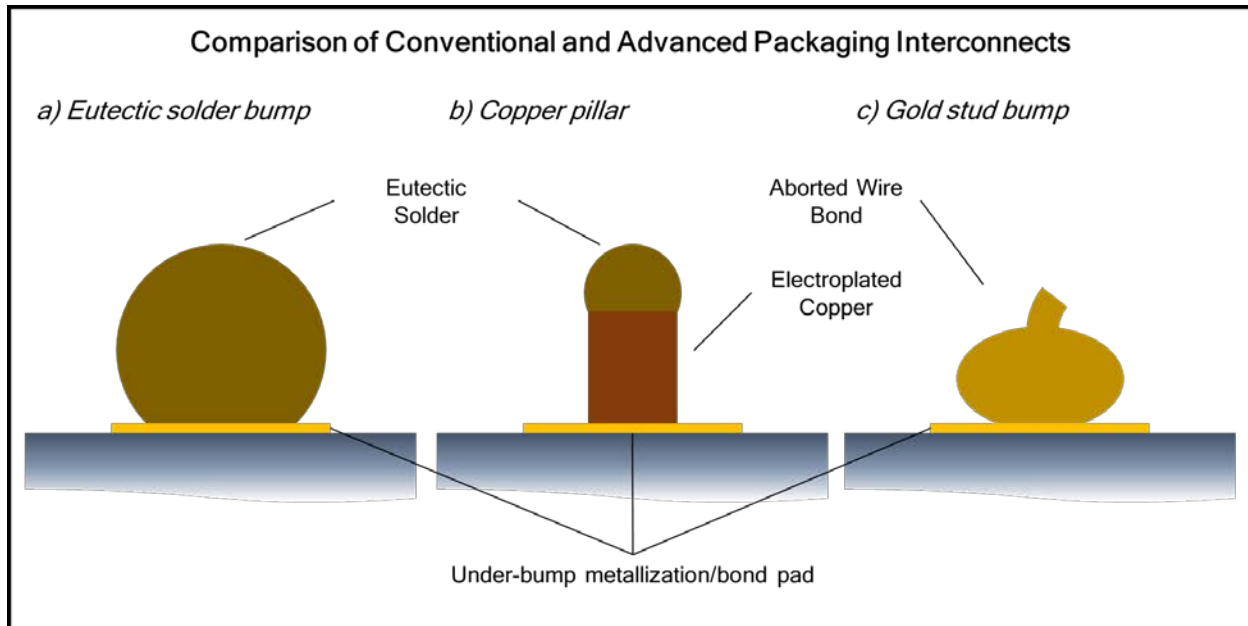


Figure 1.9. Comparison of conventional solder bumps with copper pillars and gold stud bumps.

#### A. *Copper Pillars and Gold Stud Bumps*

As alluded to previously, a number of issues with conventional eutectic solders are driving research into alternative materials for flip-chip interconnects. These issues include health-related concerns of lead-containing solders, their poor conductivity as compared to pure metal contacts, and limitations on dimension and pitch due to stencil printing processes used to fabricate eutectic bumps. The alternative materials most actively explored are copper and gold [6]. Each structure promises both improved conductivity as well as pitch and width, though there are significant differences in the structures and methods used for processing. Copper pillars are typically fabricated using additional masking and electroplating process steps and they are often capped with a small amount of eutectic solder in order to create bonds between the chip and package. On the other hand, gold stud bumps are simply wire bonds aborted immediately after the initial bond is created, and they do not contain any solder material. Figure 1.9 shows a comparison between conventional solder bumps and the two potential bump-replacement structures.

These structural differences affect the processing requirements for bonding integrated circuits to packages. First, because of the solder present in the copper post process, conventional flip-chip bonding processes are still capable of creating robust bonds between the copper pillars and the package. Conversely, thermosonic bonding at much higher process temperatures is necessary for gold stud bumps to form reliable bonds. While both of these technologies have shown promise—with copper posts appearing to be better-positioned for widespread industrial adoption—neither technology has made the leap to fully replacing conventional solder bump processes for flip-chip bonds.

### B. Through-silicon Vias (TSVs)

Finally, because the continued scaling of devices within integrated circuits has begun to slow while the demand for increased functionality in the same area has remained constant, one alternative to meet the demand for functionality is to begin stacking integrated circuits on top of each other. Currently, integrated circuits are fabricated such that the electrical connections to the active layer are only available on one side of the die. Furthermore, if wire bonding is used, that active layer must be face up in order to make external connections within a package. Therefore, the challenge with chip stacking is making vertical interconnects which can successfully contact the two active layers of the separate, stacked die.

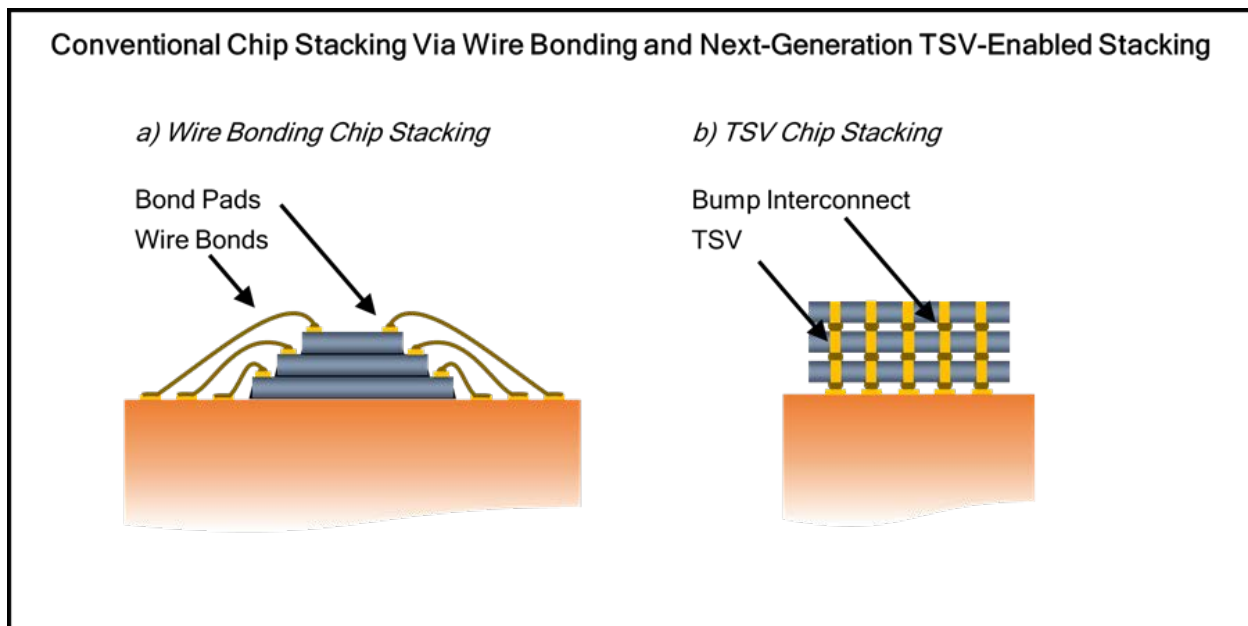


Figure 1.10. Comparison of chip stacking methods using conventional wire bonding and using chip-scale through-silicon vias.

Figure 1.10 presents a comparison of two chip stacking approaches. In the first process, multiple chips are stacked face-up, and wire bonds are extended outward from each chip down to the package substrate, where planar interconnections are used to connect each die. As is obvious in the diagram, the fan-out nature of this approach results in using more area than CSP. In order to realize CSP, a new structure called the through-silicon via (TSV) is being explored [7]. A TSV is a metal-filled trench which extends completely through a thinned silicon chip. They are typically created using a dry etching process to create a high aspect ratio trench in the silicon substrate, the trench is filled with electroplated copper, the silicon wafer is flipped and bonded to a temporary wafer, and the silicon is thinned to expose the bottom of the trench. While the TSV represents the most likely solution for enabling chip stacking of integrated circuits, the challenging processing and handling steps described have resulted in limited industrial use to date.

Because these advanced packaging structures have yet to achieve widespread adoption at an industrial scale, there is still plenty of room to explore processes and materials outside of what are considered conventional. Namely, the potential indeed

exists for metal nanoparticles deposited via inkjet printing to successfully fabricate such structures. The following section will elaborate on this potential with a discussion of the fundamentals of inkjet printing as well as the materials, such as metal nanoparticle inks, commonly used in inkjet printing.

### **1.3. Inkjet Printing**

As explained in the previous section, the semiconductor industry has advanced at an incredible pace since the 1960s, driven by a cycle of investment, performance enhancement, profit, and re-investment commonly referred to as Moore's Law. While this cycle has undeniably driven integrated circuit performance up and costs down, one constraint has remained: all of the material- and process-related advances have been required to be compatible with silicon substrates. The result of this constraint has been the development of a series of subtractive process cycles (material deposition followed by photolithography followed by etching) which factor strongly in the overall cost of the final product. While these subtractive processes are generally still necessary for producing complex, sub-micron feature sizes at incredibly high yield, they may no longer be necessary or even appropriate when required feature sizes are greater than ten microns, desired substrates are no longer rigid silicon, or costs need to be minimized as much as possible. Alternative processes may indeed be the key to meeting these new demands.

Inkjet printing, for example, is an additive process capable of producing features on the order of tens of microns and has long been used for material deposition onto non-rigid substrates. Because it is an additive process, whereby materials are deposited only where they ultimately need to be located, inkjet printing can offer potential cost savings due to both the minimization of materials needed and the minimization of process steps required for fabrication. Though inkjet printing was originally developed to produce images and text on paper via the controlled deposition of dyes, the progress of inkjet printing capabilities has led to a new research interest: the additive processing of functional electronic inks. From an industrial standpoint, this interest has been spurred by the minimization of inkjet nozzle diameters and the increasing parallelization of inkjet nozzles, e.g. modern inkjet printheads may contain over 1000 nozzles with diameters on the order of ten microns each [8]. Because the minimum feature size is roughly equivalent to the nozzle diameter, features on the order of tens of microns are now possible with inkjet printing. Today, much like the initial development for traditional semiconductor processes, the primary efforts in the inkjet-printed electronics arena are process control and reliability, material development and compatibility, and individual device fabrication and characterization rather than development of complete products. The following sections will describe the various components of modern inkjet printing systems, how different inkjet printers are classified, and the application of inkjet printing to the fabrication of electronic structures.

#### **1.3.1. Components of Inkjet Printer Systems**

Figure 1.11 depicts the physical hardware, control systems, and vision system commonly found in modern inkjet printers used for printed electronics applications. The heart of the system is the printhead/nozzle used to eject inks. An ink supply is directly attached to the printhead, and a pressure control system both forces the ink to the printhead and controls the shape of the ink meniscus at the nozzle orifice. Controlling

the meniscus is critical for stable droplet creation, to be discussed in more detail in Chapter 2. Also attached to the printhead is a jetting control system that generates and delivers electronic pulses to the nozzle, causing droplet ejection. With regard to motion control, inkjet printing systems require at least three mechanical degrees of freedom: two translational ( $X$  and  $Y$ ) and one rotational ( $\Theta$ ). These are important for two reasons. First, stage motion between or during droplet ejection events allows one to create patterns on the substrate. Second, when multi-layer structures are needed, these degrees of freedom aid in alignment before beginning printing processes. In a fixed printhead printer (as shown in Figure 1.11), a motorized stage governs all three required degrees of freedom. In non-fixed printhead systems, the stage only assumes a single translational degree of freedom, usually  $Y$ , and a motorized printhead mount provides the  $X$  degree. A fourth translational degree ( $Z$ ) is not required, but is usually also controlled using a motorized printhead mount, if desired. Most printers include a vision control system with at least two cameras to aid in substrate alignment as well as to observe ejected droplets mid-flight in order to guarantee stable jetting performance. In Figure 1.11 these are cameras CCD1 and CCD2, respectively. Finally, temperature control systems are commonly used to control the temperature of both the stage and nozzle as required by the process parameters. All of the control systems are typically controlled by a single computer system that converts an input pattern file into an output pattern of stage movement and drop ejection commands.

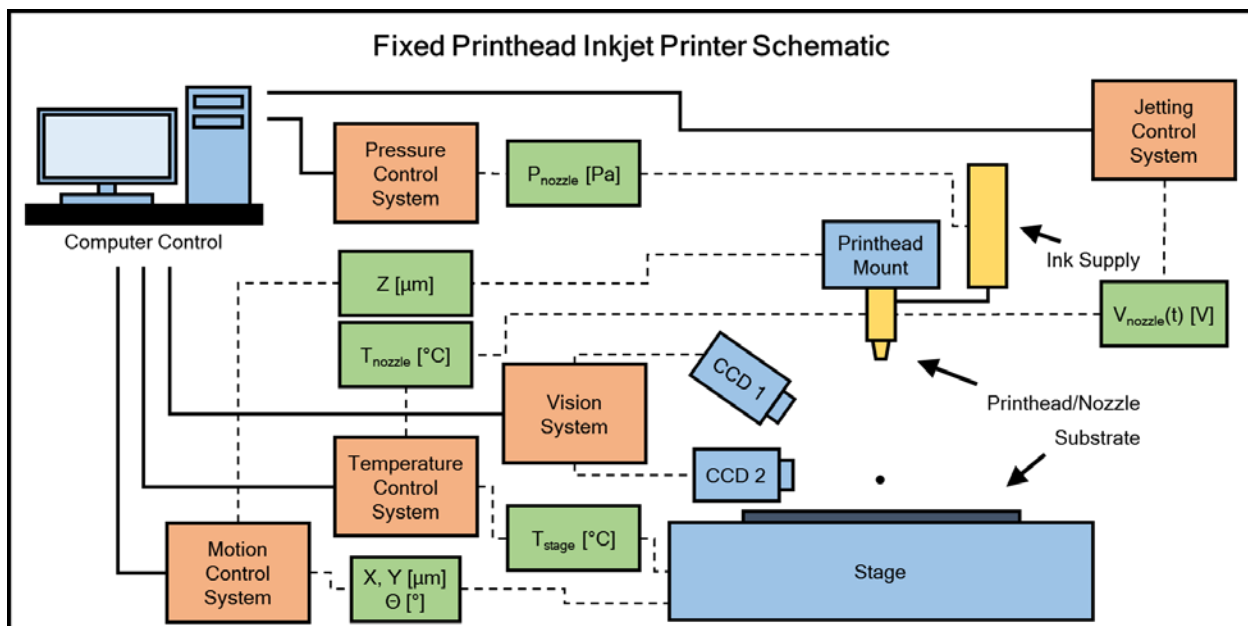


Figure 1.11. Block diagram of components of a fixed printhead inkjet printer. Blue blocks represent physical hardware, orange blocks represent control and vision systems, and green blocks represent the physical control system parameters.

### 1.3.2. Inkjet Printer Classification

Because there are so many components present in inkjet systems, many different and popular styles of inkjet printers have been developed as these components have progressed and intermixed. In order to classify the type of inkjet printing system used, three primary components are considered: the printhead, the jetting control system, and

the motion control system. As previously mentioned, the heart of inkjet printing systems is the printhead. While there are many printhead designs, in general printheads are comprised of one or more nozzles and each nozzle is connected to the jetting control system described earlier. When actuated, each nozzle will produce a droplet, but the physical manner in which the droplet is created varies with printhead design. This is the first important characteristic of inkjet printing systems, *droplet formation method*. In addition to triggering droplets, the jetting control system chosen dictates the second important characteristic, *jetting frequency*. Finally, because the motion and relative positioning of the actively jetting nozzle and the substrate dictates the pattern generated, different modes of operation for motion control systems will impose different limits on the types and shapes of patterns a printer will be able to create. Thus, the third characteristic is the *motion control mode*. These three characteristics will be discussed in further detail next.

#### A. *Droplet Formation Method*

The first characteristic used to classify inkjet printers is the formation mechanism for droplets. There are two common droplet formation methods: thermal and piezoelectric [9]. In thermal inkjet systems, a signal voltage is applied to a resistive film bordering the chamber. The resulting current increases the local internal temperature enough to cause the liquid in the chamber to boil. As a result, a small bubble of gas is created, which in turn forces a droplet of ink out of the nozzle and on onto the substrate. After the drop is ejected, the applied voltage returns to zero and the resistive film cools. The chamber refills and the process repeats. In contrast, piezoelectric nozzles are built with a film of piezoelectric material positioned along the wall of the chamber. When a signal voltage is applied across the piezoelectric material, it deflects inward at a distance proportional to the applied voltage [10]. This deflection creates an acoustic wave within the chamber that forces ink out of the nozzle. When the signal voltage returns to zero, the piezoelectric material relaxes and the acoustic wave attenuates. The chamber refills and the process repeats.

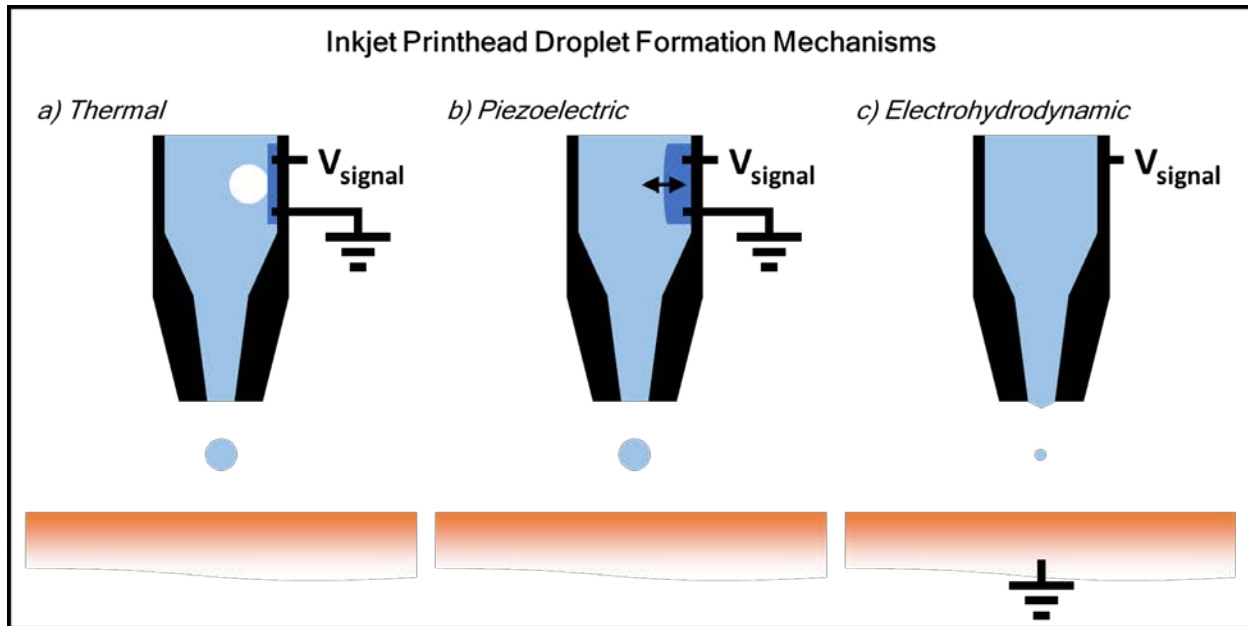


Figure 1.12. a) Thermal, b) piezoelectric, and c) electrohydrodynamic drop formation mechanisms. Droplet sizes are comparable in thermal and piezoelectric printheads, while electrohydrodynamic printheads produce much smaller droplets.

While both of these printhead designs are very effective at creating droplets, there are important differences to note between the two technologies. First, thermal inkjet heads are generally cheaper than piezoelectric heads and are therefore more commonly used in commercial printers. Second, the boiling action within thermal inkjet heads typically creates larger droplets than piezoelectric heads and droplet size is typically harder to vary when compared to voltage-controlled piezoelectric printheads. This means resolution tends to be higher and more easily controlled in piezoelectric heads. Finally, the lower operating temperature of piezoelectric printheads generally leads to longer lifetimes. For commercial inks such as water-based dyes, thermal inkjet systems produce droplets at a high enough resolution that the cost savings is justified. However, for electronic inks, to be discussed in more detail later, the intense heat required to boil the solvent is often detrimental to the ink, meaning piezoelectric printheads are preferred for printed electronic applications.

A third, less common droplet formation method based on electrohydrodynamic (EHD) forces is also worth noting. This technique is capable of producing sub-micron features and has shown potential for boosting the resolution of inkjet printing systems dramatically [11]. In EHD printheads, a large electric field is placed between the nozzle and the substrate. As a result, an ink containing even a small concentration of mobile ions forms what is called a Taylor cone at the end of the nozzle. With a high enough electric field, the tip of the cone inverts and ink will eject from the apex of the cone, accelerating toward the substrate in a very fine stream [12]. While this technique makes it possible to create very fine feature sizes, it has not yet been adapted to a high-throughput printhead and remains primarily a prototype-grade research tool. Figure 1.12 provides a comparison of the three droplet formation methods discussed here.

### B. Jetting Frequency

The second characteristic used to classify inkjet printing systems is jetting frequency, or the rate at which droplets are ejected from the nozzle. The two primary classifications are called continuous and droplet-on-demand [9]. In a continuous inkjet (CIJ) printer, the jetting control system triggers a continuous, high frequency stream of electrically-charged droplets. In order to decouple the continuous jetting from the nozzle from the pattern generation on the substrate, a collection cup is placed between the nozzle and substrate and a second signal from the jetting control system creates a lateral electric field that either directs the charged droplets into the cup when active or onto the substrate when inactive. The benefit of a CIJ system is a more reliable jetting behavior due to uninterrupted jetting. However, the main drawback of this method is the increased cost due to continuously jetting fluid which may not actually land on the substrate.

Alternatively, in droplet-on-demand (DOD) inkjet printing, a discrete droplet is ejected from the nozzle whenever the nozzle is actuated. DOD printing inherently decouples pattern generation and droplet ejection, but the non-continuous jetting increases the potential for nozzle drying/clogging which results in less reliable jetting at low frequencies. However, because DOD systems are still capable of high frequency actuation, they are considered superior to CIJ systems and the potential clogging issues associated with low frequency jetting conditions are either mitigated with additional, non-jetting-inducing perturbations [13] or simply tolerated.

Figure 1.13 compares the differences between the two jetting technologies. In this example, only two droplets reach the substrate for each technology depicted. Note both the addition of a cup and the addition of a second control signal in the CIJ system. When the drop deflection signal is high, droplets are deflected into the cup instead of onto the substrate.

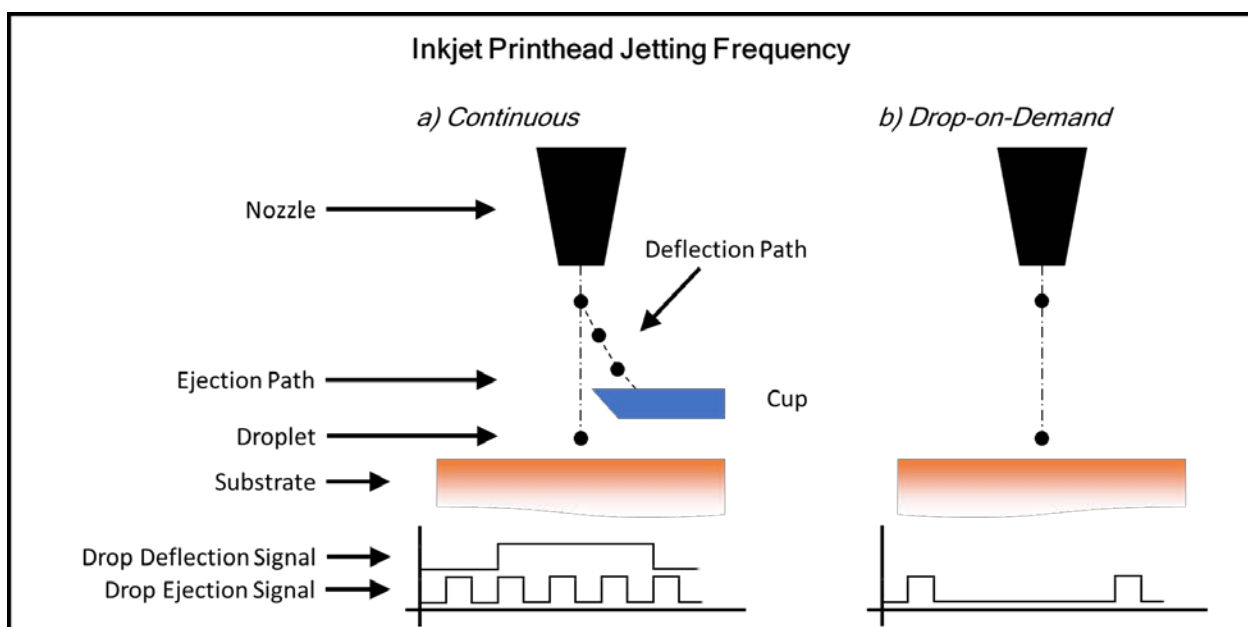


Figure 1.13. Comparison of continuous inkjet (CIJ) and droplet-on-demand (DOD) inkjet printhead operation.

### C. Motion Control Mode

The third characteristic often used to help differentiate inkjet printer type is the mode of stage motion used to create patterns on the substrate. This stage motion applies only to the X and Y directions. The two primary modes are called raster mode and vector mode. Figure 1.14 helps illustrate the differences in raster and vector mode printing for a simple slanted line connector.

Raster mode printing treats and executes the two orthogonal degrees of freedom separately during pattern generation, and these degrees of freedom are typically referred to as the scan direction and the step direction. Conventionally, the X direction is treated as the scan direction and Y direction is treated as the step direction, though these roles can be switched if needed. Raster mode printers tend to rely on a non-fixed printhead to provide the scanning degree of freedom above the stage while the stage provides the stepping degree of freedom below the printhead, though fixed printhead designs are also used. In raster printing, the printhead initially moves to a corner of the desired pattern. Then, it moves along the scan direction, placing droplets along a single line of the desired pattern as needed. When the printhead reaches the end of a single line, it pauses jetting. Next, the nozzle returns to the original location along the scanning axis and the stage beneath the printhead steps to the next required position. This process repeats until the pattern is completed.

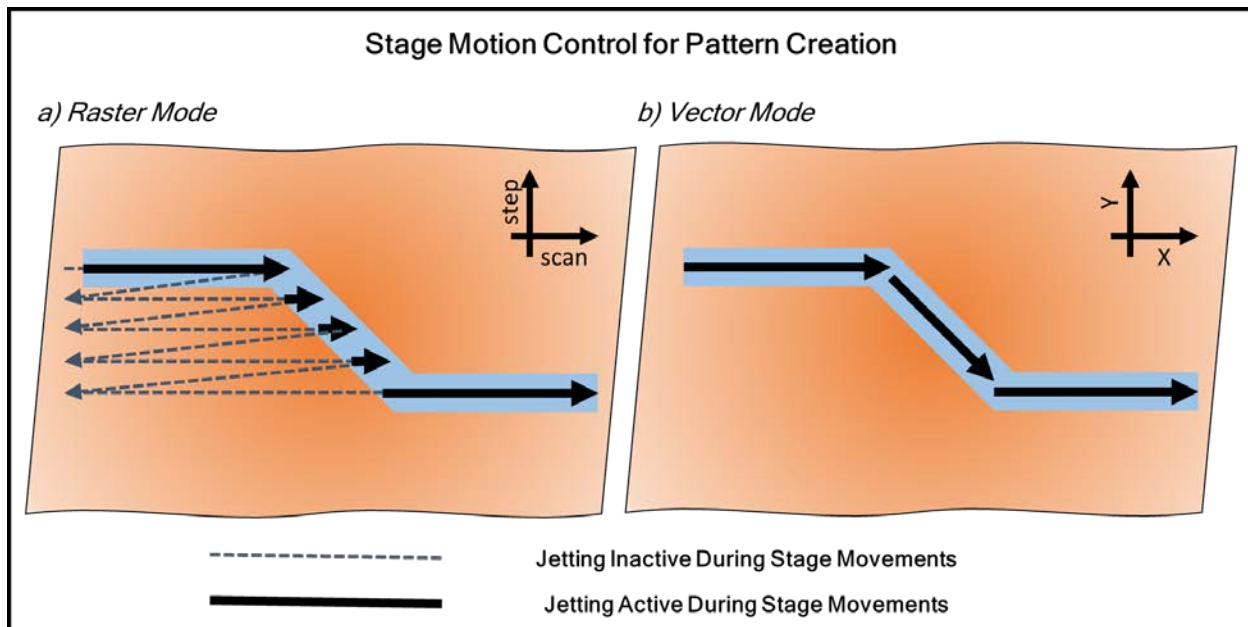


Figure 1.14. Raster mode versus vector mode printing. In raster mode printing, the total number of stage movements is greater and includes many non-jetting stage movements. In vector mode printing, all stage movements are active jetting movements. Also note the difference in naming convention for translational motion.

In contrast, vector mode printing is a much simpler process. Vector mode printing treats and executes the two orthogonal X and Y movements simultaneously, as needed, to create patterns. Unlike raster printing, the printhead does not need to begin in any

particular location of the desired pattern, but instead follows a set of motion commands, typically coordinates, as specified by the initial pattern file. In addition, like raster mode printers, vector mode printers can operate with either a fixed or non-fix printhead.

The choice of raster over vector mode imposes a large number of constraints on pattern design and generation. The biggest constraint is that only lines parallel to the scanning axis can be printed continuously in raster mode. This means the interaction of ink droplets on a substrate will occur on different timescales depending on the orientation of the line, and this timescale difference can dramatically alter the overall morphology of the printed feature (to be discussed in detail later). In vector mode printing, there is no orientation dependence because the simultaneous movement of both the X and Y directions permits the continuous pattern generation along any direction. This orientation dependence also makes pattern generation of curved features much more difficult using raster mode printing. Finally, raster mode printing almost always operates at lower throughput than vector mode printing. The requirement of scanning entire lines in order to print only a subset of the line is very inefficient, and is completely avoided in vector mode printing.

Despite the clear benefits of vector mode printing, the majority of inkjet printing systems are raster mode printers. In commercial dye-based printers used for text and photo creation, the need for precisely-timed ink interactions on a substrate is eliminated because the droplets absorb directly into the substrate instead of interacting with each other to form features on top of the substrate. In addition, because raster mode printers operate with scan and step axes, the performance of the step axis generally does not need to be as high as the scan axis, which provides an opportunity for cost savings when manufacturing the printer. For printed electronics applications, however, because pattern fidelity relies strongly upon ink interactions on the substrate and because creating features along multiple orientations is generally desirable, vector mode printing is the superior technology.

### 1.3.3. Electronic Inks for Packaging Applications

While the printer design and operation plays a large role in realizing high quality printed features, it is the materials that both establish printed electronics and differentiate it from conventional inkjet printing. Namely, the inks used serve to provide specific electronic functions such as conducting, semiconducting, or dielectric behavior on the target substrate. In the case of packaging applications, the primary function of the ink should be to create highly conductive interconnects. Therefore, after a brief discussion of the general composition and properties of electronics inks, this section will focus on the properties and processes relevant to the most commonly used conductive inks used in printed electronics: metal nanoparticle inks.

#### A. *General Electronic Inks*

Electronic inks can be thought of as two-component systems comprised of 1) a functional solid and 2) a solvent that acts to carry the solid to the substrate. The functionality of these inks is provided by the solid material carried within the ink. Despite the existence of both organic and inorganic materials that provide either conducting [14, 15, 16, 17, 18, 19], semiconducting [20, 21, 22, 23, 24, 25], or dielectric behavior [26,

27, 28, 29], certain material types perform better than others with respect to electronic performance. (For example, inorganic conductors tend to be much better than organic conductors, as will be discussed in further detail next.) Therefore, both organic and inorganic materials are often used together in order to fabricate more complicated, multi-layer devices [30, 31, 32].

With regard to the solvent component of inks, the primary function is to successfully stabilize and suspend the solid material in order to carry it to the substrate. Depending on the chemical nature of the solid and solvent chosen, inks can be described as either solutions or colloidal sols, e.g. organic inks tend to be solutions whereas inorganic inks tend to be colloidal sols. In order to minimize costs, the more material dispersed per droplet, i.e. the higher the solubility, the better. However, in colloidal inks the solids do not physically dissolve in the solvent, making the term 'solubility' invalid. Therefore, the mass of solid dispersed in a given volume or mass of solvent, often called 'solids loading' or 'mass loading', is the primary metric used to describe the amount of material dispersed per volume. These terms are often used interchangeably with 'solubility', though the physical difference in colloidal inks should be noted.

Finally, regardless of the chemical or electronic nature of the solid, each ink must typically undergo some form of post-processing in order to drive out the solvent and realize the desired physical properties of the printed layer. Some examples of these post-processing treatments may include: 1) thermal or UV crosslinking of polymer dielectrics [33], 2) thermal, laser, microwave, or IR sintering of encapsulated metallic nanoparticles [34, 35], or 3) thermal annealing of organic semiconductors [36], to name a few.

### *B. Metal Nanoparticle Inks*

Despite the very wide variety of materials and inks used in printed electronics applications, perhaps the most commonly used types of inks are inorganic metal nanoparticle inks. These inks are widely used because conductive interconnects are necessary for virtually every electronic device. The most fundamental applications are printed planar interconnects [35] and printed passive circuit components such as resistors, inductors, and capacitors [37]. Additionally, printed metal nanoparticles have been used as source, drain, and gate materials in printed thin film transistors [38], as bus bars for solar cells [39], and as antennas for RFID tags [40], to name a few more advanced functions.

In metal nanoparticle inks, the solid that is to be delivered to the substrate is a metal nanoparticle typically first synthesized using liquid-phase colloidal synthesis techniques. In general, colloidal synthesis allows for the fine control of nanoparticle size [16, 41], the importance of which will be explained shortly. Nanoparticles synthesized in liquid-phase techniques are typically comprised of a solid core of the metal surrounded by an encapsulant, which serves many functions. First, the encapsulant prevents the functional solids from interacting with each other, thereby preventing potential aggregation and precipitation within the ink. In addition, if synthesized properly, the encapsulant helps to guarantee that size distribution of the solids will be monodisperse. Monodisperse distributions are desirable because electronic inks often rely on material

size effects in order to realize the ultimately desired electronic function. Therefore, the properties of the materials deposited should likewise be monodisperse. Finally, the encapsulant directly interacts with the solvent, thereby dictating the degree of 'solubility' of the material within the solvent.

Due to their high expected electrical conductivity and their relatively simple synthetic procedures, two commonly synthesized metal nanoparticles are gold and silver [16, 17]. In each of these syntheses, as in many other syntheses, the encapsulant used is a carbon-based alkane chain with a functional group at one end. This functional group (a thiol for the gold synthesis and an amine for the silver synthesis) bonds to the metal core, leaving the long alkane chain to be exposed to the solvent. Because these chains are non-polar, these nanoparticles tend to show high solubility in non-polar, organic solvents. Therefore, metal nanoparticle inks used in inkjet printing can typically be described as colloidal suspensions of carbon-encapsulated metal nanoparticles in organic solvents.

The reason metal nanoparticles are preferred over organic alternatives is the ability to achieve films with conductivities that approach bulk metal conductivities at processing temperatures below 200 °C. This is achieved by taking advantage of the phenomenon of melting point depression, whereby nanoscale materials exhibit dramatically lower melting temperatures than their bulk counterparts (see Figure 1.15 for the melting point depression curve of gold) [42, 43]. Melting point depression occurs in very small crystals because the surface area-to-volume ratio of the nanocrystal is so high that the bonds between atoms along the surface are significantly strained. This additional strain results in decreasing the energy needed to initiate melting of the material, thereby lowering the overall melting point.

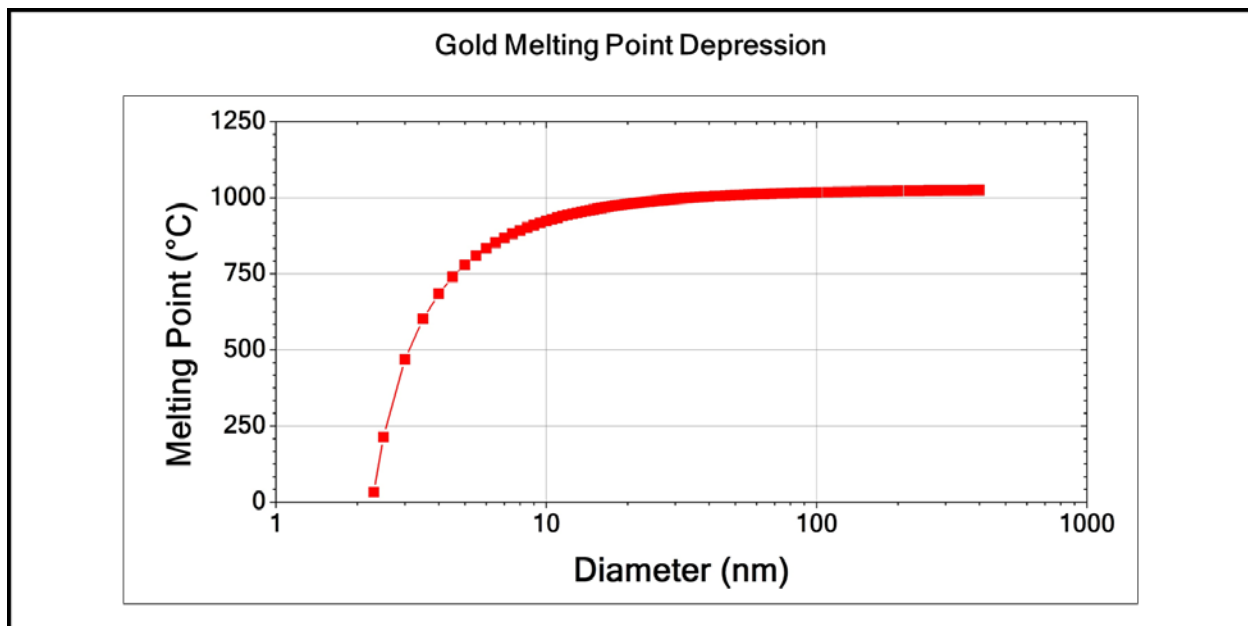


Figure 1.15. Melting point depression of gold (adapted from [42]).

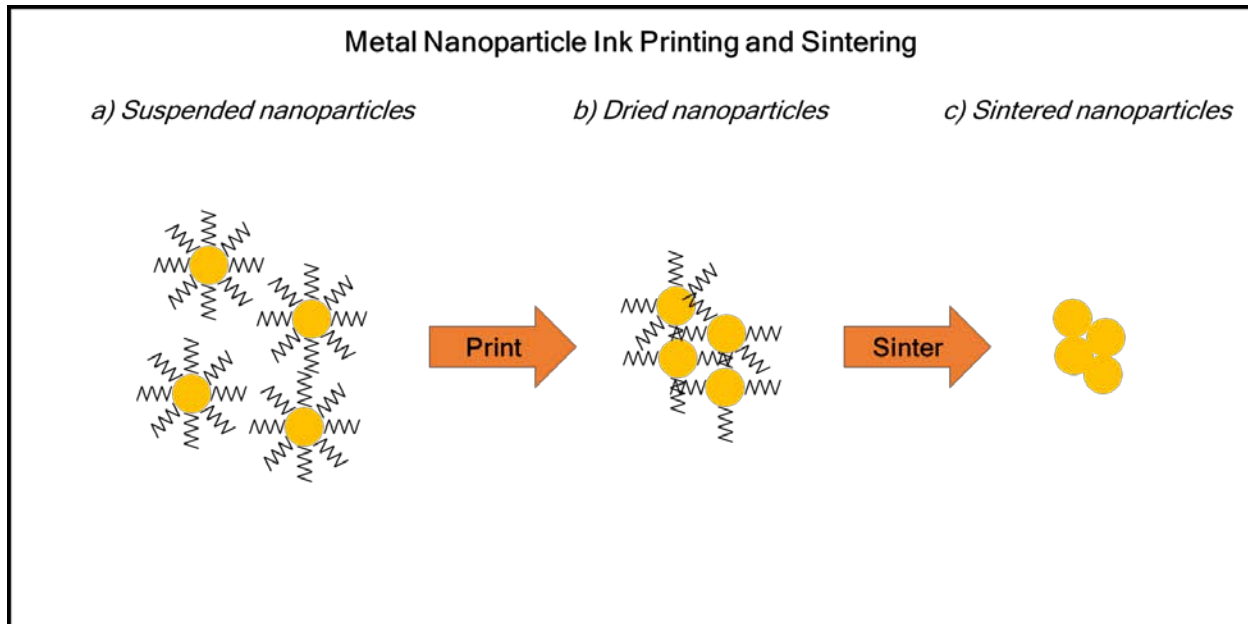


Figure 1.16. Schematic representation of nanoparticle sintering in thin films. a) Suspended nanoparticles ink inks are printed, b) dried films still contain encapsulants bound to nanoparticles preventing coalescence and conductivity, c) sintered films contain little or no encapsulant materials and the nanoparticles have coalesced to form a continuous film.

After metal nanoparticle inks are deposited and dried, they do not immediately exhibit high conductivity, i.e. they are not yet functional films. The lack of conductivity is due to the encapsulant bound to the nanoparticles. The encapsulant prevents the individually conductive particles from bonding to each other and forming a continuous film. Therefore, thermal treatments are often used in order to de-encapsulate the nanoparticles, allowing them to coalesce and sinter together to form a continuous film. Figure 1.16 shows a schematic representation of the sintering process.

During these thermal treatments, the encapsulant-nanoparticle bonds break and the unbound encapsulants act as a secondary solvent that permits unbound nanoparticles to move and coalesce with each other. The temperature at which these encapsulant-nanoparticle bonds break is clearly an important process condition. The choice of thiol-gold and amine-silver bonds are specifically selected because they result in binding energies low enough that moderate thermal treatments (less than 200 °C) are sufficient to break these bonds and create highly conductive films [44, 45]. Upon coalescing, the nanoparticles do not completely melt. Rather, the surface of the nanoparticles assumes a more liquid-like state in which atoms from one nanoparticle are more easily able to diffuse and bridge with nearest neighbors (see Figure 1.17) [46]. Because the nanoparticles do not completely melt, sintered films typically exhibit porosity. Films with higher porosity tend to have lower conductivity. In addition to porosity, unless thermal treatments are extreme, the carbon-based alkanes commonly used as encapsulants may not fully decompose. Residual carbon content in films is also cited as a reason for decreased conductivity. While extremely thin films do not typically suffer from residual carbon issues because the carbon has plenty of room to diffuse out of the very thin film, it is reasonable to expect that large volumes of trapped carbon content would more

severely affect the conductivity attainable in very thick films. This issue will be discussed in greater detail in Chapter 4.

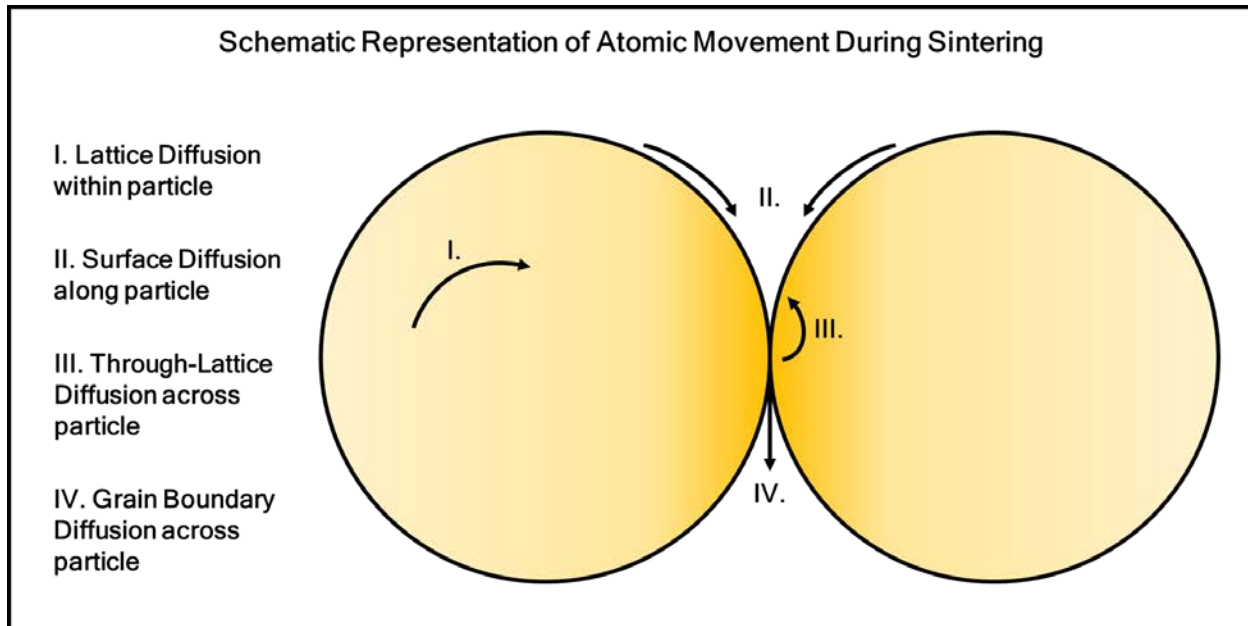


Figure 1.17. Schematic representation of material transport during sintering between particles. Mechanisms I and II do not result in film densification, whereas mechanisms III and IV each result in film densification. Adapted from [46].

#### 1.3.4. Ink-Nozzle and Ink-Substrate Interactions

Beyond simply changing the materials being printed in a specific ink, the quality and performance of inkjet-printed electronics also rely strongly upon controllable and reliable interactions between the ink and the nozzle as well as the ink and the substrate. While these interactions are critical for printing functional electronic materials, the interactions are primarily dictated by the solvents used as opposed to the functional materials being printed. Because that is the case, this section will describe the physical properties responsible for governing these interactions for general inkjet inks.

##### A. *Ink-Nozzle Interactions*

Let us first consider the interactions between the ink and the nozzle that govern droplet formation. In the nozzle, a narrow capillary containing a functional ink is supplied at one end and exposed to the environment at the opposite, open end. This ink must be ejected in a predictable, controllable manner from the open end with a high enough velocity such that air currents between the nozzle and substrate do not have enough energy to deflect the droplet and reduce the positional accuracy on the substrate. Also, the ink must refill from the supply end with sufficient speed in order to enable high frequency jetting to boost process throughput. At the open end, the surface tension of the ink prevents the fluid from simply dripping out of the nozzle. Within the nozzle, the ink viscosity must be low enough to allow the nozzle to refill before the next drop is ejected. In addition, the viscosity of the ink will determine both the amount of energy required to overcome the surface tension force in order to produce a droplet and the resulting volume and kinetic energy of the droplet. As such, surface tension and viscosity are the

critical fluid properties that dictate the ink-nozzle interaction and jetting behavior of inks [9, 30, 47, 48]. In lieu of a detailed discussion now, this interaction will be discussed at length in Chapter 2.

### *B. Ink-Substrate Interactions*

Assuming reliable droplet formation is established, let us now consider the ink-substrate interactions that govern pattern formation. The two primary concerns in pattern formation are resolution and pattern morphology. Increasing resolution is of interest because, like conventional electronics, it results in the ability to increase the function in a given area on a substrate. In printed electronic applications, substrates tend to be non-absorbing. Because of this, the spread of the droplet on the substrate will dictate the resolution of the printed feature—less spreading means higher resolution. Using Young's Equation:

$$\theta_c = \cos^{-1} \left( \frac{\gamma_{SV} - \gamma_{SL}}{\gamma_{LV}} \right) \quad (1.1)$$

where  $\theta_c$  is the droplet contact angle and  $\gamma_{SL}$ ,  $\gamma_{SV}$ , and  $\gamma_{LV}$  are the solid-liquid, solid-vapor, and liquid-vapor interface energies, respectively, it is possible to model the interaction of a droplet on the substrate [49].

The ideal contact angle ( $\theta_c$ ) should be in the range of 70-110° to achieve high resolution features. This range is high enough to minimize spreading, but not so high that printed materials do not adhere to the substrate. Figure 1.18 helps illustrate how all three interfacial energies are related to each other and affect the ultimate contact angle. In this plot, both the independent variable,  $\gamma_{SL}$ , and the parameter,  $\gamma_{LV}$ , are normalized by  $\gamma_{SV}$ . This is representative of a situation in which the surface of the substrate is left unaltered before printing. Therefore, the liquid-vapor surface energy, i.e. the ink's surface tension, and the solid-liquid surface energy play the biggest roles in determining the contact angle of the ink. For example, following a single contour, as  $\gamma_{SL}$  increases with respect to  $\gamma_{SV}$ , the contact angle monotonically increases. Furthermore, an inflection point at a contact angle of 90° occurs, regardless of the ink's surface tension, when  $\gamma_{SL}$  equals  $\gamma_{SV}$ . This can be interpreted as follows: Whenever the surface energy of the substrate is very high relative to the surface-liquid interface, the ink will wet prefer to wet the surface. Therefore, low energy surfaces are desirable for printed electronics because they improve the resolution of the printed feature. To achieve this surface energy reduction, surface modifications either applied in a blanket manner, applied directly beneath the intended printed pattern, or applied explicitly outside of the intended pattern area may be used. Some examples of these modifications are UV/Ozone, surface roughening, and self-assembled monolayer deposition, to name a few.

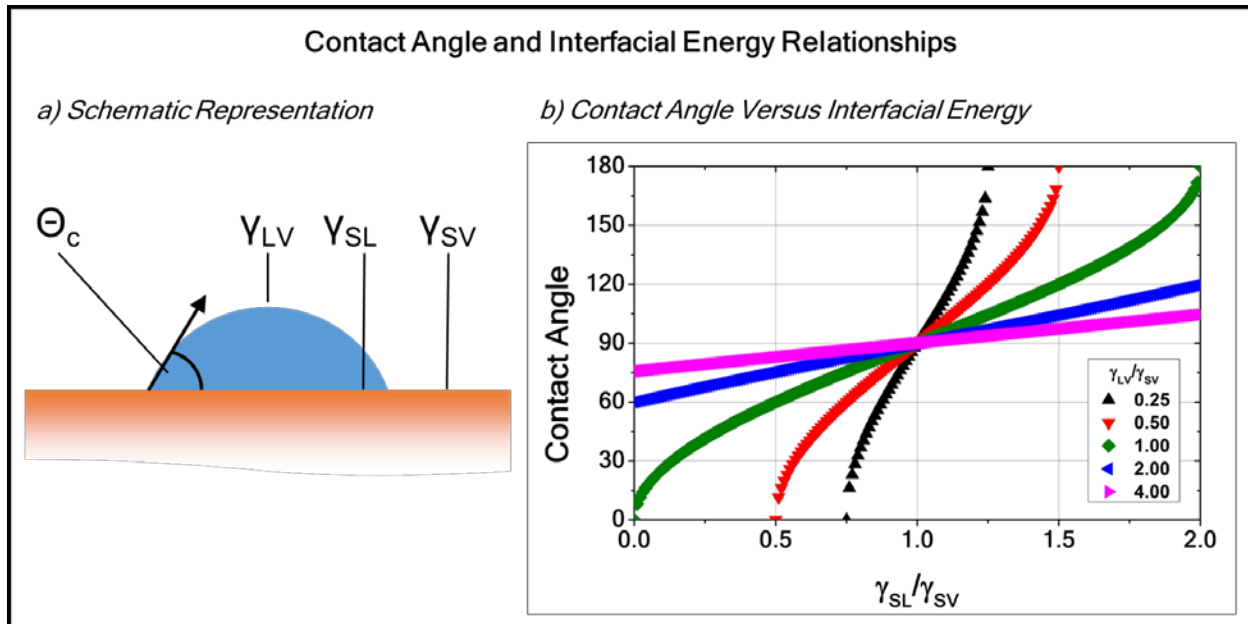


Figure 1.18. Contact angle as a function of solid-vapor to liquid-vapor interface energy ratio ( $\gamma_{SV}/\gamma_{LV}$ ) at a given surface-liquid to liquid-vapor interface energy ratio ( $\gamma_{SL}/\gamma_{LV}$ ). Because both the independent axis and parameter values are normalized by  $\gamma_{LV}$ , or surface tension, this represents the range of possible contact angles after altering surface energies when the liquid chosen has a constant surface tension. The inset schematic defines the interface energies as well as contact angle.

Alternatively, modifications may be made to the surface tension of the ink itself. Two common ways of achieving these modifications are adjusting the substrate temperature as well as including surfactants in the ink. As Figure 1.18 indicates, these modifications may either result in increased or decreased wetting, depending on the surface energy of the substrate. For example, for inks that already prefer to wet the substrate, increasing the surface tension pushes contact angle toward  $90^\circ$ , but the opposite is true for inks that do not prefer to wet the substrate. Furthermore, the surface tension of the ink has a strong effect on the effectiveness of surface modifications. For example, in the extreme case shown in Figure 1.18, when the surface tension is very high, the surface modifications have little effect on the altering the contact angle. Therefore, similar to the way it impacts jetting from a nozzle, surface tension also plays an important role in the determination of printed feature resolution.

The second concern for pattern formation is feature morphology. This may refer to the resulting cross-sectional shape of the printed feature after the solvent has dried and/or the line edge roughness of the feature. An ideal printed feature will have a hemispherical cross-section because this results in the minimum thickness variation across the width of the feature. However, due to the nature of many inks used in printed electronics, a phenomenon called the 'Coffee Ring Effect' often results in unevenly distributing printed material toward the edges of the desired features [50]. This redistribution of material is generally undesirable because it results in extremely thin and unstable films. For example, when printing dielectric layers to be used in electronic

devices, thickness variations across the dielectric will degrade the performance of the device.

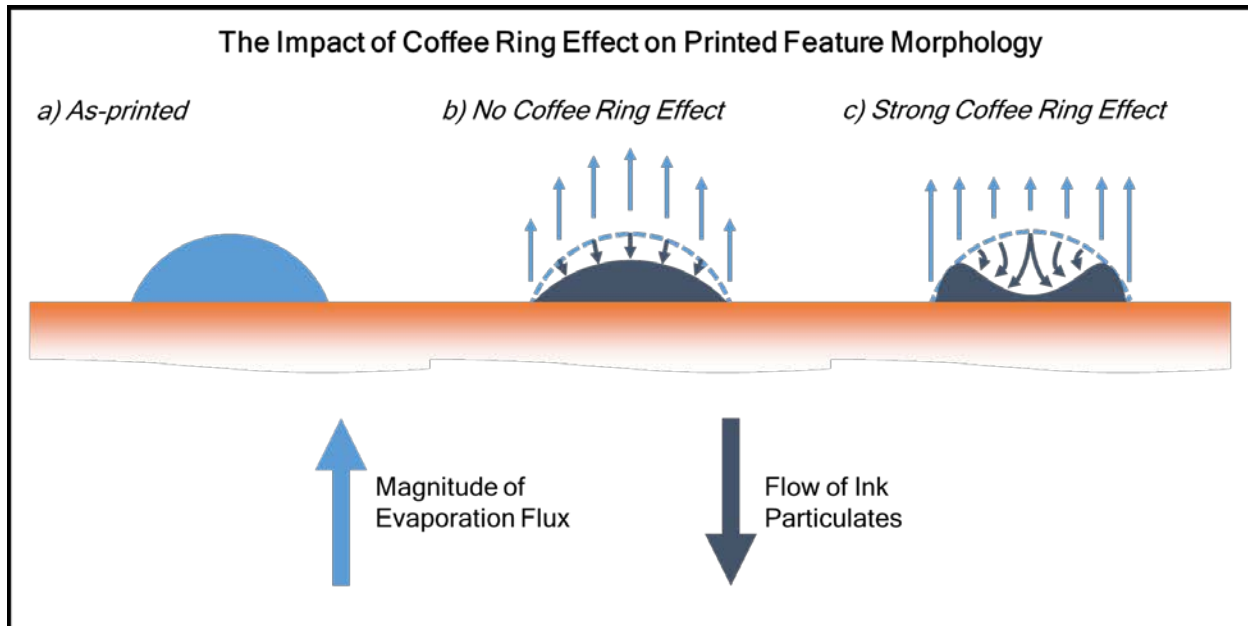


Figure 1.19. The impact of the Coffee Ring Effect on printed feature morphology. a) As-printed droplet, b) ideal dried feature where coffee ring has no effect on morphology, and c) dried feature where the Coffee Ring Effect strongly alters the ultimate morphology. Light blue lines represent evaporation flux lines and dark blue lines represent flow of particulate matter within ink.

The Coffee Ring Effect can be explained by non-uniform evaporation of the solvent and Figure 1.19 helps to illustrate this effect. In a printed feature that creates a hemispherical cap on the substrate, the evaporation rate is higher at the edge of the feature than at the center. This is due to the inherent thickness variation of the hemispherical cap. Because evaporation occurs more rapidly at the edge of the feature than the center, this causes an internal flow of material from the center to the edge as the feature dries, as shown in Figure 1.19c. If this flow is very strong, the cross-section of the fully-dried film will approach two distinct, nearly disconnected features as opposed to a single feature.

There are many ways to avoid the Coffee Ring Effect. One option is lowering the substrate temperature during printing [51]. Lower temperatures minimize the effect of the differential evaporation flux across the feature, resulting in more uniformly distributed films. A second method has been shown to combat this effect by altering the ink composition in order to produce what is known as a Marangoni flow [52, 53, 54]. In a Marangoni flow, surface tension gradients in fluids result in the flow of a fluid (and the particulate matter suspended in the fluid) from low to high surface tension. Therefore, in carefully-designed inks, an additional solvent may be added that helps to establish this Marangoni flow. Figure 1.20 illustrates how this Marangoni flow reduces the Coffee Ring Effect. When compared to the primary solvent, an ideal secondary solvent will have a higher boiling point but lower surface tension. Therefore, after the low boiling point

solvent preferentially evaporates at the edges of the feature, carrying particulates toward the edge, only the high boiling point solvent will remain. Because this solvent has a lower surface tension, a surface tension gradient exists from the edge of the feature toward the center. This gradient results in a flow of solvent back toward the center, which minimizes the effect of the initial outward flow. In this way, the evaporation rate and, again, surface tension of the ink are the key fluid properties that dictate feature morphology.

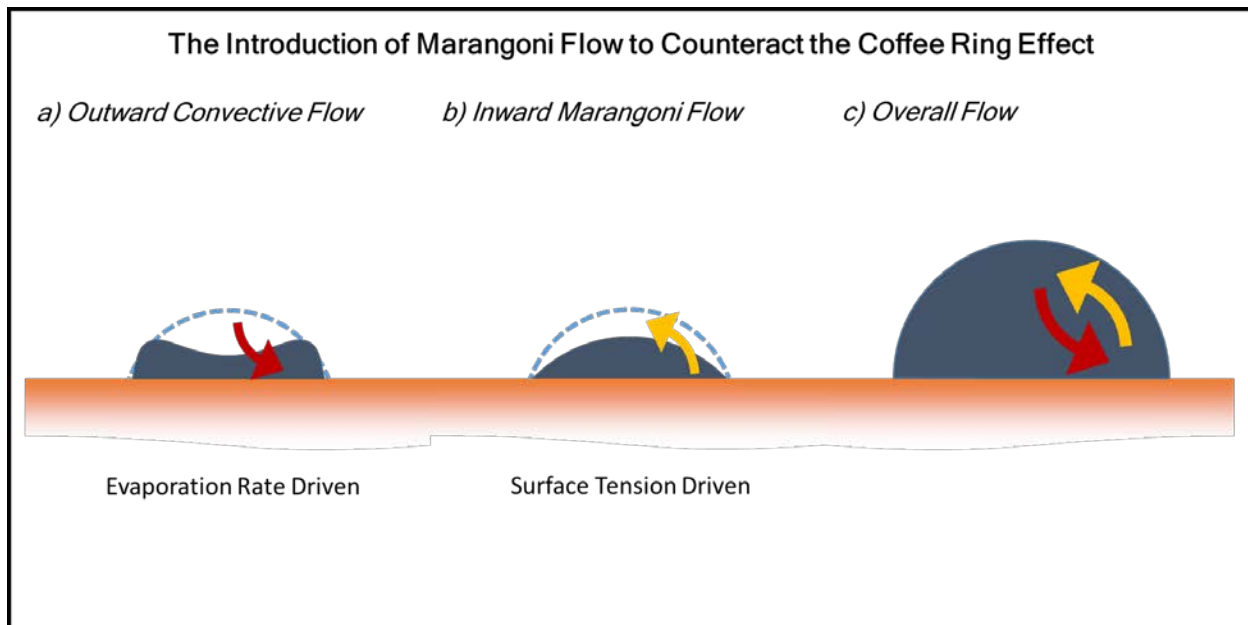


Figure 1.20. The introduction of a co-solvent to introduce an inward Marangoni flow to counteract the Coffee Ring Effect. a) The typical outward flow driven by preferential evaporation of the low boiling point primary solvent, b) the inward Marangoni flow driven by the surface tension gradient between the low surface tension secondary solvent and high surface tension primary solvent, and c) the overall flow within the droplet.

## 1.4. Dissertation Outline

While the primary interests in printed conductors have been planar applications to date, the material and process development for three-dimensional interconnects may prove to be a viable alternative to conventional packaging materials and processes. From ink design and optimization to process development and characterization, all aspects of this application will be explored in this dissertation, which will be organized in the following manner:

*Chapter Two* will visit the issues required to successfully formulate nanoparticle-based inks with an emphasis on high performance jetting. Fluid properties of ink formulations will be used to develop a feasibility window for reliable jetting, and the influence of nanoparticle loading on these fluid properties will be considered. A general route for successfully formulating a metal nanoparticle-based inkjet ink will be presented.

*Chapter Three* explores the effects of ligand composition on silver nanoparticle solubility in solvents amenable to inkjet printing. In order to identify high solubility nanoparticle formulations in such a sensitive system, a heuristic experimental procedure based on a genetic algorithm is used as opposed to traditional design of experiments techniques. In addition, the silver nanoparticle synthesis used is adapted to a robotically-controlled, high-throughput synthetic procedure and high-throughput characterization techniques in order to accelerate the discovery of desirable nanoparticles.

*Chapter Four* will discuss the process development of three-dimensional printing of metal nanoparticle inks for advanced semiconductor packages. This discussion will include three-dimensional printing of metal nanoparticle inks in order to fabricate freestanding pillars to act as replacement structures for conventional solder bumps. In addition, this chapter will describe the mechanical and electrical characterization of these nanoparticle-based structures as a function of sintering condition and describe sintering mechanisms for such structures.

*Chapter Five* will extend the process developed for solder bumps to through-silicon vias (TSVs). The process for filling and bumping TSVs in a single step will be described and characterized, and the electrical and mechanical performance of the TSVs will be explored.

*Chapter Six* will revisit the advances made in designing reliable inks with metal nanoparticles, understanding nanoparticle solubility, and developing high performance processes for advanced packaging structures. The chapter will conclude with a discussion on the future outlook for these applications.

## Chapter 2. Controlled Jetting Performance of Nanoparticle-based Ink Formulations

---

For the majority of inkjet-printed devices, the materials printed are commercially available ink formulations. While these inks tend to perform well under particular conditions, the proprietary nature of the inks means that the materials, solvents, etc. are more or less unknown. This makes the expansion/reduction of the process window and the characterization/failure analysis of printed features difficult. A clear alternative is the design of custom ink formulations that can be absolutely controlled with respect to their components and concentrations. Unfortunately, ink formulation is regarded more as an art than a systematic science, meaning there are no clear guidelines with regard to proper formulation. In this chapter, the fluid properties and performance metrics critical to reliable ink performance are discussed, a framework is developed using some of these properties as basic metrics for quantifying jetting quality, and a systematic ink design strategy is developed for formulating reliable inks loaded with metal nanoparticles.

## 2.1. Introduction

As described in the introductory chapter, the two primary interactions of concern to ink design are the ink-nozzle interaction and the ink-substrate interaction. While both of these interactions are important to understand and control, the ink-nozzle interaction can be thought of as the limiting interaction because it determines the quality and reliability of fluid delivery to the substrate. In addition, many works have already considered this ink-substrate interaction, [48, 50, 51] whereas relatively few have directly addressed ink formulation. Therefore, this chapter will emphasize only the development of reliable inks from the perspective of jetting performance.

In order to develop inks for reliable jetting, both the ink's response to actuation events within the nozzle must be understood and a clear, quantitative metric for jetting performance must be defined. Furthermore, this metric must in some way be normalized from one ink to the other, in order to fairly compare the performance of two different inks that will, necessarily, have different compositions. These fundamental nature of these two topics are discussed next, and the following section will describe the specific methodology used to formulate inks for jetting optimization.

### 2.1.1. Fundamental Operation of Piezoelectric Inkjet Nozzles

Although ink formulation is critical for all forms of solution processing, the inks discussed in this chapter will be developed with a specific solution processing method in mind: inkjet printing using piezoelectric nozzles. The non-contact, additive nature of inkjet printing and the precise control offered by piezoelectric nozzles are two important factors in focusing on this widely used subset of solution processing. In addition, the ultimate application of these processes to semiconductor packaging makes the selection of inkjet printing over other solution-processing methods a practical constraint, to be discussed in more detail in Chapter 4.

#### *A. Piezoelectric Nozzle Design*

All piezoelectric nozzle designs for inkjet printing incorporate a piezoelectric film that deforms directly against a fluid reservoir, forcing fluid out of a small orifice at the end of the reservoir. However, there are many different nozzle designs that depend mostly on the size of the piezoelectric material, the location of the piezoelectric material relative to the orifice and chamber, and the polarization direction of the piezoelectric material [10]. The most common designs are bump mode, bend mode, and shear mode. Although each of these designs will respond differently to applied voltages, the deflection distance of each of the designs is proportional to the applied voltage. This deflection distance is critical in determining the overall jetting behavior of the nozzle because it controls the energy imparted to the fluid to be ejected. Figure 2.1 shows the cross-section of a commonly used nozzle for inkjet prototyping (and the nozzle used for the entirety of this work), the MicroFab MJ-AT-XXX series of nozzle [55]. Other commonly used nozzles are manufactured by Dimatix [8], Konica Minolta [56], and Xaar [57].

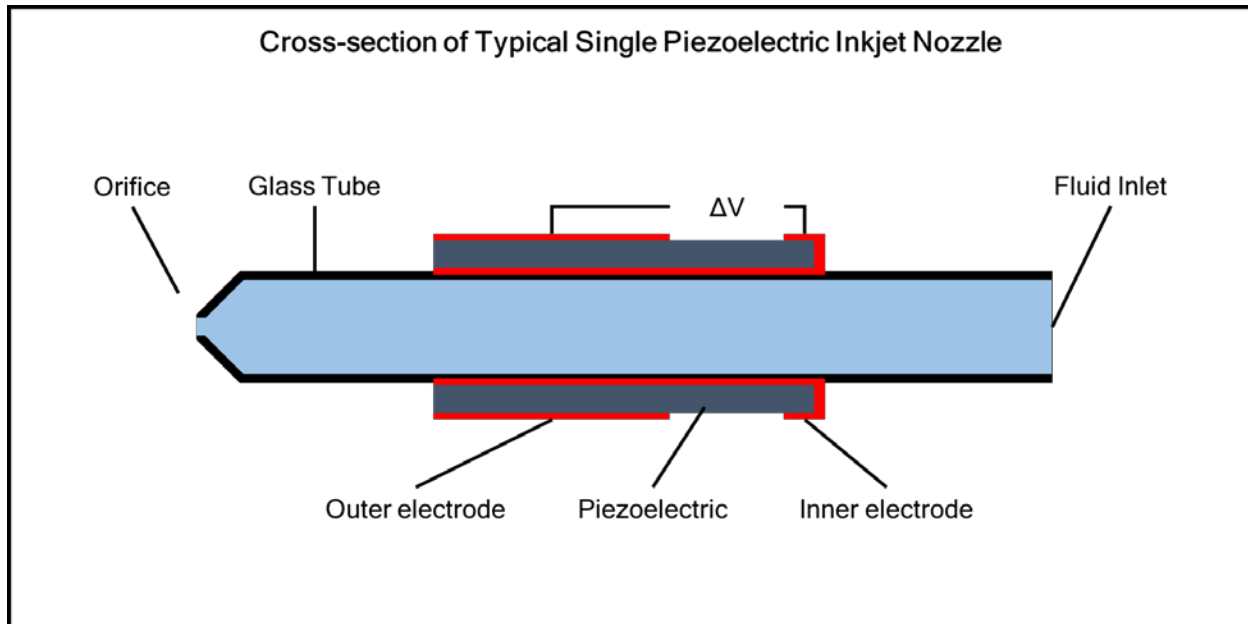


Figure 2.1. Cross-section of typical single piezoelectric nozzle, adapted from [55]. The inner and outer electrodes pictured each wrap around the glass tube completely.

### B. Principle of Operation

In piezoelectric nozzles, the production of droplets is based on instantaneous pressure wave formation at the center of the chamber. Figure 2.2 helps to illustrate the theoretical process. First, an instantaneous pulse at the center of the chamber induces a negative pressure wave that immediately begins to propagate in either direction along the chamber. Due to the boundary conditions of the chamber geometry, i.e. the supply side can be viewed as an open end and the nozzle side can be viewed as a closed end, the reflections of the pressure waves at either end behave differently. The nozzle-side wave reflects with the same negative pressure, whereas the supply-side wave reflects with the opposite sign, creating a positive pressure. If a second wave with a positive pressure is introduced at precisely the time when the reflected waves intersect, the negative reflected wave now moving toward the supply side is annihilated while the positive reflected wave now moving toward the nozzle is amplified. This amplification allows for a droplet to form at the nozzle end [58]. The ejected fluid travels very quickly, but produces a tail that results in slowing for the velocity of the head. Nominally, this tail breaks off at the orifice of the nozzle and recombines with the head to produce a single droplet.

In order to achieve this behavior, it is clear that two pressure impulses of opposite sign are necessary. The piezoelectric material lining the chamber can easily provide these pulses. When a voltage is applied to the piezoelectric, it will rapidly expand/contract depending on the polarity of the voltage change. This will produce the initial pressure wave pulse. When the voltage is held constant, no changes in the film occur, and so no new waves are introduced. However, a return to the initial voltage will produce a second pressure pulse, but of opposite sign due to the change in polarity of the voltage change. As previously described, if this return pulse is timed properly, droplet formation should occur.

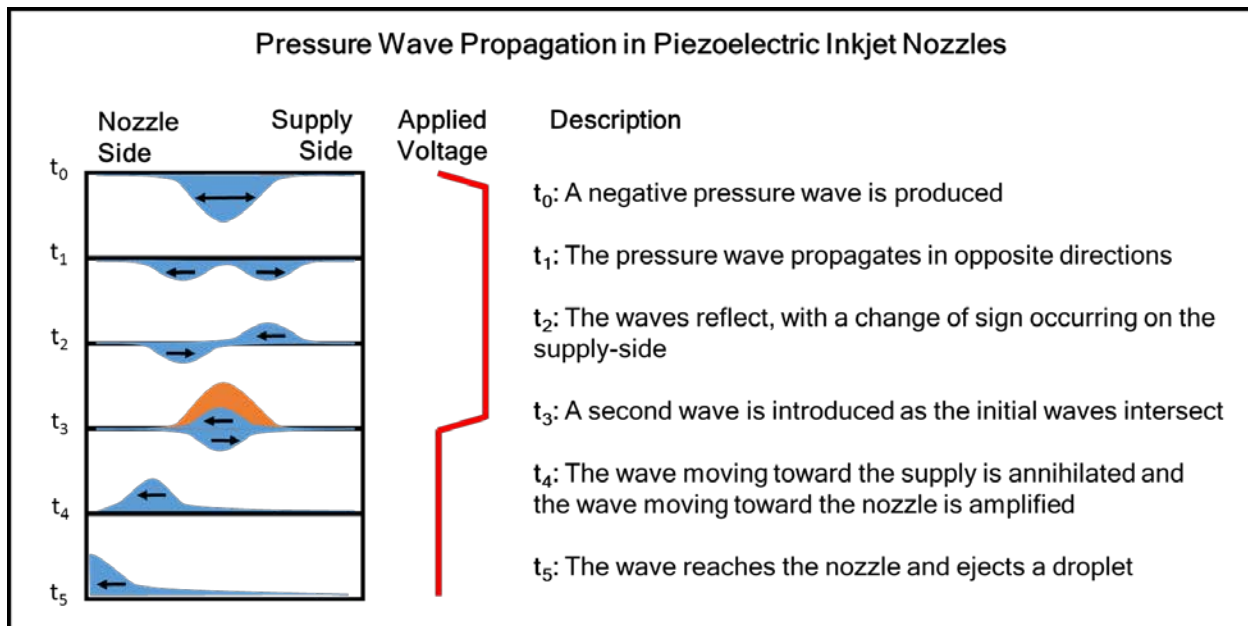


Figure 2.2. Illustration of pressure wave propagation, annihilation, and amplification in piezoelectric inkjet nozzles.

As one might expect, the timing of the second pulse is critical to the successful ejection of the droplet. Because the timing is based on the propagation rate of the pressure wave induced within the chamber, both the geometric and fluid properties of the system must be taken into account when determining the ideal timing. Based on this model for pressure propagation within the chamber, the optimal pulse width,  $t_{\text{optimum}}$ , is equivalent to the length of the chamber,  $l$ , divided by the speed of sound in the fluid being printed,  $c_{\text{ink}}$ .

$$t_{\text{optimum}} = \frac{l}{c_{\text{ink}}} \quad (2.1)$$

### C. Pulse Waveforms

The time-dependent voltage described previously is often referred to as the pulse waveform. Multiple pulse waveforms have been investigated in order to assess which waveform results in the most reliable droplet production [59, 60]. The two most common, unipolar and bipolar, will be briefly discussed here.

a. Unipolar Waveform

The basic waveform described in the previous section is referred to as a unipolar waveform. That is, the voltage applied to the piezoelectric material at any given time never changes sign. This waveform is effective at producing droplets, but the residual wave within the nozzle after droplet ejection results in oscillations of the meniscus at the nozzle orifice. If not controlled, these oscillations may result in unintentional degradation of jetting performance via satellite formation [58].

b. Bipolar Waveform

In an effort to mitigate issues like satellites, bipolar pulse waveforms are commonly used. Figure 2.3 shows a conventional bipolar pulse waveform with the eight waveform characteristics clearly identified. They are  $t_{dwell}$  and  $t_{echo}$ , the dwell and echo times between the delivery of pressure impulses,  $t_{rise}$ ,  $t_{fall}$ , and  $t_{rise2}$ , the time taken for each pulse delivery, and  $V_0$ ,  $V_+$ , and  $V_-$ , the voltages applied at steady-state and at each impulse. The addition of the second, oppositely signed, pressure impulse delivered by the dwell stage results in more rapidly annihilating the residual pulses within the chamber, thereby minimizing the likelihood of satellite formation and producing more stable droplets. For optimal jetting, typically the rise and fall times are kept very short and the echo and dwell are determined as follows:

$$t_{dwell} = t_{optimum} = \frac{l}{c_{ink}} \quad (2.2)$$

$$t_{echo} = 2 * t_{dwell} \quad (2.3)$$

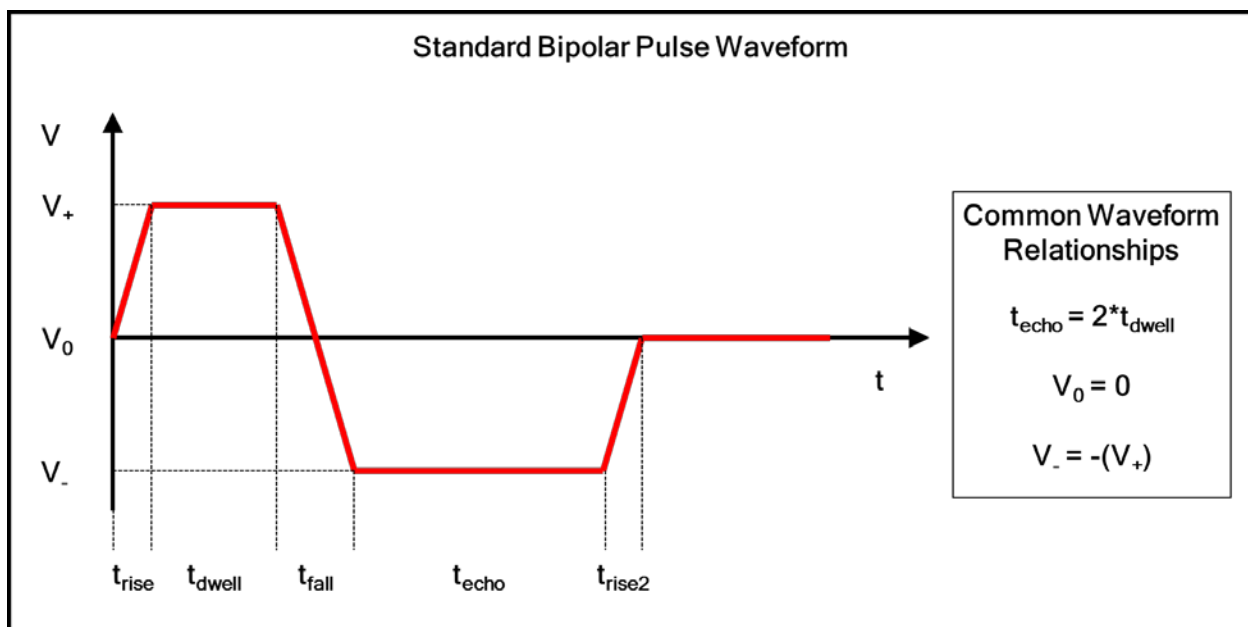


Figure 2.3. Components of a bipolar pulse waveform commonly used in inkjet printing.

### 2.1.2. Droplet Formation in Piezoelectric Inkjet Nozzles

As described in the previous chapter, there are a number of physical properties that dictate the production of reliable droplets from an inkjet nozzle [61]. Surface tension and viscosity are the two most important properties, and the effect of each will be discussed here with an emphasis on their effect on droplet formation. In addition, the effect of different jetting conditions, i.e. the pulse waveform, will be discussed due to its effect on the ejected droplet's size and speed. First, the measurement of ink physical properties is discussed.

#### A. *Measurement of Physical Properties of Inks and Droplets*

The two primary physical properties of concern for ink characterization are fluid properties and geometric properties. Fluid properties include surface tension, viscosity, density, etc. Geometric properties include drop size, drop volume, drop speed, etc. In order to measure fluid properties of inks, aliquots of the ink itself must be tested using separate equipment. These tests will be discussed more in the following section, but they include pendant drop testing for surface tension measurement, viscometry for viscosity measurement, and mass-based analysis to determine ink density. On the other hand, the geometric properties must all be determined *in situ*. This is accomplished by using high speed image acquisition during the drop ejection process. Recalling Figure 1.11, by using CCD1 it is possible to know the size, position, and velocity of droplets, thereby enabling the effective characterization of droplet quality based on ink and jetting conditions. Figure 2.4 shows a series of images taken of droplet formation as a function of time.

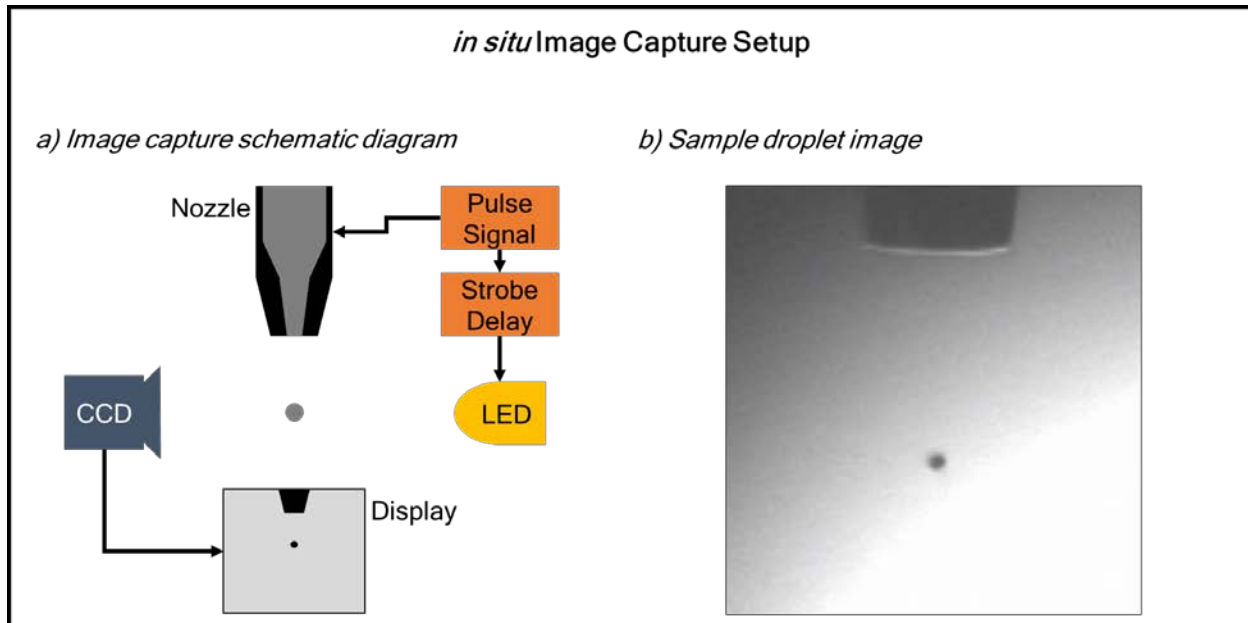


Figure 2.4. a) Schematic diagram of image capture system and b) sample photograph of a droplet in flight.

#### B. *Surface Tension, Viscosity, and Density*

Surface tension and viscosity are the two primary physical properties that determine the shape and the break-off mechanism for the droplet tail that is produced during droplet

ejection [61, 62]. Density is also important, though the effect of density is not as great as the other two properties, as will be shown. First, the ink viscosity determines the time scale of internal fluid flow within the droplet and tail. It also determines the length of the tail and the location of the thinnest part of the tail. The location of the thinnest part of the tail is critical in determining where the droplet will pinch-off. If pinch-off occurs at the meniscus, the tail and head remain connected and form a single droplet. However, if pinch-off occurs between the tail and the head of the droplet, multiple droplets may form. Surface tension is the force that drives this pinch-off. Therefore, together, viscosity and surface tension dictate the droplet break-off mechanism. The characteristic time scale of this pinch-off is related to these fluid properties as shown in the following equation.

$$t_{pinch-off} = \frac{\eta^3}{\rho\gamma^2} \quad (2.4)$$

where  $\eta$  is the viscosity,  $\rho$  is the density, and  $\gamma$  is the surface tension. The surface tension is also partly responsible for the formation of a meniscus at the orifice of the nozzle (an applied negative pressure also aids in ensuring the meniscus is maintained).

It is also important to note that both surface tension and viscosity will affect jetting performance as a function of nozzle orifice diameter. Inks with very high surface tension and/or viscosity simply will not jet from nozzles with very small orifices because the energy required to eject the droplet is too high for piezoelectric nozzles to produce. In addition, for large nozzle orifices, inviscid inks and/or inks with very low surface tension will fail to form a meniscus and droplet formation will fail. For typical nozzle diameters in the range of 30 - 60  $\mu\text{m}$ , a tolerable viscosity range is 0.5 - 40 cP and a tolerable surface tension range is 20 - 70 dyn/cm [63]. Finally, the nozzle orifice also plays a strong role in the size of the droplet ejected. The relationship is approximately linear with respect to the area of the orifice [61].

### *C. Dwell/Echo Time and Pulse Voltage*

The pulse waveform is also capable of changing the behavior of the ejected droplet. Namely, the modulation of the dwell/echo time as well as the pulse voltage will change the size and speed of the droplet. Typically, the goal of tuning the pulse waveform is to achieve higher droplet speeds, though size is also modulated. First, if the echo and dwell voltages are lengthened, the size of the droplet produced tends to increase. This is because the time during which the droplet is ejected is lengthened, allowing for more fluid to be removed from the nozzle. However, if the echo and dwell times are adjusted improperly, destructive interference between the pressure waves produced in the chamber will actually result in decreasing the droplet speed. For this reason, a peak in droplet velocity will be associated with the optimal dwell time of the ink [61, 62, 64]. In addition, in order to boost the speed of the droplets for non-optimal dwell times, an increase in pulse voltage is necessary.

#### D. Dimensionless Physical Parameters

As shown previously, the fluid properties and the nozzle dimension both strongly impact the drop formation of the ink and the pulse waveform has a strong effect on the size and speed of the droplets. However, because many inks are formulated using a wide variety of solvents, particulates, and additives, it is difficult to make direct comparisons between one ink's jetting performance and another. Therefore, in an effort to create normalized scales to systematically determine which factors most strongly impact jetting performance, many dimensionless parameters are often used. The primary four dimensionless numbers are the Reynolds number (Re), the Weber number (We), the capillary number (Ca), and the Z number (Z) [47]. Re, We, and Ca all balance two forces against each other, whereas Z balances three, as described in the following equations. Ca is the only number that does not depend on a characteristic length, which is often obtained from the nozzle orifice diameter,  $d$  (see Figure 2.5).

$$\text{Reynolds number, } Re = \frac{\text{inertial force}}{\text{viscous force}} = \frac{\rho v d}{\eta} \quad (2.5)$$

$$\text{Weber number, } We = \frac{\text{inertial force}}{\text{surface tension force}} = \frac{\rho v^2 d}{\gamma} \quad (2.6)$$

$$\text{Capillary number, } Ca = \frac{\text{viscous force}}{\text{surface tension force}} = \frac{\eta v}{\gamma} \quad (2.7)$$

$$\text{Z Number, } Z = \frac{\sqrt{\text{inertial} * \text{surface tension force}}}{\text{viscous force}} = \frac{\sqrt{\gamma v d}}{\eta} \quad (2.8)$$

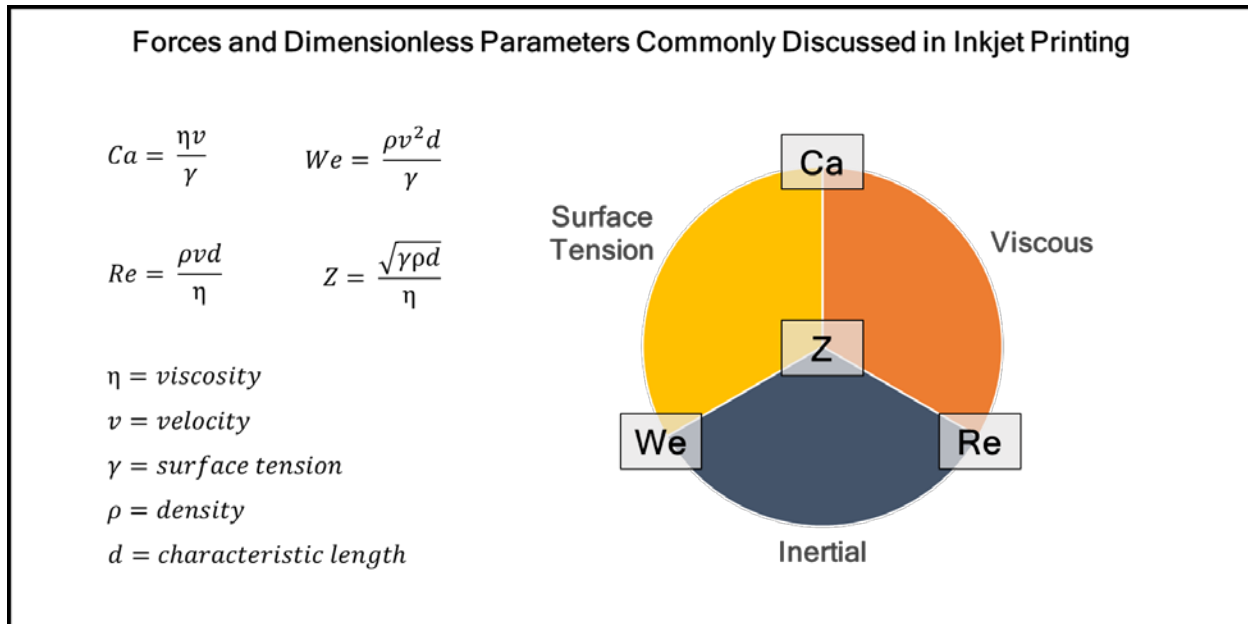


Figure 2.5. Forces and dimensionless parameters often used to quantify jetting performance.

The goal of using these dimensionless parameters is to determine a general window of feasible conditions whereby *any* ink, regardless of composition, should jet reliably. Because  $Z$  incorporates all of the forces into a single value, it has often been used as the primary metric to describe the boundaries of stable jetting performance, however those boundaries are not clearly agreed upon in the literature [47, 62, 65, 66]. The use of these parameters to empirically determine this feasibility is the primary focus of this chapter, and will be discussed at length in the following section.

## 2.2. Custom Ink Formulation for Jettability Experiments

As previously described, ink formulation is often considered more of an art than a systematic process. For practical applications in inkjet printing, the objective of ink formulation is produce an ink that a) is capable of high mass loading and b) is produces stable droplets within and across printing processes. The two main parameters to adjust are the fluid properties of the solvent system chosen, as well as the loading level of the inks. It is critical to explore a wide range of fluid properties by selecting many different solvents and to characterize the jetting using a criterion that fairly compares inks to each other. Because commercial nanoparticle formulations are proprietary mixtures, the modulation of ink composition of commercial inks is much more difficult than the modulation of ink composition in custom inks. Therefore, in this section the framework for developing and characterizing custom nanoparticle inks will be discussed. Importantly, the parameters used to quantify jetting quality will be described in detail, and compared to the conventional practices seen in literature.

### 2.2.1. Materials

All of the inks used in this particular study were synthesized using a well-known gold nanoparticle synthesis [16]. This synthesis was chosen because it is robust with regard to repeatability, size distribution, and nanoparticle solubility. That is, the nanoparticles synthesized in this method are highly soluble in a number of non-polar organic solvents, which allows for the exploration of a wide range of solvent fluid properties without having to sacrifice the potential for loading the ink to practical levels. All of the particles synthesized in this work are encapsulated with hexanethiol and have a mean diameter of 2 - 3 nm [31]. Appendix B describes the complete synthetic process.

As mentioned, these nanoparticles are highly soluble in a number of nonpolar organic solvents. To study the effect of solvent selection on jetting quality, the following solvents were used in this work: cyclohexanol, decanol, octanol, hexanol, toluene, dodecane, tetralin, anisole, o-xylene, tetrahydrofuran, alpha-terpineol, and hexane.

### 2.2.2. Ink Fluid Characterization Procedures

The fluid properties of each ink were tested according to the following procedures.

#### A. *Viscosity*

Using a Brookfield LVDV III rheometer, all formulated inks were measured to determine their viscosity. The maximum shear rates capable of this tool approached  $2 \times 10^3$  1/s, depending on the ink being tested. For comparison, shear rates observed in inkjet nozzles can be roughly two orders of magnitude larger, around  $1 \times 10^5$  1/s. Therefore, shear thinning and thickening must be taken into account in order to properly identify the viscosity of the fluid being printing. The pure solvent systems tested were assumed to be Newtonian, i.e. they did not exhibit any shear thinning or thickening behavior, due to their simple molecular structure. Therefore, relatively low shear rate measurements obtained using this rheometer were assumed to accurately identify the viscosity of the ink for higher shear conditions present during inkjet printing. Further, while it is known that very high particulate loading levels (>60% by mass) may result in non-Newtonian behavior in loaded inks [67], the loading levels of the inks tested did not exceed 30% by mass, and therefore it was assumed that they are also Newtonian.

### B. Surface Tension

Surface tension measurements were taken using a pendant drop test [68, 69, 70, 71]. In this test, a drop of fluid is pushed out of a tube with a known diameter. Then, the equatorial diameter,  $d_e$ , of the droplet is determined. Next, the diameter of the droplet a distance of one equatorial diameter above the bottom of the droplet, called  $d_s$ , is calculated. The ratio of these two diameters can be used to determine the surface tension (see Figure 2.6 for a schematic of this test). This is based on the radius of curvature of the drop and fitted using an analytical geometrical relationship. The surface tension can then be determined using well-established lookup tables based on the values for these two diameters. Using this approach, it is important to ensure that the ratio of  $D_s/D_e$  is between 0.8 - 1, which can be accomplished by adjusting the diameter of the tube where the fluid is expelled from. A custom apparatus was built and automated image processing scripts were written to calculate the surface tension of the ink being tested.

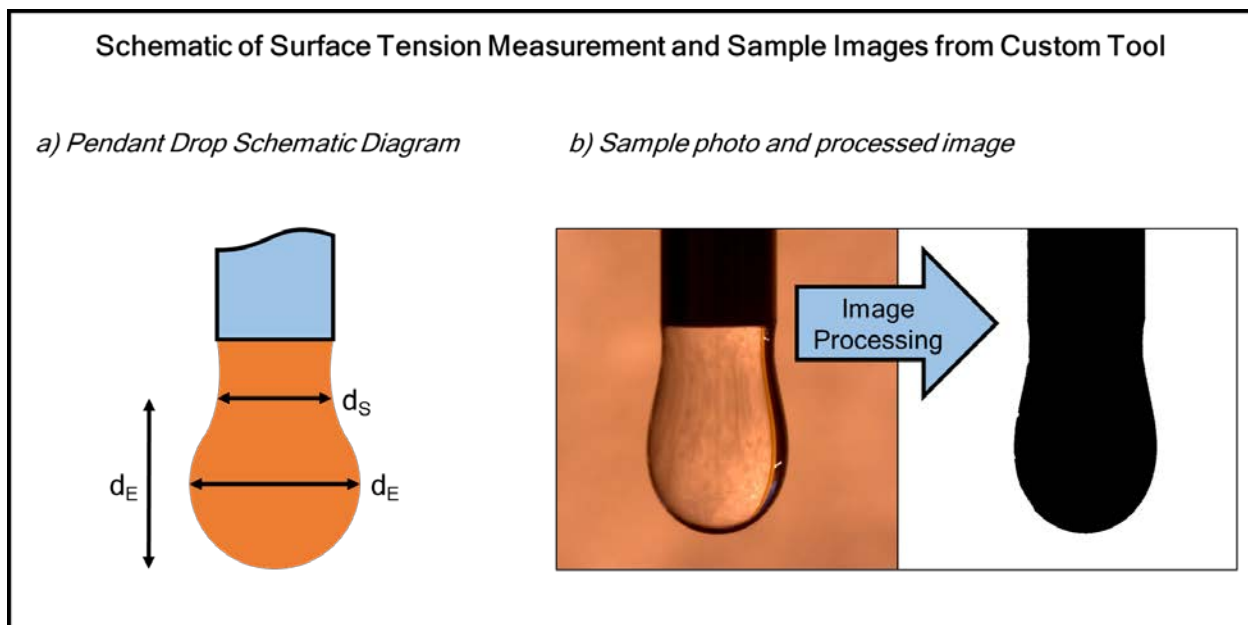


Figure 2.6. Schematic diagram of important drop measurements associated with the pendant drop measurement protocol and sample images obtained from custom-built tool when measuring water.

### C. Density

All density measurements were made by weighing different volumes of the same, well-mixed ink on a scale. Fitting the mass versus volume with a line resulted in extracting the density of the ink. Multiple volumes were tested in order to avoid the potential error of a single measurement.

#### 2.2.3. Jettability Definition and Characterization Framework

This section will discuss the particular details regarding the framework for comparing and quantifying ink jetting performance. The first step is to establish a definition and tolerance levels for ink jetting performance. This metric will be referred to as *jettability*. A

simple definition of a jettable ink is one that can be jetted stably for long periods of time. For inkjet printing applications, a number of constraints must be considered when determining the stability of the ink.

#### A. *Droplet Convergence Distance*

First, the droplets formed should converge into single droplets prior to reaching the substrate. Because the fly height of the nozzle is usually on the order of 2 mm, drop convergence prior to 1.3 mm was selected as the maximum tolerable distance. Satellite droplets may form during jetting, but as long as these droplets converge with the head droplet before this distance, the jettability was not impacted directly.

#### B. *Dwell Time Optimization*

Next, because multiple inks are being tested, the pulse waveform selected for a given ink will not be suitable for a different ink. Therefore, the pulse waveform should be optimized for each ink being tested prior to quantifying and comparing the jetting behavior. This waveform optimization is accomplished by adjusting the dwell time. Typically, the dwell and echo times are adjusted such that the maximum possible droplet velocity is achieved, however a new methodology is introduced here.

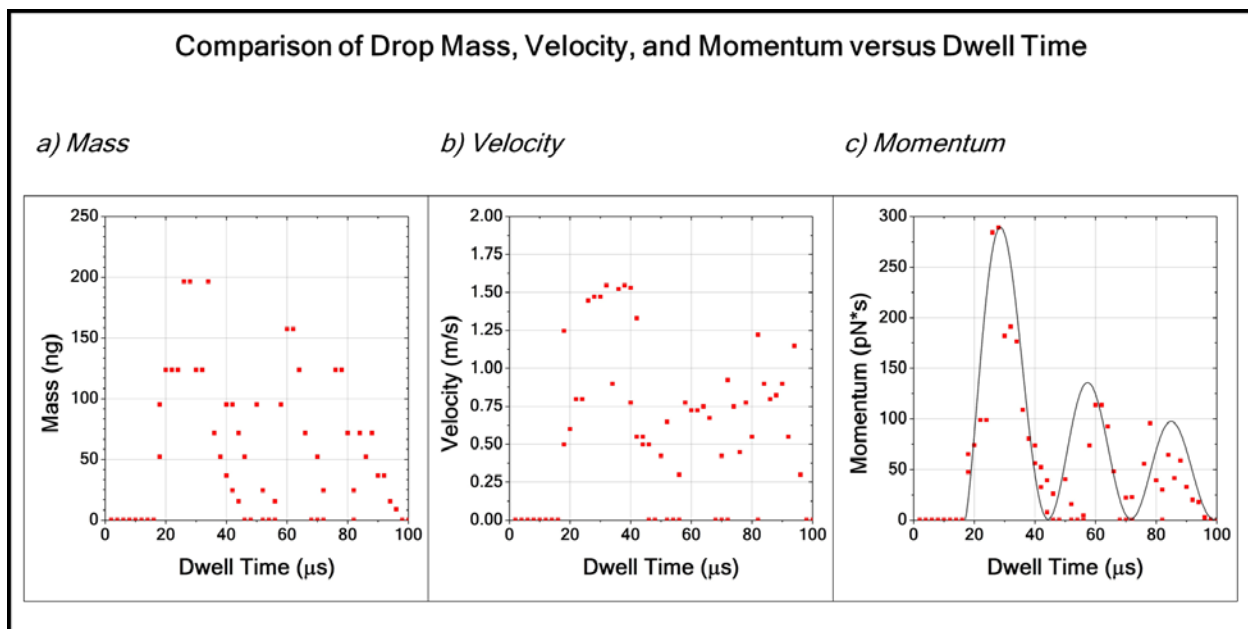


Figure 2.7. a) Drop mass, b) velocity, and c) momentum versus dwell time. Mass and velocity do not show expected periodic trend, while momentum exhibits expected periodic behavior.

Rather than used droplet velocity as the metric that determines the optimal dwell time, droplet momentum was chosen (see Figure 2.7). Momentum was selected for three reasons. First, because the applied pressure on the system will impact the ejected droplet volume, the speed of the droplets will change as a function of the applied pressure. This results in the degradation of the expected periodic velocity response as a function of dwell time, as shown in the Figure 2.7b. Second, because this applied pressure may vary both within the testing of a single ink and across the testing of multiple inks, it should be normalized. Finally, because this work inherently involves

testing multiple fluid systems, the expected droplet volume of each system will change simply due to the change in fluid properties.

Because the density of the inks tested are already known and the volume of the droplet is easily determined via *in situ* image capture systems, the momentum of the droplet is easily derived. As shown in the Figure 2.7c, the momentum versus dwell time relationship aids in restoring the expected periodic trend with dwell time. As such, the dwell time that produced the maximum droplet momentum was selected as the optimal dwell time for each ink.

### C. Jettability Characterization Framework

Combining the two constraints discussed above, it is now possible to develop a framework for testing the jettability of a particular ink. Figure 2.8 shows a schematic block diagram of the characterization framework. First, all of the fluid properties must be measured using *ex situ* testing. Next, each ink is loaded into an inkjet nozzle and jetting is initiated. Using the *in situ* image capture hardware and software, the optimal dwell time is determined for each ink by maximizing the momentum of the droplet. As per the initial constraint, any droplets that do not converge into a single droplet prior to 1.3 mm distance travelled from the nozzle are rejected as non-jettable inks. Finally, because the pulse voltage is directly responsible for adjusting the droplet velocity, as described earlier, the pulse voltage is modulated to determine the boundary of the jettable range of a particular ink. Any ink failure mechanisms due to droplet instability are noted as a function of voltage at the optimal dwell time. These failure mechanisms are discussed next.

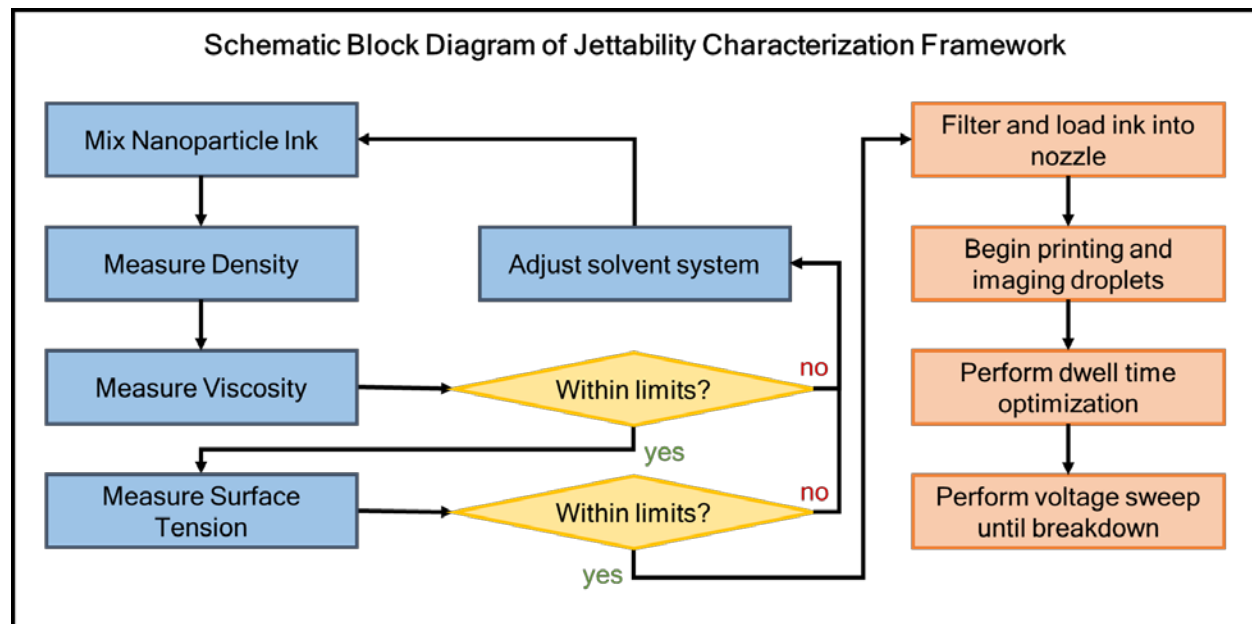


Figure 2.8. Process block diagram for jettability characterization.

### D. Jetting Failure Mechanisms

There are three major failure mechanisms common to droplet formation. They are failure to form a droplet, satellite droplet production, and multiple droplet formation.

First, multiple conditions may lead to the failure to form a droplet. The primary cause is an insufficient pressure wave amplitude within the chamber. This may be the result of too low of a driving voltage for the pulse waveform, or too high of either surface tension or viscosity of the ink. The manifestation of this failure mechanism is only slightly perceptible perturbations in the meniscus of the ink at the nozzle.

Satellite droplets, on the other hand, arise when the thinnest regions of the ejected drop's tail are located at the center of the tail. This surface tension of the ink causes the tail to break in the center as opposed to the nozzle orifice, creating secondary droplets that may or may not follow the same trajectory as the head. This not only causes the drop volume to change but also may result in drop placement accuracy issues that will make pattern formation on a substrate impossible. These satellite droplets are more common in highly viscous inks being jetting with very high driving voltages.

Finally, multiple droplets may form in inviscid inks that are subjected to wave-like instabilities during jetting [72]. When this occurs, multiple satellites are formed and the drop accuracy suffers even more than single satellite formation. Images of each of these failure mechanisms are shown in Figure 2.10.

### 2.3. Jettability Window and Ink Design Rules

Jettability windows compare the effects of two non-dimensional parameters on jetting quality. Both the  $We$ - $Re$  and the  $Ca$ - $We$  jettability window have been proposed in literature [73, 74]. Using the framework presented in the previous section, it is possible to directly compare the jetting performance of multiple inks with each other by mapping the results to a jettability window. In this work, a  $Ca$ - $We$  window was chosen. The selection of the  $Ca$ - $We$  jettability space will be explained next, along with the results for pure solvent systems, binary solvent systems, and loaded nanoparticle inks.

#### 2.3.1. $Ca$ - $We$ Jettability Window

A jettability window defined by  $Ca$  and  $We$  is chosen for this work for the following reasons. First, when considering each of the dimensionless parameters defined earlier, it is useful to observe that the surface tension force is the normalizing force for both  $Ca$  and  $We$ . Furthermore, the surface tension forces do not vary widely for all of the systems tested. The other fluid and geometric parameters not shared between the two dimensionless parameters are the nozzle diameter and the density. The nozzle diameter is kept constant for all of the tests and, similar to surface tension, there is very small variation in the density of the tested inks. Therefore, the effect of ink viscosity and drop velocity will be the two differentiating parameters. Because these two parameters are obtained from  $Ca$  and  $We$ , respectively, plotting ink  $Ca$  and  $We$  against each other will provide the most insight into the jettability of a particular system.

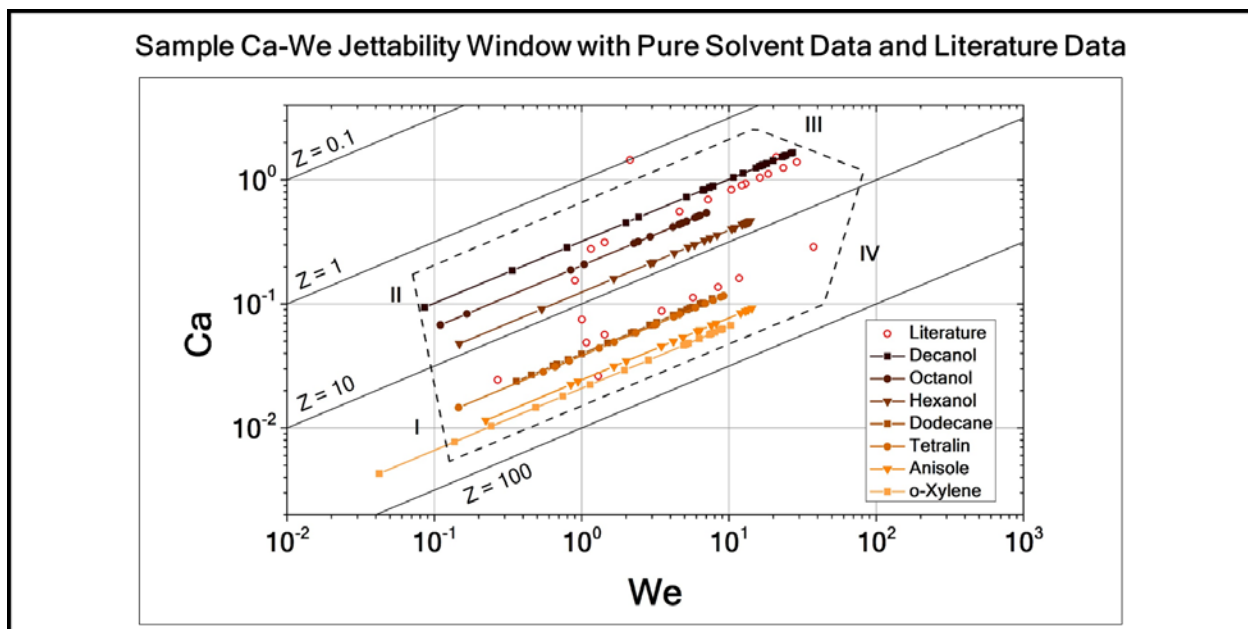


Figure 2.9.  $Ca$ - $We$  jettability window.

A sample  $Ca$ - $We$  jettability window is shown in Figure 2.9. Overlaid on the plot are  $Ca$  and  $We$  values for pure solvents tested as well as inks described in literature [58, 66, 75]. Both  $Ca$  and  $We$  vary many orders of magnitude in jettable inks, therefore plotting these values on a log-log scale is adopted. Each data point plotted in the window represents a single ink being printed at a particular velocity. The lines represent a single ink printed at multiple drop velocities. This drop velocity modulation is achieved by

altering the pulse voltage, as explained earlier. It is important to note that  $Ca$  has a linear drop velocity dependence while  $We$  has a quadratic dependence on drop velocity. Therefore, a log-log plot will produce contour lines with a slope of  $\frac{1}{2}$  for each ink tested. Plotted lines are terminated when no stable jetting condition was achieved at either higher or lower drop velocities, according to the jettability criterion previously defined. Therefore a longer line represents a wider jettability range for a given ink. Finally, because  $Ca$  is the only parameter that has a viscosity dependence, the lower and upper bounds of the window represent that minimum and maximum viscosity limits for printing. The boundaries of this window, therefore, should represent a universal window for jettability.

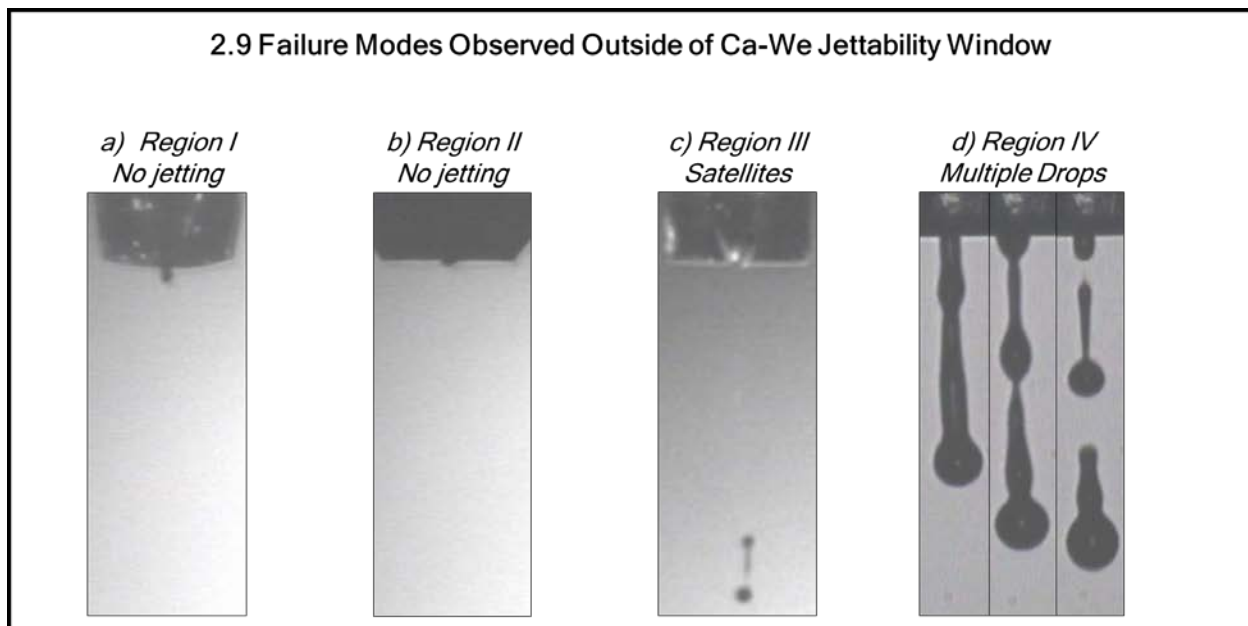


Figure 2.10. Failure modes observed when attempting to jet outside of the boundaries of the Ca-We jettability window.

Outside of the established window, jetting fails according to one of the mechanisms described earlier. These failure modes are labeled I - IV on the window. Failure modes I and II are the failure to form a droplet. These occur on the left hand side of the plot due to either high viscosity, low perturbation energy, or both. Failure mode III is satellite formation characteristic to high viscosity, high drop velocity conditions. Failure mode IV is multiple drop formation expected in low viscosity, high drop velocity conditions. Images of inks producing each of these failure modes are shown in Figure 2.10.

### 2.3.2. Modulating Jettability via Co-Solvent Addition

The results of jetting pure solvent systems are included in Figure 2.9. While these solvents may span a reasonable range with respect to their fluid properties, it is not possible to navigate the window to more stable regions with pure solvent systems alone. One option for modulating jettability, therefore, is to adjust the fluid properties based on co-solvent addition. Figure 2.11 presents a new jettability window that now includes contours for binary solvent systems identified in the legend. It is clear that these new

mixtures allow for expansion to a wider range of jettable conditions, based strictly on the composition of the ink.

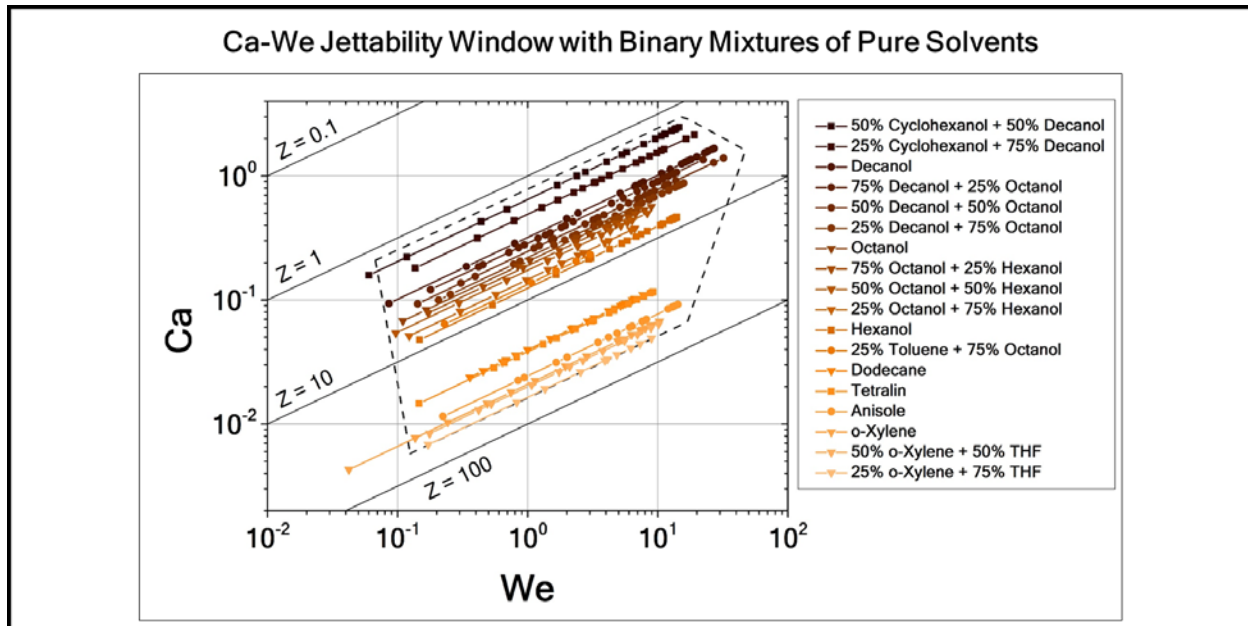


Figure 2.11. Ca-We jettability window with binary solvent mixtures included.

This can be a technique very useful in ink formulation. For example, perhaps a nanoparticle system is particularly soluble in either a very inviscid or very viscous solvent, but this solvent lies outside of the jettability window. In order to impart jettability to the ink, one might consider adding a reasonable co-solvent that modulates the viscosity of the ink such that the resulting viscosity positions the ink in the center of the jettability window. Two examples of this technique are presented next. In each of the following examples, inks containing gold nanoparticles loaded to 10% by mass were prepared in different solvent systems.

In the first example, shown in Figure 2.12, mixtures of 0%, 10%, 20%, and 30% alpha-terpineol in hexane were prepared. For the pure solvent system, hexane, the mixture was too inviscid (0.3 cP) and the ink was not jettable. This condition is represented as a dashed contour on the jettability window in Figure 2.12. As the alpha-terpineol composition increases, the viscosity of the fluid increases. At 20% alpha-terpineol, the jetting is nearly stable, but it does not persist for a long enough time to satisfy the jettability criterion. It is likely that the very high evaporation rate of hexane causes the nozzle to “skin” and prevent stable droplet formation. However, once a 30% alpha-terpineol condition was tested, the viscosity (0.96 cP) was high enough that stable droplets were able to form.

While this approach was successful, the inclusion of a large hexane component may still lead to poor stability over long time scales due to the skinning or clogging. Therefore, the opposite approach was also demonstrated. In this second example, hexane was incrementally added to alpha-terpineol. Figure 2.12 shows the result of adding hexane.

With as little as 10% added hexane, the viscosity of the ink drops from 36.5 cP (at 100% alpha-terpineol) to 23.4 cP and the ink resides well within the jettability window.

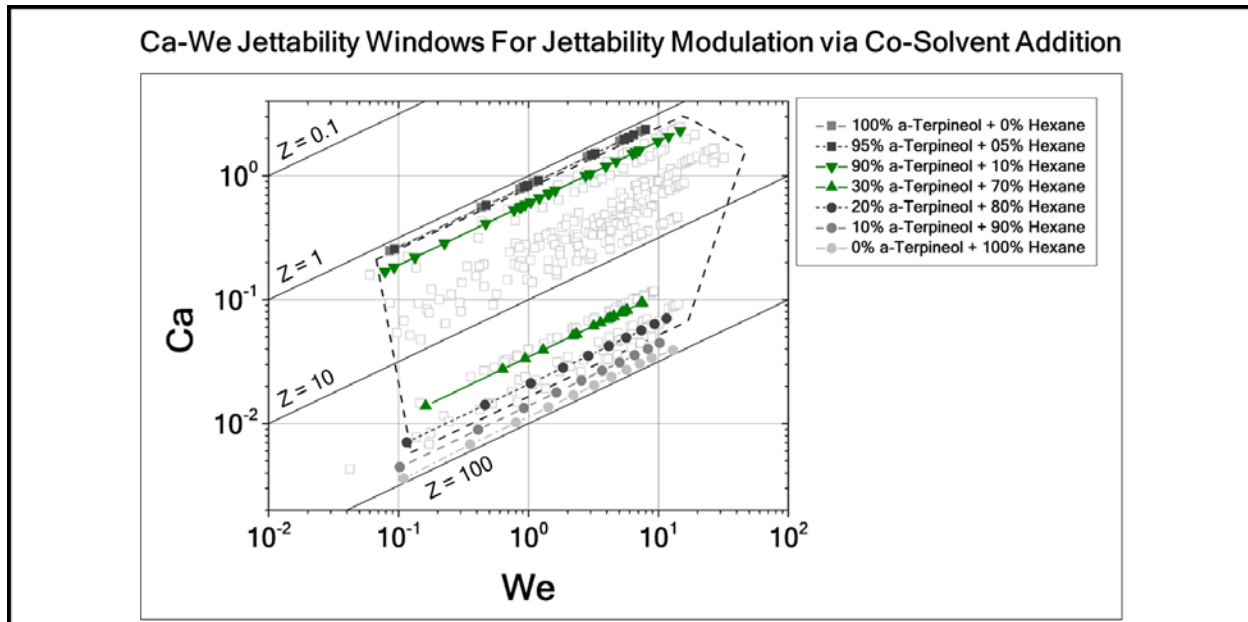


Figure 2.12. Ca-We jettability windows demonstrating the effect of co-solvent addition for moderately loaded (10% by mass) gold nanoparticle inks in hexane and alpha-terpineol. Systems highlighted in green are jettable inks whereas gray systems were not jettable.

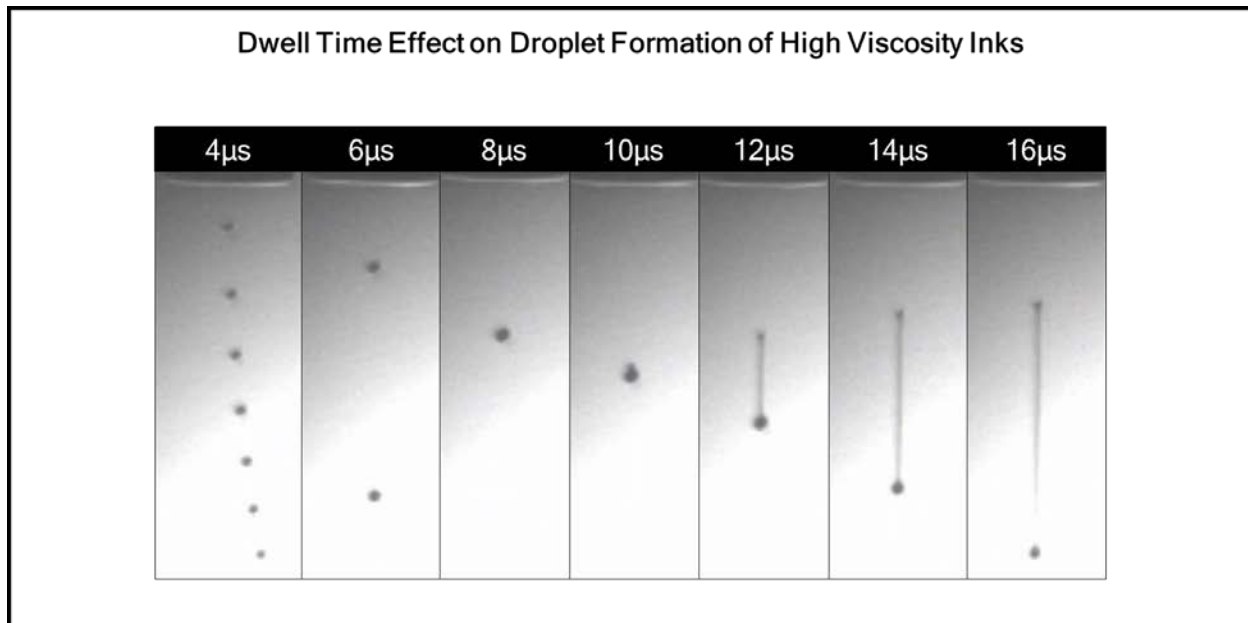


Figure 2.13. The effect of high viscosity on determining the optimal dwell time of an ink. Longer dwell times produce dramatically larger tails and shorter dwell times produce dramatically lower drop sizes, making dwell time optimization based on momentum challenging in high viscosity inks.

However, a caveat in this example exists. Because the ink lies very close to the upper boundary of the jettability window (due to its high viscosity), viscosity-related effects made the determination of an optimal dwell time impossible. This is because high viscosity inks may inhibit the chamber from refilling completely after each droplet ejection event [76]. Figure 2.13 shows a series of images of the droplet formation of this high viscosity ink as a function of dwell time. No clear optimum exists and therefore 10  $\mu$ s was taken as the optimum condition. This viscosity-dependent dwell time optimization may be explained as follows. At high viscosities, only flow into and out of the chamber is high amplitudes are used. However, this results in a large change in chamber volume. For long dwell times, the chamber is able to completely refill, but this results in an undesired increase in volume ejected during the next actuation event. Conversely, lower dwell times result in an incompletely filled chamber and, therefore, a single drop with reasonable volume is produced.

### 2.3.3. Modulating Jettability via Nanoparticle Loading

In the previous examples each of the inks tested were loaded to 10% by mass with gold nanoparticles. While this is useful at demonstrating the ability to print nanoparticle-based inks, a practical nanoparticle ink will actually have a mass loading much higher than 10%. Therefore, increasing mass loading is an additional practical constraint for ink formulation. As previously mentioned, at loading levels below 60% by mass, it is expected that the nanoparticles will not exhibit non-Newtonian behavior, however the increase of mass loading does have a direct effect on the ink viscosity. Therefore, the jettability can also be modulated by tuning the mass loading of the ink.

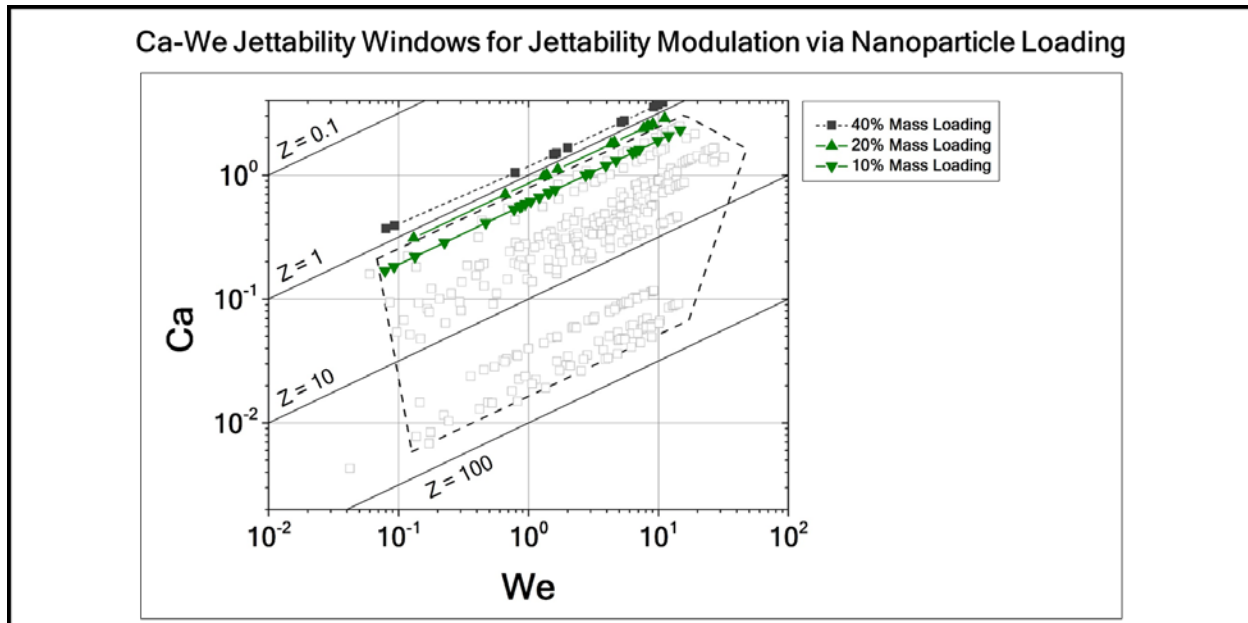


Figure 2.14. Ca-We jettability window demonstrating nanoparticle loading effect on jettability. Pure solvent and mixture data grayed out. Systems highlighted in green are jettable inks whereas systems highlighted in gray were not jettable.

In the previous example, hexane was added in order to decrease the ink viscosity and impart jettability. At 10% hexane, the ink was jettable. In order to demonstrate the effect

of mass loading on jettability, the mass loading of inks made with binary mixtures with 10% hexane in alpha-terpineol was increased until the ink was no longer jettable. Figure 2.14 presents the new jettability window with the results of this experiment. As can be seen, the 10% and 20% mass loading conditions were jettable, though the 20% condition resides very near the upper boundary of the window. It should be noted that because each data point collected still creates a line within the Ca-We space, this confirms that, as expected, high mass loading inks do not exhibit non-Newtonian effects at high drop velocities, i.e. high shear rates. Once the mass loading of the ink increases further, however, the ink no longer becomes jettable. This failure to jet was not due to nozzle clogging caused by high loading, however, because it was easy to purge the nozzle during experimentation. Rather, the viscosity at 40% mass loading (52.5 cP) is simply too high for droplet formation to be possible.

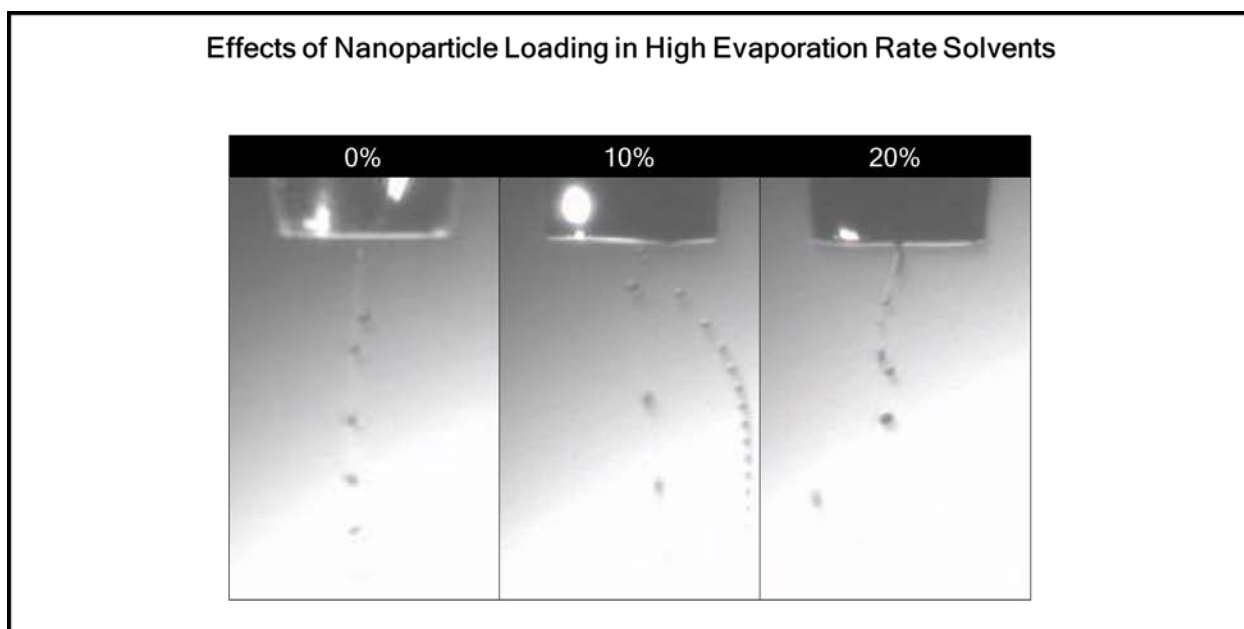


Figure 2.15. Effect of nanoparticle loading in high evaporation rate solvents.

Because the initial viscosity of the ink was very high in this last example, jettability worsened with increasing mass loading. Conversely, it may be more useful to impart jettability in inviscid systems by increasing the mass loading. This was attempted with pure hexane (see Figure 2.15) but jettability actually worsened in this system as mass loading increased. As previously mentioned, in addition to being very inviscid hexane has a very high evaporation rate. Therefore, as loading increased, the phenomenon called the ‘first-drop problem’ became more pronounced [30]. This phenomenon is the clogging of the nozzle by partially dried ink. As mass loading increases, more the particles will dry on the nozzle at a faster rate, meaning that clogging will occur sooner.

#### 2.3.4. General Ink Formulation Design Rules

Combining the results from the two previous sections describing the modulation of jettability, it is now possible to devise a general strategy for formulating reliable inks loaded with nanoparticles. The jettability window established represents a reliable guideline for ink design, and therefore an ink designer can use the interactions of the

solvent systems and nanoparticles in order to design robust inks in the following manner. First, at least one of the solvents considered should be capable of achieving a high degree of solubility for the given nanoparticle system. It is preferable that both are capable of high mass loading, however. Next, the co-solvent chosen should be combined with the primary solvent such that the predicted viscosity would position the pure binary solvent system safely within the jettability window. The primary solvent chosen should not exhibit too high of an evaporation rate, in order to avoid clogging issues related to the first-drop problem. Finally, the mass loading of the ink should be considered and increased until a practical threshold is reached. 30% mass loading represents a very practical mass loading for nanoparticle-based inks. According to this procedure, a general systematic route to formulating inks that exhibit reliable jettability is derived.

## 2.4. Summary

In piezoelectric droplet-on-demand inkjet printing, the actuation of a piezoelectric material lining the chamber of the nozzle is directly responsible for creating droplets. The relationship between the actuation and ultimate droplet formation, however, is a balance between the fluid properties of the ink and the geometric properties of the nozzle. Oftentimes, the maximization of droplet velocity is a goal, and therefore the fluid properties of the ink as well as the shape of the pulse waveform are adjusted to achieve this goal. Furthermore, when comparing the performance of multiple inks, dimensionless parameters are often used in lieu of making direct comparisons of physical properties. While this is generally good practice, care must be taken to choose the correct dimensionless parameters to compare in order to determine a true metric of jetting quality.

Using the dimensionless parameters,  $Ca$  and  $We$ , it is possible to decouple the effects of drop velocity and ink viscosity in order to develop a jettability window that guides ink formulation. This window is strongly driven by the viscosity of the inks chosen, and this viscosity can easily be modulated through both co-solvent addition as well as nanoparticle loading. With an understanding of how these two processes affect the ultimate viscosity of the ink, it is possible to develop a systematic procedure for developing reliable ink formulations.

First, the fluid properties of the ink are determined using *ex situ* testing methods. Then, *in situ* characterization of droplet size, volume, and speed are used to determine the optimal jetting waveform for a particular ink as a function of maximum drop momentum as opposed to the more commonly used maximum drop velocity. Finally, the range of jettability for each ink is determined by varying the amplitude of the pulse waveform voltage and observing failure mechanisms common to droplet formation.

## Chapter 3. Metal Nanoparticle Solubility Enhancement via Heuristic Optimization

---

As Chapter 2 highlights, one parameter that is useful for controlling the rheology and jetting conditions of a functional ink is the nanoparticle mass loading (often referred to as solubility) of the ink itself. For a given ink, a higher mass loading is desirable for two reasons. First, it expands the range available for moderating the rheological parameters of the ink in order to adjust the jetting performance. Second, in colloidal nanoparticle suspensions, a higher mass loading means more suspended material per droplet. This results in a higher overall process throughput because fewer droplets are necessary to deposit the same total amount of material. Because mass loading is such an important ink parameter, considerable efforts have been made to understand and optimize the mass loading potential for metal nanoparticles. While most efforts have been based on traditional experimental design, this chapter will describe a non-traditional approach to optimizing metal nanoparticle solubility via heuristic techniques.

### 3.1. Introduction

The design of colloidal nanoparticle suspensions with high mass loading involves understanding complicated interactions between the nanoparticle encapsulant composition/arrangement and a given solvent system. Many observations have shown that controlled changes in synthetic conditions produce a response surface with many minima and maxima with respect to solubility, and this link between encapsulation and solubility is poorly understood overall. When optimizing materials with these responses, heuristic experimental design may both more rapidly discover an optimized condition and produce a valuable dataset that provides more insightful observations with regard to understanding the underlying interaction between structure and solubility. This introduction will describe the current understanding of solubility in metal nanoparticle systems and give a brief introduction to the heuristic experimental method employed to optimize nanoparticle silver nanoparticle systems.

#### 3.1.1. Metal Nanoparticle Solubility

As previously described, the encapsulants bound to metal nanoparticles have multiple functions. First, during synthesis, encapsulants serve to stabilize and control the size and shape of the nanoparticles produced [77], which is important if size effects causing changes in thermal, electronic, or optical behavior are desired. Second, when in solution, the encapsulants are the materials that interface between the nanoparticle and a) the solvent, b) other encapsulated nanoparticles, or c) both. Thus, the encapsulants prevent the nanoparticle cores from aggregating and crashing out of solution and, therefore, play a strong role in determining the solubility of the nanoparticle.

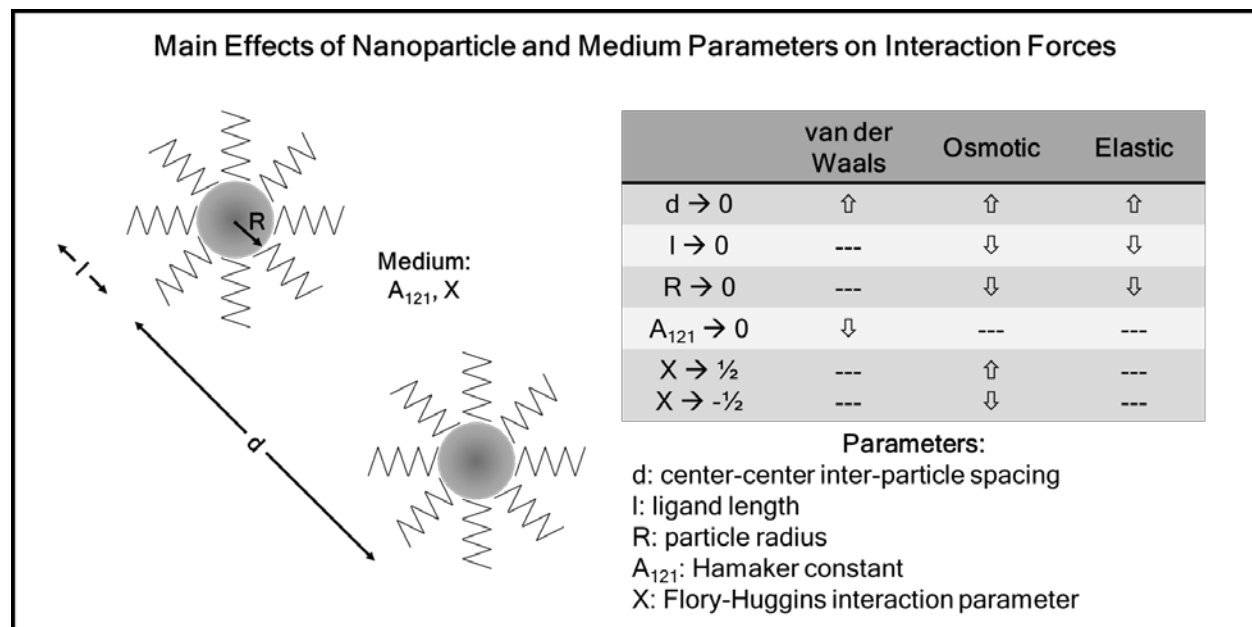


Figure 3.1. Schematic of particle-particle relationship in solution for two particles with identical encapsulation schemes and table with relationship of particle and medium parameters on strength of interaction forces.

Generally, nanoparticle solubility can be thought of as a balance of three interactions: a) the repulsive osmotic interaction between nanoparticle encapsulant and solvent, b) the

repulsive elastic interaction between nanoparticle encapsulant with encapsulants on neighboring nanoparticles, and c) the attractive van der Waals interaction nanoparticle cores with each other [78]. Together, the repulsive interactions are often referred to as the steric interactions. Figure 3.1 shows a comparison of these forces. In general, the balance of steric and van der Waals forces depends most on the length of the encapsulant and the nanoparticle separation distance and properties of the medium in which the nanoparticles are located.

The attractive van der Waals force depends most strongly on the inter-particle spacing and the dielectric properties of the medium, described by the Hamaker constant,  $A$  [79, 80]. Since increasing solubility is the objective, the increase in steric forces in order to overcome the attractive van der Waals force is necessary. Therefore, it is important to consider the two components of steric repulsive forces and their dependence on the physical nature of the nanoparticles.

Among these two forces, the osmotic force dominates. Further, the property considered most important in dictating the osmotic interaction is polarity. In many metal nanoparticle systems, encapsulants are alkane chains with functional groups that bind to the metal core [16, 17]. Therefore, the long, nonpolar hydrocarbon tail of the encapsulant interacts with the solvent system. Not surprisingly, nonpolar solvents are often the best solvents for these types of encapsulants. Water-soluble nanoparticles are, in contrast, often encapsulated with hydrophilic, polar materials such as polymers [81], peptides [82], phosphines [83], etc. The parameter that describes this interaction is the Flory-Huggins interaction parameter, which describes the quality of the solvent for a given encapsulant [84, 85]. A positive interaction parameter represents a good solvent and a negative parameter represents a poor solvent. Second, the elastic interaction force is strongly determined by the encapsulant length and particle separation. This force is only strong when the nanoparticles are very close together. This can occur when the encapsulant length is very short or when the radius of nanoparticles is very large. Therefore, longer encapsulants and larger particles should aid in improving the solubility of the nanoparticles.

While increasing the encapsulant length may aid in boosting solubility, the increase in encapsulant length tends to both increase the melting point of the encapsulant and increase the overall carbon content of the nanoparticle. Recalling from Chapter 1, the residual carbon content and porosity of sintered films are two issues responsible for degraded film conductivity. Therefore, in inkjet printing applications, this undesired increase in both required sintering temperature and residual carbon content should be avoided. As such, it is desirable to boost the solubility of the system while simultaneously reducing the encapsulant length. For single-encapsulant systems this is difficult, but the synthesis of mixed-encapsulant systems has been shown to boost the overall solubility [86]. The boost in solubility is typically explained as follows. In systems with multiple encapsulants of different lengths bound to the nanoparticle core, the exposed surface of the nanoparticle is disordered and no longer smooth, causing both the steric repulsion forces to increase as well as the van der Waals force to decrease. However, it has also been shown that the relationship between expected surface disorder and measured solubility is very difficult to predict [87, 88]. For example, in a

two-encapsulant system where the composition of the encapsulants was varied during synthesis, the resulting measure of solubility shows a strong dependence on solvent system selected and may often show a bimodal response with regard to composition [87, 89]. One possible explanation is that the encapsulants on the surface may spontaneously order into different arrangements that would either increase or decrease the ultimate solubility. Scanning tunneling microscopy was used to confirm this proposed phenomenon, but the validity of this measurement technique has been openly debated [90, 91, 92]. Despite the lack of consensus regarding the mechanism, the solubility dependence on encapsulant composition is indeed accepted as a real effect clearly meriting further investigation.

### 3.1.2. Heuristic Optimization

To date, the basis for the determination of experimental parameters has been a factorial design based on traditional design of experiments. According to this approach, the response to input conditions is determined after the experimental space is evenly divided across each of the input parameters, though the exploration of each combination of conditions is typically avoided due to resource limitations such as time and money. Therefore, a subset of the conditions is tested and the results are fitted to a response based on response surface methodology assumptions for linear, quadratic, or cubic fitting models [93].

While this approach has been proven to be very robust for many engineering applications, response surface methodologies are not effective when the true response cannot be accurately fitted to a second-order model [94]. This commonly occurs in systems with many local extrema and/or in systems with asymmetric extrema, such as the solubility response in metal nanoparticles. When these systems containing multiple extrema are tested with a limited number of experiments due to resource limitations, it is very easy to miss the extrema and to improperly predict the response to input parameters. Therefore, an alternative method must be used to discover the optimum condition in these systems.

A heuristic technique based on a genetic algorithm is one such method commonly used to both obtain a truer response surface and more rapidly identify a system's optimum condition [95]. In a genetic algorithm design, multiple sets of experimental conditions are derived and tested. Each set is derived from the previous set, whereby the best conditions in the previous set are given a strong influential weight, i.e. Darwin's theory of natural selection is applied. The genetic algorithm used in this work is the non-dominated sorting genetic algorithm II (NSGA-II) and will be briefly described now [96].

First, the experimental space is similarly, though often more finely, divided across all of the input parameters and the possible parameters are encoded for subsequent selection. The encoding method chosen is typically a binary representation of the input parameter condition. Each encoded condition is analogous to a *gene* and the collection of a string of encoded conditions is analogous to a *chromosome* (see Figure 3.2). An initial generation of chromosomes is selected randomly for evaluation. During evaluation, a physical response(s) measured is mapped to a normalized score by use of a *fitness function*. Typically a higher fitness function output indicates a higher performing

member of the population. Sometimes, fitness functions are referred to as *objective functions*, since their objective is to optimize the system based on the function's output. After each response is measured, the responses are divided into ranks based on their *dominance* over the entire population. If multiple characteristics of a system are being optimized simultaneously, this dominance is typically determined by the Pareto efficiency of the conditions [97]. The most Pareto-dominant members of the initial population are selected as the parents for the subsequent population. In order to determine the chromosomes of all subsequent population, two parent chromosomes are split and recombined to produce two children; this is called *crossover*. Random *mutations*, generated by the random flipping of bits in the resulting chromosomes, are included to reintroduce variation in the population. After crossover and mutation, the new chromosomes (a new set of binary-encoded genes) are now members of the next population. This process repeats until the experimental designer is satisfied that the global extrema has been found.

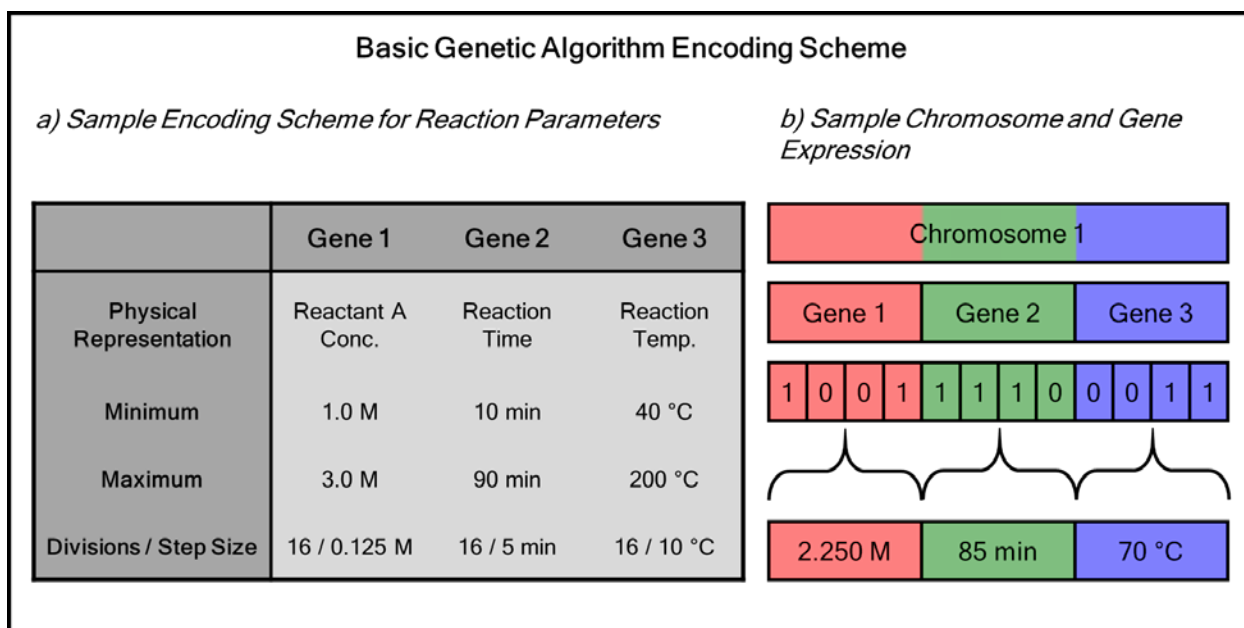


Figure 3.2. Example of a) encoding schemes used in genetic algorithms and b) how conditions are represented in gene and chromosome format.

Figure 3.3 describes the process steps involved in a single iteration of a genetic algorithm. The main benefit of this genetic algorithm is that, though it ultimately requires many more experiments than a conventional experimental design, the inherent randomness due to crossover and mutation aids in avoiding local extrema over the course of multiple generations. This results in a more rapid discovery of a true global extrema in complex systems, and is therefore well-suited to the problem of solubility enhancement for metal nanoparticles. In addition, this genetic algorithm is capable of optimizing for multiple objective functions. Therefore, not only can solubility be maximized, but the amount of required carbon-based encapsulant to effect this solubility can be simultaneously minimized. For inks used in printed electronics, optimizing these two properties should result in very high performing inks.

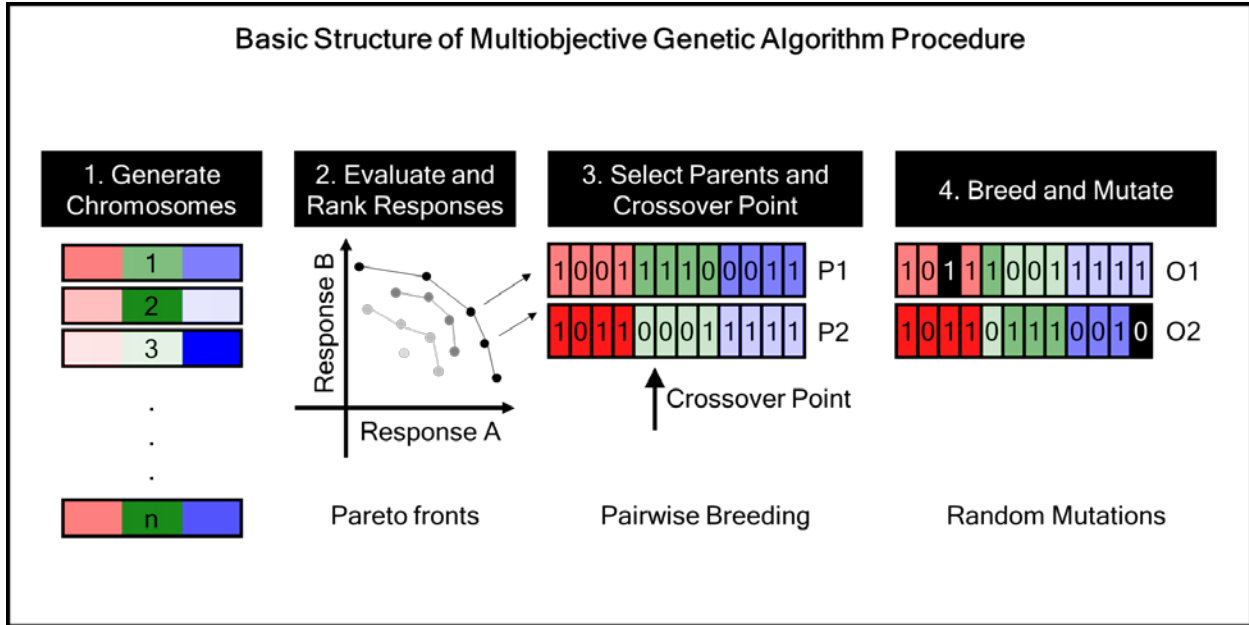


Figure 3.3. Procedure for genetic algorithm.

## 3.2. Metal Nanoparticle Synthesis

The nanoparticle synthesis studied is based on a silver nanoparticle synthesis developed at the Xerox Research Centre of Canada [17]. The following section will discuss a) the standard synthetic process, b) the modifications made to the synthetic procedure in order to achieve a high-throughput synthesis amenable to genetic algorithm experimental design, and c) the characterization techniques used to evaluate nanoparticle solubility and bound carbon content.

### 3.2.1. Standard Synthesis

The silver nanoparticle synthesis used is a very robust, single-pot, reduction reaction that produces stable, sub-10 nm particles ideal for low-temperature printed electronics applications. The basic procedure is as follows. First, both 1-alkylamines and silver acetate in powder form are added to a round bottom flask. Toluene is added and the solution is heated to 60 °C and stirred until the solution is clear and fully dissolved. Next, phenylhydrazine is added to trigger the reduction of silver and the solution rapidly turns black. At this point, the total reaction volume is approximately 300 mL. After an hour, the reaction is quenched with acetone and removed from heat. In order to extract the nanoparticles, the toluene is first removed by evaporation at a reduced pressure using a rotary evaporator. The resulting slurry is collected and rinsed with a mixture of acetone and methanol. The nanoparticles crash out of solution and are collected in a frit filter to dry. For a reaction that began with 1 g of silver acetate, the typical yield of nanoparticles is approximately 750 mg.

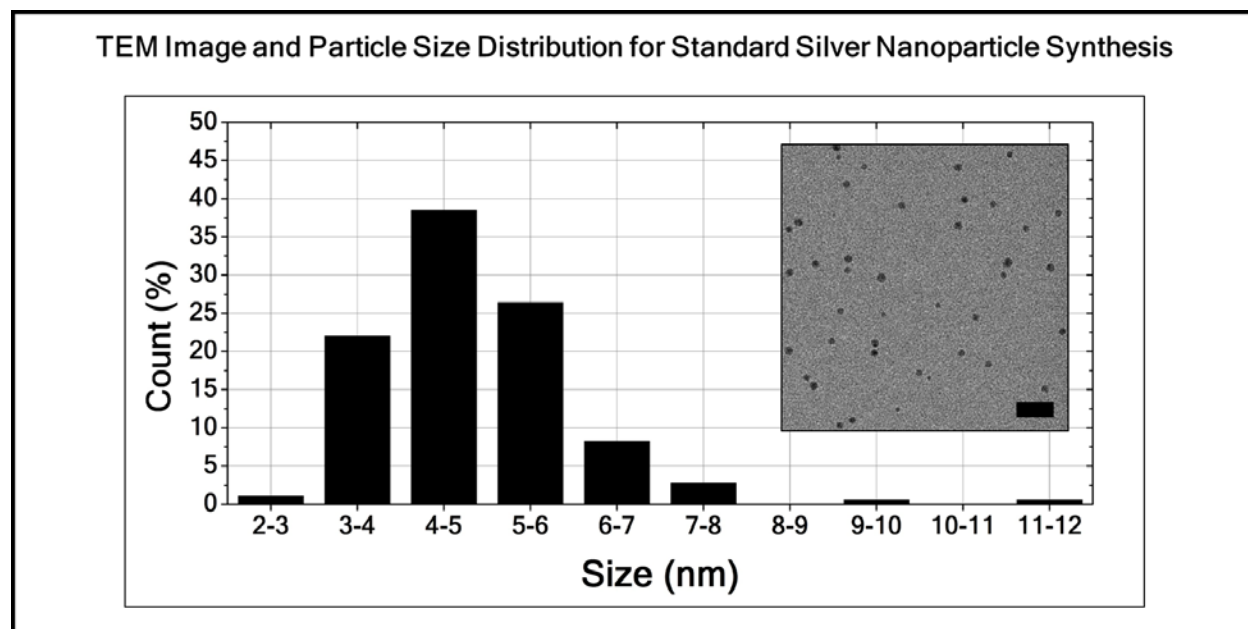


Figure 3.4. Silver nanoparticle TEM and size distribution.

The primary control variables for the standard reaction are the choice of alkylamine, molar ratio of alkylamine to silver, and molar ratio of phenylhydrazine to silver. The alkylamines used in the standard reaction were dodecylamine, tetradecylamine, hexadecylamine, and octadecylamine. Because the standard reaction used only a single encapsulant, it was necessary to modify the reaction to also include multiple

encapsulants with the added synthetic control of alkylamine composition. Figure 3.4 shows TEM images of particles produced by the standard synthesis and the associated size distribution. The size of the nanoparticles is very monodisperse with a peak distribution in the 4 - 5 nm range. See Appendix C for a detailed description of the standard reaction procedure.

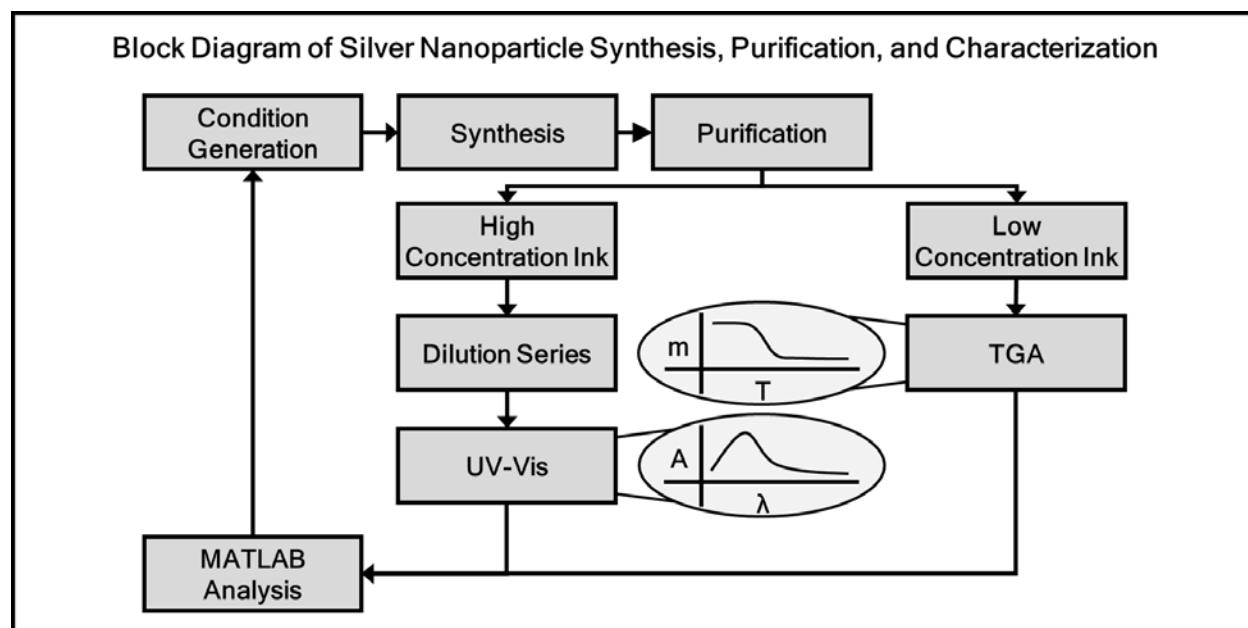


Figure 3.5. Complete functional block diagram for high throughput silver nanoparticle synthesis developed for compatibility with WANDA and high throughput UV-Vis and TGA characterization.

### 3.2.2. High-Throughput Robotic Synthesis

While the standard procedure is capable of very reliably producing nanoparticles, it is not ideal for producing the large number of reactions required by genetic algorithm designs. The two main issues are the large volumes of materials (approximately 300 mL per reaction) and the low-throughput purification procedure due to the use of a rotary evaporator. Therefore the following modifications were made to the synthesis in order to more efficiently conduct a genetic algorithm-driven experiment. Figure 3.5 shows a complete block diagram for the high-throughput synthesis, purification, and characterization of the nanoparticles.

#### A. *Scaling and Adaptation to Robotic Control*

In order to both mitigate the issue of large reaction volumes and improve the process control, the synthesis was scaled and adapted to robotic control using the Workstation for Automated Nanoparticle Delivery and Analysis (WANDA) at Lawrence Berkeley National Laboratory. WANDA is a robot that typically produces semiconducting quantum dots via the controlled dispensation of liquid reactants, and this was the first metal nanoparticle reaction made compatible with WANDA (see Figure 3.6 for deck layout used in this synthesis). Typical reaction volumes for WANDA are 20 mL and below. Therefore, both scaling the synthesis and adapting it to use liquid precursors were necessary.

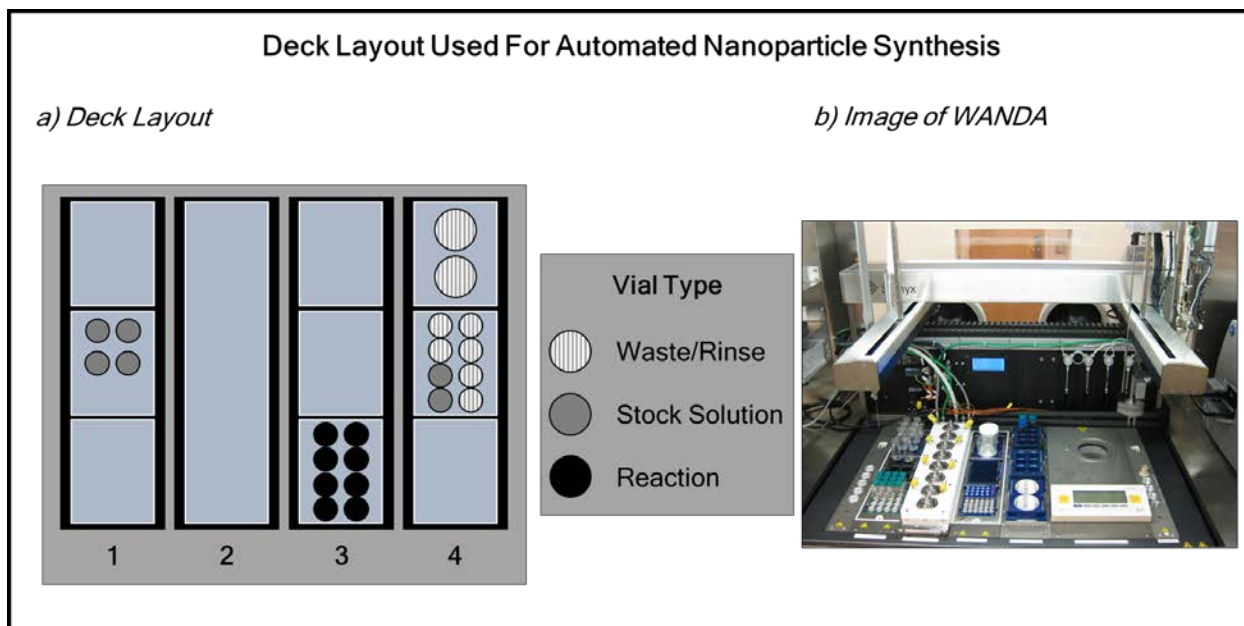


Figure 3.6. a) Deck layout of each bay used in automated nanoparticle synthesis. Bay 1 is heated to 70 °C and contains the alkylamine stock solutions. Bay 2 is made up of specialized low thermal mass reactors and is not used in this synthesis. Bay 3 is heated to 70 °C and holds the eight reaction vials. Bay 4 is kept at room temperature and holds all waste/rinse vials as well as the phenylhydrazine and acetone stock solutions. b) Photograph of WANDA deck.

Scaling the synthesis down to less than 20 mL was accomplished by first scaling all of the reactants by a factor of 10 and subsequently boosting the concentration of the reaction by scaling the required volume further by a factor of 2 - 3. It was necessary to boost the concentration in order to guarantee that the total nanoparticle yield was large enough to perform subsequent characterization tests. (A factor of 10 scaling would still require too much solvent to successfully fit into a 20 mL reaction vial.) Figure 3.7 shows a comparison of nanoparticle size distribution for the standard, large volume reaction at the standard concentration and at concentration three times higher. This reaction was executed at high molar equivalencies of encapsulant to silver, and therefore is expected to show a slightly smaller average particle size than the original reaction conditions. Looking at the distributions, a few conclusions are clear. First, there is a slight shift toward smaller nanoparticle size (as compared to Figure 3.4), which is expected. Second, the concentrated reaction results in shifting the distribution back to the 4-5 nm center. Despite the slight shift, the monodispersity of the concentrated reaction is still high, and therefore the effect of concentrating the reaction will be negligible to the overall optimization.

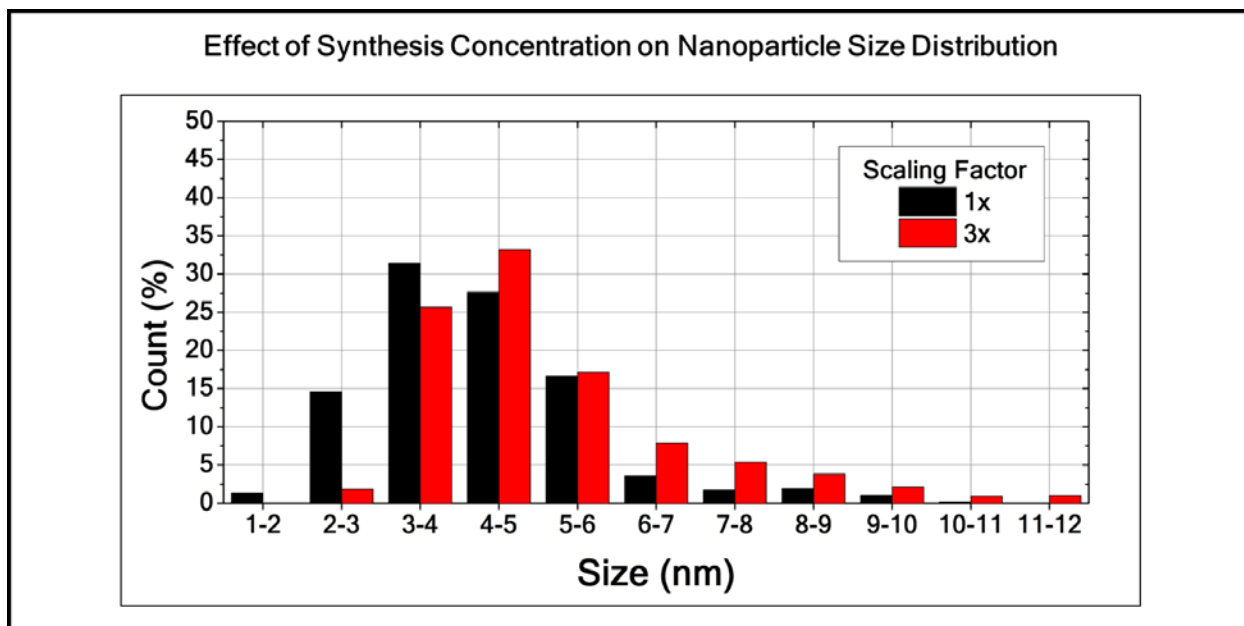


Figure 3.7. Comparison between non-scaled and scaled silver nanoparticle synthesis.

Table 3.1. Standard silver nanoparticle synthesis versus WANDA-compatible synthesis

	Standard Silver Synthesis	WANDA Silver Synthesis
Silver precursor	100 mg silver acetate powder	1 g silver acetate powder
Encapsulant reactants	Powder alkylamines	Alkylamines in toluene (1.5 M at 70 °C)
Reducing agent	Phenylhydrazine in toluene (0.09 M)	Phenylhydrazine in toluene (1.5 M)
Reaction Temperature	60 °C	70 °C
Reaction Volume	~300 mL	~15 mL
Nanoparticle Yield	~0.75 g	~0.75 g
Purification	Sequential acetone rinsing and decanting; collection in paper filter	Single acetone rinse, centrifugation, and decant; collection by pentane dissolution and transfer

Second, in order to adapt the synthesis to a liquid precursor form, each of the alkylamine encapsulants was dissolved in toluene and the phenylhydrazine was mixed in toluene to create stock solutions. Silver acetate stock solution were not used for two reasons. First, silver acetate only readily dissolves in toluene in the presence of amine and, second, at elevated temperatures the amine can trigger the reduction of silver without the presence of an additional reducing agent. Therefore, making a stock solution of the silver acetate would both impose unnecessary limitations on the process and potentially introduce error due to the premature reduction of silver. Ultimately, approximately 100 mg of powder silver acetate was added to each reaction vial before the reaction proceeded.

Because the total volume of the reaction needed to be limited to less than 20 mL, all of the stock solutions were prepared at concentrations of 1.5 M in order to minimize the total volume of added toluene when dispensing each stock solution. This concentration required the stock solutions containing the longest alkylamine (octadecylamine) to be prepared at 70 °C in order to ensure the alkylamine dissolved. Therefore, the reaction temperature used for all of the reactions was increased to 70 °C. Table 3.1 shows a comparison of the standard and WANDA-compatible silver nanoparticle reaction.

### *B. Purification*

In addition to modifying the synthetic procedure, modifications to the purification procedure were necessary. After the reactions completed, they were removed from heating plate and allowed to cool to room temperature. Each reaction was then poured into a 50 mL centrifuge tube pre-filled with 30 mL of acetone. All of the centrifuge tubes were then filled to 45 mL with addition acetone in order to account for variations in total reaction volume. After sitting for a few minutes, the reactions were centrifuged at 9000 rpm for 10 minutes, causing the nanoparticles to crash out. The supernatant was poured out and the nanoparticles were allowed to dry. After drying, pentane was added to dissolve and collect the nanoparticles at the bottom of the centrifuge tube for subsequent characterization procedures, discussed next.

### 3.2.3. Characterization

As mentioned, the two responses tested in this study were nanoparticle solubility and the carbon content bound to the nanoparticles. Two separate procedures were developed to test each of these responses.

#### *A. Nanoparticle Solubility*

First, UV-Vis spectroscopy is useful in characterizing metal nanoparticle concentration because metal nanoparticles exhibit a surface plasmon resonance that falls in the UV-Vis spectrum characteristic to the material. Therefore, if the material and test parameters are known, the Beer-Lambert Law can be applied to determine the concentration of the nanoparticles in solution by extracting the absorption of the nanoparticle solutions at the plasmon resonance peak [98]. The Beer-Lambert Law is

$$I = I_0 e^{-\epsilon Lc} \quad (3.1)$$

where  $I$  is the transmitted light intensity,  $I_0$  is the incident intensity,  $\epsilon$  is the molar absorptivity of the analyte,  $L$  is the path length of light through the sample, and  $c$  is the concentration of the sample. Therefore, the absorption at the plasmon peak,  $A_{peak}$ , should be linearly proportional to the absorption coefficient, path length, and concentration:

$$A_{peak} = \ln\left(\frac{I_0}{I_{peak}}\right) = \epsilon Lc \quad (3.2)$$

In order to test the maximum concentration of the nanoparticles synthesized, however, very high concentration samples need to be prepared. These samples would result in zero absorption using UV-Vis, and therefore dilutions of the concentrated samples were necessary to conduct the tests. A series of dilutions of each sample were prepared, with the dilution factor,  $c_d$ , known for each sample. Now, the following relationships are used:

$$c = c_d c_0 ; A_{peak} = \ln\left(\frac{I_0}{I_{peak}}\right) = \epsilon L c_d c_0 \quad (3.3)$$

Next, because the absorption is also linearly proportional to dilution factor, the slope of the absorption values versus dilution factor can be used to extrapolate the initial concentration:

$$c_0 = \frac{\partial A_{peak} / \partial c_d}{\epsilon L} \quad (3.4)$$

In order to prepare the dilution samples for testing, 1 - 2 mL of pentane was added back to the 50 mL centrifuge tubes containing dried nanoparticles and approximately 1 mL of concentrated nanoparticles were transferred to a pre-weighed 1.5 mL centrifuge tube and allowed to dry. The mass of nanoparticles in the tube was then measured, and tetradecane was added to each centrifuge tube such that the target mass loading of the nanoparticles (assuming complete dissolution) was 40%. The centrifuge tubes were vortexed and centrifuged at 10000 rpm for 15 minutes, twice. The supernatant was taken to represent the maximum solubility of the nanoparticles. 50  $\mu$ L of the supernatant was removed and added to 450  $\mu$ L to create a solution with  $c_d = 1/10$ . This was repeated serially to create solutions of  $c_d = 1/100$ , and  $1/1000$ . Starting with the  $c_d = 1/1000$  solution, seven additional dilutions were then prepared serially at  $c_d = 1/2333$ ,  $1/5444$ ,  $1/12704$ ,  $1/29642$ ,  $1/69165$ ,  $1/161384$ , and  $1/376563$ . These samples were all prepared at a constant volume of 180  $\mu$ L in order to guarantee the path length was constant for each sample. Because the molar absorptivity depends most strongly on nanoparticle dimension and our nanoparticles were all nominally identical in size, the absorptivity was assumed to be constant within the limits of experimental error for this procedure. Using the BioTek Synergy 4 UV-Vis plate reader at Lawrence Berkeley National Laboratory, the spectra of each dilution was taken from 300 to 800 nm. Each scan takes approximately 1 minute. Finally, the peak absorption values were extracted using a MATLAB script that performed blank subtraction of pure solvent spectra, machine offset correction, and automatic peak extraction (see Appendix for complete MATLAB script). The slope of each sample was extracted and used to extrapolate the initial concentration based on baseline tests performed with calibrations samples prepared at known concentrations.

### *B. Bound Carbon Content*

The second response measured was the bound carbon content on the nanoparticles. In order to measure this response, dried nanoparticles were tested with thermogravimetric analysis (TGA). In TGA, the mass of a sample is measured as a function of applied temperature. During ramps from room temperature to 500 °C, the encapsulants bound to the dried nanoparticles will first break away from the nanoparticles, initiating sintering, and eventually they will decompose. The only remaining material will be the silver from the nanoparticle cores. Therefore, measuring the difference between the initial and final mass will indicate the mass of bound carbon on the nanoparticles, and this response should be minimized. Alternatively, the ratio of final to initial mass will be a measure of the silver content on the nanoparticles, which should be maximized.

To conduct these tests, a small volume (~100 µL) of purified nanoparticles dissolved in pentane is added to an aluminum pan for analysis with a TA Instruments Q5000IR TGA-MS. The pans are allowed to dry before being ramped from room temperature to 500 °C in air at 10 °C/min. The tool allows for 25 pans to be measured in serial fashion. Despite being allowed to dry, a small amount of either adsorbed water or pentane is present in all of the samples, causing a consistent mass loss to be present at the onset of the experiment. This is a common artifact of samples transferred using high evaporation rate solvents. The actual mass loss, however, only becomes significant beyond 125 °C in each sample. Therefore, the mass loss at 125 °C is taken to be the baseline mass, with any mass loss occurring before this temperature being strictly due to pentane or water loss instead of encapsulant decomposition.

### 3.3. Heuristic Optimization Study

The following section will discuss the design of the genetic algorithm, baseline tests to confirm the reliability of the process described in the previous section, as well as the results of three iterations of the genetic algorithm.

#### 3.3.1. Parameter Space

As described earlier, the primary experimental controls for the synthesis were the encapsulant to silver molar ratio, the encapsulant composition (of up to four encapsulants), the phenylhydrazine to silver molar ratio, and the overall concentration of the reaction. See Table 3.2 for the specific parameter limits used. These variables, ranges, and step sizes make up the parameter space for the genetic algorithm used in the study. Taking into account the range of  $C_{xx}:Ag$  and the nominal concentration of encapsulant stock solution (1.5 M), a minimum step size for each component of the encapsulant stock of 0.0025 was selected in order to guarantee that the volume of stock solution required for each reaction was at least 250  $\mu$ L, or well above the tool limitation for reliable volume dispensation. To provide a more concrete sense of the breadth of potential conditions, considering only these composition variables, the parameter space includes over 10 million possible sample points. The full space is approximately 1 trillion possible conditions. This means that each generation of approximately 30 conditions covers only a billionth of the space.

Table 3.2. Parameter space definition for genetic algorithm.

Long Name	Symbolic Name	Range	Step Size
Carbon:Silver molar ratio	C:Ag	10 - 15	---
Dodecylamine fraction	$x_{C12}$	0 - 1	0.0025
Tetradecylamine fraction	$x_{C14}$	0 - 1	0.0025
Hexadecylamine fraction	$x_{C16}$	0 - 1	0.0025
Octadecylamine fraction	$x_{C18}$	0 - 1	0.0025
Phenylhydrazine:Silver molar ratio	RA:Ag	1.0 - 1.5	---
Silver Concentration	$[Ag^+]$	37.5 - 87.5 $\mu$ M	---

#### 3.3.2. Baseline Tests

Before iterating through generations, two baseline tests in order to a) calibrate the UV-Vis analysis and b) confirm the repeatability of the process as a whole. The results are discussed here.

### A. UV-Vis Calibration

Because the concentration of each dilution series for UV-Vis testing is extrapolated from the slope of peak absorption versus dilution value, a calibration series of known concentrations of silver nanoparticles was prepared in order to create a calibration curve. The silver nanoparticles used were dodecylamine-encapsulated nanoparticles synthesis via the standard synthetic procedure. Six samples were prepared at target mass loading values of 5, 10, 15, 20, 25, and 30% in tetradecane. The nanoparticles used in each sample were the product of a single reaction, but the samples were prepared independently in order to introduce the potential (but ideally not observe) for error during the preparation of each sample. Each sample was diluted to produce twenty samples with  $c_d = 1/1000, 1/2000, 1/2333, 1/4000, 1/4667, 1/5444, 1/8000, 1/9333, 1/10889, 1/12704, 1/18667, 1/21778, 1/25407, 1/29642, 1/43556, 1/50815, 1/59284, 1/101630, 1/118568, \text{ and } 1/237136$ . As Figure 3.8 indicates, each of the samples produced very linear responses with respect to  $c_d$ , as expected. In order to map the extracted slope for each sample to a true mass loading value, TGA analysis was performed on each sample in the most concentrated condition (also shown in Figure 3.8), and the measured silver content was taken as the mass loading of the sample. Plotting the extracted mass loading versus slope yields a linear calibration curve that is used for subsequent tests. Figure 3.9 shows this calibration curve.

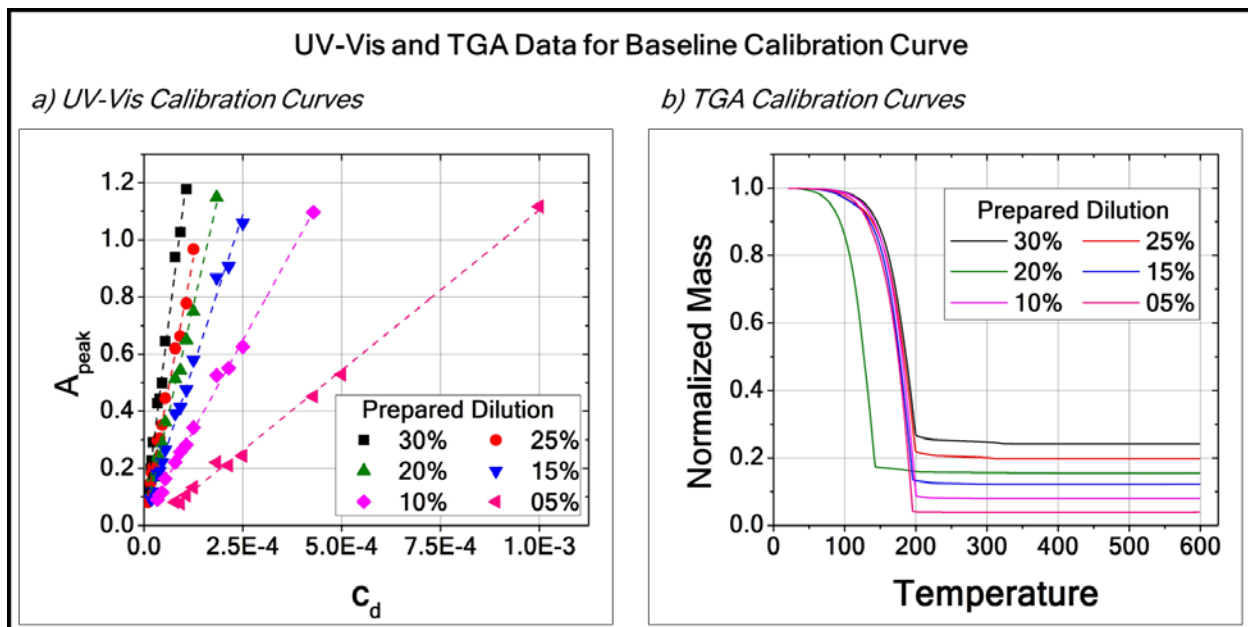


Figure 3.8. a) UV-Vis and b) TGA calibration datasets for calibration curve determination.

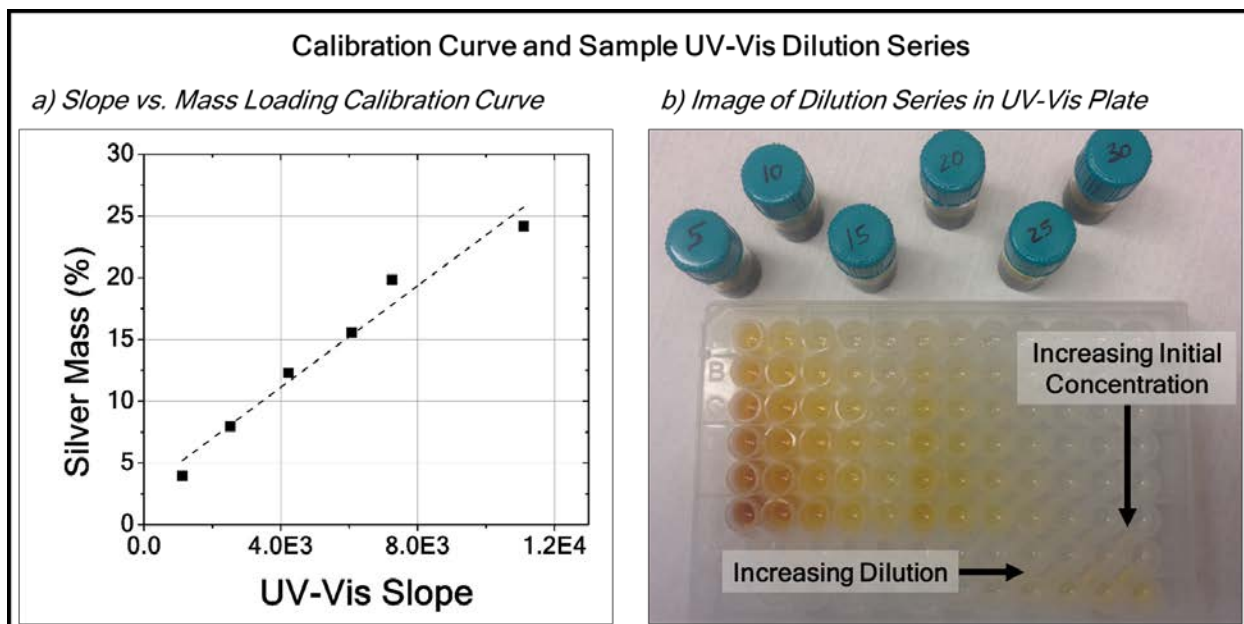


Figure 3.9. a) Calibration curve used to relate extracted UV-Vis slope and silver mass loading and b) Photograph of UV-Vis sample plate prepared for calibration series.

### *B. Process Reproducibility*

Finally, the entire process, from stock solution preparation for WANDA through UV-Vis analysis, was run to produce seven nominally identical reactions. Assuming all of the synthetic procedures, purification methods, and characterization techniques are repeatable, the resulting spectra of the nanoparticles tested with UV-Vis should be nominally the same. Figure 3.10 presents a plot of the average spectra with standard error bounds for the reaction, indicating that the reactions and process are indeed reproducible. Using this positive confirmation, the genetic algorithm experiment was initiated.

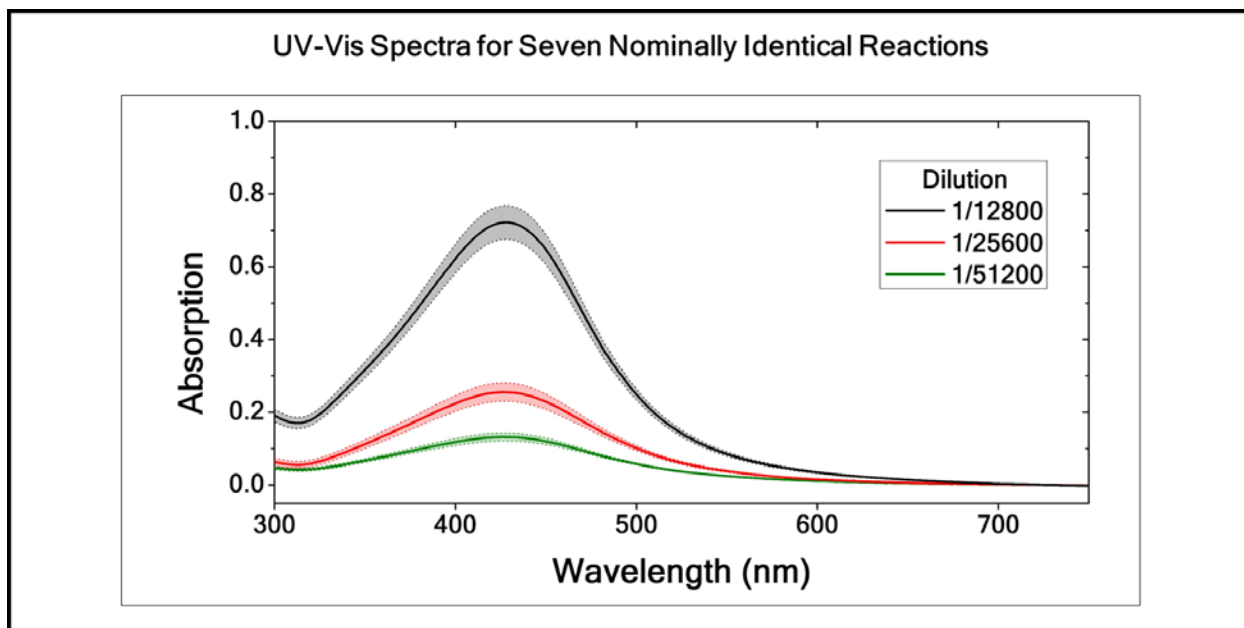


Figure 3.10. UV-Vis spectra of reactions used for repeatability test.

### 3.3.3. Multi-generation Optimization

Using WANDA, three generations of the genetic algorithm were produced. Each run on WANDA was limited to 8 reactions total, meaning 4 - 5 runs were necessary to fully prepare a single generation. Each generation was produced in a single day in order to avoid introducing error due to multiple-day processing. Purification and characterization were completed in 1 and 3 days, respectively. Therefore, a single generation of approximately 30 reactions was produced, characterized, and analyzed on the order of a week.

Figure 3.11 plots the response results of each member of the generations produced (the final population count of each the generations were 28, 32, and 33). Because the goal of this optimization problem is to maximize both mass loading and the silver mass relative to bound carbon mass, the optimum corner is the top-right of each of the plots shown. Appendix E includes tabulated experimental conditions and results for each generation. It is important to note that, as expected for systems with non-smooth response surfaces, no first or second order effects were statistically significant.

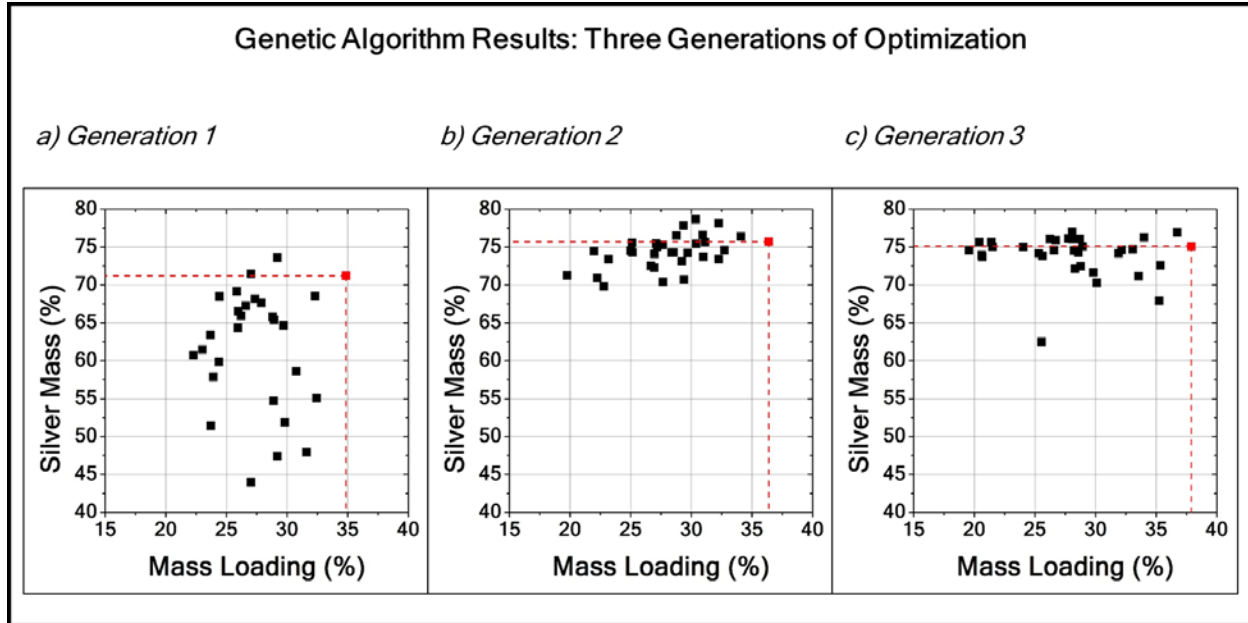


Figure 3.11. Results of three generations of genetic algorithm.

In each plot shown in Figure 3.11, the red data point represents the champion condition for that generation, based on a generation score,  $Score_{gen}$ , calculated as follows:

$$Score_{gen} = 100 * \left( \frac{ML_s}{ML_{max-gen}} \right) * \left( \frac{SM_s}{SM_{max-gen}} \right) \quad (3.5)$$

where  $ML_s$  is the sample mass loading,  $ML_{max-gen}$  is the maximum observed mass loading in the generation,  $SM_s$  is the sample silver mass, and  $SM_{max-gen}$  is the maximum observed silver mass in the generation. A global score can similarly be evaluated using  $ML_{max-global}$  and  $SM_{max-global}$ , which represent the maximum observed mass loading and silver mass, respectively, across all generation.

$$Score_{global} = 100 * \left( \frac{ML_s}{ML_{max-global}} \right) * \left( \frac{SM_s}{SM_{max-global}} \right) \quad (3.6)$$

These scores each scale from 0 - 100 and are similar to the fill factor rating used to describe solar cells. The higher the score, especially the higher the global score, the better.

Figure 3.12 shows three plots which help to summarize the effectiveness of the genetic algorithm used. In Figure 3.12a, the generation and global scores for the champion conditions of each generation are plotted. The generation scores are all very close to 100, which means that the genetic algorithm employed was successful in producing a clear champion per population. More importantly, though, is the strong improvement of

the global score, which rises from 83 to 95 across three generations. This indicates that each iteration of the algorithm not only produces a clear champion but also successfully expands the response window toward the optimum corner.

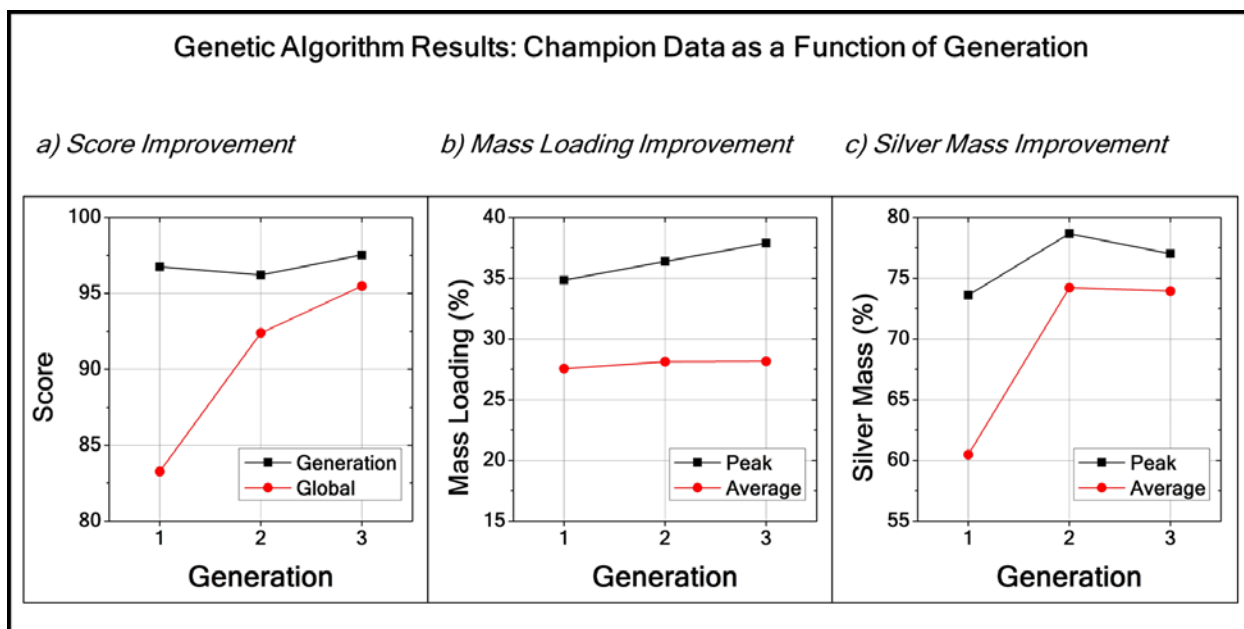


Figure 3.12. Improvement in a) score, b) mass loading, and c) silver mass as a function of generation.

Figure 3.12b plots the maximum and average mass loading as a function of generation. The algorithm has clearly led to optimization with respect to the maximum mass loading. Indeed, the maximum mass loading increases with each generation and ultimately approaches the target maximum of 40% due to the preparation procedure described previously. It is worth noting that the nearly 40% mass loading achieved is at the upper range of mass loading limits common to silver nanoparticle inks used in printed electronics. The peak mass loading of 37.9% from the third generation represents a 9% improvement from the initial peak mass loading observed in the first generation.

When considering silver mass improvement (Figure 3.12c), it is clear that the average response is approaching the maximum response as a function of generation. This indicates that algorithm has likely found a maxima with respect to silver mass. It is not possible to determine whether or not this maxima is a local or global maxima without further testing, though it is likely that very little additional improvement in silver mass should be expected for the following reason. The current maximum silver mass achieved is 78%, which equates to a carbon:silver molar ratio of approximately 2.5:1. This ratio is near the lower limit of 2.2:1 described in the original synthesis (a molar ratio of 2.2:1 would indicate a silver mass of approximately 80%).

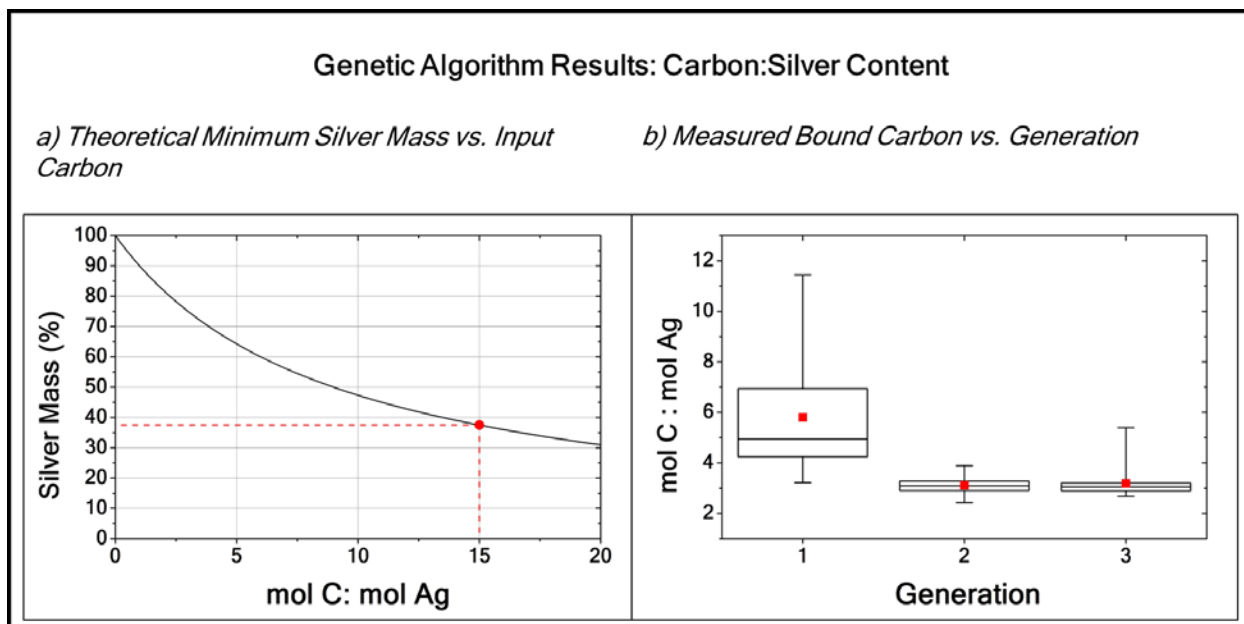


Figure 3.13. a) Relationship between theoretical minimum silver mass percent versus synthetic input condition (drop line represents upper boundary of C:Ag input parameter of genetic algorithm) and b) box and whisker plot of observed molar ratio of bound carbon to silver as a function of generation (average identified by red marker).

Figure 3.13 shows a box and whisker plot of the extracted carbon:silver molar ratio for each generation and a curve indicating the relationship between minimum mass and molar ratio (assuming all input carbon is ultimately bound to the nanoparticle). As the curve indicates, a molar ratio of 15:1 (nominally the maximum ratio possible due to the parameter space boundary definition) would produce particles with a silver mass of approximately 37.5%. Therefore, assuming our purification and characterization protocols are sound, we do not expect to observe any conditions with measured silver mass values *less* than 37.5%. Indeed, the lowest observed silver mass is 43%, further confirming the validity of the protocols developed.

In addition, it is interesting to note that the minimum observed molar ratio of 2.5:1 is significantly lower than the C:Ag input parameter for each sample. This indicates that the majority of the encapsulant material included in the synthesis is ultimately washed away during the purification step. One might expect that a lower initial molar ratio would result in a lower ultimate molar ratio, but this relationship was not statistically significant, as already stated. Despite this fact, the C:Ag input consistently decreased from 14.5:1 to 12.3:1 to 10.1:1 for each generation's champion condition.

Finally, despite the probability that the algorithm has reached a global maxima with respect to silver mass, the consistent improvement in mass loading with each generation is an encouraging result. This indicates that, indeed, the genetic algorithm is successful in discovering new configurations of encapsulant compositions that both improve solubility and maintain a low residual carbon content.

### 3.4. Summary

For printed electronic applications, inks composed of nanoparticles are more cost effective if the nanoparticles are more soluble, regardless of the cause for solubility. To date, metal nanoparticle solubility has been shown to most strongly depend on the composition of the encapsulants bound to the nanoparticle, but this dependence is poorly understood beyond the observation that it is very non-smooth as a function of encapsulant composition. Therefore, both the optimization as well as the discovery of the underlying cause for this response are interesting problems for the field of printed electronics. However, because of this unpredictable response, conventional experimental designs will not effectively elucidate the relationship between solubility and encapsulant structure, nor will they be very effective in identifying the global maximum within a given experimental space. Therefore, a non-traditional experimental design method based on a genetic algorithm was used to explore the experimental space. The goal was to both identify the optimum synthetic condition for practical applications as well as to generate a number of experimental observations inaccessible to conventional, limited designs that will ultimately lead to a deeper understanding of nanoparticle solubility.

In order to achieve these goals, a standard, high-volume silver nanoparticle synthesis was adapted to a low-volume, robotically-controlled synthesis. In addition, measurement protocols were developed in order to conduct the genetic algorithm-driven experiment in search of synthetic conditions that produce highly soluble nanoparticles with minimal bound carbon content. Ultimately, the synthesis, purification, characterization, and analysis of a single-pot silver nanoparticle synthesis were successfully adapted to high-throughput procedures that enabled rapid, reliable heuristic optimization.

Though only 93 total conditions were tested, significant improvements with respect to both silver nanoparticle solubility and bound carbon content were observed after only three iterations of the genetic algorithm. It is not possible to claim a global maximum condition was discovered, however both of the expected response boundaries were approached. Therefore, the experimental conditions for a very practical nanoparticle condition were discovered. Due to the extremely high resolution parameter space created by the algorithm, the ultimate dataset includes observations that would have likely been missed using conventional experimental methods. This dataset will serve as the foundation for subsequent detailed analysis directed toward understanding the encapsulant and solubility relationship.

## Chapter 4. Inkjet-printed Pillars for Solder Bump Replacement

---

Advanced semiconductor packaging interconnects must meet increasing demands with respect to both interconnect size/density and mechanical/electrical performance. In addition, because many of these interconnects will either be used in chip-to-chip or chip-to-package applications, they will inherently be three-dimensional in nature. While inkjet-printed metal nanoparticles have long shown the potential to provide high-performance planar interconnects, the investigation into the three-dimensional printing of these materials has hardly been explored. This chapter will discuss the requirements for advanced interconnects and the process development of three-dimensional inkjet printing. The process parameters critical to successful printing of pillars with metal nanoparticle inks will be discussed, and the performance of these pillars as a function of process condition will be explored.

## 4.1. Introduction

The successful adaptation of inkjet printing for advanced interconnects will rely on two key criteria. First, the structures fabricated using three-dimensional printing processes must overlap with the design requirements for interconnect structures of interest now and in the future. Second, the interconnect performance must be comparable to or better than performance achieved using conventional materials and processes. This section will describe both of these criteria in more detail.

### 4.1.1. Pillar Critical Dimension and Pitch Requirements

As previously mentioned, the resolution of inkjet printing is directly dependent on the wetting of inks on the substrate, which can be easily described by the contact angle,  $\Theta_c$ . However, because inks do not absorb into the substrate, both the contact angle and total volume of the ink,  $V_{\text{drop}}$ , are required to determine the critical dimension,  $d_{\text{critical}}$ , capable for inkjet-printed features. To first order, this ink volume is determined by the nozzle orifice diameter,  $d_{\text{nozzle}}$ , which commonly range from 10-100  $\mu\text{m}$  in modern inkjet nozzles. Assuming the droplet diameter is equivalent to the nozzle diameter and using the geometry of a hemispherical cap to model a droplet on a non-absorbing substrate, Figure 4.1 depicts the critical dimension of printed features as a function of both nozzle diameter and contact angle. As expected, as the contact angle approaches  $90^\circ$  (minimal spreading) and the nozzle diameter decreases, the critical dimension of printed features decreases. For example, the minimum critical dimensions attainable with two common nozzle diameters, 30  $\mu\text{m}$  and 60  $\mu\text{m}$ , are  $\sim 35 \mu\text{m}$  and  $\sim 75 \mu\text{m}$ , respectively.

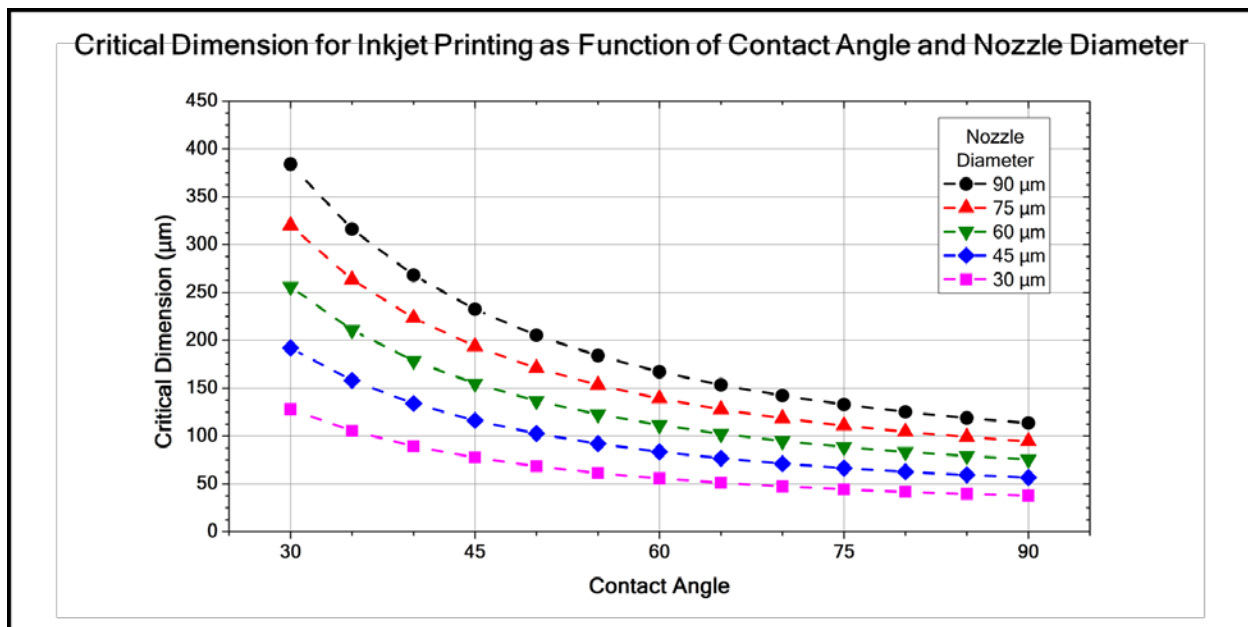


Figure 4.1. Critical dimension of inkjet-printed features as a function of contact angle and nozzle diameter.

Table 4.1 presents the pitch requirements for current and future packaging interconnects. The pitch is defined as the minimum spacing between fabricated features. Assuming the features cannot touch each other, the critical dimension (the maximum feature diameter) for a given pitch must be smaller than the pitch itself, and it

is usually on the order of half of the pitch. These critical dimension and pitch requirements must overlap with inkjet printing critical dimension and pitch capabilities in order for the application to be considered viable. For inkjet-printed features on flat substrates, the minimum pitch capable will be directly dependent on the spread of the ink on the substrate. This is because electrical shorting of interconnects must be avoided. However, as will be shown, the critical dimension of three-dimensional inkjet-printed features on flat substrates, i.e. pillars, may actually be smaller than the critical dimension of a single droplet on a substrate. When comparing these requirements with the critical dimension capabilities of inkjet printing outlined in Figure 4.1, it is clear that this range of sizes demanded is extremely well-matched with inkjet capabilities [99].

Table 4.1. Chip to substrate and substrate to board pitch requirements for packaging interconnects.

Chip to Substrate Pitch ( $\mu\text{m}$ )			
<i>Application</i>	<i>2015</i>	<i>2020</i>	<i>2025</i>
Low-end/consumer	150	150	150
Mobile	110	95	95
Peripheral	40	35	35
Cost performance	120	110	110
High performance	120	110	110
Substrate To Board Pitch ( $\mu\text{m}$ )			
<i>Conventional Boards</i>	<i>2015</i>	<i>2020</i>	<i>2025</i>
Low-end/Low-cost	500	400	400
Memory	650	650	650
Cost performance	500	400	400
High performance	800	650	650
Harsh	500	500	500
<i>Mobile Boards</i>	<i>2015</i>	<i>2020</i>	<i>2025</i>
WLCSP Area Array	100	100	100
FBGA	200	150	150

#### 4.1.2. Pillar Process and Performance Metrics

The second key criterion for inkjet-printed three-dimensional interconnects to become viable alternatives to conventional interconnects is for the printed features and/or printing processes to exhibit comparable or improved performance over conventional alternatives. For packaging applications, performance is typically defined by mechanical strength as well as electrical conductivity. In addition to physical properties, improvements to the process throughput are also important to consider because they represent a potential cost savings.

First, because pillar interconnects aim to replace conventional eutectic flip-chip solder bumps, any performance boost above conventional solder materials is desirable. Ideally, an inkjet printing pillar process would be a drop-in replacement for standard solder bumping and bonding processes. Since eutectic materials undergo reflow processes with peak processing temperatures of approximately 200 °C [100], it will be important to consider both the mechanical and electrical performance of inkjet-printed structures at or below these processing temperatures. As described earlier, gold metal

nanoparticle inks have shown conductivities approaching 70% of bulk gold conductivity in thin films processed at plastic-compatible (less than 200 °C) temperatures [31]. This conductivity level is nearly five times the conductivity of lead-tin eutectics [101]. Therefore, if pillars fabricated with metal nanoparticles exhibit conductivities comparable to thin films, these materials would offer a dramatic boost in interconnect electrical performance. With regard to mechanical performance, very little attention has been paid to the mechanical properties of thin films made with metal nanoparticle inks. Therefore, the elastic and shear performance of eutectic solders will serve as a threshold for mechanical performance of inkjet-printed pillars. Finally, because the conventional process flow for solder bump fabrication requires multiple blanket layer deposition steps as well as patterning, the additive nature of inkjet printing may provide a very large boost in throughput. Figure 4.2 compares the conventional copper pillar process with a potential inkjet process, highlighting the clear benefit of additive processing.

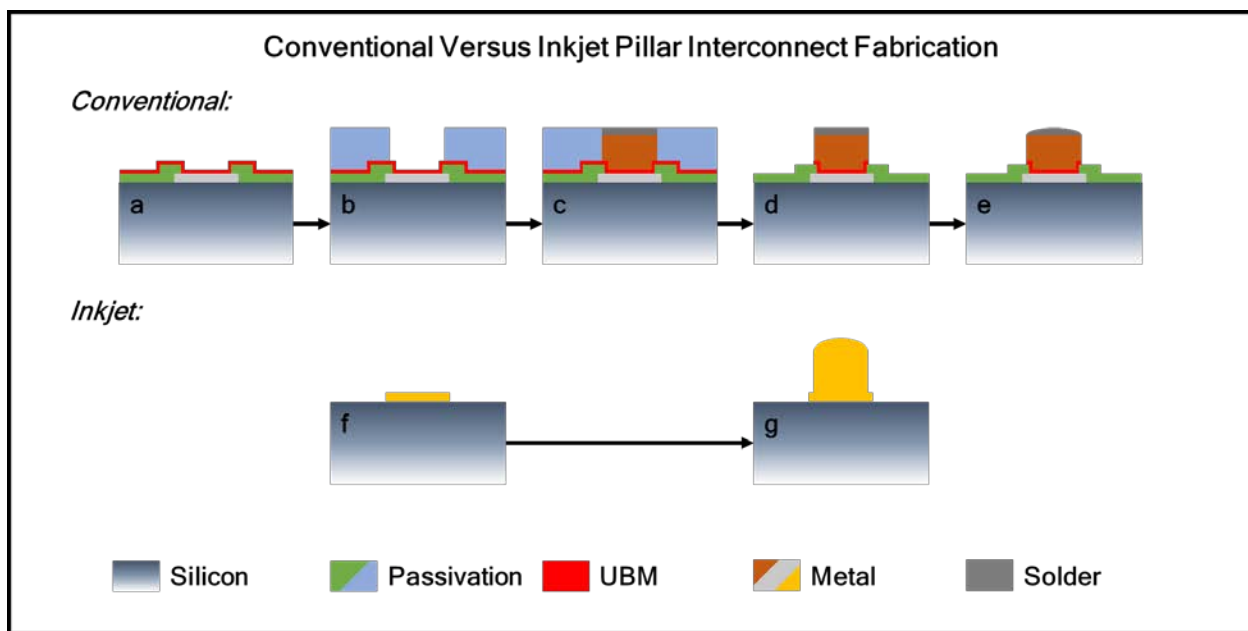


Figure 4.2. Comparison of conventional pillar fabrication process and potential inkjet process. Conventional process: a) aluminum pad passivation and under bump metallization (UBM), b) UBM passivation, c) copper electroplating and solder deposition, d) UBM passivation removal and UBM etch, e) solder reflow. Inkjet: f) bond pad metallization, g) pillar printing. Conventional process flow adapted from [102].

## 4.2. Three-dimensional Inkjet Printing Processes

As previously described, colloidal inkjet inks can be thought of two-component systems containing 1) a functional solid and 2) a solvent to carry the solid to the substrate. Just as in inkjet printing of planar structures, the end goal in three-dimensional printing is to deposit the functional solid only where it is needed and to remove the solvent via drying and curing processes. In planar printing, because the goal is to create thin films, typically only one ink droplet per area is required. This means that the solvent deposited in a given area is limited to approximately the volume of a single droplet. In contrast, the primary challenge for three-dimensional inkjet printing is that it requires multiple droplets in the same area in order to build up a freestanding feature. Because multiple droplets will result in the repeated deposition of solvent in a particular area, it is critical to remove the solvent as quickly as possible in order to prevent subsequent droplets from re-dissolving and redistributing the material already deposited. The second challenge will be successful curing of the three-dimensional structures in order to realize their full functionality.

For interconnect applications, the functional material of interest must be highly conductive. As such, the following discussion will focus solely on colloidal metal nanoparticle inks. To date, there have been very limited efforts toward three-dimensional inkjet printing of metal nanoparticle inks. Three-dimensional inkjet printing of molten solders has been pursued for many years by the MicroFab Company [103], but the added complexity of incorporating high temperature printheads in order to print materials with lower electrical conductivities than pure metals leaves much room for improvement. Within the metal nanoparticle community, both EHD printing and extrusion printing have been used to fabricate high aspect ratio features, though the efforts here have been limited to proof-of-concept demonstrations [104, 105]. In addition, the scale of EHD printing is much lower than the scale required for interconnect applications, making this a non-ideal technology for this application. Finally, there have been a few demonstrations of three-dimensional inkjet-printed metal nanoparticles, though little to no effort has been made to evaluate the performance of the successfully-printed structures [106].

This section will discuss the strategy employed in this dissertation to mitigate the issues of inkjet printing three-dimensional features using metal nanoparticle inks and provide a discussion regarding the fundamental sintering process for these materials.

### 4.2.1. Printing

The first challenge for three-dimensional inkjet-printed interconnects is to successfully create a high aspect ratio three-dimensional structure. To build pillar-like features, multiple droplets of ink at the same substrate location are necessary. However, because each droplet will introduce additional solvent to the substrate, unless the solvent volume on the substrate is minimized *during* the process, the resulting feature will be a puddle instead of high aspect ratio pillar. The goal of three-dimensional inkjet printing, therefore, is to either minimize the deposited solvent volume of each droplet or to dry the material deposited with each droplet before subsequent droplets impinge upon the substrate. For the purpose of simplification, this strategy will be referred to as a “solvent volume minimization strategy” in the remainder of the text. This section will describe the

details of the solvent volume minimization strategy, as well as strategies to improve the overall throughput of the process.

#### A. Process Control Variables

There are two primary process control variables available to control the minimization of as-deposited solvent volume, and it is useful to consider these process controls with respect to overall volumetric flow rate of the ink solvent. First, because the goal is to minimize the volume of solvent on the substrate, the volumetric flow rate of solvent on the substrate,  $Q_{sub}$ , must be controlled. Two possible routes for the ink volume to flow is to absorb ( $Q_{abs}$ ) into the substrate or two evaporate ( $Q_{evap}$ ). However, because the process of interest takes place on non-absorbing substrates, the only way to control this flow rate is by controlling the evaporation rate,  $Q_{evap}$ , of the solvent. For a given solvent,  $Q_{evap}$  is a strong function of temperature, i.e. elevated temperatures will increase evaporation rate. Therefore, the main process control variable for controlling  $Q_{sub}$  is  $T_{sub}$ .

Now, because the solvent on the substrate originates from the nozzle, it is also important to control the volumetric flow rate from the nozzle,  $Q_{nozzle}$ . This rate is dictated by the volume of the droplet,  $V_{drop}$ , and the nozzle ejection frequency,  $f_{nozzle}$ . Although  $V_{drop}$  includes both the volume of nanoparticles,  $V_{NP}$ , and solvent,  $V_{solv}$ , it is safe to assume that the solvent  $V_{solv}$  is much greater than  $V_{NP}$  due to the need to maintain low ink viscosities for inkjet printing. Furthermore, assuming that  $V_{drop}$  is constant throughout the printing process, the main process control for controlling  $Q_{nozzle}$  is  $f_{nozzle}$ .

The following equations describe the relationships between the volumetric flow rates and the non-absorbing substrate and nozzle for inkjet printing of relevant nanoparticle inks:

$$Q_{evap} \propto T_{sub}, Q_{abs} = 0, V_{solv} \gg V_{NP} \quad (4.1)$$

$$Q_{sub} = Q_{evap} + Q_{abs} = Q_{evap} \quad (4.2)$$

$$Q_{nozzle} = V_{drop} * f_{nozzle} = (V_{solv} + V_{NP}) * f_{nozzle} = V_{solv} * f_{nozzle} \quad (4.3)$$

$$\therefore Q_{sub} \propto T_{sub}, Q_{nozzle} \propto f_{nozzle} \quad (4.4)$$

Using these two process control variables,  $T_{sub}$  and  $f_{nozzle}$ , it is important to maintain process conditions such that  $Q_{sub}$  is greater than  $Q_{nozzle}$  in order to successfully fabricate three-dimensional structures. While  $T_{sub}$  is an important process control to use,

the issues associated with increasing the substrate temperature are important to address. First, elevating the substrate temperature will negatively affect the morphology of printed droplets, resulting in increasing the coffee-ring effect. Because the goal is to create a solid pillar, the effect of increasing substrate temperature should be monitored to avoid the fabrication of hollow cylinders instead. In addition, elevated substrate temperatures may adversely affect the ambient conditions at the nozzle, accelerating nozzle clogging and breaking the process entirely. When combined with moderately elevated substrate temperatures, the reduced jetting frequency will permit the solvent to dry on the substrate prior to subsequent droplets. However, the clearest drawback of reducing the jetting frequency is the overall reduction of the process throughput.

### *B. Material Optimization*

As shown,  $f_{\text{nozzle}}$  and  $T_{\text{sub}}$  are the two primary process controls available for three-dimensional inkjet printing process. In addition to process controls, materials used can also be optimized to control feature formation. First,  $Q_{\text{evap}}$  is both a temperature- as well as material-dependent control. Therefore, using inks with solvents that exhibit higher evaporation rates at a given temperature will allow for added control. Either the process temperature can be maintained and the overall throughput will increase, or the process temperature can decrease to avoid the negative impacts of elevated temperature printing while maintaining the same throughput.

In addition to altering the ink solvent, altering the ink composition such that the nanoparticle volume,  $V_{\text{NP}}$ , assumes a higher fraction of the overall drop volume will also improve the process control. A higher nanoparticle volume means that fewer droplets will be required to deposit the same amount of material onto the substrate and that individual droplet will deposit a smaller overall solvent volume onto the substrate. Increasing the volume fraction of nanoparticles in the ink is accomplished by increasing the mass loading of colloidal nanoparticles. This is a nontrivial challenge, but the benefits with respect to process throughput are likewise nontrivial. For this reason, the entirety of Chapter 3 of this dissertation is dedicated to understanding and increasing the mass loading of these colloidal nanoparticle inks.

### *C. Throughput Optimization*

Finally, because an important metric for industrial viability is process throughput, both the process controls and material optimizations discussed are consistently evaluated with respect to their ability to increase throughput. In addition to altering the process control variables or materials printed, there also exists room to improve overall throughput via parallelization of the printing process. Multiple nozzle printheads are the easiest way to accomplish this task, however, it is also possible to accomplish throughput improvement with single nozzle systems.

To this point, it has been assumed that the nozzle is stationary above a pillar being printed. However, parallelization of the process can be achieved by moving to other substrate locations to print multiple pillars. As long as the nozzle returns to the original location at the appropriate time (as dictated by  $T_{\text{sub}}$  and  $f_{\text{nozzle}}$  for the fabrication of an individual pillar), it is now possible to create multiple features within the same timeframe. This behavior is also beneficial because the actual jetting frequency of the nozzle is

increased beyond the frequency required to fabricate a single pillar. This reduces the likelihood of nozzle clogging, improving the overall process stability in addition to the throughput.

#### **4.2.2. Sintering**

The second challenge for three-dimensional inkjet-printed interconnects is to successfully achieve structures with high electrical and mechanical performance. In general, the peak electrical and mechanical performance will only be realized after curing processes are complete. In metal nanoparticle inks, these curing processes are typically thermal in nature, and they result in the sintering of metal nanoparticles to create a continuous, conductive film. As mentioned earlier, very little effort has been put toward studying the fabrication of three-dimensional nanoparticle-based structures, let alone studying the sintering behavior and mechanisms of these structures. However, as described in Chapter 1, metal nanoparticle sintering of thin films as a function of processing conditions and materials has been studied fairly extensively. Therefore, using the three-dimensional features fabricated in this study, it will be possible to study and gain insight into the sintering mechanisms in these inherently thin-film systems.

### 4.3. Three-dimensional Inkjet Printing Freestanding Pillars

The first objective of three-dimensional inkjet printing for semiconductor packaging applications is to create freestanding pillars that would act as drop-in replacements for solder bump and copper pillar processes. This section will describe the materials and characterization procedures used to fabricate pillars using the fabrication process described previously.

#### 4.3.1. Materials

Two inks were used to develop the three-dimensional inkjet printing process: commercially-available gold nanoparticle inks and custom silver nanoparticle inks.

##### *A. Commercial Gold Nanoparticle Ink*

Commercial inks were initially used because they provide stable and reliable jetting conditions, minimizing the impact of jetting condition on the overall process being developed and studied. The commercial ink chosen was a gold nanoparticle ink produced by the Harima Chemicals Group, called NPG-J [107]. While this ink provided reliable jetting conditions, the prescribed sintering treatment for thin film applications is 250 °C, which is higher than the thermal budget of standard solder ball processes. In addition, due to the proprietary nature of the ink, materials such as the specific solvent(s) and additive(s) used in the ink are unknown to the user, making process development via material optimization very difficult.

##### *B. Custom Silver Nanoparticle Ink*

Because of these reasons, a simple custom-synthesized silver nanoparticle ink was formulated in order to demonstrate process control via material optimization. The custom ink was a simple colloidal suspension of dodecylamine-encapsulated silver nanoparticles in dodecane. As will be shown, the use of this ink enabled both the reduction of required thermal treatments for sintering as well as an increase in process throughput.

#### 4.3.2. Characterization

In order to quantify the printing process as well as sintering-dependent pillar properties, morphological, mechanical, electrical, and compositional properties of pillars are studied. The following sections describe the tests used in further detail.

##### *A. Morphological*

Both scanning electron microscopy (SEM) and laser confocal microscopy are used to image pillars as a function of both the printing and sintering controls. The height and width of pillars are extracted in order to determine the aspect ratio of pillars as well as to study the compaction of the pillars as a function of sintering condition.

##### *B. Mechanical*

In order to characterize the mechanical properties of printed pillars, two techniques are used. First, nanoindentation of pillars is used as a means of extracting the elastic modulus of the structures as a function of sintering process conditions [108]. The particular tool used was a Hysitron TI 750 Series TriboIndenter. Nanoindentation tests involve forcing a diamond tip into a material with a controlled load while monitoring the

depth of the diamond tip in the material. After the maximum desired load is reached, the load is released and the material elastically responds by forcing the now-embedded tip upward. Measuring the force and displacement upon unloading allows for the extraction of the reduced elastic modulus,  $E_r$ , of the material according to the following equation:

$$E_r = k \frac{dP/dh}{\sqrt{A_p(h_c)}} \quad (4.5)$$

where  $k$  represents a material- and geometry-related constant,  $dP/dh$  represents the slope of the unloading segment of the load,  $P$ , versus displacement,  $h$ , curve, and  $A_p(h_c)$  represents the projected tip contact area at the contact depth,  $h_c$ .

The second mechanical test used is a solder ball bond test via a Nordson Dage 4000 bond tester. This shear test follows JEDEC standard, JESD22-B117A, and allows for both the quantification of bump and/or pillar shear strength as well as qualification of shear failure mode [109]. In bond testing, a flat tip is forced at constant lateral velocity onto the bond/pillar. During the test, the force at the tip is recorded until the structure breaks, indicated by a sudden drop in measured force. Optical inspection post-failure reveals the failure mode of the structure. The nominal failure mode is crack propagation through the bump/pillar because the force measured in this failure mode will directly correlate to the property of the material, which is the desired output of the test.

### C. *Electrical*

The ideal property to test with regard to electrical characterization of interconnect structures is conductivity. In order to test conductivity in freestanding pillars, a special four-point probe setup was used (see Figure 4.3). In this setup, pillars were first printed directly onto gold pads with room for landing two probe tips, one to force current and one to measure the voltage at the base of the pillar. Then, two additional probe tips were carefully landed on the top of the pillar. One of these probes acted as the current source,  $I_{source}$ , and the other acted as the voltage measurement probe for the top of the pillar,  $V_{top}$ . Using the following equations (and modeling the pillar as perfect cylinder with known height,  $h_{pillar}$ , and radius,  $r_{pillar}$ ), the pillar resistance,  $R_{pillar}$  can be measured and the conductivity,  $\sigma_{pillar}$ , can be extracted:

$$R_{pillar} = \frac{V_{bottom} - V_{top}}{I_{source}} \quad (4.6)$$

$$\sigma_{pillar} = \frac{1}{R_{pillar}} * \left( \frac{h_{pillar}}{\pi * r_{pillar}^2} \right) \quad (4.7)$$

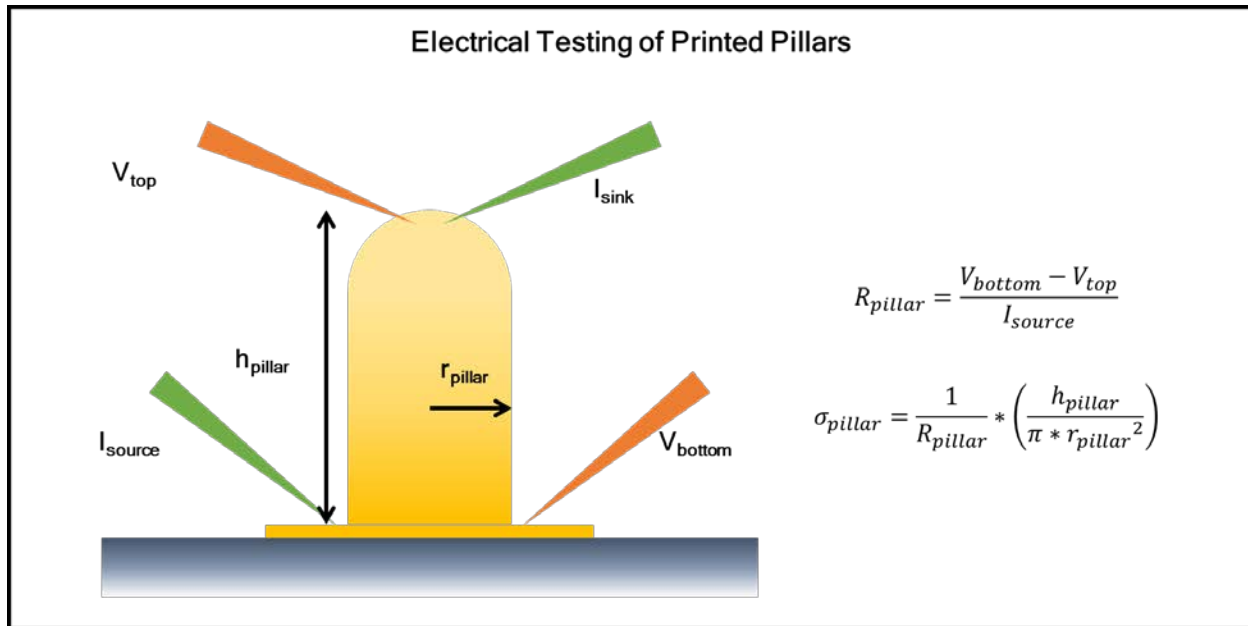


Figure 4.3. Schematic representation of pillar electrical testing setup and cylinder-based model for resistivity extraction.

#### *D. Compositional*

Finally, because residual carbon content and porosity in sintered structures may each degrade mechanical or electrical performance, both the composition and structure of pillars as a function of sintering condition are studied. Using a focused ion beam (FIB), pillars are milled in half in order to first provide insight on the internal structure. Then, energy-dispersive x-ray (EDX) analysis is used to observe the relative concentration of metal and carbon as a function of both position and sintering condition. In this way, the compositional and structural properties of the sintered pillars can be related to the mechanical and electrical properties, permitting the development of a sintering mechanism model for these three-dimensional inkjet-printed structures.

#### **4.3.3. Process Development with Commercial Gold Nanoparticle Ink**

In order to avoid confounding complications related to poor jetting performance, nozzle clogging, complex ink formulation, etc., a stable, commercially-available nanoparticle ink was first used to develop the process for three-dimensional printing. Using Harima Chemical's NPG-J gold nanoparticle ink, the solvent volume minimization strategy was studied and characterized. It is important to note that the structures sintered in the study are sintered using thermal sintering techniques on a hotplate. The results are described next.

#### *A. Morphology, Aspect Ratio, and Compaction*

Using the solvent volume minimization strategy, the two primary controls are jetting frequency and substrate temperature. For this ink, the frequency and temperature ranges tested were 0.167 - 0.500 Hz and 80 - 100 °C, respectively. Figure 4.4 shows SEM images of the resulting structures as a function of printing condition. Each image is the product of 50 droplets and was taken after the printed structures were sintered. As expected, higher temperatures and lower frequencies result in facile fabrication of pillar

structures whereas low temperatures and high frequencies result in puddles. For example, at 0.500 Hz, fabrication pillars is only possible with substrate temperatures at 100 °C. In contrast, at 0.167 Hz, fabrication bumps/pillars is possible at temperatures spanning the entire range.

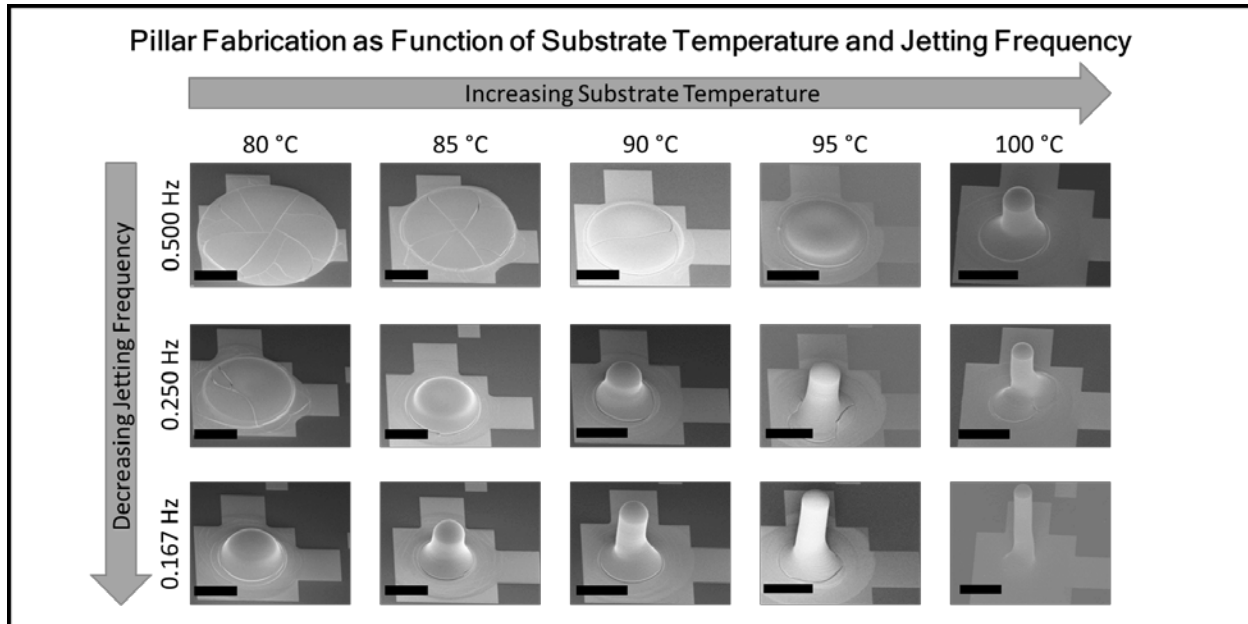


Figure 4.4. Pillar fabrication as a result of modulating substrate temperature and jetting frequency. Higher temperatures and lower frequencies result in higher aspect ratio pillars. All pillars printed with 50 total drops and all scale bars represent 100  $\mu\text{m}$ .

It is worth noting that the bounds of this range were expanded and tested in all directions, though pillar fabrication became unreliable outside of this window and therefore they are not pictured. Lower temperatures simply required too much time for the solvent to dry, and so the fabrication of pillars rapidly became impractical. At higher temperatures, ejected droplets became unstable and nozzle clogging due to solvent evaporation in the nozzle became an issue. With regard to jetting frequency, higher frequencies required higher temperatures, and so the boundary could not be expanded significantly. Lower frequencies were used as well, though primarily to extend the process for lower substrate temperature as opposed to higher substrate temperatures. This is because lower frequencies require longer pauses between droplet ejections. The longer the wait, the higher the likelihood of nozzle clogging, especially at higher substrate temperatures.

By inspecting Figure 4.4 further, it is clear that the aspect ratio of the pillars is a strong function of printing condition. This true because both the height and width are affected by printing condition. Figure 4.5 shows the dependence of width, height, and aspect ratio as a function of printing condition. In high temperature, low frequency conditions, pillars are much narrower and taller than low temperature, high frequency conditions. At a constant frequency, the width of the pillar narrows as the temperature increases, likely due to the decreased amount of spreading seen at higher temperatures. In contrast, at a constant temperature, the width of the pillar increases as with increasing frequency. It is

likely this is because the increased solvent volume forces the spread of the ink because it cannot evaporate as rapidly. Figure 4.5 shows that with just 50 droplets, pillars with aspect ratios approaching 6:1 are possible using these moderate printing conditions.

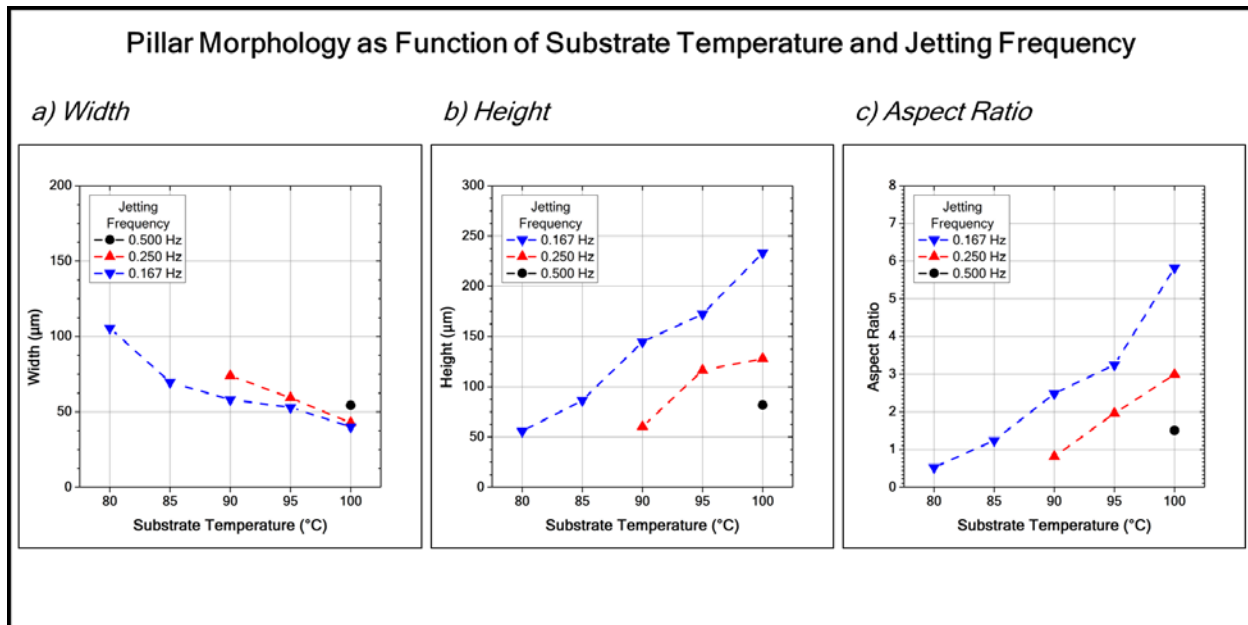


Figure 4.5. Pillar a) width, b) height, and c) aspect ratio as extracted from SEM images (see Figure 4.4).

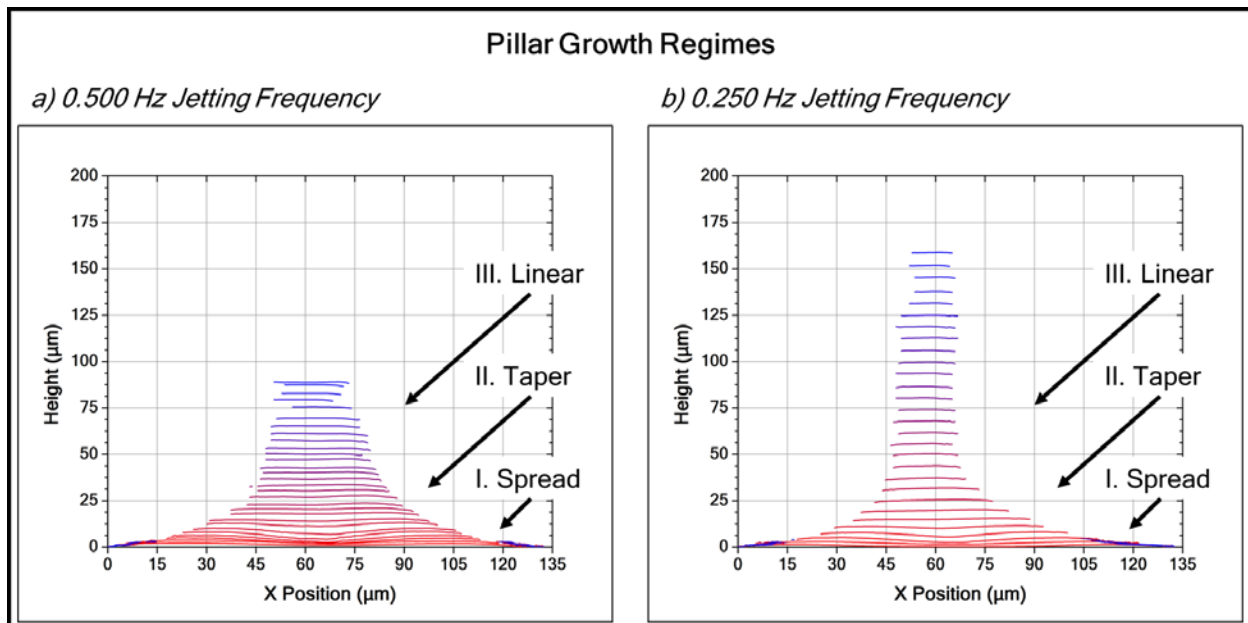


Figure 4.6. Pillar growth regimes (spreading, tapering, linear growth) for sample pillars printed at a) 0.500 Hz and b) 0.250 Hz. Plot created by using white light interferometry to measure a series of pillars printed with an increasing number of total droplets. Scans were stacked in the plot, using substrate as common reference. 30 total drops used to print tallest pillars.

Further, Figure 4.4 also offers insights into the pillar growth process. Regardless of printing condition, there exist three primary regimes of pillar growth, as described by Figure 4.6. First, the initial droplet that lands on the substrate spreads to form a wide, thin layer. Like most thin film printing processes, this spreading can be described and controlled by the wetting interaction of the substrate and ink. After this initial drop, however, the subsequent drops begin landing on the dried/drying ink rather than the initial substrate. Therefore, the wetting conditions have changed. Under these new conditions, the subsequent drops land *within* the previously-deposited droplet and exhibit progressively decreased spreading. Because the drop volume is constant, but the spreading is diminished, this results in a tapered growth regime. Finally, when the structure has narrowed enough, subsequent droplets land and spread *around* the structure as opposed *within* the structure. This results a regime of linear pillar growth and typically occurs when the width of the pillar approaches the diameter of the printed droplets.

Applying the principles of pillar growth described above, it is actually possible to create three-dimensional structures with more complicated geometries. Figure 4.7 shows three such examples. All structures printed in this figure were printed at the same substrate temperature. However, the jetting frequency was modified during the process in order to modulate the structure width. In each structure, high frequency printing was first used to create the wide base of the structure. Then, using lower frequencies and very slight (5  $\mu\text{m}$ ) steps between drop ejections, narrow branches can be extended upward and outward from the central base. In this way, both hexagonal and cactus-like structures were fabricated.

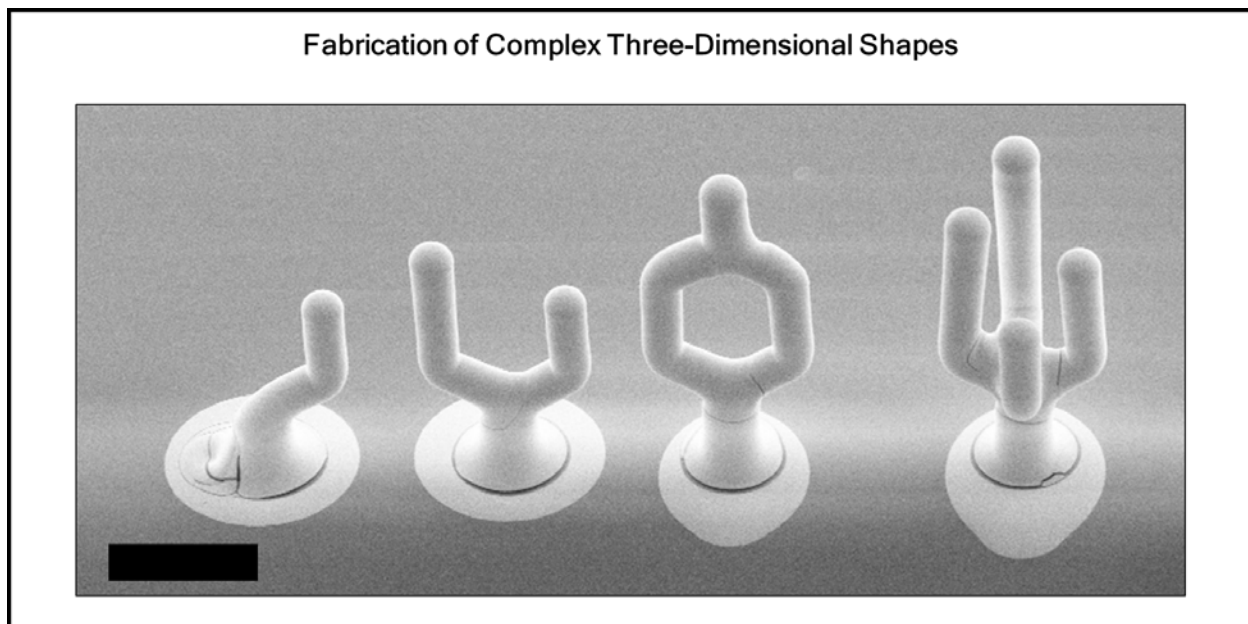


Figure 4.7. Complex three-dimensional shapes fabricated using principles learned from simple freestanding pillar fabrication. Scale bar represents 200  $\mu\text{m}$ .

For packaging applications, the pillars printing must exhibit high aspect ratios and therefore take advantage of the linear pillar growth regime. However, these structures

generally need not exceed more than 100  $\mu\text{m}$  for practical applications. While taller features are certainly possible using this process, the linear growth regime does not always exhibit constant width. In fact, at extremely tall pillar heights, the width of the printed pillars begins to widen and approach widths seen when printing at lower substrate temperatures. There may be two reasons for this widening. First, at extremely tall pillar heights there likely exists a non-trivial temperature gradient from the base to top of the printed pillar, which may cause the printing behavior to approach behaviors observed at lower printing temperatures. In addition, if the nozzle fly height is constant, the travel distance between the nozzle and pillar is consistently decreasing. If even a small amount of solvent evaporation occurs mid-flight, which is possible due to the increased substrate temperatures, then the reduction of the travel distance will also reduce the mid-flight evaporation and result in increasing the drop volume deposited on the top of the pillar. Both of these effects may be at play for extremely tall structures (see widening at the top of the structures shown in Figure 4.7), though neither have been observed to affect the pillar morphology for structures printed within the necessary limits for packaging applications.

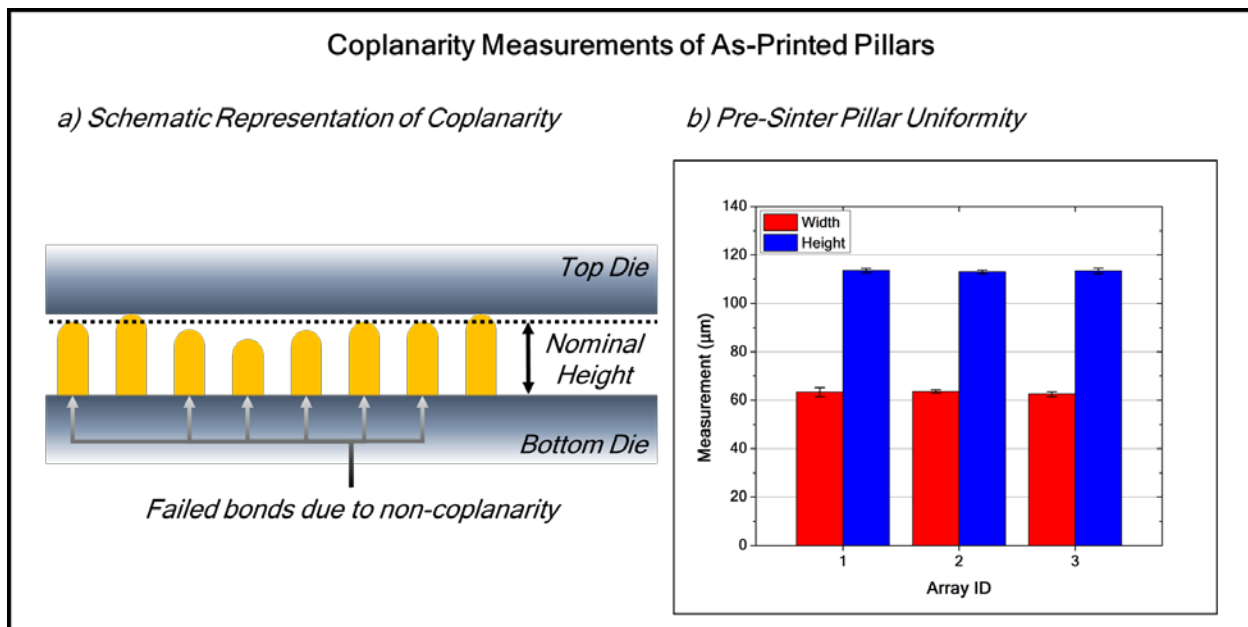


Figure 4.8. a) Schematic representation of coplanarity and b) coplanarity measurements of pillars printed in multiple arrays. In the schematic representation (a) non-coplanar bonds may fail due to gaps between the top and bottom die during bonding.

Coplanarity is a key concern for process reliability for packing applications. Coplanarity refers to the variation of bump height across a die, and this must be minimized as much as possible. Non-coplanar bumps may result in incomplete bonds during the flip chip process, as depicted in Figure 4.8. This non-coplanarity is especially critical in CSP because stresses may cause the package to warp [110]. In order to assess the overall process reliability as well as coplanarity, arrays consisting of 20 pillars each were printed with a 0.125 Hz jetting frequency, 110  $^{\circ}\text{C}$  substrate temperature, and with 30 drops each. The height and width of these printed arrays was tested for three separate arrays prior to any sintering, and the results are also shown in Figure 4.8. (As opposed

to SEM imaging, confocal laser microscopy was used in this study due to the rapid nature of the testing process.) Both the height and the width of these structures are very uniform, indicating a very robust process with a high degree of coplanarity suitable for package interconnect applications.

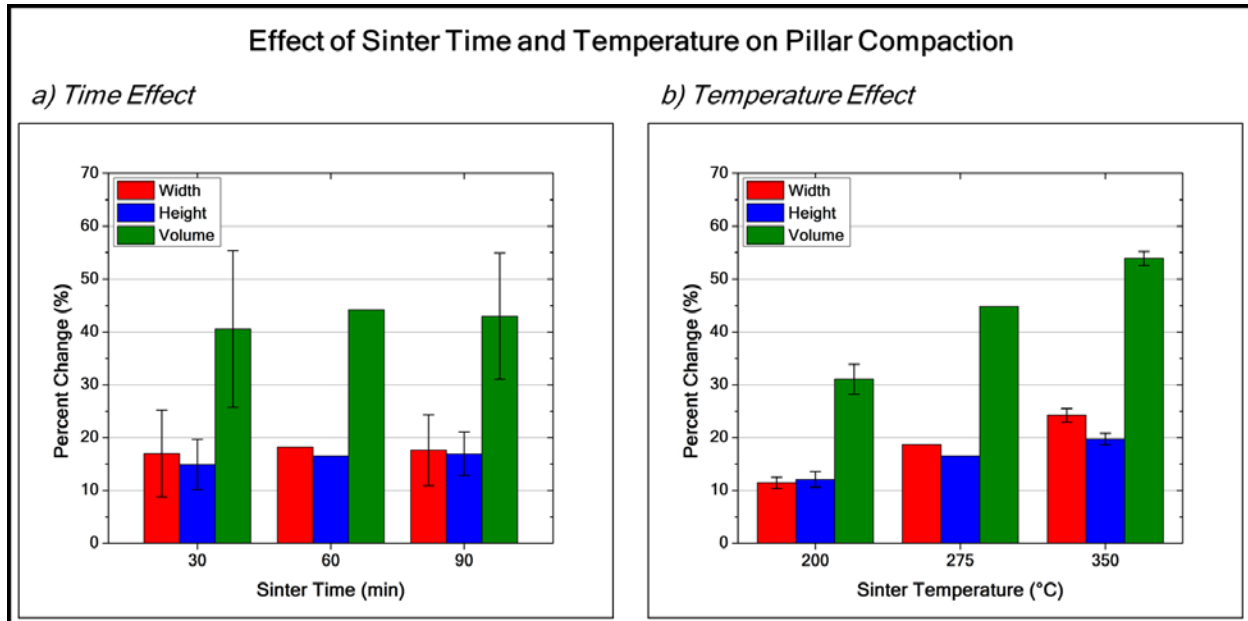


Figure 4.9. Effect of sinter time (a) and temperature (b) on pillar compaction as determined from fractional factorial design. Center time and temperature conditions shown without error bars due to no replicates on the center point. The effect of sinter time is insignificant, whereas the effect of sinter temperature is much stronger.

Finally, in order to understand the effects of sintering on pillar morphology, the same arrays used to test coplanarity were sintered under varying conditions and the height and width changes were measured. Similar to thin film nanoparticle sintering, the sintering of three-dimensional structures comprised of carbon-encapsulated nanoparticles should exhibit volume compaction as the encapsulant diffuses. From these measurements, the pillar volume was extracted using a perfect cylinder as a model. The experimental conditions were determined using a fractional-factorial design with a single center point. The two treatments were sinter time and temperature. Figure 4.9 shows the effect of both treatments on pillar morphology, described in terms of percent change from the initial morphology. As Figure 4.9 shows, the treatment with the strongest effect is the sinter temperature (neither sinter time alone nor the interaction of sinter time and temperature show strong effects). In the highest sinter temperature condition, 350 °C, pillar volume compaction of up to 53% was observed, with both pillar height and width compaction providing significant components to the overall pillar compaction. Despite the significant compaction of the pillars, the intra-array variation across all tested arrays was as low as 1.27  $\mu\text{m}$  and 0.95  $\mu\text{m}$  for height and width, respectively, indicating that the pillars both pre- and post-sinter treatments exhibit highly uniform, coplanar geometries.

### B. Mechanical and Electrical Properties

Having demonstrated that printed pillar morphology is suitable for packaging applications, the next most important properties to consider are the mechanical and electrical properties of the structures as a function of sinter condition. It is imperative these properties are comparable to solder bump properties with similar thermal treatments if inkjet-printed structures aim to be a drop-in replacement for solder bump materials and processes.

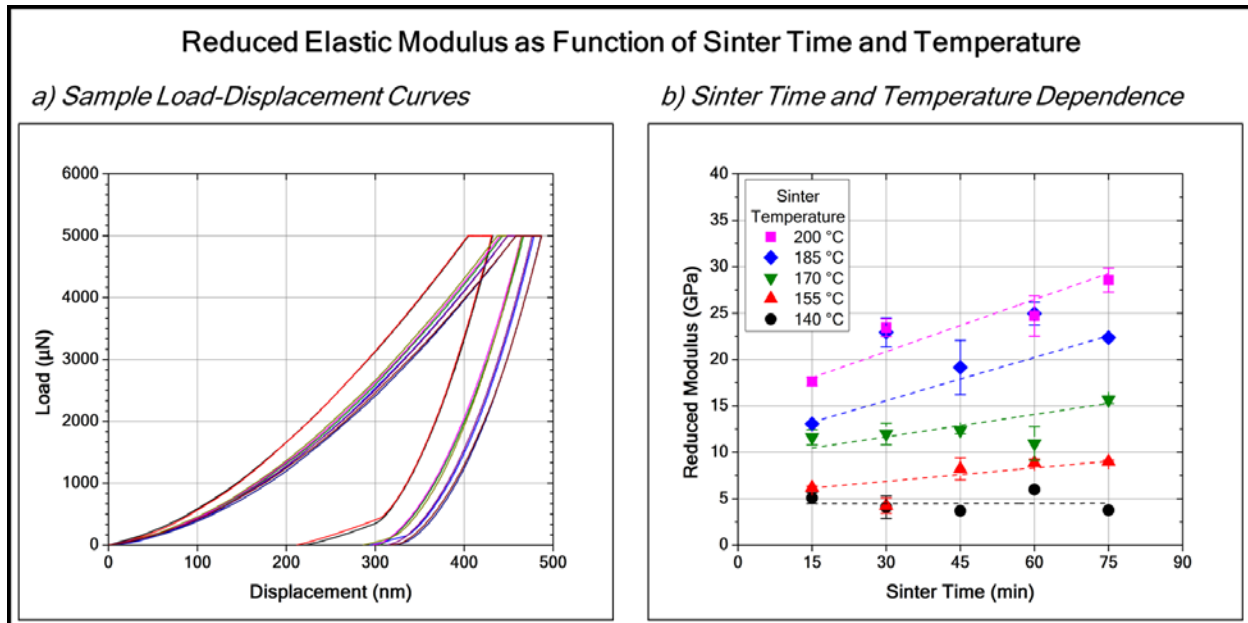


Figure 4.10. Nanoindentation testing as a function of sinter time and temperature. Left plot shows sample load-displacement data collected for multiple pillars sintered at 200 °C for 75 minutes and right plot shows entire dataset.

First, the mechanical properties tested are the elastic modulus as well as shear strength. Arrays of printed pillars were first subjected to sinter treatments ranging from 15 - 75 minutes and 140 - 200 °C and then tested via nanoindentation in order to probe the elastic response. (It is important to note these tests probe only the top of the pillars. This will be discussed further in the sintering mechanism section.) Figure 4.10 presents the results of the nanoindentation test. As shown, for sinter treatments less than 170 °C, moderate to no improvement in pillar modulus is observed. However, for treatments above 170 °C, significant increases of elastic modulus are observed, and a linear relationship with sinter time becomes clear. This linear time dependence is likely related to the compaction/densification of the pillars previously discussed. The most extremely sintered pillar exhibited a modulus of approximately 30 GPa, which is approximately 35% of the bulk gold modulus and a comparable modulus to lead-tin eutectics commonly used in solder balls.

Next, the shear strength and failure mechanisms of printed pillars were studied, likewise as a function of sinter condition. Figure 4.11 presents a schematic for failure mechanisms observed, the shear strength response as a function of pillar sinter temperature (all sinter times were one hour), failure mechanism distribution. All pillars

tested were printed on thermally-evaporated gold pads. Below 150 °C, no improvement beyond as-printed pillars is observed and the primary failure mechanism at 150 °C was interfacial failure. This may be caused by a number of reasons, though it is most likely due to residual carbon-content present at the interface preventing the metal nanoparticles from forming a solid bond with the metal pads. At higher sintering conditions, this carbon-based material will likely both out-diffuse further as well as being to decompose, resulting in improved adhesion. Indeed, at 200 °C and above, the shear strength increases and the failure mechanism distribution begins to shift toward through-pillar failures as opposed to interfacial failures. At 200 °C, the shear strength observed, approximately  $2.5 \text{ mg}/\mu\text{m}^2$ , is comparable to eutectic shear strength, meaning that both elastic and shear responses at 200 °C, i.e. temperatures under typical peak reflow conditions, provide comparable performance. In addition, sinter treatments at 300 °C result in shear strengths (approximately  $7.8 \text{ mg}/\mu\text{m}^2$ ) nearly equivalent to shear strengths guaranteed by industrial copper and gold pillar processes.

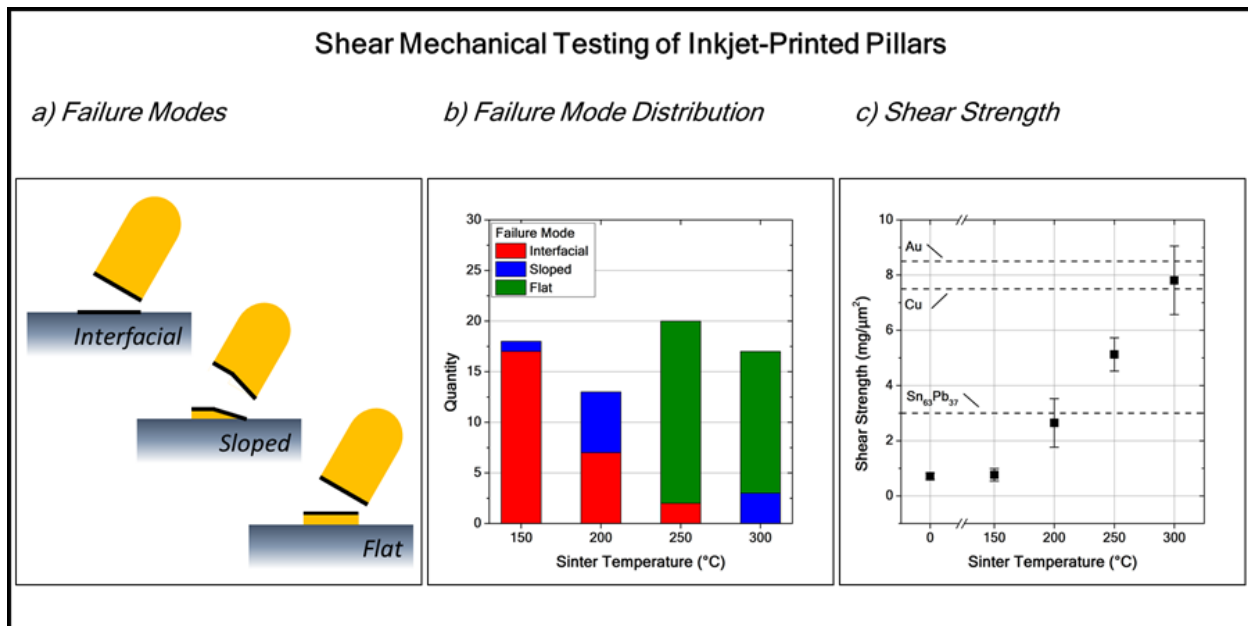


Figure 4.11. Shear failure modes, failure mode distribution, and shear strength versus sinter temperature for inkjet-printed gold pillars. Lead-tin, copper, and gold shear strengths plotted for reference. All samples sintered for one hour.

Figure 4.12 shows a comparison of pillar shear interfaces. It is clear there is a radial porosity dependence in the structures. As described, in pillars sintered at low temperatures, interfacial failures dominate. As the sinter temperature increases, however, ductile shear interfaces become more evident and dominant. In the case of sloped ductile failures (common at moderate sinter temperatures), the shear interface through the pillar is initially ductile, but the lack of densification and/or cracks present within the structure result in the shear interface sloping downward to the interface. Flat ductile failures, on the other hand, are more common in pillars sintered at higher temperatures, and are characterized by shear interfaces being mostly or completely flat across the structure.

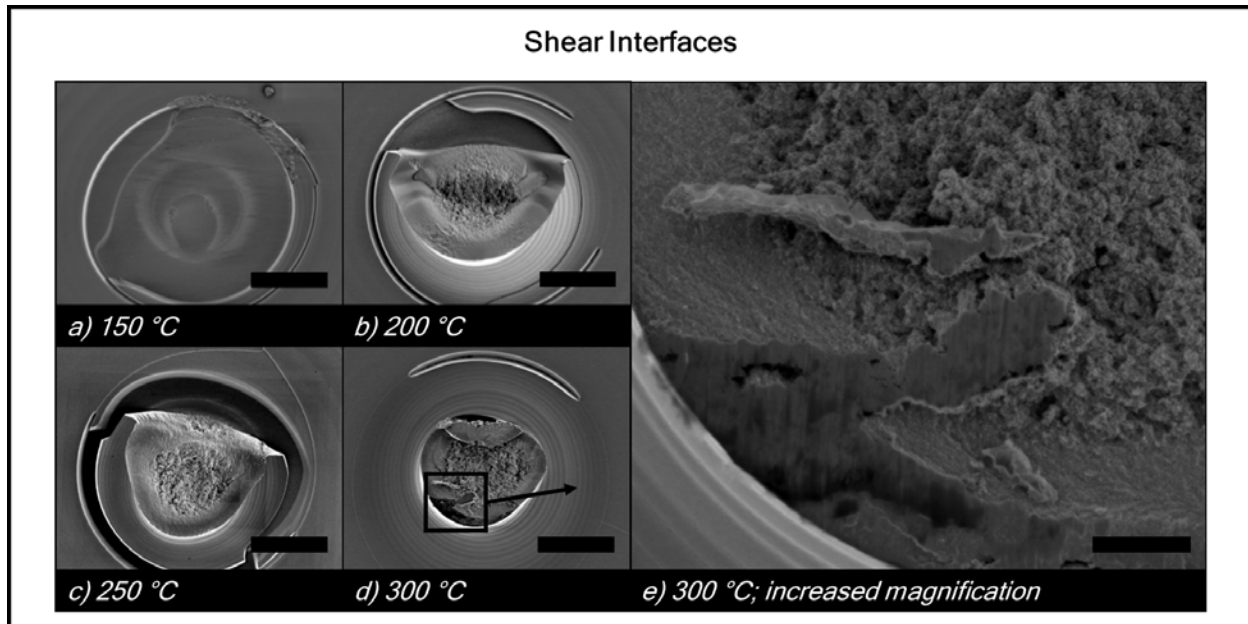


Figure 4.12. SEM images of shear interfaces as a function of sintering temperature and their failure modes: a) interfacial, b) sloped, c) flat, and d) flat. Panel e) is an enhanced view of the image in panel d). Scale bars in a) - d) are 40  $\mu\text{m}$  and scale bar in e) is 5  $\mu\text{m}$ .

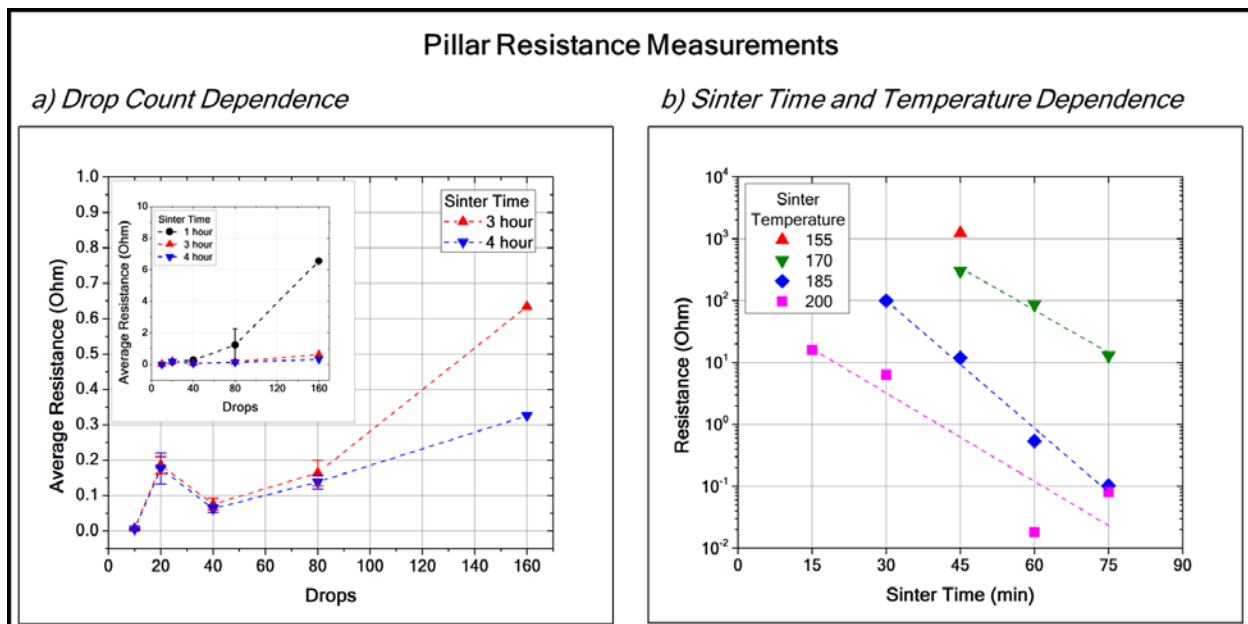


Figure 4.13. Pillar resistance measurements as a function of a) drop count and b) sinter time and temperature. All measurements made with HP-4155 semiconductor parameter analyzer. Inset of panel (a) adds 1 hour sinter condition in order to demonstrate clearly non-linear resistance as a function of drop count.

Next, the electrical performance of sintered structures is considered. Figure 4.13 presents a plot of measured pillar resistance as a function of drop count and sinter time. Similar to the nanoindentation test, electrical testing probes the bottom and top of the pillars, not the center of the structure. Therefore, if there exists a gradient in the pillar's

electrical properties such that at some point throughout the pillar there is a non-conductive segment, this will manifest itself as a non-conductive pillar. Using a perfect cylinder as a model for the geometry of the pillar and assuming the structure has uniform electrical properties, the measured resistance through the structure should be a linear response of height. While the electrical properties of the structure are not uniform at the onset of sintering, it is reasonable to assume the properties will be uniform upon the completion of sintering. Also, as described earlier, the linear growth regime will result in a linear response in pillar height as a function of drop count, therefore the measured pillar resistance should exhibit a linear response with drop count *if the pillar is sintered completely*. As expected, pillars with fewer drop counts exhibit lower measured resistance, however the response is not linear as a function of drop count until the total sinter time reaches four hours. At this point, it is safe to assume the pillars are sintered to completion, and the resistivity can be extracted using the geometry of the pillar.

Although the confirmation of complete sintering is important, the measured resistance as a function of sinter condition is the most important response for practical applications. Figure 4.13 also shows this response for the same pillars used in the nanoindentation experiment described previously. Similar to this experiment, the response at low sinter conditions is minimal. In fact, the 140 °C sinter condition is not even shown on the plot because the resistance of these pillars was above the measurement capability of the parameter analyzer used for testing. Above 150 °C, however, there is a clearly conductive pathway and the resistance exhibits an exponential response as a function of sinter time. This is likely due to the exponential nature of encapsulant diffusion. As the temperature increase, this diffusion rate accelerates and the time to achieve high conductivity decreases. Using the perfect cylinder geometric model, the peak conductivity observed in nanoparticle-based pillars is 13.2  $\mu\Omega\text{-cm}$ , or 16% of bulk gold conductivity and, importantly, higher than conventional eutectic conductivity. Thus, at sintering temperatures of 200 °C, printed nanoparticle pillars have been shown outcompete conventional eutectic materials in the two most critical metrics to interconnect performance, mechanical and electrical performance.

### C. Composition

As already observed during the inspection of the shear test failure modes, the sintered pillars exhibited non-homogenous structure. Namely, the exterior of the pillars were denser than the interior, and this observation was used to explain the shear strength response as a function of sintering conditions. However, in order to gain further insight into the nature of these mechanical and electrical responses, pillars were milled using a focused ion beam (FIB) in order to inspect the internal structure throughout the pillars as opposed to solely at the interface.

Three pillars were milled with FIB. The first was sintered at 150 °C for 15 minutes, the second was sintered at 175 °C for 45 minutes, and the third was sintered at 200 °C for 75 minutes. Figure 4.14 shows each of these pillars after milling was complete. Qualitatively, the appearance of the milled interfaces were very different as a function of sintering condition. In the 150 °C and 175 °C samples, pillars exhibit a typical “waterfall effect” which commonly occurs in composite materials with highly disparate atomic masses [111]. Because the main components of these pillars are carbon and gold, not

only are the conditions needed for the observation of the waterfall effect met, but the severity of the effect may also be indicative of the residual carbon content in the sintered structures. That is, a higher residual carbon content should manifest itself in a more pronounced waterfall effect. In addition to the waterfall effect, the 150 °C pillar showed evidence of many cracks throughout the structure. These cracks diminished as the sintering condition became more extreme, consistent with increased compaction as well as improved mechanical/electrical performance.

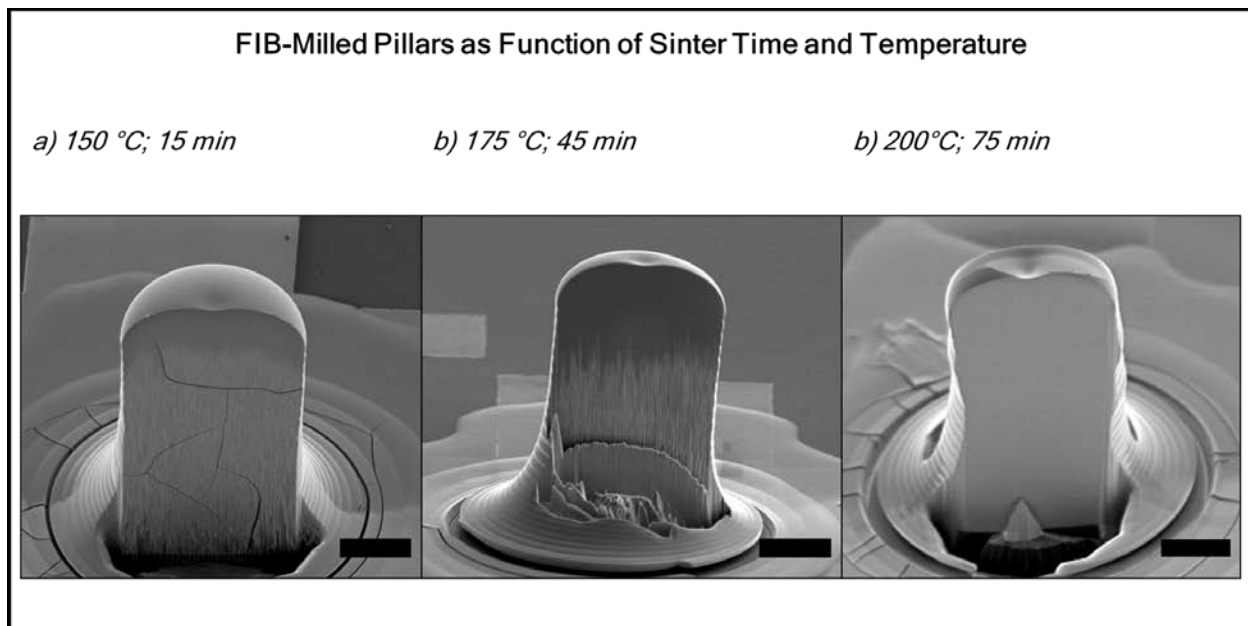


Figure 4.14. SEM images of printed gold pillars after cross-sectional FIB milling. From (a)-(c), as pillar sintering becomes more extreme, the presence of cracks and the Waterfall effect diminish, qualitatively indicating a lower residual carbon concentration.

In addition to the qualitative observations provided from FIB milling, energy dispersive x-ray (EDX) analysis was used to map the chemical composition of the sintered pillars in various locations. Due to the fact that rough surfaces are not amenable to reliable EDX scans, only the smooth, 200 °C pillar was tested. Prior to testing, additional FIB polishing processes in five locations were performed. Figure 4.15 shows the five polished sections and the corresponding EDX scans for the polished areas. Each scan shows two peak signals, one for carbon and one for gold. Using the relative peak heights for the carbon and gold signals, it is possible to gain a quantitative perspective on the chemical composition of the sintered structure. In the two lower locations and the center location, the gold signal dominates the scan, however the two areas at the top of the pillar show comparable carbon and gold signals. This indicates the pillar has a higher residual carbon content near the top of the pillar than at the bottom. In addition, the colored scans shown in Figure 4.15 provide additional qualitative insight. The colored scans indicate that the residual carbon content in topmost areas is primarily located toward the center of the structure. Using the quantitative and qualitative results observed from the FIB and EDX analysis, it can be concluded that as sintering processes proceed, the residual carbon content both decreases in quantity and the

centroid of this residual carbon content shifts upward and toward the center of the structures.

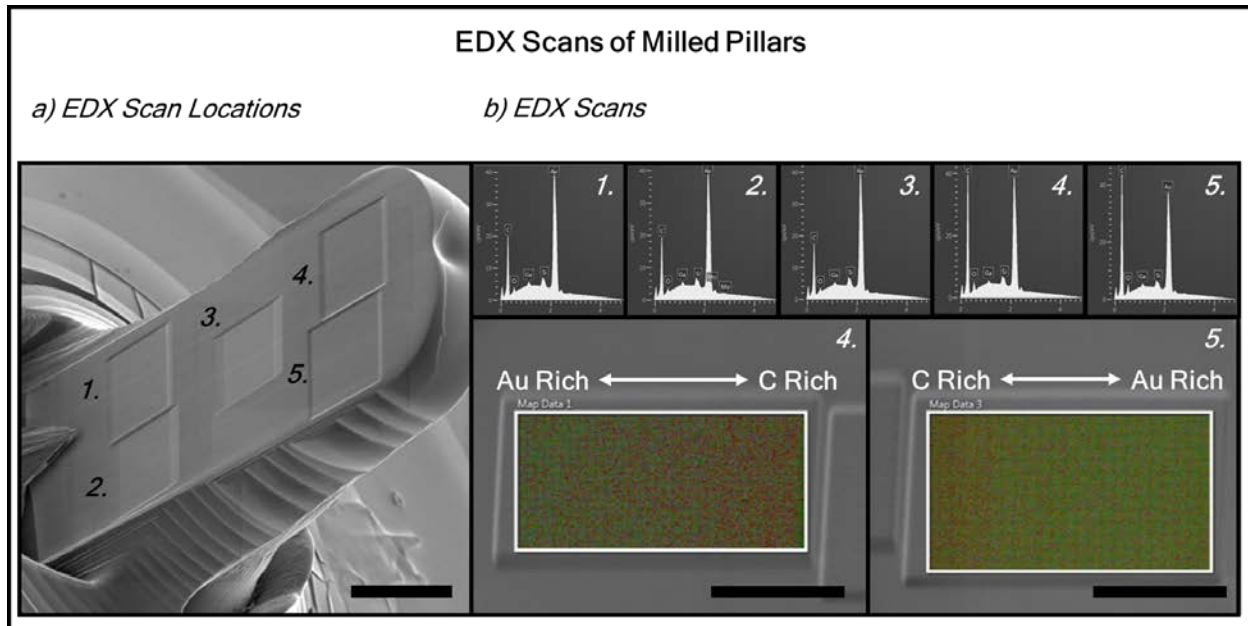


Figure 4.15. a) SEM image of milled and polished pillar with five scan locations labeled. b) Top row: average EDX scans of locations 1 - 5 showing carbon (left) and gold (right) peaks; bottom row: colors scans showing concentration gradient of carbon (red) and gold (green).

#### D. Sintering Mechanism in Three-dimensional Structures

Combining the morphological, mechanical, electrical, and compositional responses to sintering, it is possible to describe a sintering mechanism for three-dimensional structures composed of carbon-encapsulate metal nanoparticles. Similar to thin films, sintering is associated with the removal and redistribution of the carbon-based encapsulant. Figure 4.16 presents a schematic cross-section view of this process. The primary focus should be placed on the movement of the sintering front, which represents the boundary between densely-packed sintered nanoparticle material and more porous, non-sintered regions containing large amounts of carbon.

Because heat is applied at the base of the pillar during sintering, sintering initiates at the base of the pillar and progresses upward. Also, because the free carbon at the center of the structure will require more time to diffuse out of the system, it is expected that the exterior of the structures will sinter more quickly. As Figure 4.16 indicates, while this processes is proceeding, both the width and height of the structure are compacting. In addition, as sintering proceeds, the thermal conductivity of the dense material will be higher than non-sintered material, allowing for more rapid heat transfer through this material. This will serve to enhance the preferential sintering along the outside of the pillar as the front progresses upward. Ultimately, the sintering front will reach the top of the pillar and this results in the onset of electrical conductivity as well as the decrease of elasticity, consistent with electrical and mechanical observations discussed. This dense exterior will also serve as an additional barrier to internal carbon diffusion, causing the

residual carbon to be trapped near the center and top of the structure, consistent with both shear strength failure analysis and EDX analysis.

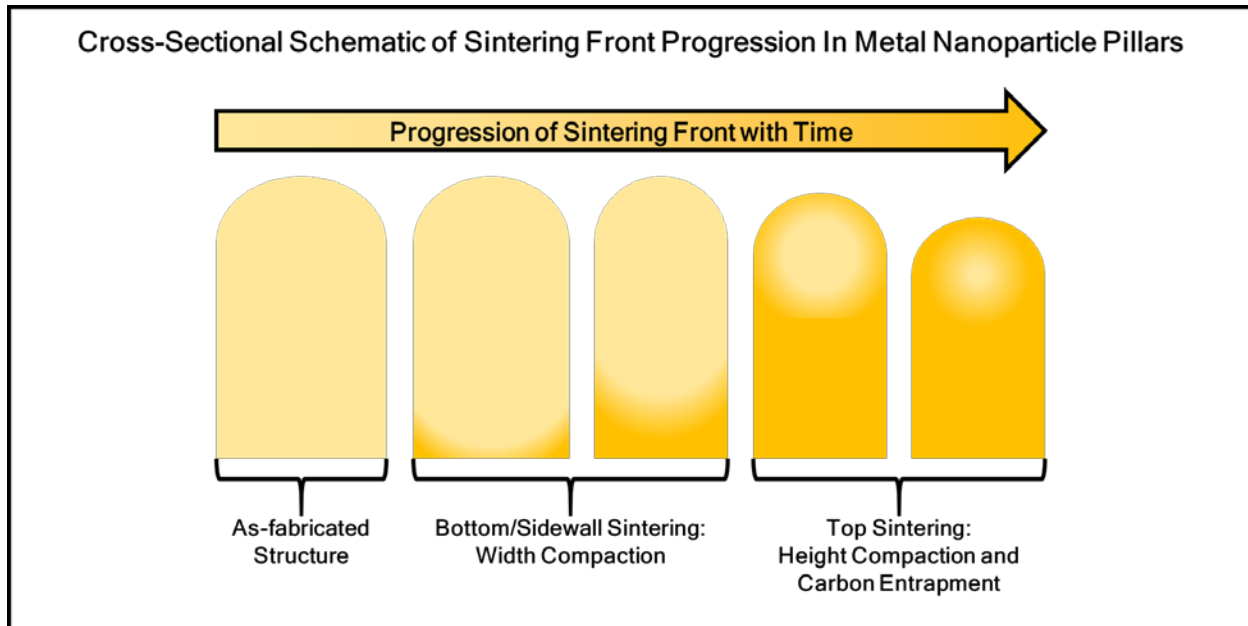


Figure 4.16. Sintering front progression in cross-sectional view of nanoparticle pillars accounting for height compaction, width compaction, and residual carbon entrapment. Darker shading represents sintered material and lighter shading represents non-sintered material.

According to this model, the breaking and subsequent diffusion of the encapsulant material plays the most significant role in the determination of the structure's ultimate morphology and material properties at a particular sintering condition. This general understanding provides invaluable insight for the design and optimization of nanoparticle inks when three-dimensional structures being the target application for these inks. Both the minimization of carbon content as well as the reduction of required process temperatures will be the primary thrusts of nanoparticle ink design, and the next section will describe advances made with a custom silver nanoparticle ink.

#### 4.3.4. Process Advancement with Custom Silver Nanoparticle Ink

In order to achieve improved mechanical and electrical performance at either equivalent or reduced process temperatures, custom nanoparticle inks with limited carbon encapsulation were formulated. As described earlier, the only components in this ink are dodecylamine-encapsulated silver nanoparticles in dodecane. These inks were also used to demonstrate effective die-to-die bonding using metal nanoparticle interconnects as a proof of concept for direct solder bump replacement materials/processes.

##### A. Pillar Fabrication

Arrays of custom silver pillars were fabricated using the same technique as that used to create pillars with the commercial gold ink, however the difference in ink formulation required a shift in the process control window. Specifically, the use of dodecane as the primary solvent resulted in the reduction of required process temperature (from approximately 100 °C down to 60 °C) and an increase in jetting frequency (from 0.167

Hz up to 2.75 Hz) for this ink as compared to the commercial ink. Figure 4.17 presents SEM images of the pillars fabricated as a function of temperature and frequency for the most reliable printing range: 70-80 °C and 0.25-1.00 Hz. Figure 4.18 shows a table of the entire range tested and the associated failure modes when pillar fabrication was not possible.

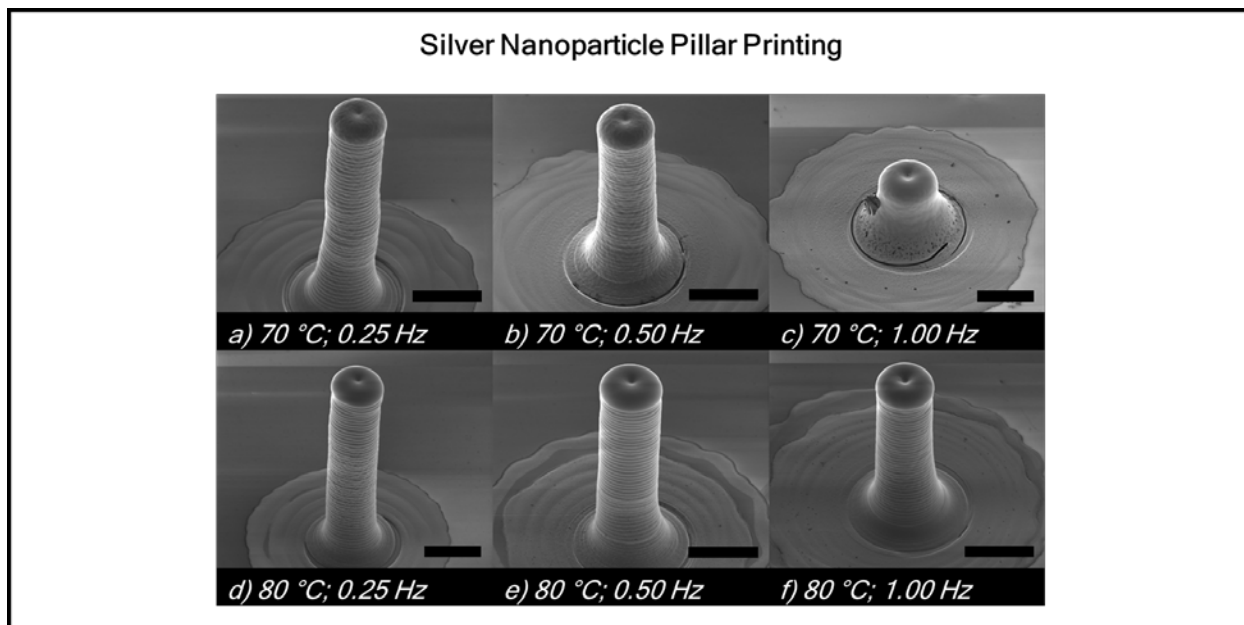


Figure 4.17. Pillars printed using custom silver nanoparticle ink. Substrate temperatures that result in the most reliable pillar formation for this ink are between 70 °C (a - c) and 80 °C (d - f). Jetting frequencies between 0.25 - 1.00 Hz shown in images. All pillars fabricated with a total of 40 drops and all scale bars represent 50  $\mu\text{m}$ .

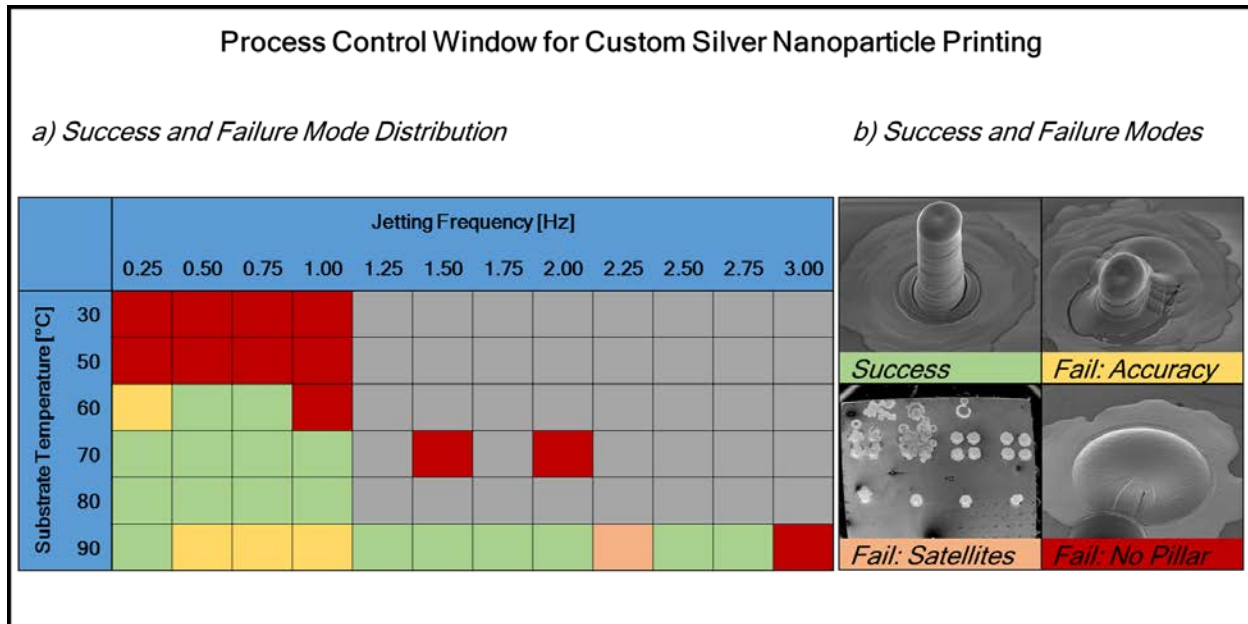


Figure 4.18. Process control window tested for silver nanoparticle ink. a) Success of failure modes as a function of substrate temperature and jetting frequency. Colors match failure modes shown in (b). Grey blocks were not tested.

Similar to printing with the commercial ink, failures at low temperature, high frequency conditions are due to the inability to remove solvent quickly enough to produce pillar structures. At higher temperatures, nozzle clogging caused yield issues due to unreliable jetting accuracy as well as satellite droplet formation.

### *B. Die Bonding*

After the reliable process window was successfully defined for this ink, four by four arrays of silver pillars were printed onto pre-fabricated gold bond pads. After printing, flip-chip thermocompression bonding was used to attach these die to larger die with complementary gold bond pads in order to create daisy-chained structures for the purposes of both mechanical and electrical testing. The image shown in Figure 4.19 represents the nominal cross-section between two die and the printed interconnect as well as a successfully bonded array of silver nanoparticle pillars.

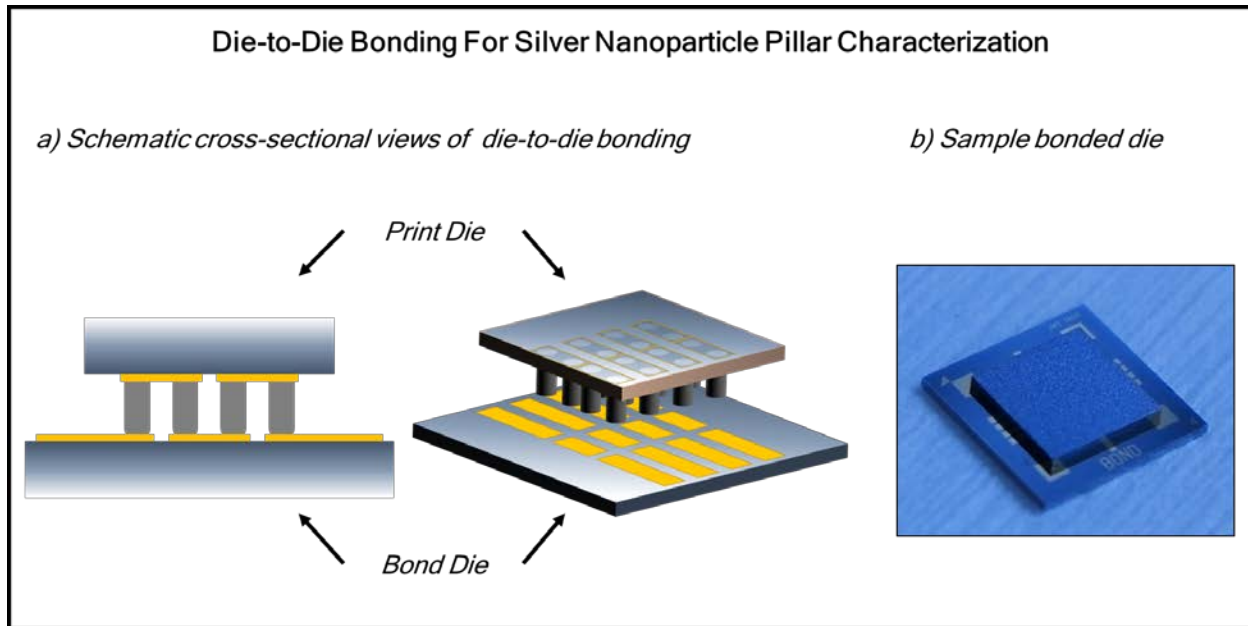


Figure 4.19. Die-to-die bonding schematic and sample.

The primary process controls available during bonding are bond time, bond temperature, and bond pressure. In all of the tests the minimum tool bond pressure of 2N was used in order to minimize the likelihood of over-compressing and collapsing the printed interconnects. Collapsed bonds would likely result in the electrical shorting of the bond pads and result in unreliable electrical characterization. During die bonding, cross-sectional views of the die were obtained in order to determine the gap height pre- and post-bonding. A non-zero gap height after bonding was complete is indicative of a non-collapsed bond. Finally, using the previously described elastic characterization and sintering mechanism of freestanding pillars, moderate sintering treatments were performed on some of the die before bonding in order to impart mechanical rigidity to the pillars and reduce the likelihood of collapsed bonds. The following section will refer to this sintering step as a pre-bond sinter process.

### C. Mechanical and Electrical Properties

The mechanical properties of the bonded die were tested using the same Nordson Dage 4000 bond tester used to characterize the shear strength of individual pillars. Using the die shear module, the shear strengths of bonded die as a function of pre-bond sintering condition as well as bonding conditions. The results are listed in Table 4.2. The peak performance of 196 g<sub>f</sub> was achieved in case where the pillars were pre-sintered at 200 °C for 5 minutes and then bonded at 200 °C for 15 minutes. This shear strength value indicates an average of approximately 12 g<sub>f</sub> per bond. Upon optical inspection with SEM (shown in Figure 4.20), the diameter of the bond tested was observed to be approximately 50 μm. This geometry and measured shear strength equate to a bond strength of approximately 6.23 mg/μm<sup>2</sup>, which is approximately two times greater than both the observed bond strengths in conventional lead-tin eutectic flip-chip bonds and the bond strength measured in commercial nanoparticle pillars sintered at comparable temperatures [112].

Table 4.2. Die shear strength for arrays of silver nanoparticle pillars as a function of pre-bond sinter condition and bond profile.

Die Shear Strength For Silver Nanoparticle Arrays						
Bond ID	Pre-Bond Sintering		Bonding		Alignment Gap ( $\mu\text{m}$ )	Shear Strength ( $g_f$ )
	Temperature ( $^{\circ}\text{C}$ )	Time (min)	Temperature ( $^{\circ}\text{C}$ )	Time (min)		
6	100	15	100	5	37	39
7	200	5	200	5	28	196
8	100	5	100	5	56	0
9	200	15	200	5	56	117

The cause for the non-monotonic response to pre-bond sintering and bond parameters seen in Table 4.2 was better understood after the post-shear optical inspection shown in Figure 4.20. Figure 4.21 presents a histogram of bond shear failure locations for each die tested. As the histogram shows, the low shear strength sample had no bonds while high shear strength samples each exhibited intra-bond failures. The primary difference between Bond 9 and Bond 7 is that the interfaces in Bond 9 were much smaller areas than Bond 7. In die exhibiting low shear strength, little to no material was transferred from the print-side die to the bond-side die (see Figure 4.20). For example, some pillars simply compressed rather than transferring any material to the bond-side die. This lack of material transfer resulted in poor mechanical robustness during shear testing. While this explains the measured shear strength response, a full root-cause analysis of why certain pillars bonded while others did not bond has been left for future work. Likely contributors to the inconsistent bonding may be insufficient bond pressure, bond pad cleanliness issues, and insufficient control over the pre-bond sintering process, to name a few.

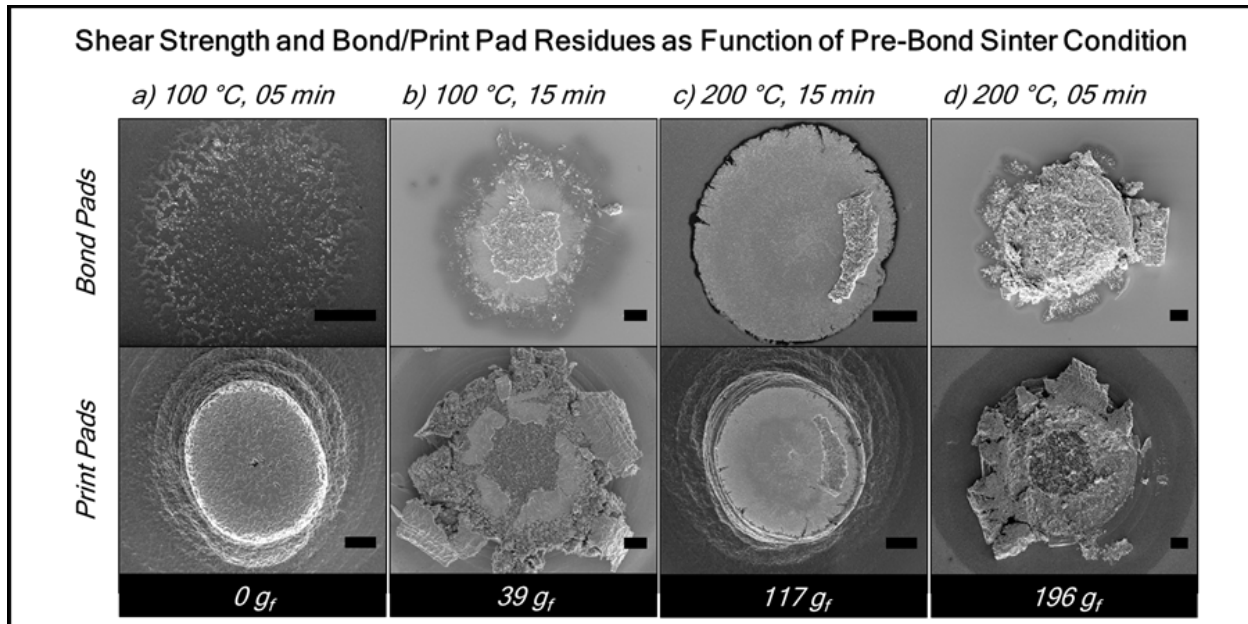


Figure 4.20. Post-shear SEM inspection of bond failures as a function of pre-bond sintering condition. Top row of images is the residue of transferred material from the printed pillar to the bond pad. Bottom row of images in the remainder of the printed pillar after bonding was complete. Force listed at the bottom of each column of figures is the shear force required for the full die. All scale bars represent 10  $\mu\text{m}$ .

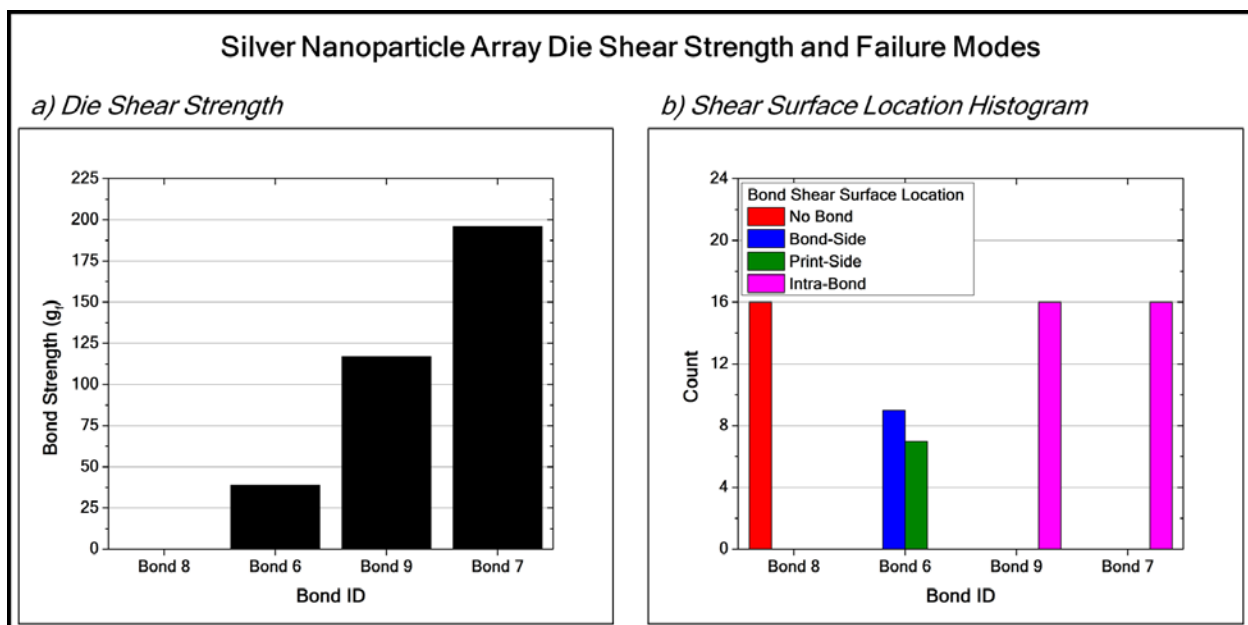


Figure 4.21. Die shear strength and shear failure modes for silver nanoparticle arrays. Each array contained 16 printed and bonded pillars.

Finally, the electrical properties of the sintered pillars were tested using the daisy-chained structures of the bonded die. Pad-to-pad resistances were measured to eliminate the effect of contact resistance from the probes. For single rows including four bonded pillars, the extracted average resistance of the best bonds was approximately 200 m $\Omega$ .

Unfortunately, this resistance is higher than anticipated (translating to a resistivity of 590  $\mu\Omega\text{-cm}$ ). It is likely that this high resistance is dominated by contact resistances between the pillars and pads as opposed to the pillars themselves, though additional work is necessary to ascertain the true cause of the unexpectedly high resistance.

#### 4.4. Summary

Two fundamental aspects of inkjet printing processes help to establish the overlap between printing processes and packaging applications: 1) the additive nature of the inkjet printing and 2) the facile incorporation of novel, high-performance materials such as metal nanoparticles. In addition, while interconnect scaling will continue, inkjet printing resolution and pitch capabilities are well-matched to the current and future demands for advanced interconnects. However, because inkjet-printed interconnects have primarily been confined to planar applications, the key remaining challenge is the development and characterization of processes for three-dimensional interconnect applications.

Because inkjet printing of metal nanoparticle inks has largely been applied only to thin film applications, both fabrication processes for three-dimensional features and properties of sintered structures need to be studied. A simple fabrication approach called the solvent volume minimization strategy has been described. It is based on minimizing the residual solvent volume on a substrate prior to subsequent droplets landing and it offers a controllable and tunable approach to printing high aspect ratio features.

Using this strategy, the three-dimensional inkjet printing of freestanding interconnects using both commercial as well as custom nanoparticle inks has been demonstrated. Substrate temperature and jetting frequency act as the primary process controls during fabrication. Upon characterizing the mechanical and electrical properties, it is clear that the nanoparticle-based features outcompete conventional materials and processes. In addition, using a combination of optical, mechanical, electrical, and compositional characterization techniques, a model for sintering in these large structures was developed and verified. While these results are indeed very promising, additional materials optimization as well as the characterization and understanding of bonding processes will prove vital to the adoption of this process in an industrial setting.

## Chapter 5. Inkjet-printed Through-silicon Vias for Chip Stacking

---

Advanced packaging interconnects need not be limited to features such as pillars that rest on the surface of a chip or board. Indeed, interconnects that extend through the chip or board may facilitate the integration of numerous technologies into a single, thin, small-footprint structure. Stacking multiple layers of logic, memory, sensors, communication networks, etc. into a single stack would be a powerful advancement for the semiconductor industry, and the technology viewed as the most likely to achieve this goal is the through-silicon via (TSV). Similar to Chapter 4, this chapter will describe the unique process development for fabricating functional TSV structures using metal nanoparticles and inkjet printing. Comparisons will be made to both the conventional TSV fabrication process as well as the inkjet-printed pillar process, and the electrical and mechanical characterization for arrays of printed TSVs will be presented.

## 5.1. Introduction

As described in Chapter 1, the TSV is a high aspect ratio, highly conductive interconnect that extends entirely through a thinned silicon chip. As opposed to stacked chips with fanned out wire bond interconnects, TSVs offer the ability to stack thinned chips without increasing the overall footprint of the stack. Because of this, the TSV is considered the most attractive option for realizing chip stacking in future applications. However, the development of TSVs is still in the early stages and both the materials and processes used for TSV fabrication have yet to be firmly established. This section will discuss the conventional pathway for fabricating TSVs and, similar to Chapter 4, establish the potential for inkjet printing to serve as an alternative process for TSV fabrication.

### 5.1.1. TSV Critical Dimension and Pitch Requirements

TSVs serve a number of purposes within the packaging landscape. As the following section will describe in further detail, TSVs can be easily scaled from 10-100  $\mu\text{m}$  in diameter. Indeed, a demand exists for TSVs that span this entire range. Table 5.1 presents the critical dimension and pitch requirements for both pillars and TSVs for near- and long-term interconnect structures.

Table 5.1. Interconnect metrics for current and future package substrates. Interconnect methods defined as: WB = wire bonding, FC = flip chip, TSV = through silicon via. All data extracted from 2012 Tables of [99].

Package Substrates						
Metric	Low-Cost (PBGA)			Mobile (SiP, PoP)		
	2015	2020	2025	2015	2020	2025
Interconnect Method	WB	WB	WB	WB / FC	WB / FC	WB / FC
Interconnect Pitch ( $\mu\text{m}$ )	80	80	60	50	50	50
Minimum TSV Diameter ( $\mu\text{m}$ )	80	60	60	80	70	60
Minimum TSV Pitch ( $\mu\text{m}$ )	250	220	220	275	250	250
Metric	Cost Performance (PBGA)			High Performance (S-BGA)		
	2015	2020	2025	2015	2020	2025
Interconnect Method	FC	FC	FC	FC + TSV	TSV	TSV
Interconnect Pitch ( $\mu\text{m}$ )	100	95	90	120	110	90
Minimum TSV Diameter ( $\mu\text{m}$ )	80	70	55	100	70	55
Minimum TSV Pitch ( $\mu\text{m}$ )	275	250	250	275	250	250

In contrast to fabricating freestanding structures, when inkjet printing is used to fill pre-fabricated trenches similar to those used in TSVs, the critical dimension for this application will depend primarily on the drop diameter and placement accuracy. In other words, the smaller the droplet and the higher the placement accuracy, the smaller the TSV able to be filled using inkjet printing. Combining the inkjet printing capabilities and the design requirements for pillar and TSV applications highlighted in Table 5.1, it is easy to see that inkjet printing is capable of producing feature sizes and pitches that directly overlap with low- to medium-density TSV applications.

### 5.1.2. TSV Process and Performance Metrics

While inkjet printing processes appear compatible with TSV processes due to an overlap in dimensional capability, the question that remains is whether or not inkjet-based materials and processes will outperform conventional TSV processes and materials. However, unlike the electroplated copper pillars and gold stud bump processes that are widely accepted as the next generation of highly-scaled interconnects, the standard processes and materials to be used in TSVs are still being explored. Therefore, the introduction of inkjet printing and novel materials to TSV process flows may indeed be a significant contribution.

There are four main process steps in TSV fabrication process flows, highlighted by Figure 5.1 [113]. First, a trench must be fabricated. Next, the trench must be lined with an insulator and filled with a conductive material. Then, in order to interconnect the TSV with another chip or board, vertical interconnects similar to solder bumps or pillars must be fabricated. Finally, the chip containing the TSV must be thinned in order to expose the bottom of the TSV and enable the electrical interconnection through the chip, once stacked.

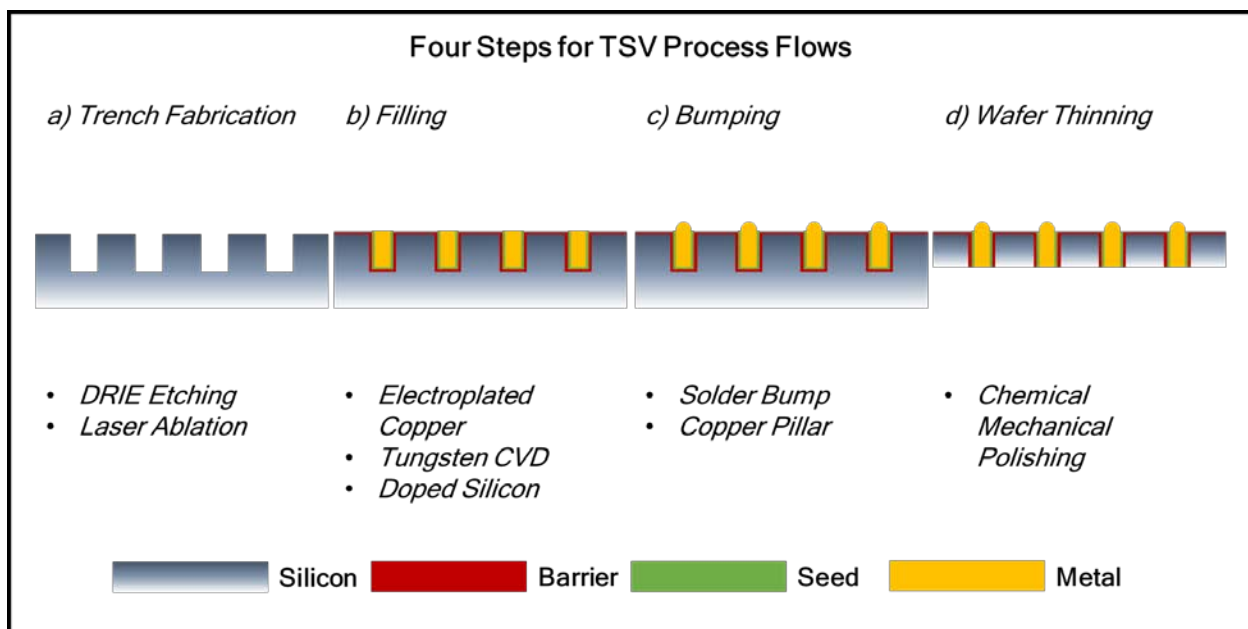


Figure 5.1. The four steps common to all TSV process flows: a) trench fabrication, b) trench filling, c) bumping, and d) wafer thinning.

To date, a number of different materials and processes have been proposed for fabricating TSVs. With respect to trench fabrication, the most commonly used technique is a deep reactive ion etch (DRIE) process known as the Bosch process [114]. In this process, an alternating  $\text{SF}_6$  and  $\text{C}_4\text{F}_8$  plasma produces a highly anisotropic etch through silicon, creating trenches with nearly vertical sidewalls. For many TSV process flows, this is the method used to create the trenches, although laser drilling is also being explored [115]. An additional design consideration for trench fabrication is the timing relative to the fabrication of the logic layers in the silicon chip. Figure 5.2 highlights the three approaches, named via-first, via-middle, and via-last. While each of these

approaches have both positive and negative attributes [116], the common thread with each is the fabrication of trenches using the Bosch process or laser.

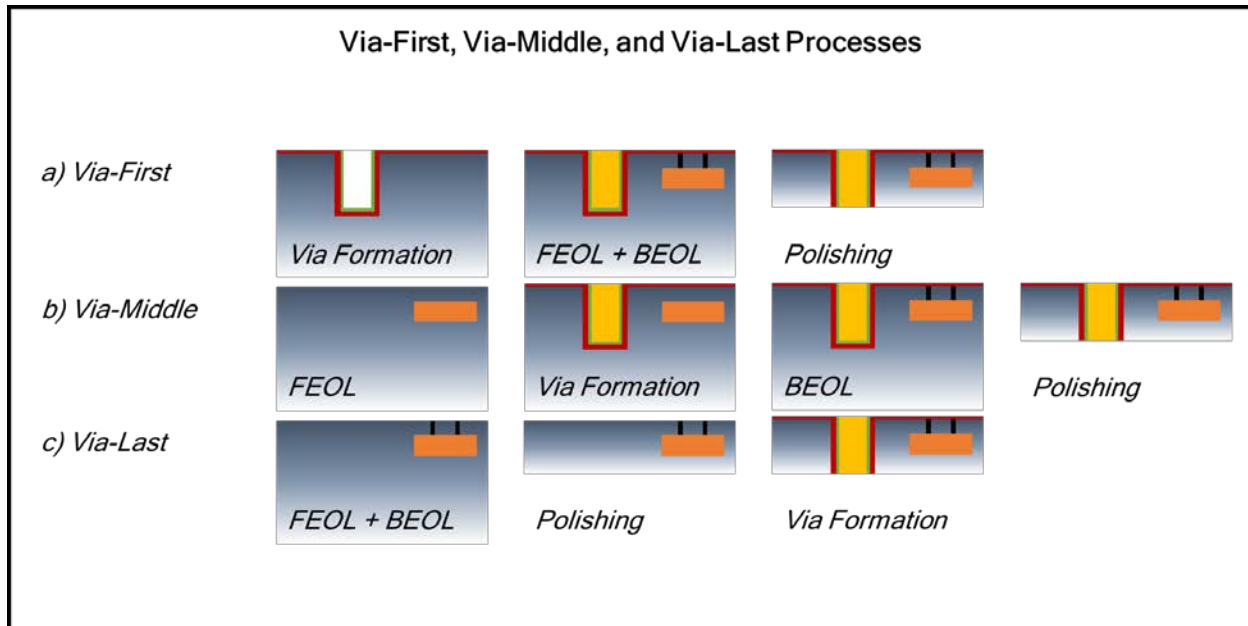


Figure 5.2. Comparison of a) via-first, b) via-middle, and c) via-last TSV process flows. FEOL refers to front-end-of-line logic processes, BEOL refers to back-end-of-line metallization processes. Adapted from [117].

Furthermore, because inkjet printing will not be used to etch vias, the focus of inkjet-based processes should be placed on TSV filling and bumping, the second and third steps in traditional TSV process flows. The most common processes for TSV filling are copper electroplating and tungsten CVD [118, 119]. Isolated, highly-doped silicon columns have also received some attention [120]. The conventional material used for TSVs is copper, which has a higher conductivity than even bulk gold. Because of this, inkjet-printed materials are unlikely to outperform the electrical performance of conventional TSVs. However, TSVs are typically capped with conventional flip-chip bumps in order to interconnect multiple chips. This serial process flow involving lithography-dependent electroplating or CVD, electrochemical polishing to remove excess copper or tungsten, and stencil-printed solder bumping leaves much room for improvement with respect to process throughput. Because inkjet printing is additive, if three-dimensional printing processes are successfully developed, the potential to fill and bump a TSV in a single process step becomes a possibility.

The final step in TSV fabrication typically involves thinning the chip, which is usually accomplished using chemical mechanical polishing. The purpose of this step is to expose the bottom side of the vias prior to stacking. Again, because inkjet-printed materials and processes, do not have a place in optimizing this aspect of the TSV process flow, attention will be paid to the filling and bumping process. Indeed, a via filling strategy that 1) scales well for medium- to high-density TSV layouts, 2) requires minimal materials, 3) maintains thermal budget restrictions established for back-end-of-line processing, and 4) enables both die-scale and wafer-scale fabrication compatibility

will be a particularly impactful achievement. Figure 5.3 compares a conventional TSV process flow with an ideal inkjet printing TSV fill and bump process flow, clearly demonstrating the throughput improvement possible with inkjet printing processes.

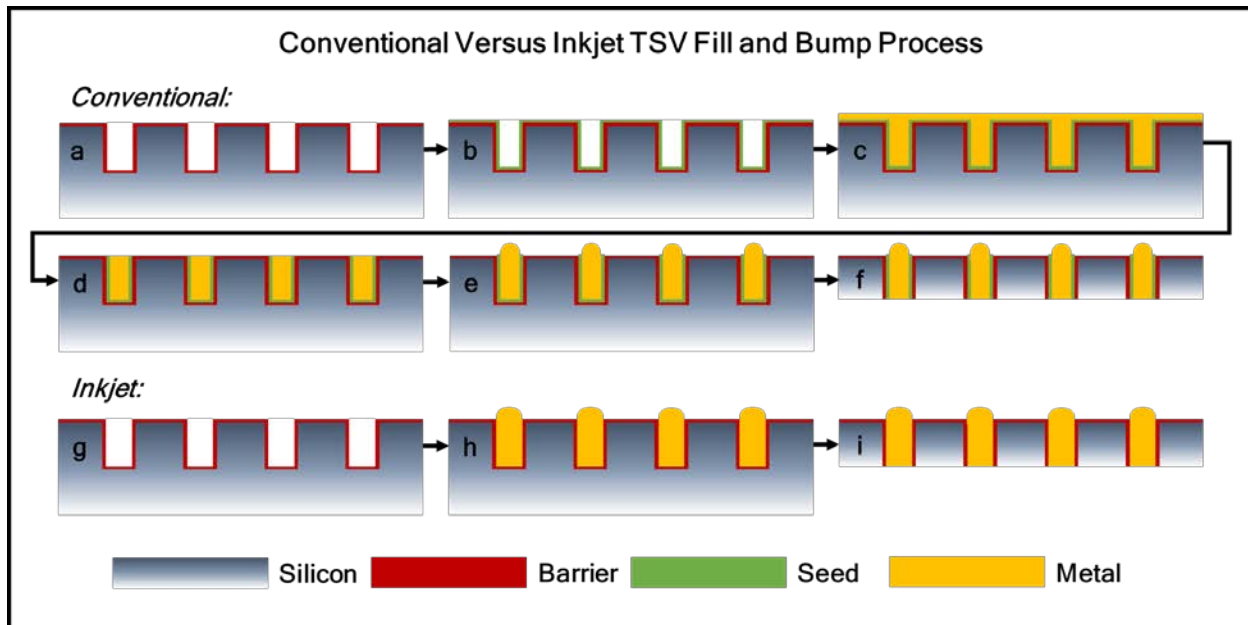


Figure 5.3. Comparison of conventional versus inkjet-printed TSV fill and bump process. In conventional process (a - f), trenches in silicon are first coated with a dielectric barrier layer to prevent conduction (a), they are subsequently coated with a seed layer for electroplating (b), electroplated (c), polished to remove excess electroplated metal (d), bumped (e), and thinned (f). In contrast, inkjet-printed processes (g - i) also start with trenching coated with barrier layers (g), but are then filled and bumped in a single step with inkjet printing (h), and thinned (i). Conventional process adapted from [117].

## 5.2. Three-dimensional Inkjet Printing Through-silicon Vias (TSVs)

Therefore, building on the success of three-dimensional printing of freestanding structures, the same principles were used to develop a process to fully fill and bump pre-existing TSVs. The following discussion will describe the materials and characterization techniques employed as well as the demonstration and evaluation of successfully stacked die.

### 5.2.1. Materials

#### A. Inks

The only ink used in the process development for TSVs was Harima NPG-J gold nanoparticle ink. Because the filling of pre-existing TSVs requires both precise and accurate jetting performance, Harima NPG-J was used exclusively rather than using a custom nanoparticle ink with less reliable jetting performance.

#### B. Substrates

Two different substrates were used for filling pre-existing TSVs: silicon and silicon-on-insulator (SOI). In each case, TSVs were first fabricated using conventional DRIE Bosch processes at wafer scale followed by wafer dicing in order to obtain individual die for printing targets. In the silicon wafers, target etch depths were 100  $\mu\text{m}$  deep. The SOI wafer etch stopped at the 2  $\mu\text{m}$  thick buried oxide (BOX), resulting in an etch depth equal to the device layer thickness which was also 100  $\mu\text{m}$ .

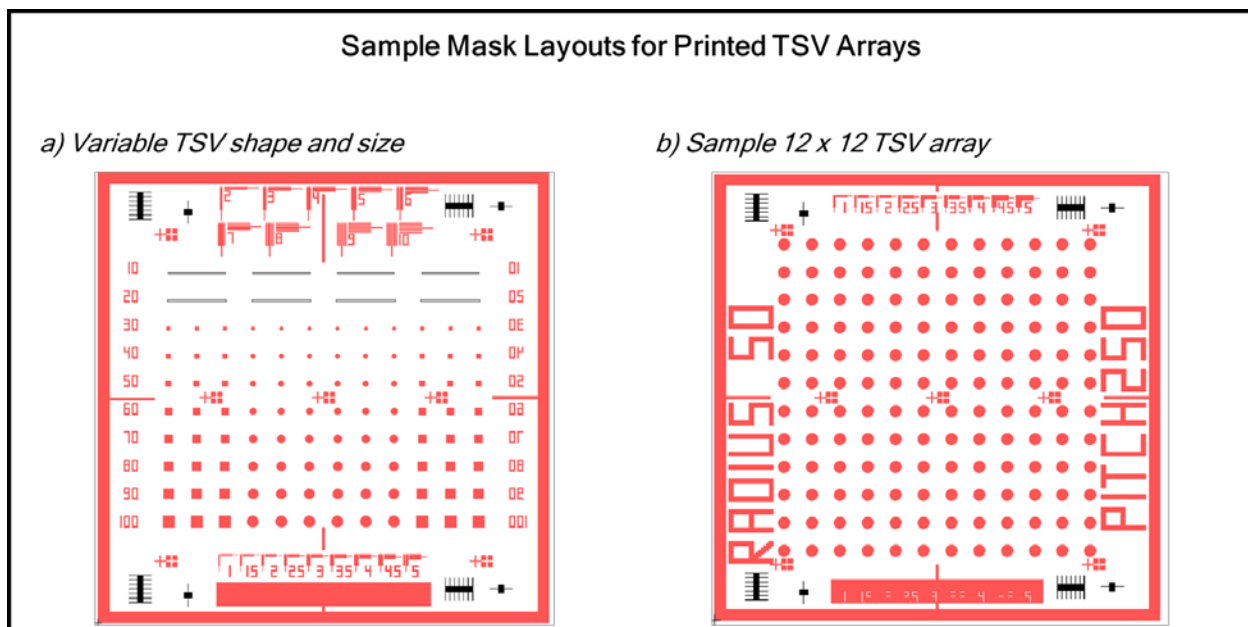


Figure 5.4. TSV mask layout samples. a) Variable shape and size for square and round TSVs ranging from 10  $\mu\text{m}$  to 100  $\mu\text{m}$  in side length and diameter, respectively. b) 12 x 12 array of 50  $\mu\text{m}$  radius TSVs with a pitch of 250  $\mu\text{m}$ .

For initial tests, both square and circular trenches were fabricated and filled. The critical feature dimension (square side length and circle diameter) for these trenches ranged from 10 - 100  $\mu\text{m}$ . The trenches were fabricated in square arrays with pitches equal to

1.5, 2, and 2.5 the critical feature dimension. Figure 5.4 is a sample layout from the mask used for TSV etching.

### 5.2.2. Characterization

In order to qualify the filling and bumping performance, optical, mechanical, and electrical tests were used. In some instances, described further below, additional fabrication steps were necessary for successful testing. For the purpose of investigating the electrical and mechanical performance of bonds, all bonding processes were performed at 250 °C according to the prescribed sinter temperature of the Harima NPG-J ink. Similar to the work with freestanding pillars, we expect to only see reasonable electrical and mechanical performance after the printed features have had an opportunity to sinter. All bonding was performed using the same Finetech Fineplacer Lambda flip-chip bonder used for die bonding with freestanding pillars.

#### A. Morphology

Both optical and electron microscopy were used for the qualification of the printing process as well as the investigation into bond quality. First, these techniques were necessary for determining the number of drops required for filling and bumping TSVs at a given jetting frequency, substrate temperature, and trench dimension. Second, using a dicing saw to create cross sections, SEM images were taken in order to investigate the nature of filling within both un-bonded and bonded samples. Finally, optical microscopy was used to investigate the surface of die after mechanical testing.

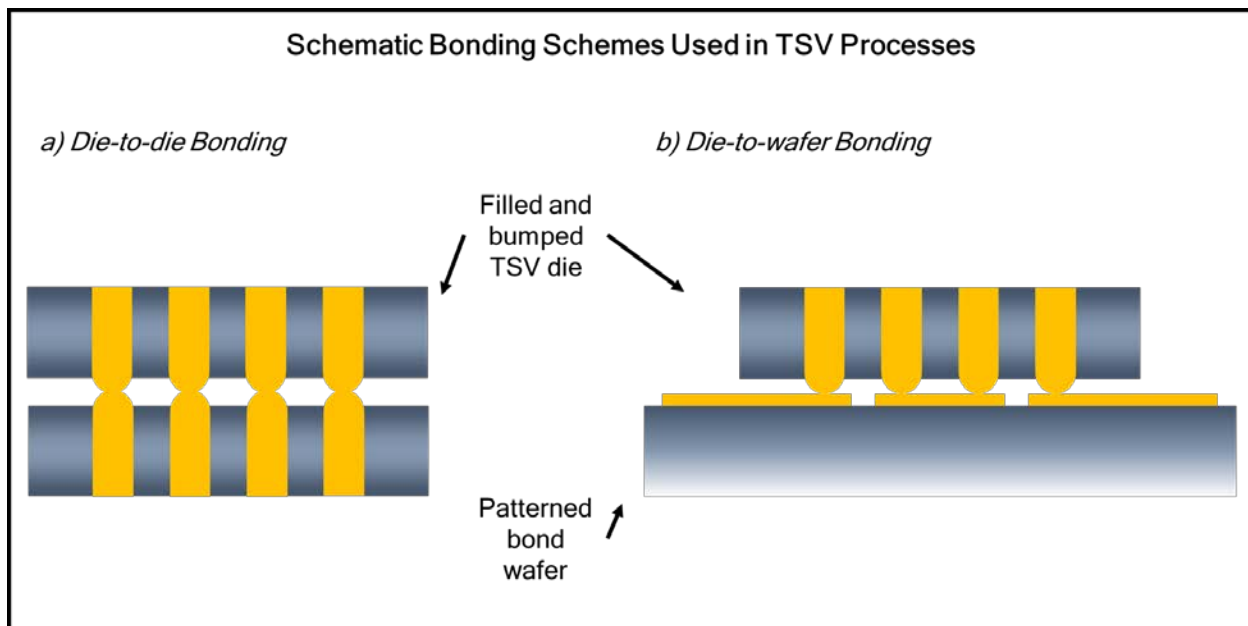


Figure 5.5. Bonding schemes used for TSV processes.

#### B. Mechanical

Both die-to-die and die-to-wafer bonding were used. See Figure 5.5 for cross-sections of these bond schemes. Using the die shear capability of the Nordson Dage 4000 bond tester, successfully bonded die were subject to die shear testing in order to determine the average shear strength of the bonds after bonding and sintering. Die shear tests

were performed at a shear rate of 300  $\mu\text{m/s}$ . In order to accurately test the bond strength of the bonds between the two stacked die, the bottom die was affixed to a large carrier wafer using a cyanoacrylate adhesive and allowed to dry overnight before testing.

### C. Electrical

Finally, electrical testing of the confined TSVs structures required additional fabrication processes (see Figure 5.6). First, only SOI samples were used for the preparation of electrical test structures. After printing and bonding, the handle of the SOI die were removed using an isotropic  $\text{SF}_6$  dry etch process. The exposed BOX was then patterned and etched with a buffered oxide etch in order to access the bottom of printed TSVs. Finally, an additional photolithography step was used to pattern an Al-Si metal layer deposited via sputtering, resulting in a daisy-chained structure similar to the one used for electrical testing of freestanding pillars.

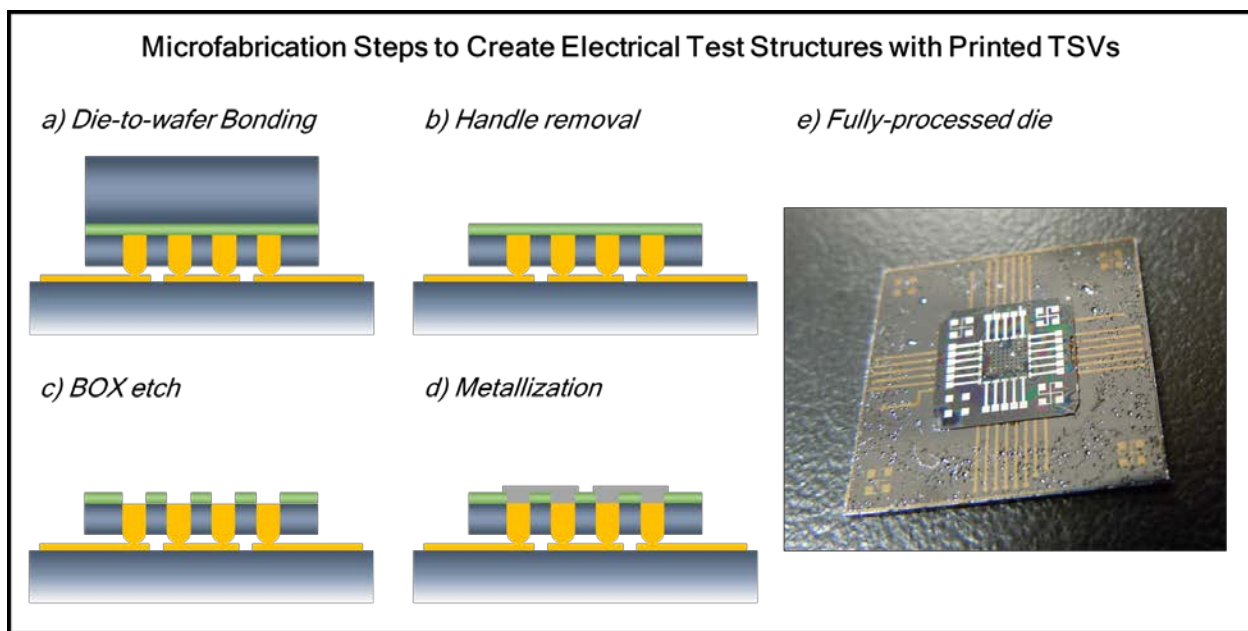


Figure 5.6. Post-bonding microfabrication steps taken in order to produce electrical test structures with inkjet-printed TSVs.

### 5.2.3. Process Development with Commercial Gold Nanoparticle Ink

Based on the process developed for printing freestanding pillars, the following discussion details the process used for filling and bumping TSVs as well as bonding and characterizing the TSVs.

#### A. Comparison with Freestanding Pillar Process

While the process developed for filling and bumping TSVs is based on the freestanding pillar process, i.e. using the jetting frequency and substrate temperature to control the solvent evaporation during the process, there are a few notable differences.

First, because filling TSVs involves depositing the liquid ink into a confined trench, the ink should not spread on the substrate during the beginning the printing process. This is beneficial with regard to scaling of the process, because the pitch and feature size

achievable will be dependent on the etched TSV size and pitch rather than the wetting properties of the ink. The caveat with this, however, is that if the droplet diameter is larger than the trench diameter, unintended spreading on the surface of the substrate may result in inadvertent shorting between trenches. Because the droplet diameter is roughly the same dimension of the nozzle orifice diameter, this means that the minimum diameter accessible for inkjet-printed TSV filling will be on the order of the smallest nozzle diameter which provides reliable jetting performance. For modern inkjet nozzles, this limit is near 20  $\mu\text{m}$  in diameter.

Another implication of this nozzle and TSV diameter relationship is that the overall process throughput will be affected by the selection of nozzle diameter. Because throughput is directly dependent on the total number of droplets required for fabrication, the minimization of droplets per TSV is important. This can be achieved by matching the droplet diameter to the TSV diameter as closely as possible. If the droplet diameter is too large, there exists a risk of droplets landing on the substrate surface, as described earlier. If the droplet diameter is too small, the unnecessary reduction in drop volume will require an increased number of droplets and reduce the throughput.

Finally, the confinement of the droplets in an enclosed trench makes the removal of solvent even more critical for the TSV process than the planar pillar process. If the solvent does not evaporate quickly enough, residual solvent may be trapped inside the pillar by subsequent drops. This may result in porosity in the final structure, and potentially result in electrically open interconnects.

### *B. Filling and Bumping*

Initial filling experiments involved determining the process conditions amenable to dense TSV filling. The process controls explored were jetting frequency, substrate temperature, total number of droplets, and droplet burst count. Droplet burst count, a metric unexplored in pillar printing, refers to the number of droplets ejected consecutively during drop ejection events. Because TSVs are confined structures where initial spreading does not adversely affect the scaling of the process, increasing the number of droplets ejected per event was explored in order to potentially boost the overall throughput of the process.

Figure 5.7 shows the initial results of the droplet burst count effect on filling quality. In this experiment, all of the TSVs used were 60  $\mu\text{m}$  deep and 100  $\mu\text{m}$  in diameter. The substrate temperature was 130  $^{\circ}\text{C}$  and the jetting frequency between droplet bursts is 0.167 Hz. The droplet burst count is varied from 2 drops per burst to 4 drops per burst. As droplet burst count increases, the quality of the filling degrades rapidly as evidenced by the increasing roughness and porosity of the filling. This is likely due to the inclusion of solvent in the trench which eventually evaporates after being trapped in the structure. In addition, more droplets per burst resulted in overflow of the trenches, which is not an acceptable result. Ultimately, because droplet burst counts of greater than two resulted in extremely adverse effects, all subsequent experiments were performed with only a single droplet ejected per burst.

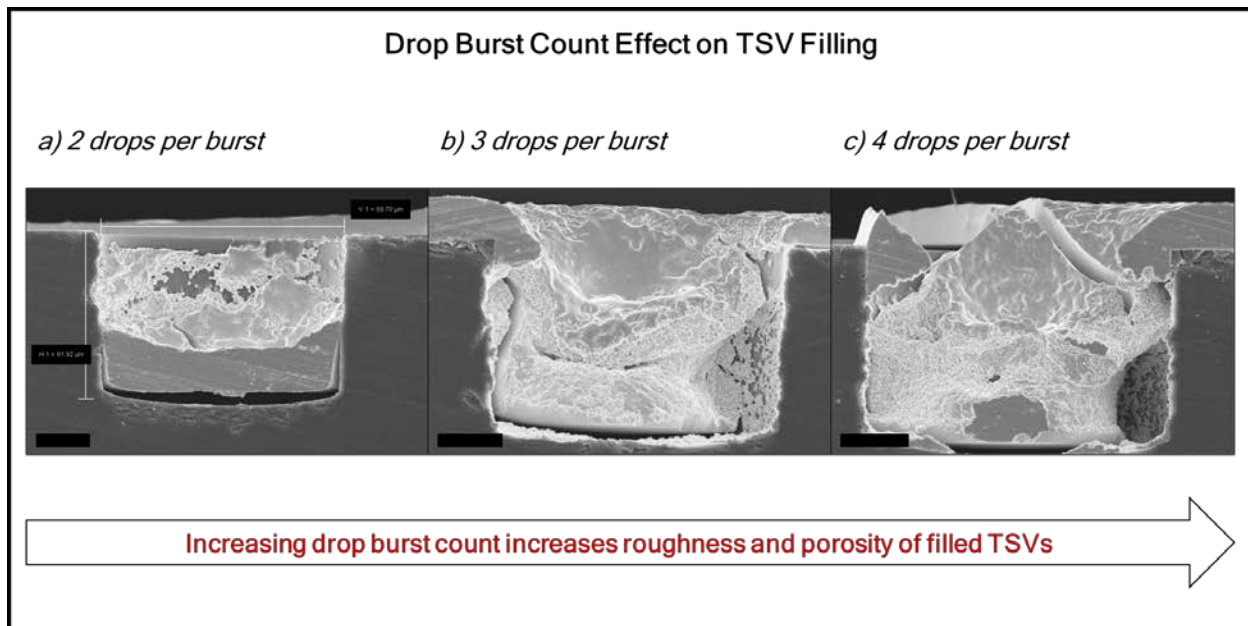


Figure 5.7. Effect of drop burst count during printing on TSV filling. All scale bars represent 20  $\mu\text{m}$ .

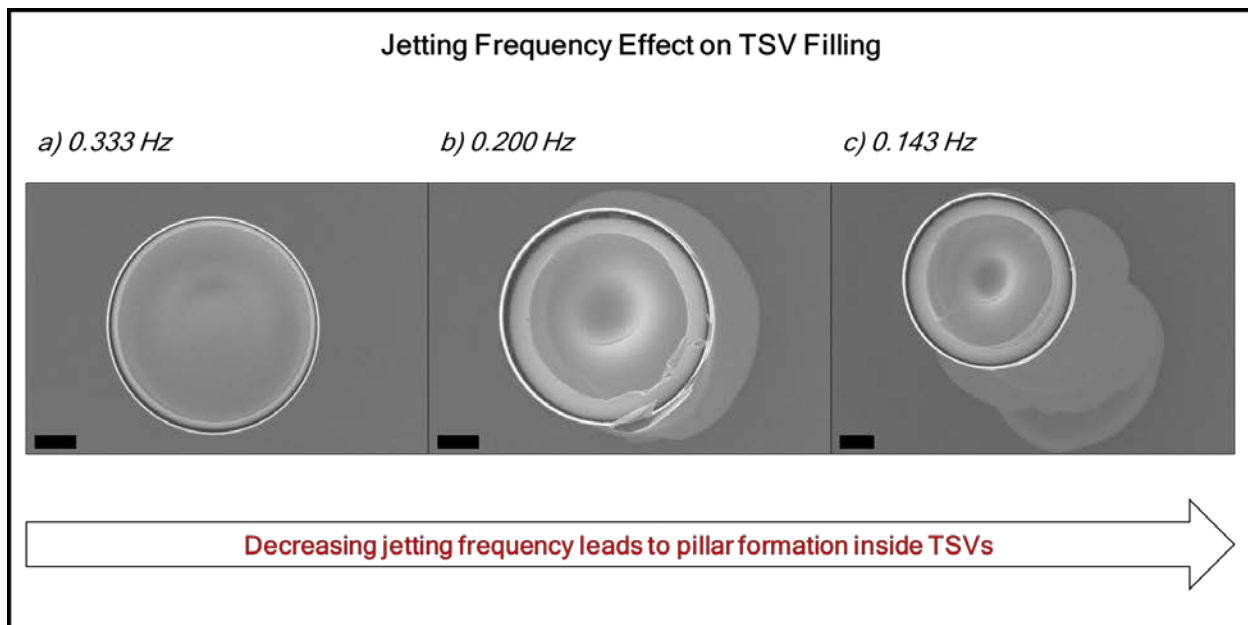


Figure 5.8. Jetting frequency effect on TSV filling. All scale bars represent 20  $\mu\text{m}$ .

Next, the jetting frequency was modulated in order to establish the optimum condition for solvent evaporation between droplet ejection events. Figure 5.8 shows that, like freestanding pillars, lower jetting frequency results in higher aspect ratio features. However, because the features are confined within the TSV trench rather than being printed on a planar surface, higher aspect ratio printing in TSVs manifests itself as pillars forming *inside* the trench rather than the deposited liquid expanding to fully fill the diameter of the trench. Trenches shown in Figure 5.8 are all printed with 90  $\mu\text{m}$  deep wells, 100  $\mu\text{m}$  diameter trenches, 70 total droplets, and 140  $^{\circ}\text{C}$  substrate temperature.

At a 0.333 Hz jetting frequency, the entire diameter of the trench is filled. In contrast, 0.200 Hz, and 0.143 Hz printing results in visible pillars within the trenches.

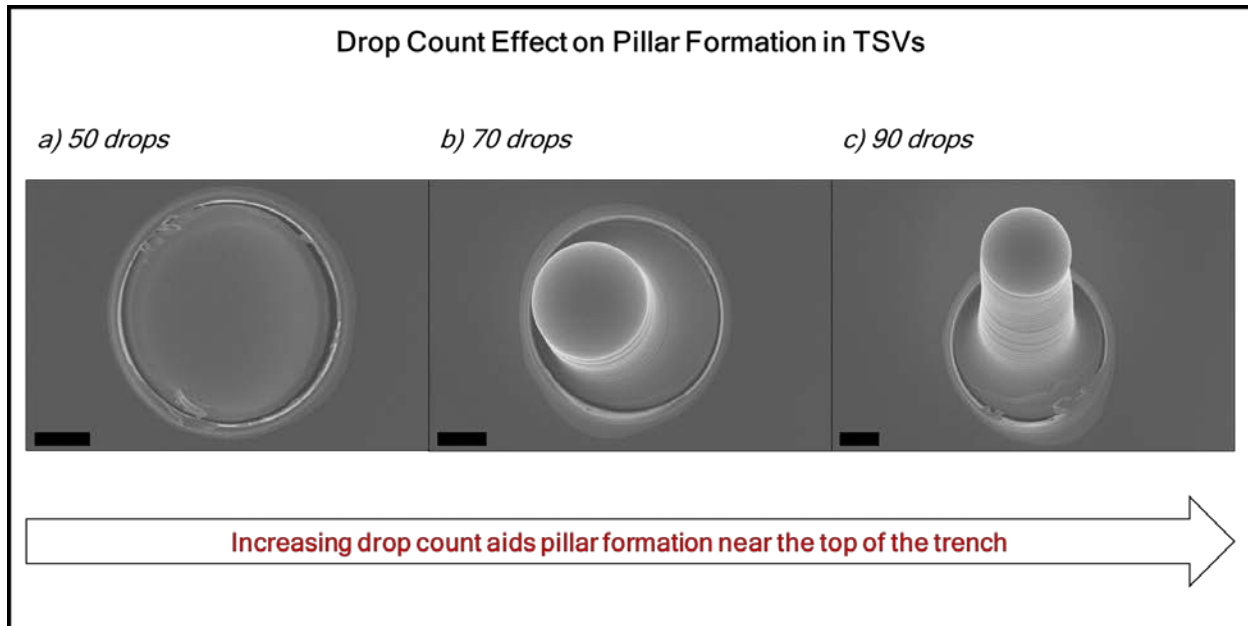


Figure 5.9. Drop count effect on TSV filling. All scale bars represent 20  $\mu\text{m}$ .

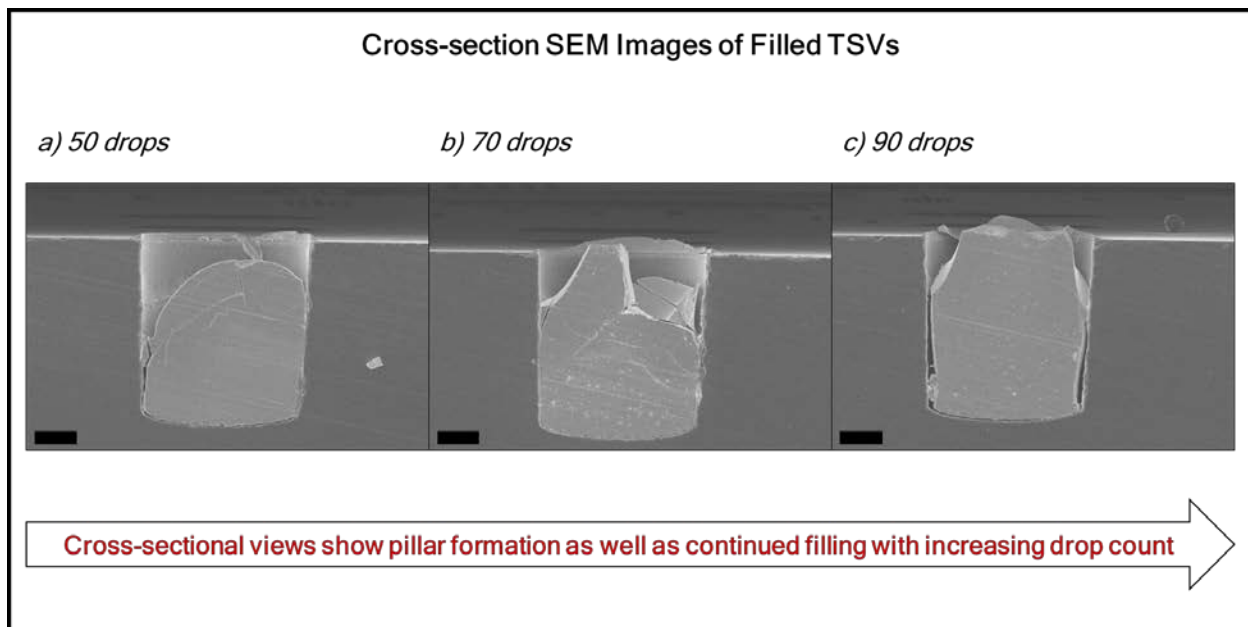


Figure 5.10. Cross-section SEM images of printed TSVs as a function of drop count. In the 70 and 90 drop conditions, pillars that formed were broken during dicing. All scale bars represent 20  $\mu\text{m}$ .

A similar experiment was run with smaller, 80  $\mu\text{m}$  diameter trenches (see Figure 5.9). However, rather than modulating drop frequency, the total number of droplets was varied to understand the progression of filling and pillar formation. In this experiment, the jetting frequency was held at 0.143 Hz and the substrate temperature held at 140

°C. As can be seen in the angled-view SEM images, the 50 drop condition appears to fill the trench evenly without producing pillars. However, the 70 and 90 drop conditions both produce bumps that extend beyond the surface of the trench. Figure 5.10 provides cross-sectional images of the same die. For the 70 and 90 drop conditions, pillars formed and extended beyond the trench surface, as observed in the top-down images, but were broken off during cross-section sample preparation.

Regardless of the presence of pillars, the cross-sectional samples prepared in the experiment confirm that TSV filling via inkjet printing can result in dense filling of the TSV trench. As described earlier, this is an important quality to confirm as porous TSVs may result in both poor mechanical and electrical performance. As shown in the 90 droplet sample, the filled TSV does show a few sidewall voids near the bottom of the trench. In these trenches, no post-etch processing was performed, i.e. no additional insulating layers were deposited and no surface modification procedures were performed to alter the wetting of the ink along the trench walls. In the future, these films and processes can be explored to help reduce the presence of sidewall voids.

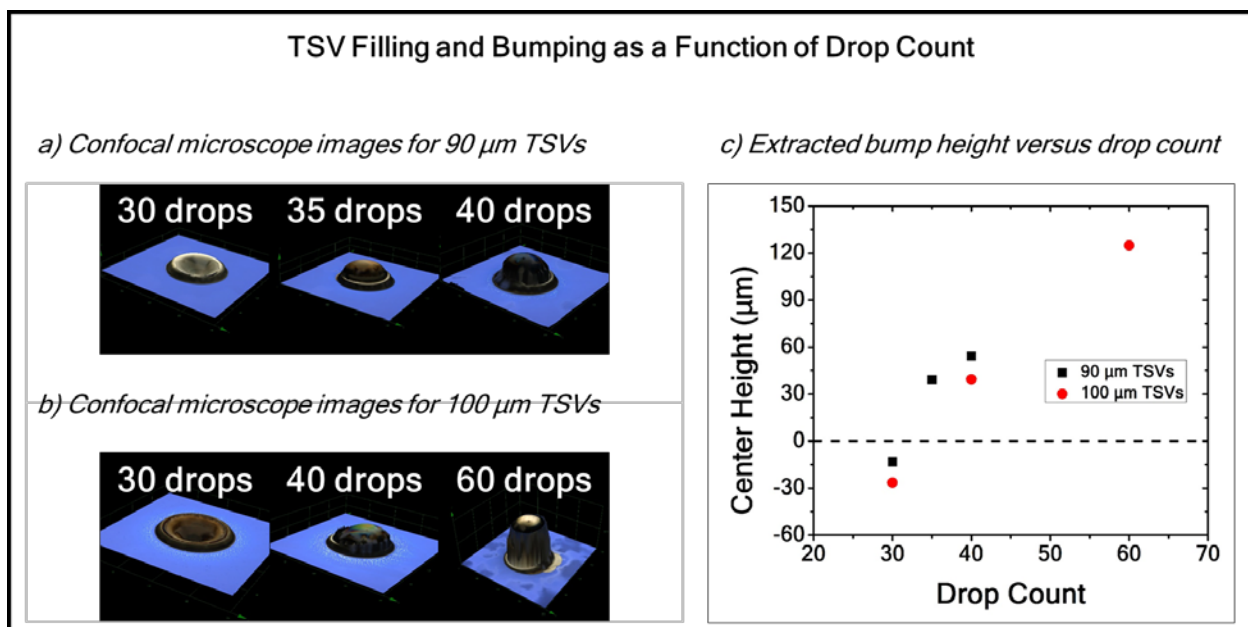


Figure 5.11. Laser confocal images of filled and bumped TSVs as a function of drop count for a) 90  $\mu\text{m}$  TSVs and b) 100  $\mu\text{m}$  TSVs. c) Extracted heights plotted as the center height of the printed TSV with respect to the silicon surface.

Finally, because the desired structure is a fully-filled TSV with a moderately-sized bump rather than a large pillar extending far beyond the surface, additional tuning experiments were performed to determine the most appropriate printing conditions for achieving this structure. Using laser confocal microscopy to scan the height difference between the top of filled TSVs and the top surface of the trench, it is possible to rapidly determine the optimum drop count for given trench diameters and printing conditions. Figure 5.11 highlights this process for both 90  $\mu\text{m}$  and 100  $\mu\text{m}$  diameter TSVs. These TSVs were printed at a slightly lower substrate temperature (120 °C) and jetting frequency (0.125 Hz) in order to avoid pillar formation initiating far below the silicon surface. In the plot

shown, negative values represent incompletely filled TSVs and positive values represent fully filled and bumped TSVs. As shown, roughly 35 and 40 drops total resulted in bump heights of 30  $\mu\text{m}$  for the 90  $\mu\text{m}$  and 100  $\mu\text{m}$  TSVs, respectively. These conditions confirm the ability to successfully fill and bump TSVs in a single process step using inkjet printing.

### C. Bonding

With successful filling and bumping established, die were next bonded to each other and to pre-patterned wafers to confirm the ability to use this process in chip stacking applications. Figure 5.12 shows two side-view optical images of die before and after die-to-wafer bonding as well as a cross-sectional SEM of die-to-die bonds. As the two side-view images indicate, the bumped TSV die creates an alignment gap before bonding, but this gap almost completely disappears during the bonding process. This is similar to the compression observed during the bonding of pillar arrays. This redistribution of material is similar to reflow observed in conventional eutectic solder bumps. Although complete collapse between die is not ideal due to the potential for electrical shorts between pads, this analog to reflow is useful property of the bonding process as it helps mitigate potential non-coplanarity issues if all of the filled and bumped TSVs do not have the same bump height.

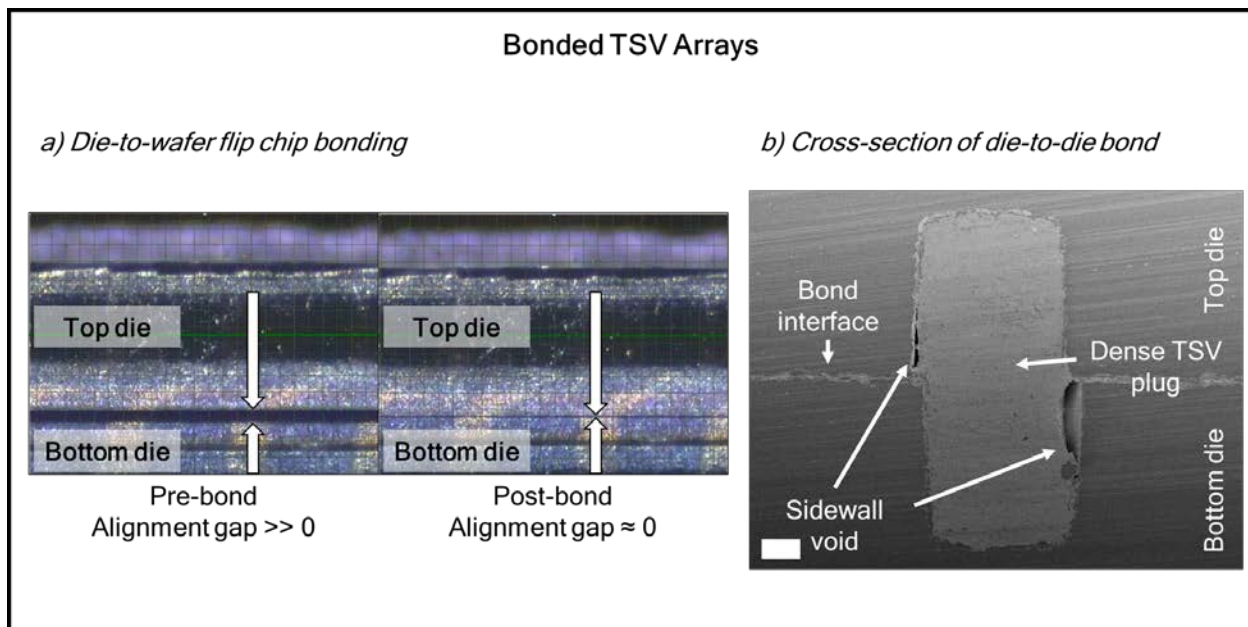


Figure 5.12. Images of a) die-to-wafer bonds before and after bonding and b) cross-sectioned die-to-die TSV bond. The arrows in a) identify the pre- and post-bond alignment gap. Scale bar in b) represents 20  $\mu\text{m}$ .

Figure 5.13 shows top-down optical images of filled and bumped TSVs after their die-to-wafer bonds were broken. These are the same die printed and described in Figure 5.11. As expected, as drop count and therefore bump height increases, the wider the subsequent spreading of material during flip-chip bonding. In the 35 and 40 drop case, a considerable amount of spreading on the surface of the bond pad wafer is observed, but the 30 drop condition resulted in minimal to no spreading on the bond pads. While

minimizing the spreading is important, especially for higher density TSV applications, the degree of spreading observed was not sufficient to cause shorting in these die. Therefore, both mechanical and electrical testing were possible without further process development.

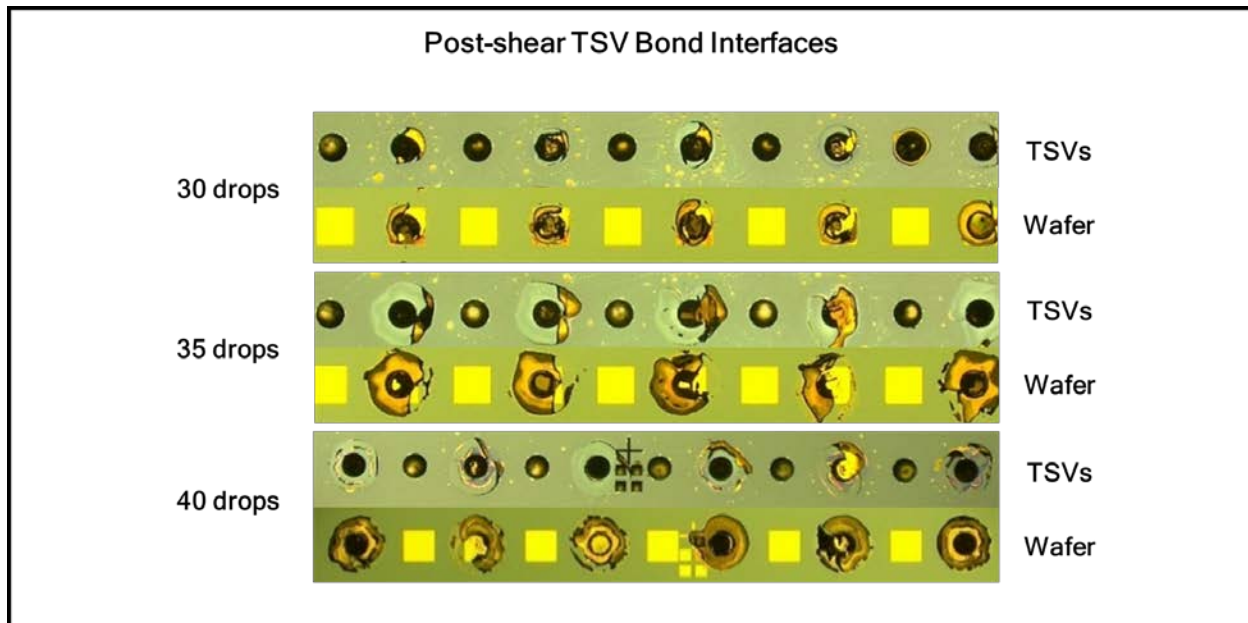


Figure 5.13. Post-shear bond interfaces for die-to-wafer bonded TSV arrays.

#### D. Mechanical and Electrical Properties

As described earlier, mechanical and electrical tests were conducted using die shear tests and probing daisy-chained structures, respectively. In order to extract the average shear properties of a single filled, bumped, and bonded TSV, arrays of TSVs were printed and bonded to pre-patterned bond pads on a silicon wafer. Figure 5.14 shows the die shear test schematic and the results of shear testing multiple 12-by-12 arrays. The best performance achieved was 1.9 kg<sub>f</sub> for the entire array, or an average pillar shear resistance of 13.2 g<sub>f</sub> per bond or approximately 1.68 mg/μm<sup>2</sup> per bond.

Finally, electrical tests were performed using the daisy-chain structures described previously. Figure 5.15 shows intermediate and complete processing results for post-bonding processes. The ultimate structure was intended to have daisy-chained bonds along the entire perimeter of the die. However, as can be seen, the metal deposition process was not perfectly optimized, resulting in incomplete bonds along the perimeter. Despite this shortcoming, it was possible to measure bonds pairwise. The highest performance achieved in the bumped and bonded TSVs was 35 mΩ per bond. Using a 100 μm tall, 50 μm diameter cylinder as a model for the geometry of the TSV, this is equivalent to approximately 300 μΩ-cm, or roughly ten times lower conductivity that freestanding pillars.

The table in Figure 5.15c summarizes a comparison of measured results for mechanical and electrical performance of both pillars and TSVs fabricated with Harima NPG-J. While the overall shear strength of the die is high, the shear strength per bond is much

lower than shear strength observed in printed pillars, similar to the lower electrical performance observed in the TSVs. There are a few likely explanations. First, due to bond profile restrictions, only 10 minute bond profiles were used for simultaneous bonding and sintering at 250 °C. Second, because the TSV is a confined structure, sintering within this structure will likely not proceed in the same manner as sintering in freestanding pillars. Namely, there is a higher likelihood that diffusion of the encapsulant material will be further restricted by the geometry of the structure. This may result in lower performance at similar sintering time and temperature profiles.

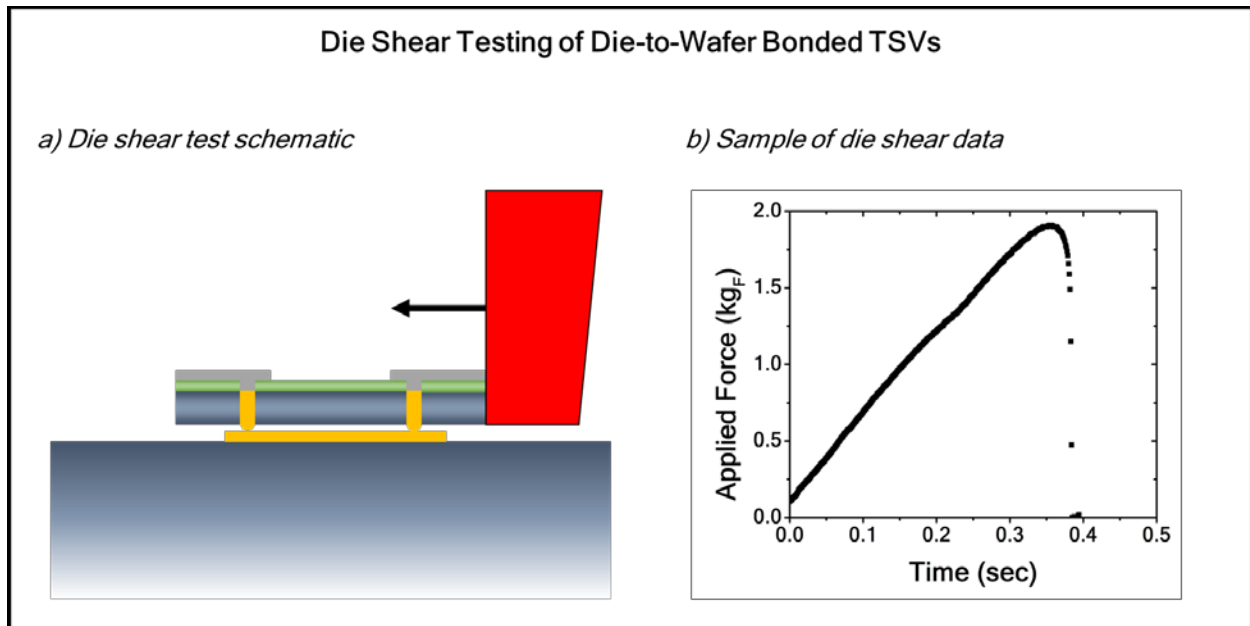


Figure 5.14. Die-shear testing of die-to-wafer bonded TSV arrays.

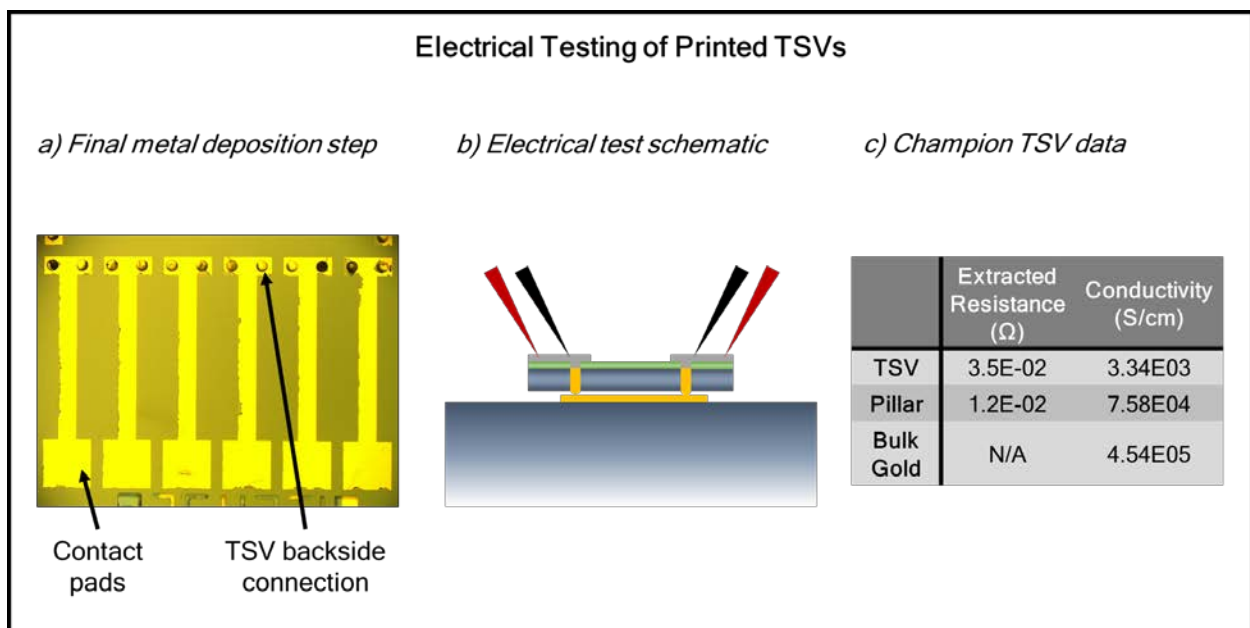


Figure 5.15. Optical images of fully-processed TSVs used in electrical testing.

### 5.3. Summary

TSVs represent the most likely route to heterogeneous chip stacking, a technological capability that promises to continue advancing the performance of integrated circuits while maintaining thin profiles and small footprints. However, because the TSV process and materials development is still in the early stages, plenty of room exists for the exploration of applying inkjet printing processes to TSV filling and bumping process flows.

Using a process based on the same three-dimensional printing process developed for freestanding pillars, robust TSVs have been demonstrated using a commercial gold nanoparticle inkjet ink as the interconnect metal. While the performance of the printed TSVs described is not as high as printed pillars fabricated with the same ink, the ability to use inkjet printing and metal nanoparticle inks to successfully fill and bump TSVs in a single process step is a significant result. As will be discussed in the final chapter of this dissertation, there are many areas primed for improvement. However, this process, when combined with low density TSV arrays, has the potential to dramatically reduce the process costs for integrating and stacking multiple chips onto each other.

## Chapter 6. Conclusions and Outlook

---

This dissertation has thoroughly explored many aspects of inkjet printing as well as the direct application of inkjet printing material and processes to the semiconductor packaging industry. This final chapter will review the primary results and conclusions of each of the main subjects addressed within this dissertation as well as include a brief discussion on the future outlook of each subject.

## 6.1. Nanoparticle-based Ink Formulation

### 6.1.1. Review

The first subject of this work is the development of a systematic protocol for design custom nanoparticle-based inks. As opposed to commercial inks, custom inks provide the benefit of a) having complete control over the contents of the ink and b) the potential for introducing new materials to the inkjet printing arena. Unfortunately, the design of nanoparticle inks has long been considered an art, and therefore a protocol for even basic ink formulation was not readily available until this work was completed.

While ink designers should consider the interactions of the ink with both the nozzle (jetting) and the substrate (wetting), the ink design strategy presented focused only on the jetting aspect of ink formulation. This is primarily because jetting can be considered a limiting function, i.e. without a reliably jetting ink, modulation and design of the wetting characteristics of the ink on a substrate is not possible.

In order to develop this strategy, both the ink formulation and ink characterization required standardization. With regard to ink formulation, all inks must be thoroughly tested with *ex situ* methods to determine the critical fluid properties that affect jetting, viscosity, surface tension, and density. Special care must also be taken to be aware of any shear rate viscosity dependence, i.e. non-Newtonian behavior. With regard to characterization, the pulse waveform of each ink tested should be first optimized to maximize the drop momentum as opposed to drop velocity because this normalizes for any issues related to pressure difference within and across ink formulations. Then, the drop velocity and volume must be measured in order to derive two dimensionless parameters,  $Ca$  and  $We$ , which can be used to describe the jetting behavior of one ink relative to another.

Finally, methods for modulating the jettability of an ink were introduced based on co-solvent addition and nanoparticle loading. Both of these methods prove to be very useful in altering an inks jettability, and are therefore the primary means of adjusting an inks composition in a systematic manner aimed at creating reliable jetting. This systematic procedure is the main product of this body of work.

### 6.1.2. Future Work

As described earlier, the procedure developed is a powerful tool for ink formulation and may have a large impact in guiding the design for custom inkjet inks in research and development level settings. However, this procedure focuses primarily on the development of ink formulations based on the interactions of the ink with the nozzle alone. Future work in this area should extend ink development to include the interaction between the ink and the substrate as well. Due to the nature of printed electronics, various substrates should be considered, including rigid silicon as well as plastics commonly used to fabricate flexible electronic devices.

Furthermore, the ink formulation procedure developed thus far knowingly excludes additional components such as surfactants and other additives that are common in commercial ink formulations. These components may be added for a number of

reasons, some of which may be more related to the ink-substrate interaction as opposed to the ink-nozzle interaction. Regardless of their application, it is widely accepted that additional ink components are necessary for deriving optimal ink performance. Therefore, an additional extension to this body of work which includes the incorporation of these components is logical next step.

Finally, the work included here is limited to strictly metal nanoparticle inks. A clear expansion of this work would include the investigation of alternative materials relevant to printed electronics, such as metal oxide nanoparticles for semiconductors or dielectrics as well as alternative conductive materials such as carbon nanotubes.

## 6.2. Heuristic Optimization of Nanoparticle Solubility and Chemistry

### 6.2.1. Review

The second body of work presented in this dissertation is related to a subset of the ink design process, metal nanoparticle solubility. Both increasing metal nanoparticle solubility as well as understanding the how nanoparticle solubility is affected by the encapsulant composition were the goals of this work. In order to achieve this practical goal and gain this insight, however, a large number of experimental observations are necessary.

Therefore, a heuristic search algorithm based on a genetic algorithm called NSGA-II was applied to the discovery of desirable metal nanoparticles. One of the benefits of the NSGA-II algorithm is its inherent capability to optimize systems based on multiple criteria. For the nanoparticle optimization described, the two criteria selected were nanoparticle solubility and nanoparticle carbon content. The goal was to increase solubility while decreasing carbon content.

Because metal nanoparticle syntheses are not very fast processes, the silver nanoparticle synthesis targeted for optimization was first adapted to a high-throughput, robotically-controlled synthesis. In addition, high-throughput protocols based on UV-Vis and TGA were developed in order to successfully produce large populations of synthetic conditions in a very short period. In this way, the combination of high-throughput synthesis and analysis was responsible for enabling the practical application genetic algorithm to this synthetic optimization.

Ultimately, in only three generations, the nanoparticle system exhibited a maximum boost in solubility of nearly 10%, and the minimum bound carbon content was also decreased to approximately 25% of the total nanoparticle mass.

### 6.2.2. Future Work

These optimized results are very exciting because they both indicate that genetic algorithms are an effective means of nanoparticle discovery and they produced a very practical nanoparticle system for inkjet printing applications. Unfortunately, though, further investigation into the cause for solubility was not completed. These types of studies often require low-throughput or challenging techniques such as TEM, STM, and NMR. It is not practical to include these techniques in a high-throughput process because they would act as a bottleneck. Therefore, developing models for solubility as a function of encapsulant composition and structure would be an exciting next step.

Initial studies based on observations of individual synthetic conditions that produce very different solubilities may help guide initial results. For example, understanding if encapsulant composition shifts result in changes in encapsulant organization on the nanoparticle surface is an important relationship to understand. Furthermore, while the nanoparticle size distribution should nominally not be strongly affected by the synthetic conditions tested in this work, it is possible that even slight changes in nanoparticle size (and therefore radius of curvature and encapsulant organization) may affect the ultimate solubility.

Finally, extending the solubility study to include alternative solvents as well as alternative encapsulants may help elucidate the relationship between encapsulant composition and nanoparticle solubility. For example, solvents such as toluene and short-chain alkanes are highly successful at suspending these nanoparticles. In addition, branched alkyl chains may also improve the solubility of nanoparticles while helping further reduce the total carbon content. Performing these studies using the same genetic algorithm approach may yet again result in the rapid identification of high performing materials.

## 6.3. Three-dimensional Inkjet Printing for Semiconductor Packages

### 6.3.1. Review

The final two chapters of this dissertation explored two new applications for inkjet printing within the arena of semiconductor packaging: solder bump replacement and TSV filling. The expected benefits of introducing inkjet printing to packaging are twofold. First, inkjet printing may present a cost reduction due to the additive nature of the process. Second, inkjet printing allows for the direct incorporation of novel materials such as metal nanoparticles. The challenges for this project were the process development for three-dimensional printing of these metal nanoparticles as well as the characterization of these materials with regard to their electrical and mechanical performance when compared to conventional processes.

The process developed for three-dimensional printing is a very useful contribution to the inkjet printing community because it identifies the fundamental controls for three-dimensional printing of inks: substrate temperature and jetting frequency. The identification of these important controls will inform the future design of inks more amenable to three-dimensional printing, and were sufficient to permit the custom design of inks described within this dissertation.

With regard to the applications targeted, both pillar and TSV structures were successfully fabricated and characterized. For pillars, the electrical and mechanical properties achieved outperformed conventional materials. The TSV performance presented was acceptable for initial process development, but further work in either process or material optimization is needed to improve TSV performance. Finally, this body of work included the first in-depth study of the mechanics of sintering in very thick structures comprised of metal nanoparticles. A basic model for sintering was presented based on advanced characterization techniques for pillar sintered on hotplates. The results indicate there may be a performance limitation of the materials due to an unavoidable inclusion of carbon-based encapsulant within the structures.

### 6.3.2. Future Work

With regard to both the pillar printing process as well as the TSV filling and bumping process, there are many avenues for future research and development. With respect to the pillar process, although the process proved to be very repeatable, a study investigating the underlying mechanism that dictates the growth of three-dimensional features using these materials would be of huge interest to the community. While the jetting frequency and substrate temperature are clearly important process parameters, a deeper exploration into the material and fluid properties of the ink may help generalize the process to other inks. Indeed, establishing a pillar process for copper nanoparticle inks would also be an industrially-relevant material system worth pursuing.

For both the pillar and TSV processes alike, alternative sintering techniques such as laser or microwave processes and their effects on the electrical and mechanical performance of the structures should be considered. Furthermore, investigation into the bonding of the features is also necessary. Because these structures contain both metal and carbon, the development of robust bonding techniques and advanced analysis of

the bonds created will be very important to understand. Investigating the relationship between the already-deposited metallization layer and the printed structure as a function of bond conditions such as time, temperature, and force would be solid initial study.

Finally, with respect to the TSV process alone, the current process was pushed to only a 70  $\mu\text{m}$  critical dimension as the most extreme process attempted. Further scaling of the process to smaller critical dimensions should be possible through scaling of the nozzle dimension, though this work has yet to be completed. In addition, the application of custom inks should also be considered in order to further boost performance of these structures.

## 6.4. Conclusion

An ever-present motivation for this entire work is the exploration of inkjet printing and metal nanoparticles as alternative processes and materials for electronics manufacturing. Much like the historical progression of the electronics industry, the advancement of these processes and materials require specific advances in a broad set of subjects such as chemistry, materials science, electrical engineering, etc. While this may seem to be a daunting task on the surface, the potential for printed electronics to have a large impact on the electronics industry as a whole is still very high. The key to realizing this impact, however, is in the narrowing of the applications and materials targeted for advancement. Metal nanoparticle inks represent perhaps one of the simplest inks to be applied in printed processing because their goal and optimization is always the same: to be conductive. In addition, the application of inkjet printing as a potentially disruptive process for the electronics industry will require that resolution of inkjet printing should overlap strongly with the processes it should replace. In that way, packaging applications make a strong case for the call to new, cheaper processing via inkjet printing. Though it will take focused efforts on many fronts, the future of printed electronics remains bright.

# References

---

- [1] R. Tummala, E. J. Rymaszewski and A. G. Klopfenstein, *Microelectronics Packaging Handbook*, Springer US, 1997.
- [2] K. B. Unchwaniwala and M. F. Caggiano, "Electrical Analysis of IC Packaging with Emphasis on Different Ball Grid Array Packages," in *Electronic Components and Technology Conference*, Orlando, FL, 2001.
- [3] G. S. Baghria, N. Kumar, D. Sharma and S. Kalra, "Die bonding techniques and methods," *EE Times*, 9 July 2012. [Online]. Available: [http://www.eetimes.com/document.asp?doc\\_id=1279750](http://www.eetimes.com/document.asp?doc_id=1279750). [Accessed 22 September 2015].
- [4] P. Elenius and L. Levine, "Comparing Flip-Chip and Wire-Bond Interconnection Technologies," *Chip Scale Review*, pp. 81-87, July/August 2000.
- [5] G. E. Moore, "Cramming more components onto integrated circuits," *Electronics*, vol. 38, no. 8, pp. 114-117, 1965.
- [6] M. Lee, M. Yoo, J. Cho, S. Lee, J. Kim, C. Lee, D. Kang, C. Zwenger and R. Lanzone, "Study of Interconnection Process for Fine Pitch Flip Chip," in *Electronic Components and Technology Conference*, San Diego, CA, 2009.
- [7] S. Savastiouk, "Moore's Law--The Z Dimension," *Solid State Technology*, p. 84, January 2000.
- [8] Fujifilm USA, "Printheads," Fujifilm USA, 2015. [Online]. Available: [http://www.fujifilmusa.com/products/industrial\\_inkjet\\_printheads/print-products/printheads/index.html#See\\_All](http://www.fujifilmusa.com/products/industrial_inkjet_printheads/print-products/printheads/index.html#See_All). [Accessed 29 05 2015].
- [9] B. Derby, "Inkjet Printing of Functional and Structural Materials: Fluid Property Requirements, Feature Stability, and Resolution," *Annu. Rev. Mater. Res.*, vol. 40, pp. 395-414, 2010.
- [10] H. Wijschoff, "The dynamics of the piezo inkjet printhead operation," *Physics Reports*, vol. 491, no. 4-5, pp. 77-177, 2010.
- [11] J.-U. Park, M. Hardy, S. J. Kang, K. Barton, K. Adair, D. K. Mukhopadhyay, C. Y. Lee, M. S. Strano, A. G. Alleyne, J. G. Georgiadis, P. M. Ferreira and J. A. Rogers, "High-resolution electrohydrodynamic jet printing," *Nature Materials*, vol. 6, pp. 782-789, 2007.
- [12] G. Taylor, "Disintegration of Water Drops in and Electric Field," *Proceedings of the Royal Society of London, Series A, Mathematical and Physiscal Sciences*, vol. 280, no. 1382, pp. 383-397, 1964.
- [13] P. Hoisington and D. A. Gardner, "Ink jet printing". United States of America Patent US8708441 B2, 2005.
- [14] W. H. Kim, A. J. Makinen, N. Nikolov, R. Shashidhar, H. Kim and Z. H. Kafafi, "Molecular organic light-emitting diodes using highly conducting polymers as anodes," *Applied Physics Letters*, vol. 80, no. 20, pp. 3844-3846, 2002.
- [15] Y. H. Kim, C. Sachse, M. L. Machala, C. May, L. Muller-Meskamp and K. Leo, "Highly Conductive PEDOT:PSS Electrode with Optimized Solvent and Thermal

- Post-Treatment for ITO-Free Organic Solar Cells," *Advanced Functional Materials*, vol. 21, no. 6, pp. 1076-1081, 2011.
- [16] M. Brust, M. Walker, D. Bethell, D. J. Schiffrin and R. Whyman, "Synthesis of thiol-derivatised gold nanoparticles in a two-phase Liquid-Liquid system," *Journal of the Chemical Society, Chemical Communications*, no. 7, pp. 801-802, 1994.
- [17] Y. Li, Y. Wu and B. S. Ong, "Facile Synthesis of Silver Nanoparticles Useful for Fabrication of High-Conductivity Elements for Printed Electronics," *Journal of the American Chemical Society*, vol. 127, no. 10, pp. 3266-3267, 2005.
- [18] A. Kamyshny, J. Steinke and S. Magdassi, "Metal-based Inkjet Inks for Printed Electronics," *The Open Applied Physics Journal*, vol. 4, pp. 19-36, 2011.
- [19] J. Perelaer, P. J. Smith, D. Mager, D. Soltman, S. K. Volkman, V. Subramanian, J. G. Korvink and U. S. Schubert, "Printed electronics: the challenges involved in printing devices, interconnects, and contacts based on inorganic materials," *Journal of Materials Chemistry*, vol. 20, pp. 8446-8453, 2010.
- [20] H. Siringhaus, T. Kawase, R. H. Friend, T. Shimoda, M. Inbasekaran, W. Wu and E. P. Woo, "High-Resolution Inkjet Printing of All-Polymer Transistor Circuits," *Science*, vol. 290, no. 5499, pp. 2123-2126, 2000.
- [21] W. Cao and J. Xue, "Recent progress in organic photovoltaics: device architecture and optical design," *Energy and Environmental Science*, vol. 7, pp. 2123-2144, 2014.
- [22] B. Geffroy, P. I. Roy and C. Prat, "Organic light-emitting diode (OLED) technology: materials, devices, and display technologies," *Polymer International*, vol. 55, pp. 572-582, 2006.
- [23] K. Nomura, H. Ohta, K. Ueda, T. Kamiya, M. Hirano and H. Hosono, "Thin-Film Transistor Fabricated in Single-Crystalline Transparent Oxide Semiconductor," *Science*, vol. 300, no. 5623, pp. 1269-1272, 2003.
- [24] S. T. Meyers, J. T. Anderson, C. M. Hung, J. Thompson, J. F. Wager and D. A. Keszler, "Aqueous Inorganic Inks for Low-Temperature Fabrication of ZnO TFTs," *Journal of the American Chemical Society*, vol. 130, no. 51, pp. 17603-17609, 2008.
- [25] D.-H. Lee, S.-Y. Han, G. S. Herman and C.-h. Chang, "Inkjet printed high-mobility indium zinc tin oxide thin film transistors," *Journal of Materials Chemistry*, vol. 19, pp. 3135-3137, 2009.
- [26] H. Klauk, M. Halik, U. Zschieschang, G. Schmid and W. Radlik, "High-mobility polymer gate dielectric pentacene thin film transistors," *Journal Of Applied Physics*, vol. 92, no. 9, pp. 5259-5263, 2002.
- [27] P. Vicca, S. Steudel, S. Smout, A. Raats, J. Genoe and P. Heremans, "Low-temperature-cross-linked poly(4-vinylphenol) gate-dielectric for organic thin film transistors," *Thin Solid Films*, vol. 519, no. 1, pp. 391-393, 2010.
- [28] G. Adamopoulos, S. Thomas, P. H. Wobkenberg, D. D. C. Bradley, M. A. McLachlan and T. D. Anthopoulos, "High-Mobility Low-Voltage ZnO and Li-Doped ZnO Transistors Based on ZrO<sub>2</sub> High-k Dielectric Grown by Spray Pyrolysis in Ambient Air," *Advanced Materials*, vol. 23, no. 16, pp. 1894-1898, 2011.
- [29] K.-k. Han and S. Seo, "Fabrication of Sol-Gel Alumina Dielectric for Low-Voltage

- Operating Pentacene Transistor," *Japanese Journal of Applied Physics*, vol. 50, p. 04DK17, 2011.
- [30] P. Calvert, "Inkjet Printing for Materials and Devices," *Chemical Materials*, vol. 13, pp. 3299-3305, 2001.
- [31] D. Huang, F. Liao, S. Molesa, D. Redinger and V. Subramanian, "Plastic-Compatible Low Resistance Gold Nanoparticle Conductors for Flexible Electronics," *Journal of the Electrochemical Society*, vol. 150, no. 7, pp. G412-G417, 2003.
- [32] S. E. Molesa, S. K. Volkman, D. R. Redinger, A. d. I. F. Vornbrock and V. Subramanian, "A high-performance all-inkjetted organic transistor technology," in *International Electron Devices Meeting*, San Francisco, Ca, 2004.
- [33] B. S. Cook, J. R. Cooper and M. M. Tentzeris, "Multi-Layer RF Capacitors on Flexible Substrates Utilizing Inkjet Printed Dielectric Polymers," *IEEE Microwave And Wireless Components Letters*, vol. 23, no. 7, pp. 353-355, 2013.
- [34] S. Wunscher, R. Abbel, J. Perelaer and U. S. Schubert, "Progress of alternative sintering approaches of inkjet-printed metal inks and their application for manufacturing of flexible electronic devices," *Journal of Materials Chemistry C*, vol. 2, pp. 10232-10261, 2014.
- [35] J. Perelaer, B.-J. d. Gans and U. S. Schubert, "Inkjet Printing and Microwave Sintering of Conductive Silver Tracks," *Advanced Materials*, vol. 18, no. 16, pp. 2101-2114, 2006.
- [36] S. K. Volkman, S. Molesa, B. Mattis, P. C. Chang and V. Subramanian, "Inkjetted Organic Transistors Using a Novel Pentacene Precursor," in *MRS Proceedings*, San Francisco, CA, 2003.
- [37] S. Molesa, D. R. Redinger, D. C. Huang and V. Subramanian, "High-quality inkjet-printed multilevel interconnects and inductive components on plastic for ultra-low-cost RFID applications," in *MRS Proceedings*, San Francisco, CA, 2003.
- [38] H.-Y. Tseng and V. Subramanian, "All inkjet-printed, fully self-aligned transistors for low-cost circuit applications," *Organic Electronics*, vol. 12, no. 2, pp. 249-256, 2011.
- [39] T. Kaydanova, M. F. A. M. v. Hest, A. Miedaner, C. J. Curtis, J. L. Alleman, M. S. Dabney, E. Garnet, S. Shaheen, L. Smith, R. Collins, J. I. Hanoka, A. M. Gabor and D. S. Ginley, "Direct Write Contacts for Solar Cells," in *Photovoltaic Specialists Conference*, Lake Buena Vista, FL, 2005.
- [40] A. Rida, L. Yang, R. Vyas and M. M. Tentzeris, "Conductive Inkjet-Printed Antennas on Flexible Low-Cost Paper-Based Substrates for RFID and WSN Applications," *IEEE Antennas and Propagation Magazine*, vol. 51, no. 3, pp. 13-23, 2009.
- [41] M. J. Hostetler, J. E. Wingate, C.-J. Zhong, J. E. Harris, R. W. Vachet, M. R. Clark, D. Londono, S. J. Green, J. J. Stokes, G. D. Wignall, G. L. Glish, M. D. Porter, N. D. Evans and R. W. Murray, "Alkanethiolate Gold Cluster Molecules with Core Diameters from 1.5 to 5.2 nm: Core and Monolayer Properties as a Function of Core Size," *Langmuir*, vol. 14, no. 1, pp. 17-30, 1998.
- [42] P. Buffat and J.-P. Borel, "Size effect on melting temperature of gold particles,"

- Physical Review A*, vol. 13, no. 6, pp. 2287-2298, 1976.
- [43] P. Pawlow, *Zeitschrift fur Physikalische Chemie*, vol. 65, no. 1, p. 545, 1909.
- [44] H. Gronbeck, A. Curioni and W. Andreoni, "Thiols and Disulfides on the Au(111) Surface: The Headgroup-Gold Interaction," *Journal of the American Chemical Society*, vol. 122, pp. 3839-3842, 2000.
- [45] V. Romanov, C.-K. Siu, U. H. Verkerk, H. E. Aribi, A. C. Hopkinson and K. W. M. Siu, "Binding Energies of the Silver Ion to Alcohols and Amides: A Theoretical and Experimental Study," *Journal of Physical Chemistry A*, vol. 112, pp. 10912-10920, 2008.
- [46] J. R. Greer and R. A. Street, "Thermal cure effects on electrical performance of nanoparticle silver inks," *Acta Materialia*, vol. 55, no. 18, pp. 6345-6349, 2007.
- [47] J. E. Fromm, "Numerical Calculations of the Fluid Dynamics of Drop-on-Demand Jets," *IBM Journal of Research Development*, vol. 28, no. 3, pp. 322-333, 1984.
- [48] B. Derby and N. Reis, "Inkjet Printing of Highly Loaded Particulate Suspensions," *MRS Bulletin*, vol. 28, no. 11, pp. 815-818, 2003.
- [49] T. Young, "An Essay on the Cohesion of Fluids," *Philosophical Transactions of The Royal Society of London*, vol. 95, pp. 65-87, 1805.
- [50] R. D. Deegan, O. Bakajin, T. F. Dupont, G. Huber, S. R. Nagel and T. A. Witten, "Capillary flow as the cause of ring stains from dried liquid drops," *Nature*, vol. 389, pp. 827-829, 1997.
- [51] D. Soltman and V. Subramanian, "Inkjet-Printed Line Morphologies and Temperature Control of the Coffee Ring Effect," *Langmuir*, vol. 24, no. 5, pp. 2224-2231, 2008.
- [52] H. Hu and R. G. Larson, "Marangoni Effect Reverses Coffee-Ring Deposition," *The Journal of Physical Chemistry B*, vol. 110, pp. 7090-7094, 2006.
- [53] E. L. Talbot, A. Berson and C. D. Bain, "Drying and Deposition of Picolitre Droplets of Colloidal Suspensions in Binary Solvent Mixtures," in *International Conference on Digital Printing Technologies and Digital Fabrication*, Springfield, VA, 2012.
- [54] R. Bhardwaj, X. Fang and D. Attinger, "Pattern formation during the evaporation of a colloidal nanoliter drop: a numerical and experimental study," *New Journal of Physics*, vol. 11, p. 075020, 2009.
- [55] MicroFab Technologies, Inc., "Ink-Jet Microdispenser," MicroFab Technologies, Inc., [Online]. Available: <http://www.microfab.com/a-basic-ink-jet-microdispensing-setup/basicsetup-ink-jet-microdispenser>. [Accessed 28 August 2015].
- [56] Konica Minolta, "Inkjet Print Head," Konica Minolta, 2015. [Online]. Available: <http://www.konicaminolta.com/inkjet/inkjethead/>. [Accessed 28 August 2015].
- [57] Xaar, "Xaar Printhead Matrix," Xaar, 14 September 2012. [Online]. Available: <http://www.xaar.com/en/MediaDocuments/Printhead-Matrix-Sept14.pdf>. [Accessed 28 August 2015].
- [58] D. B. Bogy and F. E. Talke, "Experimental and Theoretical Study of Wave Propagation Phenomena in Drop-on-Demand Ink Jet Devices," *IBM Journal and Research and Development*, vol. 28, no. 3, pp. 314-321, 1984.
- [59] H. Y. Gan, X. Shan, T. Eriksson, B. K. Lok and Y. C. Lam, "Reduction of droplet

- volume by controlling actuating waveforms in inkjet printing for micro-pattern formation," *Journal of Micromechanics and Microengineering*, vol. 19, p. 055010, 2009.
- [60] MicroFab Technologies, Inc., "MicroFab Technote 99-03 Drive Waveform Effects on Ink-Jet Device Performance," 30 September 1999. [Online]. Available: <http://www.microfab.com/images/pdfs/technote99-03.pdf>. [Accessed 28 August 2015].
- [61] H. Wijsschoff, "Structure- and Fluid-Dynamics in Piezo Inkjet Printheads," Herman Wijsschoff, Océ Technologies B.V., Venlo, Venlo, The Netherlands, 2008.
- [62] D. Jang, D. Kim and J. Moon, "Influence of Fluid Physical Properties on Inkjet Printability," *Langmuir*, vol. 25, pp. 2629-2635, 2009.
- [63] MicroFab Technologies, Inc., "Microdispensing," MicroFab Technologies, Inc., [Online]. Available: <http://www.microfab.com/biomedical/microdispensing>. [Accessed 31 August 2015].
- [64] P. Wilson, C. Lekakou and J. F. Watts, "Systematic Design and Process Optimization for the Inkjet Printing of PEDOT:Poly(styrenesulfonate)," *Journal of Micro- and Nano-Manufacturing*, vol. 2, p. 011004, 2014.
- [65] N. Reis and B. Derby, "Ink Jet Deposition of Ceramic Suspensions: Modeling and Experiments of Droplet Formation," in *MRS Proceedings*, San Francisco, CA, 2000.
- [66] J. Tai, H. Y. Gan, Y. N. Liang and B. K. Lok, "Control of Droplet Formation in Inkjet Printing Using Ohnesorge Number Category: Materials and Processes," in *Electronic Packaging Technology Conference*, Singapore, 2008.
- [67] N. J. Wagner and J. F. Brady, "Shear thickening in colloidal dispersion," *Physics Today*, vol. 62, no. 10, pp. 27-32, 2009.
- [68] C. E. Stauffer, "The Measurement of Surface Tension by the Pendant Drop Technique," *The Journal of Physical Chemistry*, vol. 69, no. 6, pp. 1933-1938, 1965.
- [69] B. Song and J. Springer, "Determination of Interfacial Tension from the Profile of a Pendant Drop Using Computer-Aided Image Processing: Theoretical," *Journal of Colloid and Interface Sciences*, vol. 184, pp. 64-76, 1996.
- [70] B. Song and J. Springer, "Determination of Interfacial Tension from the Profile of a Pendant Drop Using Computer-Aided Image Processing: Experimental," *Journal of Colloid and Interface Science*, vol. 184, pp. 77-91, 1996.
- [71] S. Fordham, "On the Calculation of Surface Tension from Measurements of Pendant Drops," *Proceedings of the Royal Society of London A*, vol. 194, pp. 1-16, 1948.
- [72] H. Dong, W. W. Carr and J. F. Morris, "Experimental study of drop-on-demand drop formation," *Physics of Fluids*, vol. 18, p. 072102, 2006.
- [73] B. Derby, "Inkjet printing ceramics: From drops to solid," *Journal of the European Ceramic Society*, vol. 31, no. 14, pp. 2543-2550, 2011.
- [74] E. Kim and J. Baek, "Numerical study on the effects of non-dimensional parameters on drop-on-demand droplet formation dynamics and printability range in the up-scaled model," *Physics of Fluids*, vol. 24, p. 082103, 2012.

- [75] M.-H. Tsai and W.-S. Hwang, "Effects of Pulse Voltage on the Droplet Formation of Alcohol and Ethylene Glycol in a Piezoelectric Inkjet Printing Process with Bipolar Pulse," *Materials Transactions*, vol. 49, no. 2, pp. 331-338, 2008.
- [76] K. A. M. Seerden, N. Reis, J. R. G. Evans, P. S. Grant, J. W. Halloran and B. Derby, "Ink-Jet Printing of Wax-Based Alumina Suspensions," *Journal of the American Chemical Society*, vol. 84, no. 11, pp. 2514-2520, 2001.
- [77] S. Nath, S. Jana, M. Pradhan and T. Pal, "Ligand-stabilized metal nanoparticles in organic solvent," *Journal of Colloid and Interface Science*, vol. 341, pp. 333-352, 2010.
- [78] K. D. Sattler, *Handbook of Nanophysics: Nanoparticle and Quantum Dots*, CRC Press, 2010.
- [79] H. C. Hamaker, "The London-van der Waals attraction between spherical particles," *Physica*, vol. 4, no. 10, pp. 1058-1072, 1937.
- [80] E. M. Lifshitz, "The Theory of Molecular Attractive Forces between Solids," *Journal of Experimental Theoretical Physics*, vol. 2, no. 1, pp. 73-84, 1956.
- [81] E. Oh, K. Susumu, R. Goswami and H. Mattoussi, "One-Phase Synthesis of Water-Soluble Gold Nanoparticles with Control over Size and Surface Functionalities," *Langmuir*, vol. 26, no. 10, pp. 7604-7613, 2010.
- [82] J. A. Tullman, W. F. Finney, Y.-J. Lin and S. W. Bishnoi, "Tunable Assembly of Peptide-coated Gold Nanoparticles," *Plasmonics*, vol. 2, no. 3, pp. 119-127, 2007.
- [83] M. G. Warner, S. M. Reed and J. E. Hutchison, "Small, Water-Soluble, Ligand-Stabilized Gold Nanoparticles Synthesized by Interfacial Ligand Exchange Reactions," *Chemistry of Materials*, vol. 12, no. 11, pp. 3316-3320, 2000.
- [84] M. L. Huggins, "Solutions of Long Chain Compounds," *Journal of Chemical Physics*, vol. 9, p. 440, 1941.
- [85] P. J. Flory, "Thermodynamics of High Polymer Solutions," *Journal of Chemical Physics*, vol. 10, pp. 51-61, 1942.
- [86] A. M. Jackson, J. W. Myerson and F. Stellacci, "Spontaneous assembly of subnanometre-ordered domains in the ligand shell of monolayer-protected nanoparticles," *Nature Materials*, vol. 3, pp. 330-336, 2004.
- [87] J. W. Myerson, "Anomalous solubility behavior of mixed monolayer protected metal nanoparticles," 2005.
- [88] K. Wang, "Effect of Multiple Alkanethiol Ligands on Solubility and Sintering Temperature of Gold Nanoparticles," 2010.
- [89] A. Centrone, E. Penzo, M. Sharma, J. W. Myerson, A. M. Jackson, N. Marzari and F. Stellacci, "The role of nanostructure in the wetting behavior of mixed-monolayer-protected metal nanoparticles," *Proceedings of the National Academy of Sciences of the United States of America*, vol. 105, no. 29, pp. 9886-9891, 2008.
- [90] Y. Cesbron, C. P. Shaw, J. P. Birchall, P. Free and R. Levy, "Strip Nanoparticles Revisited," *Small*, vol. 8, no. 24, pp. 3714-3719, 2012.
- [91] M. Yu and F. Stellacci, "Response to "Stripy Nanoparticles Revisited"," *Small*, vol. 8, no. 24, pp. 3720-3726, 2012.

- [92] J. Stirling, I. Lekkas, A. Sweetman, P. Djuranovic, Q. Guo, B. Pauw, J. Granwehr, R. Levy and P. Moriarty, "Critical Assessment of the Evidence for Striped Nanoparticles," *PLoS ONE*, vol. 9, no. 11, p. e108482, 2014.
- [93] G. E. P. Box and K. B. Wilson, "On the Experimental Attainment of Optimum Conditions," *Journal of the Royal Statistical Society. Series B (Methodological)*, vol. 13, no. 1, pp. 1-45, 1951.
- [94] M. J. Alvarez, L. Ilzarbe, E. Viles and M. Tanco, "The Use of Genetic Algorithms in Response Surface Methodology," *Quality Technology and Quantitative Management*, vol. 6, no. 3, pp. 295-307, 2008.
- [95] J. Holland, *Adaptation in Natural and Artificial Systems*, Ann Arbor, MI: The University of Michigan Press, 1975.
- [96] K. Deb, A. Pratap, S. Agarwal and T. Meyarivan, "A Fast and Elitist Multobjective Genetic Algorithm: NSGA-II," *IEEE Transactions on Evolutionary Computation*, vol. 6, no. 2, pp. 182-197, 2002.
- [97] F. Y. Cheng and D. Li, "Multiobjective Optimizaiton of Structures with and Without Control," *Journal of Guidance, Control, and Dynamics*, vol. 19, no. 2, pp. 392-397, 1996.
- [98] D. F. Swinehart, "The Beer-Lambert Law," *Journal of Chemical Education*, vol. 39, no. 7, pp. 333-335, 1962.
- [99] The International Technology Roadmap for Semiconductors, "Assembly and Packaging," 2012.
- [100] Microsemi, "Standard Reflow Profile for Standard and Lead-Free Packages," April 2012. [Online]. Available: [http://www.microsemi.com/document-portal/doc\\_view/131105-solder-reflow-leadfree](http://www.microsemi.com/document-portal/doc_view/131105-solder-reflow-leadfree). [Accessed 24 August 2015].
- [101] National Institute of Standards and Technology, "Database for Solder Properties with Emphasis on New Lead-Free Solders," 11 February 2012. [Online]. Available: [http://www.msed.nist.gov/solder/NIST\\_LeadfreeSolder\\_v4.pdf](http://www.msed.nist.gov/solder/NIST_LeadfreeSolder_v4.pdf). [Accessed 24 August 2015].
- [102] M. Gerber, C. Beddingfield, S. O'Connor, M. Yoo, M. Lee, D. Kang, S. Park, C. Zwenger, R. Darveaux, R. Lanzone and K. Park, "Next Generation Fine Pitch Cu Pillar Technology - Enabling Next Generation Silicon Nodes," in *IEEE Electronic Components and Technology Conference*, Lake Buena Vista, FL, 2011.
- [103] D. J. Hayes, W. R. Cox and M. E. Grove, "Micro-Jet Printing of Polymers and Solder for Electronics Manufacturing," *Journal of Electronics Manufacturing*, vol. 8, no. 3, pp. 209-216, 1998.
- [104] K. Murata, "Direct Fabrication of Super-Fine Wiring and Bumping by Using Inkjet Process," in *Polymers and Adhesives in Mircoelectronics and Photonics*, Odaiba, Tokyo, 2007.
- [105] J. A. Lewis, "Direct Ink Writing of 3D Functional Materials," *Advanced Functional Materials*, vol. 16, pp. 2193-2204, 2006.
- [106] S. H. Ko, J. Chung, N. Hotz, K. H. Nam and C. P. Grigoropolous, "Metal nanoparticle direct inkjet printing for low-temperature 3D micro metal sturcture fabrication," *Journal of Micromechanics and Microengineering*, vol. 20, no. 12, p. 125010, 2010.

- [107] Harima Chemicals Group, "R & D - New Functional Materials," Harima Chemicals Group, 2015. [Online]. Available: [https://www.harima.co.jp/en/randd/products/new\\_materials.html](https://www.harima.co.jp/en/randd/products/new_materials.html). [Accessed 24 August 2015].
- [108] W. C. Oliver and G. M. Pharr, "Measurement of hardness and elastic modulus by instrumental indentation: Advances in understanding and refinements to methodology," *Journal of Materials Research*, vol. 19, no. 1, pp. 3-20, 2005.
- [109] JEDEC, "JESD22-B117A Solder Ball Shear," JEDEC, 2014. [Online]. Available: [www.jedec.org/sites/default/files/docs/22b117A.pdf](http://www.jedec.org/sites/default/files/docs/22b117A.pdf). [Accessed 24 August 2015].
- [110] K. J. Puttlitz and K. A. Stalter, *Handbook of Lead-Free Solder Technology for Microelectronics Assemblies*, New York, NY: CRC Press, 2004.
- [111] R. Anderson and S. J. Klepeis, *Introduction to Focused Ion Beams*, Boston, MA: Springer, 2005.
- [112] D. R. Frear, J. W. Wang, J. K. Lin and C. Zhang, "Pb-Free Solders for Flip-Chip Interconnects," *Journal of Materials*, vol. 53, no. 6, pp. 28-32, 2001.
- [113] S. Speisshoefer, Z. Rahman, G. Vangara, S. Polamreddy, S. Burkett and L. Schaper, "Process integration for through-silicon vias," *Journal of Vacuum Science Technology A*, vol. 23, no. 4, pp. 824-829, 2005.
- [114] F. Laermer and A. Schilp, "A method for anisotropic etching of silicon". Germany Patent DE4241045 C1, 26 May 1992.
- [115] K. Takahashi and M. Sekiguchi, "Through Silicon Via and 3-D Wafer/Chip Stacking Technology," in *2006 Symposium on VLSI Circuits*, Honolulu, HI, 2006.
- [116] A.-C. Hsieh and T. Hwang, "TSV Redundancy: Architecture and Design Issues in 3-D IC," *IEEE Transaction on Very Large Scale Integration Systems*, vol. 20, no. 4, pp. 711-722, 2012.
- [117] A. P. Singulani, "Advanced Methods for Mechanical Analysis and Simulation of Through Silicon Vias," Vienna University of Technology, Vienna, Austria, 2014.
- [118] U. Kang, H.-J. Chung, S. Heo, D.-H. Park, H. Lee, J. H. Kim, S.-H. Ahn, S.-H. Cha, J. Ahn, D. Kwon, J.-W. Lee, H.-S. Joo, W.-S. Kim, D. H. Jang, N. S. Kim, J.-H. Choi, T.-G. Chung, J.-H. Yoo, J. S. Choi, C. Kim and Y.-H. Jun, "8 Gb 3-D DDR3 DRAM Using Through-Silicon-Via Technology," *IEEE Journal of Solid-State Circuits*, vol. 45, no. 1, pp. 111-119, 2010.
- [119] J. A. Burns, B. F. Aull, C.-L. Chen, C.-L. Chen, C. L. Keast, J. M. Knecht, V. Suntharalingam, K. Warner, P. W. Wyatt and D.-R. W. Yost, "A wafer-scale 3-D circuit integration technology," *IEEE Transactions on Electron Devices*, vol. 53, no. 10, pp. 2507-2516, 2006.
- [120] M. Rimskog and T. Bauer, "High density Through Silicon Via (TSV)," in *Symposium on Design, Test, Integration, and Packaging of MEMS/NOEMS, 2008.*, Nice, France, 2008.
- [121] T. W. Kelley, P. F. Baude, C. Gerlach, D. E. Ender, D. Muyres, M. A. Haase, D. E. Vogel and S. D. Theiss, "Recent Progress in Organic Electronics: Materials, Devices, and Processes," *Chemistry of Materials*, vol. 16, pp. 4413-4422, 2004.
- [122] Chemical Sciences and Society Summit, "Organic Electronics for a Better Tomorrow: Innovation, Accessibility, Sustainability," Royal Society of Chemistry,

- San Francisco, 2012.
- [123] J. Lu, K.-S. Moon and C. P. Wong, "High-k Polymer Nanocomposites as Gate Dielectrics for Organic Electronics Applications," in *IEEE Electronic Components and Technology Conference*, Reno, NV, 2007.
- [124] V. Subramanian, P. C. Chang, J. B. Lee, S. E. Molesa and S. K. Volkman, "Printed Organic Transistors for Ultra-Low-Cost RFID Applications," *IEEE Transactions On Components And Packaging Technologies*, vol. 28, no. 4, pp. 742-747, 2005.
- [125] C. D. Dimitrakopolous and D. J. Mascaró, "Organic thin-film transistors: A review of recent advances," *IBM Journal of Research and Development*, vol. 45, no. 1, pp. 11-27, 2001.
- [126] H. Kang, R. Kitsomboonloha, J. Jang and V. Subramanian, "High-Performance Printed Transistors Realized Using Femtoliter Gravure-Printed Sub-10 um Metallic Nanoparticle Patterns and Highly Uniform Polymer Dielectric and Semiconductor Layers," *Advanced Materials*, vol. 24, no. 22, pp. 3065-3069, 2012.
- [127] M. Baklar, P. H. Wobkenberg, D. Sparrowe, M. Gonclaves, I. McCulloch, M. Heeney, T. Anthopolous and N. Stingelin, "Ink-jet printed p-type polymer electronics based on liquid-crystalline polymer semiconductors," *Journal of Materials Chemistry*, vol. 20, pp. 1927-1931, 2010.
- [128] K. Tetzner, K. A. Schroder and K. Bock, "Photonic curing of sol-gel derived HfO<sub>2</sub> dielectrics for organic field-effect transistors," *Ceramics International*, vol. 40, no. 10, pp. 15753-15761, 2014.
- [129] DuPont Teijin Films, "Properties of various high performance films," DuPont Teijin Films, [Online]. Available: [http://www.tejindupontfilms.jp/english/product/hi\\_film.html](http://www.tejindupontfilms.jp/english/product/hi_film.html). [Accessed 03 06 2015].
- [130] DuPont, "DuPont Kapton HN Technical Data Sheet," DuPont, 2011. [Online]. Available: <http://www.dupont.com/content/dam/assets/products-and-services/membranes-films/assets/DEC-Kapton-HN-datasheet.pdf>. [Accessed 03 06 2015].
- [131] D. Tobjork and R. Osterbacka, "Paper Electronics," *Advanced Materials*, vol. 23, no. 17, pp. 1935-1961, 2011.
- [132] Corning, "Corning Willow Glass," Corning, 2015. [Online]. Available: <http://www.corning.com/worldwide/en/products/display-glass/products/corning-willow-glass.html>. [Accessed 03 06 2015].

# Appendix A

## Related Publications

---

The following is a list of all conference proceedings and journal publications that directly relate to this work.

- [1] J. A. Sadie, S. K. Volkman, V. Subramanian, "Demonstration of Inkjet-Printed Nanoparticle-based Inks for Solder Bump Replacement," in *Proceedings of 45<sup>th</sup> International Symposium on Microelectornics (IMAPS 2012)*, p. 419-424, 2012.
- [2] N. Quack, J. Sadie, V. Subramanian, M. C. Wu, "Through Silicon Vias and Thermocompression Bonding Using Inkjet-Printed Gold Nanoparticles for Heterogeneous MEMS Integration," in *Proceedings of 17<sup>th</sup> International Conference on Solid-State Sensors, Actuators, and Microsystems (IEEE Transducers 2013)*, p. 834-837, 2013.
- [3] J. A. Sadie, N. Quack, M. C. Wu, V. Subramanian, "Droplet-on-demand Inkjet-filled Through-silicon Vias (TSVs) as a Pathway to Cost-efficient Chip Stacking," in *Proceedings of 46<sup>th</sup> International Symposium on Microelectronics (IMAPS 2013)*, p. 866-871, 2013.
- [4] J. A. Sadie, V. Subramanian, "Three-dimensional Inkjet-printed Interconnects Using Functional Metallic Nanoparticle Inks," *Advanced Functional Materials.*, vol. 24, p. 6834-6842, 2014.
- [5] H. C. Nallan, J. A. Sadie, R. Kitsomboonloha, S. K. Volkman, V. Subramanian, "Systematic Design of Jettable Nanoparticle-based Inkjet Inks: Rheology, Acoustics, Jettability," *Langmuir*, vol. 30, no. 44, p. 13470-13477, 2014.
- [6] J. A. Sadie, H. C. Nallan, S.K. Volkman, V. Subramanian, "Systematic Ink Design and Solubility Enhancement via Genetic Algorithm for Nanoparticle-based Inkjet Inks," in *Proceedings of 31<sup>st</sup> International Conference on Digital Printing Technologies and Digital Fabrication (NIP/DigiFab 2015)*, 2015.
- [7] J. A. Sadie, S. K. Volkman, E. M. Chan, K-S. Sohn, V. Subramanian, "Metal Nanoparticle Solubility Enhancement via Heuristic Optimization," *Advanced Materials*, submitted.

# Appendix B

## Gold Nanoparticle Synthesis Procedure

---

### Chemicals

Hydrogen tetrachloroaurate(III) hydrate ( $\text{HAuCl}_4 \cdot x\text{H}_2\text{O}$ )

1-Dodecanethiol ( $\text{C}_{12}\text{H}_{26}\text{S}$ )

1-Octanethiol ( $\text{C}_8\text{H}_{17}\text{SH}$ )

1-Hexanethiol ( $\text{C}_6\text{H}_{13}\text{SH}$ )

1-Butanethiol ( $\text{C}_4\text{H}_9\text{SH}$ )

Sodium borohydride ( $\text{NaBH}_4$ )

Tetraoctylammonium Bromide ( $\text{C}_{32}\text{H}_{68}\text{BrN}$ )

Toluene ( $\text{C}_7\text{H}_8$ )

Deionized water

Ethanol ( $\text{C}_2\text{H}_5\text{OH}$ )

Acetone( $(\text{CH}_3)_2\text{CO}$ )

### Laboratory Equipment

Rotary Evaporator

High-frequency sound wave generator

Glass filtration frit

### Synthesis Process

The synthesis procedure consists of three main steps, of which different conditions yields different-sized nanocrystals. The reaction steps and the respective conditions are as follows: (1) temperature of the  $\text{NaBH}_4$  reduction step (2) the mole ratio of dodecanethiol:  $\text{HAuCl}_4 \cdot x\text{H}_2\text{O}$  (3) the rate of addition of  $\text{NaBH}_4$ .

- Add 12.10g of tetraoctylammonium bromide to a vigorously stirred solution of 645mL toluene. (Organic phase)
- Add 2.5g of  $\text{HAuCl}_4 \cdot x\text{H}_2\text{O}$  to 200mL of deionized water. This should be a yellow solution. (Aqueous phase)
- Mix the aqueous phase in the vigorously stirred organic phase. The aqueous phase should now be clear and the organic phase should be orange-brown.
- Isolate the organic phase and add the desired molar ratio amount of thiol. The solution must be stirred for 10 minutes at room temperature. The solution should become pale yellow or colorless if the mole ratio is greater than 2.
- Adjust the solution to the desired reduction temperature. (Use room temperature)
- Mix  $\text{NaBH}_4$ , 3.065g in 200mL of deionized water. (Reduction solution)
- Vigorously stir the organic phase as the reduction solution is added in. The reduction solution can be added over a period of 10s, 2min, or 15min. (Use 10s) The solution should now become very dark.
- Stir the solution for 30min at the reduction temperature, then for 3hr. at room temperature.

*(Murray Method)*

- Isolate the organic phase and remove all the solvent in a rotary evaporator. Do not allow the temperature to exceed 50<sup>0</sup>C to prevent partial decomposition of large gold cluster.
- Suspend the particles in 241.2mL of ethanol and sonicate the suspension briefly for complete dissolution of byproducts.
- Collect particles on a glass filtration frit. Wash with at least 645mL of ethanol and 1.210mL of acetone.
- Air dry particles or dry in vacuum.

**Physical properties of Reactants**

Chemical	Formula	Molecular Weight (g/mol)	Melting Point (°C)	Boiling Point (°C)	Density (g/mL)
Hydrogen tetrachloroaurate(III) hydrate	HAuCl <sub>4</sub> ·xH <sub>2</sub> O	339.79			3.900
1-Octadecanethiol	C <sub>18</sub> H <sub>39</sub> SH	286.5582	29-31	204-210	0.847
1-Dodecanethiol	C <sub>12</sub> H <sub>25</sub> SH	202.40		266-283	0.845
1-Octanethiol	C <sub>8</sub> H <sub>17</sub> SH	146.30		197-200	0.843
1-Hexanethiol	C <sub>6</sub> H <sub>13</sub> SH	118.24		150-154	0.838
1-Butanethiol	C <sub>4</sub> H <sub>9</sub> SH	90.19		98	0.842
Sodium borohydride	NaBH <sub>4</sub>				
Tetraoctylammonium Bromide	(C <sub>8</sub> H <sub>17</sub> ) <sub>4</sub> BrN	546.82	97-99		
Toluene	C <sub>6</sub> H <sub>5</sub> CH <sub>3</sub>	92.1402	-93	110.6	0.867
Deionized water	H <sub>2</sub> O	18.0152	0	100	0.955
Ethanol	C <sub>2</sub> H <sub>5</sub> OH	58.0798	-94.3	56.2	0.7857
Acetone	C <sub>3</sub> H <sub>6</sub> O	46.0688	-114.1	78.3	0.789

**Mole Ratio of Thiol:Gold**

Hydrogen tetrachloroaurate(III) hydrate = 2.5g (0.00736 mol)

Chemical	1:1		3:1		4:1		1/12:1	
Octadecanethiol	2.109068g	2.4900mL	6.327205g	7.4701mL	8.436273	9.9602mL	0.175756g	0.2075mL
Dodecanethiol	1.489664g	1.7588mL	4.468992g	5.2763mL	5.958656g	7.0350mL	0.124139g	0.1466mL
Octanethiol	1.076768g	1.2713mL	3.230304g	3.8138mL	4.307072g	5.0851mL	0.089731g	0.1059mL
Hexanethiol	0.870246g	1.0274mL	2.610739g	3.0823mL	3.480986g	4.1098mL	0.072521g	0.08562mL
Butanethiol	0.663798g	0.7837mL	1.991395g	2.3511mL	2.655194g	3.1348mL	0.055317g	0.06531mL

**Materials**

Chemical	CAS	Supplier	Catalog Number	Purity	Volume (L) / Mass (g)	Cost
Hydrogen tetrachloroaurate(III) hydrate	16903-35-8	Strem	79-0500	99.9	25 g	1298
Tetraoctylammonium bromide	14866-33-2	Sigma	294136	98	25 g	113
Sodium borohydride	16940-66-2	Strem	93-1118	98	50 g	29
Sodium borohydride	16940-66-2	Sigma	71321	99	25 g	47

# Appendix C

## Silver Nanoparticle Synthesis Procedure

---

### Chemicals

Silver acetate ( $\text{AgC}_2\text{H}_3\text{O}_2$ )

1-Dodecylamine ( $\text{C}_{12}\text{H}_{27}\text{N}$ )

1-Tetradecylamine ( $\text{C}_{14}\text{H}_{31}\text{N}$ )

1-Hexadecylamine ( $\text{C}_{16}\text{H}_{35}\text{N}$ )

1-Octadecylamine ( $\text{C}_{18}\text{H}_{39}\text{N}$ )

Phenylhydrazine ( $\text{C}_6\text{H}_8\text{N}_2$ )

Toluene ( $\text{C}_7\text{H}_8$ )

Acetone ( $\text{C}_3\text{H}_6\text{O}$ )

### Laboratory Equipment

1000 mL round-bottom flask for synthesis

Beakers for purification

Heated oil bath

Rotary Evaporator

### Synthesis Process

The synthesis involves three steps: nanoparticle formation in organic solution, nanoparticle extraction via rotary evaporation, and nanoparticle purification and washing. The synthesis involves using phenylhydrazine as a reducing agent and the appropriate alkyl amine as an encapsulant. The main variable condition is the molar ratio of alkyl amine to silver.

- Measure desired mass of silver acetate for reaction (typically 1 g or 5.99 mmol)
- Measure appropriate mass of alkyl amine to achieve desired molar ratio of alkyl amine:silver (typically on order of 5-10 mmol alkyl amine: 1 mmol silver)
- Add both materials to round-bottom flask and pour in 40 mL toluene per 1 mmol of silver
- Dissolve solution in oil bath at 60 °C. The solution should appear clear when dissolution of silver acetate and alkyl amine is complete.
- Measure appropriate mass of the reducing agent, phenylhydrazine, to achieve the desired molar ratio of reducing agent:silver (typically on order of 0.5-2 mmol reducing agent: 1 mmol silver)
- Dissolve reducing agent in toluene with a ratio of ~1 mmol reducing agent: 100 mmol toluene
- Mix dissolved reducing agent to stirring solution over the course of 5 minutes and allow to react for one hour at 60 °C. The solution should appear black.
- After one hour, quench reaction with 3 mL acetone.
- Use rotary evaporator to remove solvents from solution. A brown slurry will result

- Crash NPs with acetone. Use 100 mL acetone per 1 mmol silver. Allow NPs to settle for at least 10 minutes, and then decant supernatant.
- Repeat wash step above until supernatant appears perfectly clear.
- Add approximately 100 mL acetone to washed NPs and transfer to Buchner funnel with P5 filter paper for final washing and collection.
- DO NOT pull vacuum through Buchner funnel until all of the acetone has passed through (only pull vacuum to aid in drying nanoparticles after solvent has passed)
- Collect NPs and store in cold environment.

### Physical Properties of Reactants

Chemical	Formula	Molecular Weight (g/mol)	Melting Point (°C)	Boiling Point (°C)	Density (g/mL)
Silver Acetate	AgC <sub>2</sub> H <sub>3</sub> O <sub>2</sub>	166.91	---	---	3.26
1-Dodecylamine	C <sub>12</sub> H <sub>27</sub> N	185.35	~30	~248	0.806
1-Tetradecylamine	C <sub>14</sub> H <sub>31</sub> N	213.40	~39	162	0.8571
1-Hexadecylamine	C <sub>16</sub> H <sub>35</sub> N	241.46	44	330	0.813
1-Octadecylamine	C <sub>18</sub> H <sub>39</sub> N	269.51	51	232	0.86
Phenylhydrazine	C <sub>6</sub> H <sub>8</sub> N <sub>2</sub>	108.14	19.5	243.5	1.0978
Toluene	C <sub>7</sub> H <sub>8</sub>	92.1402	-93	110.6	0.867
Acetone	C <sub>3</sub> H <sub>6</sub> O	46.0688	-114.1	78.3	0.789

# Appendix D

## MATLAB Automated UV-Vis Analysis

---

```

%% UVVis_Combine
% This script will run the UVVis_Import command multiple times in order to
% combine multiple plates into a collective dataset

function [Plate,Spec,Data] = UVVis_Combine(count)

%Define Plate and Spec structs
Plate = struct('tot',[],'well_row',[],'well_col',[],'well_tot',[]);
Spec = struct('start',[],'step',[],'stop',[],'length',[],'spec',[]);
Data_temp = struct('plate_no',[],'well_no',[],'well_ID',[],...
    'well_row',[],'well_col',[],'well_data',[]);

%Initialize local variables
files = repmat({''},count,1);
rows = zeros(count,1);
cols = zeros(count,1);

rows_tot = 0;
cols_tot = 0;
well_tot = 0;

%Ask user which files to select
for i=1:count
    fprintf('File #%d. Enter name: ',i);
    files(i) = cellstr(input('','s'));
    fprintf('\tRows:\t\t');
    rows(i) = input('');
    fprintf('\tColumns:\t');
    cols(i) = input('');
    rows_tot = rows_tot + rows(i);
    cols_tot = max(cols_tot,cols(i));
    well_tot = well_tot + rows(i)*cols(i);
end
fprintf('Hit 0 to join by column. 1 to join by row.: ')

%Update Plate struct based on user input
Plate.tot = count;
Plate.well_row = rows_tot;
Plate.well_col = cols_tot;
Plate.well_tot = well_tot;

%Define Data struct
Data(well_tot) = struct('plate_no',[],'well_no',[],'well_ID',[],...
    'well_row',[],'well_col',[],'well_data',[]);

%Import data, fill out Data struct, and extract Spec struct
wells_start = 1;
for i=1:count
    [~,Spec,Data_temp] = UVVis_Import_2(files{i},rows(i),cols(i),i);
    wells_final = wells_start + rows(i)*cols(i)-1;
    Data(wells_start:wells_final) = Data_temp;
    wells_start = wells_final+1;
end

%Update values in Data struct
for i=1:Plate.well_tot
    Data(i).well_no = i;
    if Data(i).plate_no > 1
        Data(i).well_row = Data(i).well_row + (Data(i).plate_no-1)*rows(Data(i).plate_no-1,1);
    end
end
end

```

```

%% UVVis_Import_2
% This function will import tab-delimited UV-Vis spectra and place into
% three structs defining Well count, Spectrum details, and Data

function [Plate, Spec, Data] = UVVis_Import_2 (FileToRead,rows,cols,plate)
%% Open file and determine well count, scan parameter, and header size

% Clear variables, set scan strings to search for, and grab first line
well_match = 'Plate Type';
scan_match = 'Spectrum [';
fid = fopen(FileToRead);
tline = fgets(fid);
HeaderLines = 0;

%Define plate struct
Plate(1) = struct('plate_no',[],'well_row',[],'well_col',[],'well_tot',[]);

%Define spectrum struct
Spec(1) = struct('start',[],'step',[],'stop',[],'length',[],'spec',[]);

while ischar(tline)
    %Quit when end of header reached
    if strfind(tline,'Wavelength') ~= 0
        break
    end

    %Increment header counter
    HeaderLines = HeaderLines + 1;

    %Extract number of wells
    if strfind(tline,well_match) ~= 0
        div = textscan(tline,'%s');
        div_length = length(div{1,1});
        div_num = str2double(div{1,1});
        div_finite = isfinite(div_num);
        for i=1:div_length
            if div_finite(i)==1
                wells_total = div_num(i);
            end
        end
    end

    %Extract scan parameters
    if strfind(tline,scan_match) ~= 0
        [~,remain] = strtok(tline,['');
        div = textscan(remain,'%s');
        start_length = length(div{1,1}{1,1});
        spectrum_start = str2double(div{1,1}{1,1}(2:start_length-2));
        end_length = length(div{1,1}{3,1});
        spectrum_end = str2double(div{1,1}{3,1}(1:end_length-2));
        step_length = length(div{1,1}{5,1});
        spectrum_step = str2double(div{1,1}{5,1}(1:step_length-1));
    end

    %Grab next line
    tline = fgets(fid);
end

%close file
fclose(fid);

%Output all important extracted data to struct
Plate.plate_no = plate;
Plate.well_row = rows;
Plate.well_col = cols;
Plate.well_tot = rows*cols;
if rows*cols ~= wells_total
    warning('Extracting data from partial plate');
end
Spec.start = spectrum_start;
Spec.stop = spectrum_end;

```

```

Spec.step = spectrum_step;
Spec.length = (spectrum_end - spectrum_start)/spectrum_step + 1;
Spec.spec = transpose(spectrum_start:spectrum_step:spectrum_end);

%% Read data into array. Treat empty wells as empty cells in array.

%Define Data struct based on total number of wells
Data_temp(96)=struct('plate_no',[], 'well_no',[], 'well_ID',[], ...
    'well_row',[], 'well_col',[], 'well_data',[]);

Data(Plate.well_tot)=struct('plate_no',[], 'well_no',[], 'well_ID',[], ...
    'well_row',[], 'well_col',[], 'well_data',[]);

%Create formatSpec variables for reading files, including skip end of line
%for scans shorter than the whole length of the line
formatSpec_text = '%s';
formatSpec_data = '%s';
for i=1:96
    formatSpec_text = strcat(formatSpec_text, '%s');
    formatSpec_data = strcat(formatSpec_data, '%f');
end
formatSpec_text =strcat(formatSpec_text, '%*[\n]');
formatSpec_data =strcat(formatSpec_data, '%*[\n]');

%Open file and read in data to temp arrays
fid = fopen(FileToRead);
text = textscan(fid,formatSpec_text,1, 'delimiter', '\t', 'HeaderLines', HeaderLines);
data = textscan(fid,formatSpec_data,Spec.length, 'delimiter', '\t', 'TreatAsEmpty', '?????');

%Assign well_no, well_ID, well_col, and well_row values
for i=1:96
    Data_temp(i).plate_no = plate;
    Data_temp(i).well_no = i;
    Data_temp(i).well_ID = ['P', num2str(plate), '_', text{1,i+1}{1,1}];
    col_ind = mod(i,12);
    if col_ind == 0
        Data_temp(i).well_col = 12;
    else
        Data_temp(i).well_col = col_ind;
    end
    Data_temp(i).well_row = floor((i-1)/12+1);
end

%Rewrite data into final array
for i=1:96
    for j=1:Spec.length
        Data_temp(i).well_data(:,1)=data{1,i+1};
    end
end

%Transfer desired data to final struct
count = 0;
for i=1:96
    if Data_temp(i).well_row <= rows && Data_temp(i).well_col <= cols
        count = count + 1;
        Data(count).plate_no = Data_temp(i).plate_no;
        Data(count).well_no = Data_temp(i).well_no;
        Data(count).well_ID = Data_temp(i).well_ID;
        Data(count).well_col = Data_temp(i).well_col;
        Data(count).well_row = Data_temp(i).well_row;
        Data(count).well_data = Data_temp(i).well_data;
    end
end

%% Close file
fclose(fid);

```



```

end
sets_list((sets_tot-row_rep):sets_tot-1,1:col_rep) = row_rep_list;

sets_legend = repmat({''},sets_tot,3);
for i=1:sets_tot
    temp_in = num2str(sets_list(i,:));
    temp_in = regexprep(temp_in,' 0','');
    temp_in = regexprep(temp_in,' ','');
    sets_legend{i,1} = temp_in;
    sets_legend{i,2} = ['Rxn ',temp_in];
    sets_legend{i,3} = ['Rxn ',temp_in];
    if i==max(sets_tot)
        sets_legend{i,2} = 'Rxn All';
        sets_legend{i,3} = 'Rxn All';
    end
end

%% Ask user to define column x values
fprintf('----COLUMN DILUTION FACTORS----\n');
fprintf('\tEnter the dilution factor for each of the following columns.\n');
col_labels = repmat({''},Plate.well_col,2);
col_labels_sort = col_labels;
col_x = zeros(col_sample_tot,2);
for i=1:col_sample_tot
    fprintf('\tColumn %d: ',col_sample_list(i));
    temp_in = input('','s');
    col_labels{col_sample_list(i),1}=col_sample_list(i);
    col_labels{col_sample_list(i),2}=['1/',temp_in];
    col_x(i,1) = col_sample_list(i);
    col_x(i,2) = 1/str2double(temp_in);
end
for i=1:col_blank_tot
    col_labels{col_blank_list(i),1}=col_blank_list(i);
    col_labels{col_blank_list(i),2} = 'Blank';
end
%%Sort col_x and col_labels in ascending order (with blanks last)
col_x = sortrows(col_x,2);
for i=1:col_sample_tot
    col_labels_sort{i,1} = col_x(i,1);
    col_labels_sort{i,2} = col_labels{col_labels_sort{i,1},2};
end
for i=1:col_blank_tot
    col_labels_sort{i+col_sample_tot,1}=col_blank_list(i);
    col_labels_sort{i+col_sample_tot,2} = 'Blank';
end
col_labels = col_labels_sort;

%% Ask user to rename sets
fprintf('----RENAME DATASETS---\n\t');
temp_in = input('Enter 1 to rename set: ');
for i=1:sets_tot
    if temp_in == 1
        fprintf('\tDataset #%d is "%s". Rename to: ',i,sets_legend{i,2});
        sets_legend{i,3} = input('','s');
    end
end

%% Initialize struct for individual well analysis
%Include imported name, real name, flags, plot data, corrected plot data,
%peak intensity, peak wavelength, fwhm
fprintf('\n----IND_ANALYSIS STRUCT INITIALIZATION:');
Ind_Analysis(Plate.well_tot,1)=struct('plate_no',[],'well_no',[],'well_ID',[],...
    'well_name',[],'well_col',[],'well_row',[],'well_blank_flag',[],...
    'well_NaN_flag',[],'well_dil_frac',[],'well_dil_fact',[],'well_plot_color',[],...
    'datasets',[],'series',[],'well_data',[],'well_data_oc',[]);
for i=1:Plate.well_tot
    %Copy initial data directly from imported spectrum data
    Ind_Analysis(i).plate_no = Data(i).plate_no;
    Ind_Analysis(i).well_no = Data(i).well_no;
    Ind_Analysis(i).well_ID = Data(i).well_ID;
    Ind_Analysis(i).well_name = {};

```

```

Ind_Analysis(i).well_col = Data(i).well_col;
Ind_Analysis(i).well_row = Data(i).well_row;
Ind_Analysis(i).well_blank_flag = 0;
Ind_Analysis(i).well_data = Data(i).well_data;
Ind_Analysis(i).well_NaN_flag = ismember(1, isnan(Ind_Analysis(i).well_data));
Ind_Analysis(i).well_dil_frac = col_labels{col_x == Ind_Analysis(i).well_col, 2};
Ind_Analysis(i).well_dil_fact = col_x(col_x == Ind_Analysis(i).well_col, 2);
Ind_Analysis(i).well_data_oc = zeros(Spec.length, 1);
Ind_Analysis(i).peak = struct('I', NaN, 'lambda', NaN, 'FWHM', NaN);

%Set datasets
if ismember(Ind_Analysis(i).well_col, col_sample_list)==1
    [row, ~]=find(ismember(sets_list, Ind_Analysis(i).well_row));
    if isempty(row) == 0;
        Ind_Analysis(i).datasets=transpose(row);
    end
end

%Update series list
for j=1:length(Ind_Analysis(i).datasets)
    sets_index = Ind_Analysis(i).well_row;
    dataset_search = Ind_Analysis(i).datasets(j);
    Ind_Analysis(i).series(j) = find(sets_list(dataset_search, :)==sets_index);
end

%Update blank flag
if ismember(Ind_Analysis(i).well_col, col_blank_list)==1
    Ind_Analysis(i).well_blank_flag = 1;
    Ind_Analysis(i).well_dil_fact = NaN;
end

%Rename Sample_IDs
if isempty(Ind_Analysis(i).well_name)
    Ind_Analysis(i).well_name = Ind_Analysis(i).well_ID;
end
end
fprintf('\t\t\t\t\tCOMPLETE\n');

%% Initialize struct for dataset analysis
fprintf('----SET_ANALYSIS_INITIALIZATION:');
Set_Analysis(sets_tot, 1) = struct('number', [], 'name', [], 'rep_tot', []);
for i=1:sets_tot
    Set_Analysis(i).number = i;
    Set_Analysis(i).name = sets_legend{i, 3};
    Set_Analysis(i).rep_tot = nnz(sets_list(i, :));
    Set_Analysis(i).series(Set_Analysis(i).rep_tot, 1) = struct('number', [], ...
        'set_number', [], 'name', [], 'data', [], 'data_oc', []);
    for j=1:Set_Analysis(i).rep_tot
        Set_Analysis(i).series(j).number = j;
        Set_Analysis(i).series(j).set_number = sets_list(i, j);
        Set_Analysis(i).series(j).name = sets_legend(Set_Analysis(i).series(j).set_number, 3);
        Set_Analysis(i).series(j).data = nan(Spec.length, col_sample_tot);
        Set_Analysis(i).series(j).data_oc = nan(Spec.length, col_sample_tot);
        Set_Analysis(i).series(j).peak(col_sample_tot) =
struct('col', [], 'I', [], 'lambda', [], 'FWHM', []);
    end
    Set_Analysis(i).stat_spec = struct('min', [], 'max', [], 'avg', [], ...
        'stdev', [], 'stderr', [], 'n', []);
    Set_Analysis(i).I_peak(col_sample_tot) = struct('col', [], ...
        'min', [], 'max', [], 'avg', [], 'stdev', [], 'stderr', [], 'n', []);
    Set_Analysis(i).I_peak_fit = struct('ind_start', [], 'ind_stop', [], ...
        'slope', [], 'intercept', [], 'rsq', [], 'n', []);
    Set_Analysis(i).lambda_peak(col_sample_tot) = struct('col', [], ...
        'min', [], 'max', [], 'avg', [], 'stdev', [], 'stderr', [], 'n', []);
    Set_Analysis(i).FWHM(col_sample_tot) = struct('col', [], ...
        'min', [], 'max', [], 'avg', [], 'stdev', [], 'stderr', [], 'n', []);
    Set_Analysis(i).Plot = NaN(2, 1);
end
end
fprintf('\t\t\t\t\tCOMPLETE\n');

%% Reorganize Ind_Analysis struct columns

```







# Appendix E

## Complete Heuristic Optimization Dataset

Generation 1									
Reaction	C:Ag	$x_{C12}$	$x_{C14}$	$x_{C16}$	$x_{C18}$	RA:Ag	[Ag <sup>+</sup> ] mM	Mass Loading [%]	Silver Mass [%]
1	14.5343	0.2250	0.3450	0.0850	0.3450	1.2310	0.0663	34.85	71.22
2	13.1175	0.1625	0.1500	0.2975	0.3900	1.1695	0.0398	29.83	51.87
3	13.6784	0.2875	0.2825	0.3850	0.0450	1.0497	0.0638	30.75	58.61
4	14.4756	0.2550	0.2600	0.2600	0.2250	1.1356	0.0522	29.20	73.60
5	13.4857	0.1875	0.3675	0.0000	0.4450	1.1889	0.0401	31.62	47.91
6	10.9988	0.3025	0.3000	0.3025	0.0950	1.3353	0.0552	27.01	43.97
7	14.6302	0.0475	0.0400	0.4375	0.4750	1.2432	0.0517	23.67	63.41
8	13.2546	0.3250	0.4175	0.1675	0.0900	1.3088	0.0614	28.89	54.69
9	11.3872	0.3700	0.0925	0.3875	0.1500	1.0336	0.0408	27.86	67.64
10	14.7976	0.2350	0.2725	0.4050	0.0875	1.1837	0.0586	24.42	68.46
11	11.7935	0.2875	0.1525	0.1500	0.4100	1.3292	0.0520	29.20	47.42
12	14.5873	0.2450	0.0325	0.2575	0.4650	1.1534	0.0721	23.92	57.87
13	12.8040	0.2950	0.2950	0.1825	0.2275	1.2854	0.0628	23.00	61.46
14	11.5544	0.1750	0.0000	0.3375	0.4875	1.3621	0.0541	26.20	65.94
15	14.5084	0.3000	0.2250	0.3000	0.1750	1.4624	0.0647	27.02	71.47
16	12.3897	0.1975	0.1350	0.1875	0.4800	1.1221	0.0699	32.32	68.50
17	13.6673	0.2200	0.1125	0.2200	0.4475	1.3210	0.0565	25.96	66.51
18	12.0166	0.0325	0.2200	0.2275	0.5200	1.1929	0.0808	22.29	60.73
19	11.8809	0.2100	0.3175	0.2100	0.2625	1.1818	0.0465	24.37	59.86
20	10.1136	0.2250	0.2375	0.3900	0.1475	1.0321	0.0709	27.35	68.19
21	10.1019	0.3675	0.6200	0.0125	0.0000	1.3034	0.0561	32.43	55.05
22	13.4270	0.1250	0.0000	0.3250	0.5500	1.0012	0.0543	26.60	67.23
23	13.6104	0.3625	0.1525	0.0250	0.4600	1.0887	0.0845	29.71	64.67
24	12.3467	0.1300	0.1750	0.3525	0.3425	1.4681	0.0689	23.71	51.41
25	12.8366	0.0300	0.4075	0.4750	0.0875	1.2187	0.0410	28.94	65.38
26	12.5365	0.3900	0.3925	0.0300	0.1875	1.0949	0.0386	28.81	65.79
27	12.5841	0.1875	0.2575	0.2775	0.2775	1.3062	0.0556	25.94	64.35
28	12.2183	0.0350	0.1425	0.3000	0.5225	1.4181	0.0554	25.83	69.19
Generation 2									
Reaction	C:Ag	$x_{C12}$	$x_{C14}$	$x_{C16}$	$x_{C118}$	RA:Ag	[Ag <sup>+</sup> ] mM	Mass Loading [%]	Silver Mass [%]
1	14.3967	0.2325	0.4575	0.0750	0.2350	1.1587	0.0586	30.92	76.59
2	10.3000	0.4225	0.1075	0.2225	0.2400	1.2981	0.0696	32.25	78.16
3	13.3298	0.1800	0.0825	0.3175	0.4200	1.2841	0.0525	26.96	74.09
4	12.7002	0.2500	0.1775	0.2800	0.2925	1.2136	0.0538	27.65	75.28
5	14.5314	0.2575	0.3350	0.1425	0.2650	1.1389	0.0584	25.13	74.30
6	14.4785	0.2225	0.2700	0.2050	0.3025	1.2277	0.0601	40.11	70.34
7	13.0427	0.2000	0.3400	0.1500	0.3100	1.1841	0.0443	31.14	75.64
8	13.5997	0.2500	0.4275	0.3025	0.0200	1.2443	0.0569	25.11	75.55
9	11.3048	0.3675	0.4525	0.1075	0.0675	1.2428	0.0579	22.24	70.92
10	13.2274	0.2050	0.1325	0.2825	0.3800	1.0639	0.0653	28.53	74.27
11	12.8432	0.3025	0.3225	0.2825	0.0900	1.1079	0.0684	19.75	71.26
12	14.2522	0.3550	0.3500	0.0950	0.2000	1.2534	0.0525	27.17	75.03
13	12.7927	0.3300	0.2775	0.2250	0.1675	1.3039	0.0509	29.39	70.70
14	11.3667	0.2150	0.2100	0.3375	0.2350	1.1146	0.0701	26.93	72.32
15	11.1391	0.2075	0.1650	0.2425	0.3850	1.0396	0.0707	30.41	75.43
16	13.2506	0.2375	0.2350	0.1425	0.3850	1.1641	0.0684	30.98	73.72

17	12.3962	0.3025	0.3450	0.2250	0.1250	1.2668	0.0630	26.68	72.55
18	12.8107	0.3600	0.2025	0.1950	0.2425	1.2338	0.0621	22.77	69.79
19	12.8336	0.1875	0.3275	0.1625	0.3225	1.1971	0.0693	28.39	74.25
20	13.1328	0.2000	0.2250	0.3325	0.2425	1.4311	0.0559	27.66	70.44
21	13.6895	0.1850	0.2100	0.2825	0.3225	1.1726	0.0652	23.17	73.42
22	10.9416	0.3850	0.3525	0.2550	0.0075	1.2138	0.0624	29.22	73.11
23	12.8387	0.2925	0.5075	0.1600	0.0400	1.1393	0.0575	28.77	76.51
24	13.6104	0.3625	0.1525	0.0250	0.4600	1.0945	0.0845	32.26	73.43
25	13.4857	0.1000	0.2075	0.3550	0.3375	1.1889	0.0401	29.70	74.24
26	14.5084	0.3000	0.2250	0.3000	0.1750	1.4624	0.0763	21.97	74.47
27	13.1175	0.1825	0.1650	0.3275	0.3250	1.1695	0.0398	30.34	78.67
28	11.5544	0.1075	0.0000	0.4975	0.3950	1.3621	0.0541	34.09	76.38
29	11.3872	0.3700	0.0925	0.3875	0.1500	1.0336	0.0813	32.73	74.61
30	11.0387	0.325	0.4175	0.1675	0.09	1.3088	0.0614	27.09	75.46
31	10.1136	0.1225	0.4575	0.2975	0.1225	1.0321	0.0709	29.35	77.81
32	12.2183	0.0325	0.205	0.2775	0.485	1.4181	0.0554	25.00	74.50
Generation 3									
Reaction	C:Ag	x <sub>C12</sub>	x <sub>C14</sub>	x <sub>C16</sub>	x <sub>C118</sub>	RA:Ag	[Ag <sup>+</sup> ] mM	Mass Loading [%]	Silver Mass [%]
1	14.0893	0.4250	0.1400	0.2000	0.2300	1.2550	0.0669	21.52	75.05
2	10.4679	0.3550	0.3075	0.1250	0.2125	1.2965	0.0552	28.71	76.09
3	14.4408	0.1875	0.2400	0.2600	0.3125	1.2112	0.0599	31.89	74.17
4	13.2110	0.2025	0.2575	0.1075	0.4325	1.1893	0.0462	35.24	67.92
5	13.0902	0.1675	0.2550	0.2200	0.3575	1.1770	0.0408	28.78	72.46
6	12.3512	0.2200	0.2525	0.1650	0.3625	1.1791	0.0414	33.54	71.17
7	13.2635	0.1550	0.2950	0.2075	0.3425	1.1887	0.0429	20.66	73.71
8	13.2649	0.1450	0.2600	0.2925	0.3025	1.1843	0.0415	25.55	62.50
9	12.9485	0.2500	0.4100	0.2625	0.0775	1.2968	0.0580	26.56	74.61
10	11.6924	0.3275	0.4325	0.2050	0.0325	1.2563	0.0603	28.07	77.01
11	12.0422	0.1650	0.4200	0.2500	0.1650	1.0426	0.0621	25.33	74.17
12	12.4681	0.1900	0.4925	0.1175	0.2000	1.1482	0.0674	28.31	72.14
13	12.7035	0.2275	0.1700	0.2225	0.3800	1.1473	0.0402	24.04	75.02
14	12.8037	0.1625	0.1400	0.2850	0.4125	1.1444	0.0695	25.61	73.87
15	14.4307	0.2525	0.4025	0.0850	0.2575	1.2247	0.0598	28.91	75.09
16	14.5028	0.2100	0.3900	0.0775	0.3225	1.1650	0.0651	32.15	74.62
17	10.4059	0.3100	0.0200	0.3425	0.3275	1.3237	0.0656	33.99	76.29
18	11.4510	0.1650	0.1300	0.3800	0.3225	1.3365	0.0581	19.55	74.60
19	12.0928	0.1600	0.0650	0.4550	0.3175	1.3510	0.0572	21.40	75.66
20	12.3028	0.2350	0.4250	0.2175	0.1225	1.1504	0.0544	29.80	71.69
21	12.9383	0.2500	0.4400	0.1400	0.1700	1.1493	0.0586	28.56	74.25
22	13.1560	0.2825	0.2875	0.1650	0.2600	1.1541	0.0674	20.61	73.96
23	13.5664	0.1975	0.4625	0.0875	0.2525	1.1666	0.0464	28.09	76.06
24	13.9478	0.2175	0.1650	0.3100	0.3075	1.1616	0.0520	30.10	70.33
25	13.6104	0.1800	0.0850	0.3950	0.3400	1.0945	0.0845	35.34	72.60
26	10.1136	0.1400	0.4100	0.3175	0.1325	1.0321	0.0709	27.77	76.14
27	13.1175	0.1525	0.1425	0.2850	0.4200	1.1695	0.0398	28.22	74.56
28	10.1019	0.2175	0.3850	0.0100	0.3875	1.3034	0.0561	36.72	76.93
29	11.8930	0.1625	0.1500	0.2950	0.3925	1.1695	0.0398	33.06	74.69
30	12.8387	0.2900	0.5050	0.1650	0.0400	1.1393	0.0813	20.42	75.64
31	11.3872	0.3325	0.0875	0.435	0.145	1.0336	0.0813	26.71	75.92
32	11.3872	0.315	0.2025	0.34	0.1425	1.0336	0.0813	26.23	76.06
33	10.1136	0.0975	0.3575	0.2625	0.2825	1.0321	0.0709	37.89	75.11